Linking *in situ* crystallisation and magma replenishment in the Rum Layered Intrusion, NW Scotland

LUKE NATHAN HEPWORTH

Thesis submitted for the degree of Doctor of Philosophy in Earth Science

October 2018

Keele University

ABSTRACT

Layered intrusions offer an exceptional opportunity to study magmatic processes operating in the upper crust, including the concentration of world class precious-metal deposits. Despite the importance for understanding igneous processes and mineral resources, the fundamental construction mechanism of these intrusions is not well understood. The Rum Layered Suite (RLS) in NW Scotland represents an archetypal open-system layered intrusion that formed as part of the North Atlantic Igneous Province ~60 Ma. The peridotite cumulates within the RLS are poorly studied, where formation is typically attributed to the early stages of batch-fractionation from picritic and basaltic magma. This study focuses on the peridotite cumulates from Unit 10 in the Eastern Layered Intrusion (ELI) and Western Layered Intrusion (WLI). The cumulates contain abundant harrisite, an unusual skeletal-olivine bearing peridotite that crystallised *in situ*. Harrisite layers are used to represent picrite sills, with features of harrisite in Unit 10 and WLI, inconsistent with processes occurring on the magma chamber floor, also highlighting multiple replenishment events. The unusual olivine morphology in harrisites is controlled by the crystal mush temperature on intrusion, enhancing undercooling (i.e., chilling). Picrite emplacement caused a reaction with intercumulus plagioclase, forming Cr-spinel seams *in situ* alongside harrisite. The seam formed in discrete intra-mush melt channels where spinel chemistry, texture, and precious-metal enrichment is controlled by melt flux. Lateral magma intrusion and melt migration was facilitated by slow gravitational collapse of the crystal mush, producing planar shear zones and hot tears in a high-crystallinity framework. Repeated sill emplacement caused widespread dissolution to pre-existing cumulate and recrystallisation of primary mineralogy *in situ* by infiltrating melt. The evidence presented here is used to argue against traditional magma chamber models of layered intrusion growth, where the RLS instead represents a sill complex, consisting of numerous sill-like replenishment events into pre-existing feldspathic cumulate. The upward growth of layered sequences typically attributed to relative age is refuted as sill emplacement is random. As such, the structural position of cumulate sequences in layered intrusions, especially for structurally low ultramafic cumulates, cannot be used as an indicator of relative age. The sill complex model for layered intrusion growth is not restricted to the RLS, where evidence presented here supports sill emplacement mechanisms even in the largest layered intrusions.

ACKNOWLEDGEMENTS

I'm immeasurably grateful to Brian O'Driscoll for inviting me to study some incredible rocks and allowing me to flex my imagination and apply it to the geology of Rum to what I hope is great affect. Thanks a lot for putting up with my constant stream of spurious, unfounded speculation, and helping me refine it into something more tangible. Ralf Gertisser is thanked for the very same, and for guidance and opportunities (and humour) during my time at Keele. It was a humbling experience. During this tremendous test of endurance, Amy Gough, Adam Jeffery, and Steve Rogers are appreciated enormously for entertaining friendship with me for four long years without anything to show for it. Rebecca Wiltshire, Amy Parker, and Tom Cain are thanked as much. I sincerely hope you'll continue to humour friendship with me into academia and beyond, and join me on the dancefloor when the lights go down and we face the music. For the constant encouragement, and that one time I burst drunkenly into hysterical tears and phoned you at three in the morning because my paper was rejected (for the second time…out of four), I thank my Mother and Darren. Their boundless care and understanding throughout the whole process was a comforting glow even on the dimmest of days. With assistance and support during the collection of various data sets, I greatly acknowledge Peter Greatbatch and David Wilde for countless thin sections and awkward sample preparation, and to Andreas Kronz for teaching me about microprobe analysis at the University of Göttingen. Stephen Daly is thanked for letting me loose in the laboratory at University College Dublin, and to Mick Murphy for his assistance and patience with me during some complicated analysis. Rich Burgess is also thanked for assistance all thing I.T, and for his humour in the office. Discussions with Henry Emeleus are very much appreciated on various aspects of Rum geology. For time spent on the most beautiful island in the world, I'm so grateful for the experience of being part of the community on Rum, if only for a few months a year, and for the endless hospitality I was presented with from the moment I stepped off the ferry. Fliss Fraser is thanked in particular for accommodating me each year, and for periodically checking if I actually came back from the field. Scottish National Heritage are thanked for permissions to sample the geology, and to Lesley Watt for logistical assistance on Rum, ensuring I don't anger any revenge seeking eagles, or other murderous wildlife. To my examiners, I hope there is something new to be gained. I enjoyed it a lot.

DEDICATION

‘’DEEP PEACE OF THE RUNNING WAVE TO YOU
DEEP PEACE OF THE FLOWING AIR TO YOU
DEEP PEACE OF THE QUIET EARTH TO YOU
DEEP PEACE OF THE SHINING STARS TO YOU
DEEP PEACE OF THE SON OF PEACE TO YOU’’

‘’DEEP PEACE OF THE RUSHING STEAMS TO YOU
DEEP PEACE OF THE ROARING GALES TO YOU
DEEP PEACE OF THE ENDURING PEAKS TO YOU
DEEP PEACE OF THE PIERCING COLD TO YOU
DEEP PEACE OF THE GLARING SUN TO YOU
DEEP PEACE OF THE ROAMING DEER TO YOU
DEEP PEACE OF THOSE CURIOUS COOS TO YOU
DEEP PEACE OF THE GRASSY GLENS TO YOU
DEEP PEACE OF THAT GRAND OLD HOME TO YOU
DEEP PEACE OF THE CROWN OF CLOUD TO YOU
DEEP PEACE OF THE DIAMOND ISLE TO YOU’’

For Joan Hilda Moriarty
(for Nan)

DEEP PEACE TO YOU

CONTENTS

COMMONLY USED ABBREVIATIONS

RLS	Rum Layered Suite
ELI	Eastern Layered Intrusion
WLI	Western Layered Intrusion
CI	Central Intrusion
LLF	Long Loch Fault
LP	Lower Peridotite (Unit 10)
UP	Upper Peridotite (Unit 10)
AMP	Ard Mheall Peridotite Member (WLI
UAM	Upper Ard Mheall Member (WLI)
TSM	Transitional Member (WLI)
HBM	Harris Bay Member (WLI)
CSD	Crystal size distribution
SD	Spatial distribution

LIST OF FIGURES AND TABLES

CHAPTER 1 – INTRODUCTION

1.1 RATIONALE

Layered mafic-ultramafic intrusions offer an exceptional opportunity to study the processes of magmatic differentiation and solidification within upper crust, particularly the accumulation of crystal mushes and processes operating within the crystal framework (Sparks *et al.*, 1985; Tepley & Davidson, 2003; Holness, 2005; Humpreys, 2009; Tegner *et al.*, 2009; O’Driscoll *et al.*, 2009a; Namur & Charlier, 2012; Holness *et al.*, 2013; 2015; 2017a; Namur *et al.*, 2014; Leuthold *et al.*, 2014; Veksler *et al.*, 2015; Namur *et al.*, 2015). Although the study of layered intrusions contributes to the understanding of magmatic differentiation and phase petrology, many layered intrusions host economic reserves of critical metals such as chromium, vanadium, and precious metals such as the platinum-group elements (Mungall & Naldrett, 2008). Understanding the fundamental construction mechanisms of layered intrusions and the magmatic processes operating during long and complex solidification histories is important when elucidating processes responsible for the concentration of high grade ore-deposits.

1.2 THE HISTORICAL INTERPRETATION OF LAYERED IGNEOUS ROCKS

Layered intrusions can be broadly demarcated into two groups; ‘closed-system’ where the entire intrusion was formed from a single pulse of magma, such as the Skaergaard Intrusion, Greenland (Wager & Deer, 1939); or ‘open-system’ in which the intrusion consists of multiple pulses of magma, such as the Bushveld Complex, South Africa (Eales & Cawthorn, 1996), and the Rum Layered Suite, Scotland (Brown, 1956; Wadsworth, 1961). In closed-system layered intrusions, the magma chamber is viewed as a crystal-free body of magma crystallising inwards, with constant crystal settling (or flotation) onto the floor or roof, culminating in a feature known as the ‘sandwich horizon’ where the roof, floor, and walls meet, typically comprising the evolved, refractory components such as alkali feldspar and quartz (Wager & Deer, 1939; McBirney, 2002). Open-system layered intrusions can be more complex, formed from multiple batches of magma, each with a potentially very distinct composition, resulting in a variety of mafic and ultramafic cumulate sequences with no (or disrupted) stratigraphic fractionation trend (e.g., Tanner *et al*., 2014). Many open-system layered intrusions, despite the variations in size or mineralogy, have the same broad structure. The Bushveld Complex, Stillwater Complex (USA), and Rum Layered Suite all have ultramafic (typically olivine-rich) cumulates towards the structural base, transitioning to more evolved components such as plagioclase and pyroxene, with plagioclase with increasing height (Brown, 1956; Jackson, 1961; Wadsworth, 1961; Wilson, 2015).

The experimental work of Bowen (1915) into magmatic differentiation, coupled with the discovery of the Skaergaard Intrusion by Wager & Deer (1939), has had a profound effect on layered intrusion petrology, particularly the processes involved in the generation of magmatic layering, and the evolution and conceptualisation of magmatic systems. As such, the ultramafic–mafic transition with height has historically been interpreted as the younging direction, driven by gravity settling as in sedimentary environments (Fig. 1.1). This is particularly true where the sequence follows the simple fractionation trend in basaltic liquids from olivine–plagioclase–clinopyroxene (*cf*. Morse, 1980). Gravity-driven growth overwhelms the literature, with crystal settling from a ‘resident magma’ typically at the heart of many processes in layered intrusions irrespective of lithology (see Wager & Brown, 1968; Namur *et al*., 2015). Though prevalent, the concepts of crystal settling have not gone unchallenged, where field or petrographic features are incompatible with gravity-driven growth of layers, and require re-examination, instead invoking the sinking of crystal rafts or clumps, or discarding the concept entirely, and instead suggesting crystallisation *in situ* (Campbell, 1978; McBirney & Noyes, 1979; Huppert & Sparks, 1981). The process of *in situ* crystallisation in layered intrusions is still an underrepresented process, but one which has gained recent favour where field studies have highlighted features that cannot be explained by crystal settling, and where textural studies have come to similar conclusions, suggesting a more prevalent process *in situ* than currently understood (e.g., Campbell, 1978; O’Driscoll *et al*., 2007a; 2009a; 2010; Latypov *et al*., 2013; 2015; 2017). The study of igneous textures has been key in interpreting the development of igneous bodies, and of significantly more importance where these bodies have cooled slowly, giving them the potential to have undergone various, quantifiable physical and magmatic processes that can alter the texture (Boudreau, 1994; Higgins, 1998; 2002; 2006; Boorman *et al*., 2004; Holness, 2007; 2005;

O'Driscoll *et al*., 2007; 2008; 2009a; 2010; Barnes & Jones, 2013; Hunt *et al*., 2016). Of the studies into the textural development of layered intrusions, *in situ* crystallisation is discussed more widely, where quantitative textural analysis does not show typical gravity-driven processes, and instead reveal the importance of post-cumulus (post-accumulation) processes such as compaction, filter-pressing, and textural coarsening (Higgins, 2002; 2006; Boorman *et al*., 2004). Textural studies which quantify the textural changes in pre-existing cumulate caused by replenishment often highlight the dynamic, open-system nature of layered intrusions, not only at the magma chamber floor, but also within the crystal mush where contact metamorphic, and metasomatic effects can drastically alter the original textures of the cumulate (Holness, 2007; Holness *et al*., 2007; Leuthold *et al*., 2014; 2015). Furthermore, so-called 'non-dynamic' features that do not result from large-scale movement of melt of crystals shares parallels with solid-state re-ordering within shear zones in high-strain metamorphic environments, resulting in prominent features such as mineralogically segregated banding that have strong similarities to layering observed in igneous intrusions (Boudreau & McBirney, 1997; Boudreau, 2011; Glazner & Boudreau, 2011; Namur *et al*., 2015).

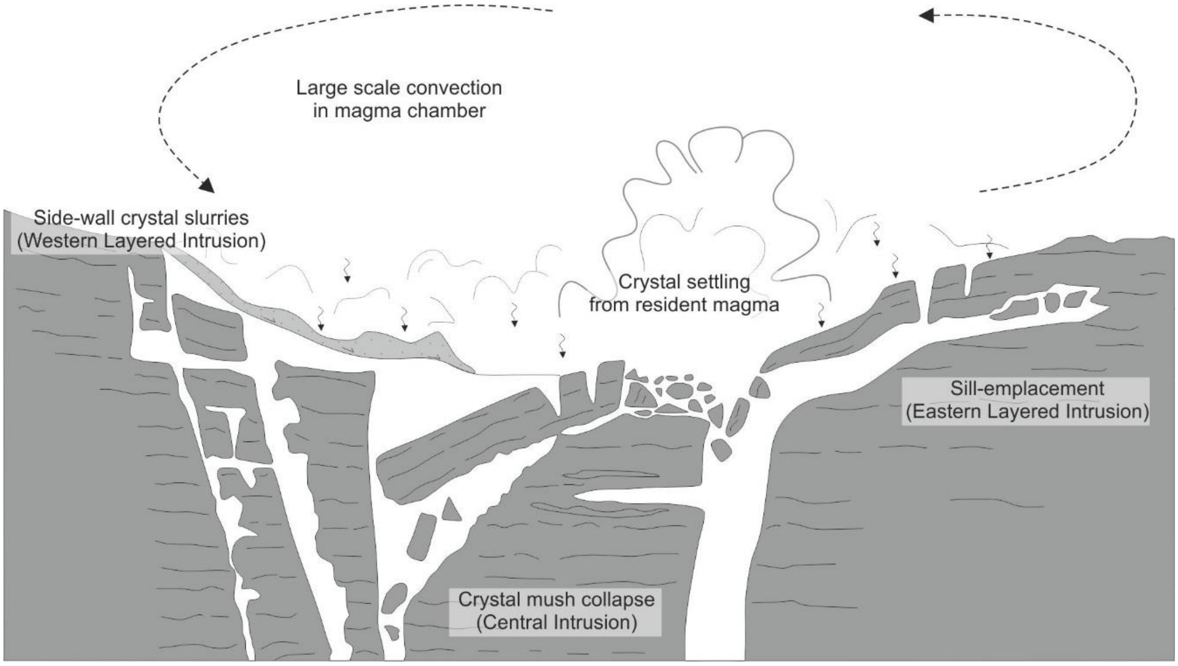

◀FIGURE 1.1: Classic conceptualisation of a layered intrusion 'magma chamber' modified from Emeleus *et al*. (1996) of the Rum Layered Intrusion (RLS). Commonly prescribed processes in layered intrusion development such as convection, crystal settling, slurry replenishment, and sill-emplacement are illustrated. See text for details.

1.2.1 Sill emplacement and the mechanics of crystal mushes in layered intrusions

The structural position at which a new layer is formed or added (i.e., replenishment) in layered intrusions is almost unanimously assumed to be the magma-mush interface; between the resident magma and crystal pile at the base of the chamber, where crystals are accumulating (Fig. 1.1). There are very few interpretations to the contrary, where magma is instead introduced into the cumulate sequence as a sill. Bédard *et al.* (1988) noted intrusive, non-stratiform and discontinuous contacts of the Unit 9 peridotite in the Rum Eastern Layered Intrusion in Scotland and went on to interpret this cumulate body as a sill, suggesting the possibility that many of peridotites of Rum could form this way (Fig. 1.1). The intrusive, sill-like emplacement of the Unit 9 peridotite was later supported by textural and geochemical evidence for modification and reactions with the host crystal mush and invading sill (Holness *et al.*, 2007). Similar interpretations were made in Caledonian layered intrusions in Norway where a strong emphasis was placed on sill and host reactions (Tegner & Robins, 1996). More recently, out-of-sequence layers have been identified via high-resolution geochronology in the Bushveld Complex, arguing against vertical build-up of crystal mushes, and proving the existence of sill-like emplacement, forming distinct layers within layered intrusions, questioning traditional magma chamber models (Mungall *et al.*, 2016; Wall, 2016). Due to the paucity of sill emplacement models in layered intrusions compared to traditional gravity-driven models, the physical properties of crystal mushes is largely unknown, despite playing a crucial role in determining how the crystal framework accommodates the intrusion of potentially large volumes of magma, while maintaining parallelism (Marsh, 2002; Mungall *et al.*, 2016). Silicate crystal mushes are good natural analogues for metal castings studied in material science, where they consist of a framework of crystals and an interstitial liquid (Lahaie & Bouchard, 2001; Eskin *et al.*, 2004). Natural silicate crystals mushes undergo mechanical processes similar to the metal castings, in particular, ‘hot tearing’, where intergranular (or interdendritic) lines of weakness form and fill with the interstitial liquid parallel to the cooling direction. Hot tearing has been implemented to explain a range of well-oriented and textured distinct schlieren and lenses in lava flows and shallow intrusions (Philpotts *et al.*, 1996; Geshi, 2001; Marsh, 2002). The Marginal Border Series of the Skaergaard Intrusion has also proved a pertinent area of study for hot tearing and the mechanical behaviour of crystal mushes. The margins crystallised without any structural support from the main magma body, resulting in strong lateral pulling stress, forming a range of well-oriented, texturally (and chemically) distinct zones across the layered gabbros from the accumulation of melt into these hot tears (Humphreys & Holness, 2010; Namur *et al*., 2013). Importantly, the studies show that the crystal mush is a very mobile, dynamic environment, where mechanical (and sub-solidus) shearing, fracturing, and melt migration can occur, instead of a common assumption that post-cumulus processes are limited to grain movement as flows and slurries (Maier *et al*., 2013) or compaction (Holness *et al*., 2017a).

1.2.2 The concentration of precious-metal enriched spinel horizons in layered intrusions

Spinel (Cr-spinel) horizons are a common feature of open-system layered intrusions, found in an extreme spectrum of scales from millimetres to metres thick, and laterally extensive over centimetre–kilometres (Fig. 1.2). The spinel horizons can demarcate two distinct lithologies (e.g., Irvine, 1977; Mondal & Mathez, 2007; O’Driscoll *et al*., 2010; Latypov *et al*., 2015) or be found within seemingly homogeneous cumulate (e.g., Voodouw *et al*., 2009; O’Driscoll *et al*., 2009a; Campbell & Murck, 1993), without any textural or field variation within the spinel horizon between the two settings. There does not appear to be any specific section in the layered sequence or any particular lithology the horizons occur with, as they have been found hosted within anorthosites and peridotites (Jackson, 1961; Henderson & Suddaby, 1971; Campbell & Murck, 1993; O’Driscoll *et al*., 2009a; Voodouw *et al*., 2009; Mukherjee *et al*., 2017), or between feldspathic, pyroxenitic, and peridotitic cumulates (Irvine, 1977; Roach & Roeder, 1998; Mondal & Mathez, 2007; O’Driscoll *et al*., 2010; Wilson, 2015; Latypov *et al*., 2015). Where thick, near-monomineralic spinel horizons occur in the stratigraphy, thinner horizons or stringers of spinel are typical near to the ‘main horizon’ (Cameron, 1977; O’Driscoll *et al*., 2009a; O’Driscoll *et al*., 2010; Latypov *et al*., 2015).

The concentration of spinel horizons in layered intrusions can be considered a two-fold problem, as the basic chemical requirements which crystallise extreme concentrations of spinel must be met, but also the physical process by which it can accumulate into often near-monomineralic layers. Spinel horizons represent a marker for replenishment, which like many concepts in layered intrusions is focused around gravity-driven processes at the magma chamber floor. The formation of extreme (and sudden) abundances of spinel in the sequence, typically only found in trace concentrations in mafic-ultramafic rocks, is further complicated by the complex chemical requirements that fractionate large amounts of non-cotectic concentrations of spinel. Irvine (1977) proposed, adapted from a previous model (Irvine, 1975), that spinel-saturation could be achieved by magma mixing. He suggested that the input of newly replenished primitive magma could mix with a more evolved resident magma, the hybrid of which is driven off the cotectic and into the spinel field (Fig. 1.3). Adaptations of this model have been applied in other layered intrusions. Spandler *et al.* (2005) suggested that the same broad reaction of Irvine (1977) could be achieved by the assimilation of felsic country rock, evidenced by inclusions within spinel from the Ultramafic Series of the Stillwater Complex, USA. Assimilation was proposed in the Rum Layered Suite for spinel horizons between sequence units, delimiting peridotite and anorthosite, where O'Driscoll *et al.* (2009a; 2010) argued that felsic (feldspathic) cumulate was assimilated, forming a hybrid liquid with a bulk composition within the spinel field (Fig. 1.3; Morse, 1980). The model has also been recently applied to the Merensky Reef of the Bushveld Complex, with emphasis on the ability of the hybrid liquid to become superheated, enhancing thermo-mechanical erosion of cumulate, allowing for depressions, culminations, and overhangs to develop within the horizon (Latypov *et al*., 2013; Latypov *et al*., 2015).

The accumulation of spinel horizons has been variably adapted, but typically invokes a form of gravity-driven concentration (e.g., Jackson, 1961; Henderson & Suddaby, 1971; Lipin, 1993). Magma fountaining, where less dense magma enters the magma chamber, increases the efficiency of mixing, where the voluminously crystallised spinel settles down to the floor (Campbell *et al*., 1983; Barnes & Naldrett, 1986). A process of mechanical sorting was suggested by Maier & Barnes (2008) and Maier *et al.* (2013), where the density contrast of the various minerals within the stratigraphy can effectively sort themselves into near-monomineralic layers along shallowly dipping slopes, supported by basic experimental constraints (Forien *et al*., 2016). There have been suggestions that the magma was already saturated in spinel on entry into the chamber, carrying a dense cargo of spinel crystals (Mondal & Mathez, 2007), but which also assumes the crystals settled into the concentrated

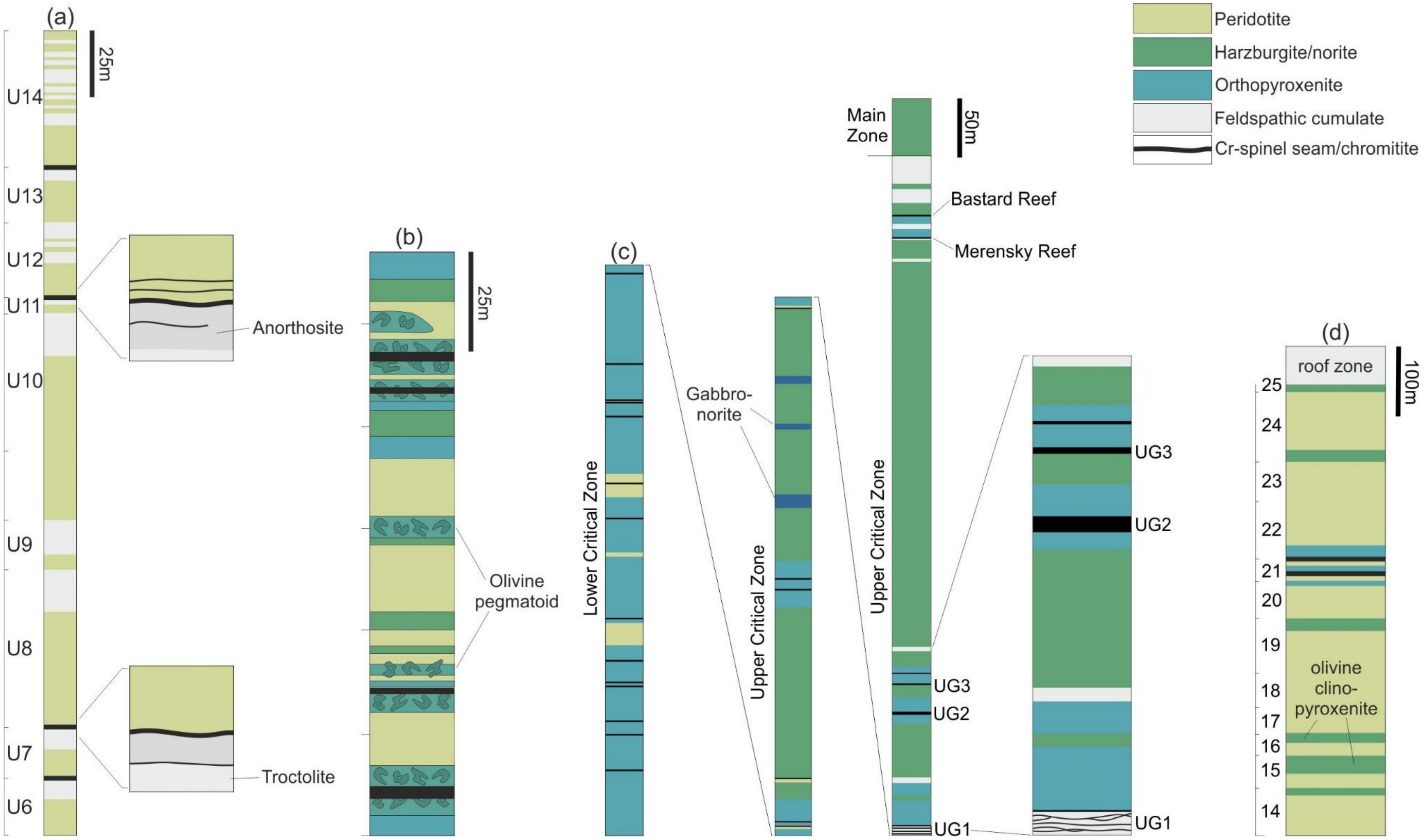
(a)
25m
U14
U13
U12
U11
U10
U9
U8
U7
U6
Anorthosite
Troctolite
(b)
25m
Olivine pegmatoid
(c)
Lower Critical Zone
Gabbro-norite
Upper Critical Zone
Main Zone
50m
Bastard Reef
Merensky Reef
Upper Critical Zone
UG3
UG2
UG1
(d)
roof zone
100m
25
24
23
22
21
20
19
18
17
16
15
14
olivine clino-pyroxenite
Peridotite
Harzburgite/norite
Orthopyroxenite
Feldspathic cumulate
Cr-spinel seam/chromitite

◀FIGURE 1.2: Schematic lithological logs for Cr-spinel (and chromitite) seam bearing cumulate sequences from (a) the Rum Layered Intrusion, adapted from Emeleus *et al.* (1996) and O'Driscoll *et al.* (2009a; 2010), (b) Ultramafic Series, Stillwater Complex, modified after Campbell & Murck (1993), (c) Critical Zone, Bushveld Complex, after Mondal & Mathez (2007), and (d) Muskox Intrusion after Irvine (1977).

layer present today. Cyclic changes in the chemistry of thick spinel horizons in the Bushveld Complex were suggested to be from a stratified sheet of magma slowly crystallising upwards *in situ* (Junge *et al.*, 2014). More recently, typically corroborated by detailed field observation, spinel horizons have been suggested to crystallise *in situ*. Culminations, depressions, or even overhangs where the thickness of the spinel horizon does not change thickness, is not possible by crystal settling is strong support for crystallisation *in situ* (O'Driscoll *et al.*, 2010; Latypov *et al.*, 2013; Latypov *et al.*, 2015; 2017). Despite the variable mechanisms of spinel concentration, the models described above assume accumulation or crystallisation at the magma chamber floor or magma mush interface. O'Driscoll *et al.* (2009a) noted subsidiary spinel stringers beneath sequence unit spinel seam in the Rum Layered Suite and argued for formation as a result of melt infiltration downward from the magma chamber floor, supported by quantitative textural analysis.

Anastomosing spinel horizons hosted in anorthosite have also been taken to assume petrogenesis within the crystal mush, where crystal settling could not account for the braided nature of the horizon (Voodouw *et al.*, 2009), and cross-cutting relationships of spinel seams in the same cumulate package used to infer formation within the crystal mush (Mukherjee *et al.*, 2017). Layer-parallel apophyses of harzburgite rimmed with spinel were described by Ballhaus (1988) and later by Latypov *et al.* (2015), also pointing to spinel petrogenesis away from the main magma chamber floor, and within the crystal mush. Late-stage reorganisation and remobilisation of spinel into discrete layers within the crystal mush was suggested by Maier & Barnes (2008), which assumes already present spinel.

However, while important observations, these models assume the source of magma is from the magma chamber floor by infiltrating or sills connected to the main magma sheet (O'Driscoll *et al.*, 2009a; Latypov *et al.*, 2015; 2017; Mukherjee *et al.*, 2017), and is not necessarily representing discrete replenishment events, unrelated to the overlying and underlying cumulate. Recent high-resolution geochronology of layers within the Bushveld Complex by Mungall *et al.* (2016) included

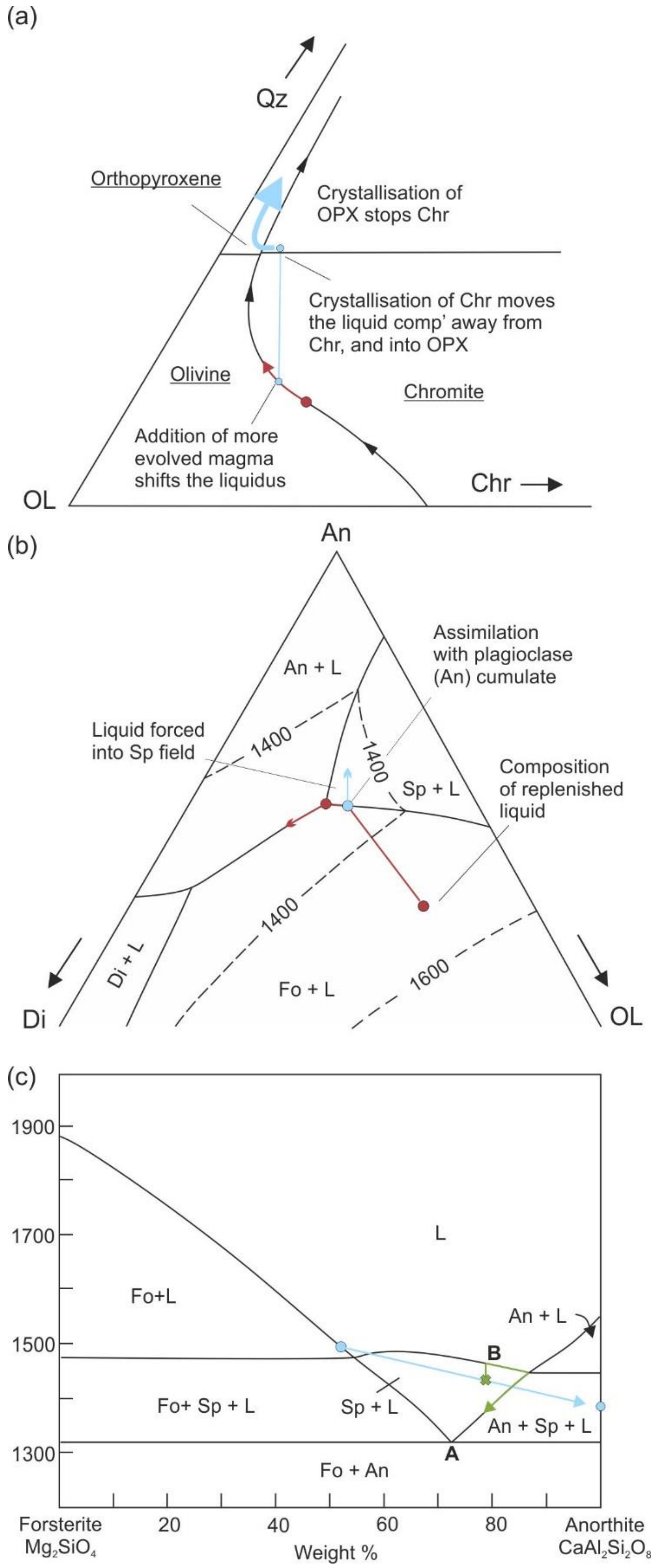

FIGURE 1.3: Phase relations for Cr-spinel crystallisation in mafic melts. (a) Projected Ol-Chr-Qz (olivine, chromite, and quartz, respectively) system from Irvine (1977), with the described mixing reaction between two melts in order to crystallise Cr-spinel (chromite). (b) Pseudo-ternary phase diagram for the Fo-An-Di-Sp system after Morse (1980), with the postulated mixing line between primitive and evolved (or feldspathic) components, resulting in a spinel-saturated melt (O'Driscoll *et al*., 2009a; 2010). (c) Binary phase diagram for the system An-Fo with the same reaction described in (b), whereby a binary mixing line between a feldspathic (An) component and primitive (Fo) component result in a liquid within the spinel (Sp) field, adapted from Morse (1980) and O'Driscoll *et al*. (2009a; 2010).

major spinel horizons, where they found them to be younger than the surrounding cumulate, suggesting they are not co-genetic with surrounding cumulate layers, and instead represent individual replenishment events, emplaced as sills directly into pre-existing cumulate.

The physical and chemical mechanisms by which spinel horizons concentrate in layered intrusions has significant economic implications as many spinel horizons host high-grade deposits of platinum-group elements (Naldrett *et al*., 2008). Understanding these processes, particularly the relationships with magma emplacement (replenishment) and the crystal mush is vital when attempting to elucidate the processes that concentrate platinum-group elements. There are strong similarities with the Rum Layered Suite and actively exploited layered intrusions such as the Bushveld Complex (Latypov *et al*., 2015; Wilson, 2015), and Stillwater Complex (Jackson, 1961; Campbell & Murck, 1993), and while several orders of magnitude smaller, the Rum Layered Suite is also enriched in platinum-group elements, typically within spinel horizons (Butcher *et al*., 1999; Pirrie *et al*., 2000; Power *et al*., 2000; Power *et al*., 2003; O'Driscoll *et al*., 2009b). The comparatively small size of the Rum Layered Suite provides insight into processes often obscured by the scale of large intrusions where field evidence is typically limited using drill core, and critical observations are missed (Latypov *et al*., 2015), with the potential to reveal intriguing physical and chemical processes that may be scaled to the larger intrusions, providing key insight into the construction of layered intrusions and the precious-metal enrichment therein.

1.2 GEOLOGICAL BACKGROUND

1.2.1 The Geology of Rum

The Rum Complex was formed as part of the British and Irish Palaeogene Igneous Province, an area of extensive magmatism along the north-western coast of the British Isles (Fig. 1.4; Bell & Emeleus, 1988), from the incipient opening of the North Atlantic ~60 Ma (Hamilton *et al*., 1998). The igneous complex on Rum is situated on a locally uplifted Precambrian ridge between the Mesozoic Inner Hebrides and Sea of the Hebrides basins between Rum and Skye (Binns *et al*., 1974). The pre-Palaeogene rocks on Rum are dominated by a thick, shallowly north-westerly dipping succession of

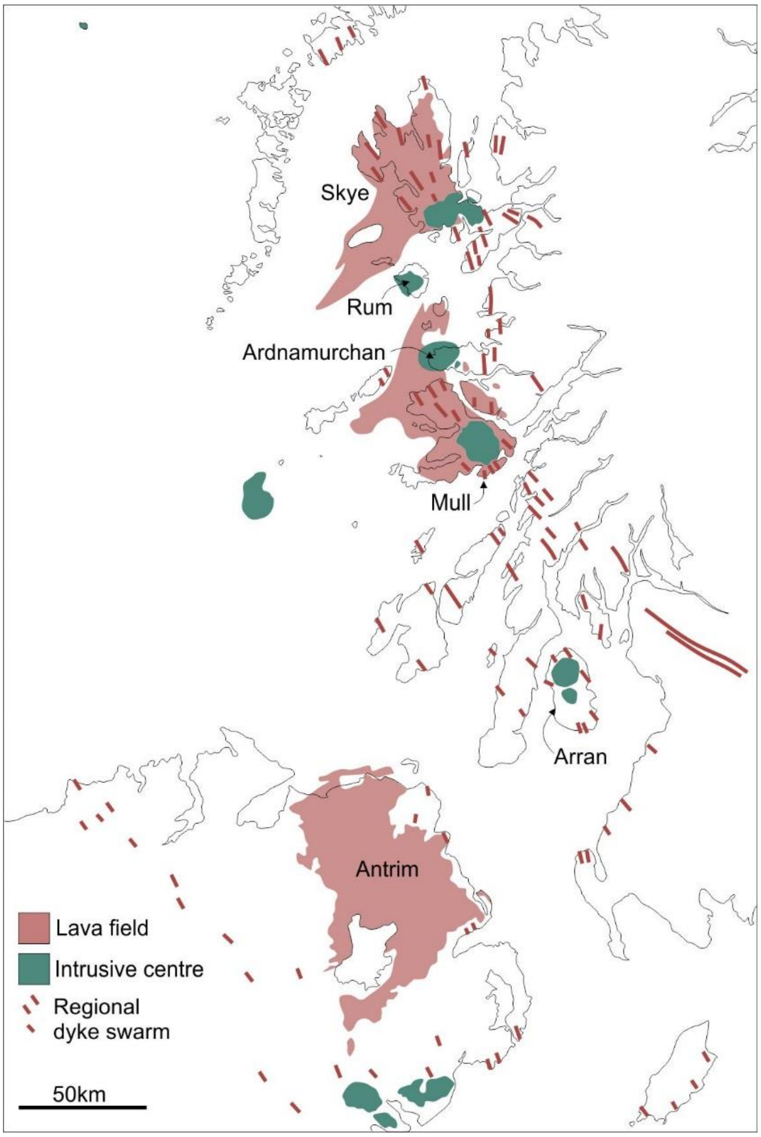

FIGURE 1.4: Distribution of intrusive igneous centres and lava fields associated with the British and Irish Palaeogene Igneous Province. From Emeleus & Bell (2005).

Neoproterozoic sandstones belonging to the Torridon Group (Emeleus, 1997). These sandstones are situated on Archaean basement gneisses which do not outcrop *in situ* but occurs as rafts within the igneous complex, typically in proximity to the margin of the layered intrusion. Largely allochthonous Mesozoic (Triassic–Jurassic) sediments are present along the margins of the igneous complex (Emeleus, 1997).

Palaeogene igneous activity on Rum is marked by two stages of magmatism, an earlier acidic episode (Stage 1), and a later, mafic-ultramafic episode (Stage 2). Stage 1 was dominated by acidic volcanism proposed to have occurred within a caldera bound by the Main Ring Fault (Fig. 1.5), where volcanic breccias, ignimbrites, and debris flow deposits can be found in the Northern and Southern Marginal Zones related to very short lived explosive activity prior to the emplacement of the layered intrusion (Troll *et al*., 2000; 2004; 2008). The Western Granite, though not bound by the Main Ring Fault like the explosive activity, is considered to be the intrusive equivalent to this acidic activity (Petronis *et al*., 2009). Stage 2 comprises the emplacement of the layered intrusion and various smaller mafic intrusions around the complex, including mafic and ultra-mafic plugs (Wadsworth, 1994; Holness *et al*., 2010). The Rum Layered Suite was dated using U-Pb zircon geochronology of late-stage pegmatite segregations located in the CI, providing an age of 60.53± 0.08 Ma (Hamilton *et al*., 1998), marginally older than the Stage 1 volcanism, pointing to (pene-) contemporaneous emplacement of the complex with the waning Stage 1 volcanism (Troll *et al*., 2008). There is no consensus on the relative age between the three components within the RLS, though the structural level has been used to infer age, with the Western Layered Intrusion structurally lower, thus being older than the Eastern Layered Intrusion (Wadsworth, 1961).

The Rum Layered Suite can be divided into three distinct portions based on typical lithology, and structural level within the complex; the Western Layered Intrusion (WLI) at the base, the Eastern Layered Intrusion (ELI) at the top, and the Central Intrusion (CI) within the centre of the complex. The WLI (Chapter 3) is composed of a thick sequence of layered peridotites, including the type locality for the skeletal-olivine dominated peridotite ‘harrisite’ (Harker, 1908; Wager *et al*., 1960; Wadsworth, 1961; Donaldson, 1974), which generally dip shallowly towards the east. The ELI (Chapter 2), comprising the highest elevation on Rum, consists of sixteen macro-rhythmic units, each consisting of a peridotite base, and a troctolite ± olivine gabbro top (Brown, 1956; Volker & Upton, 1990) that dip shallowly towards the west. The CI at the centre of the complex is the most structurally and lithologically diverse portion of the RLS, consisting of a wide variety of plagioclase and olivine cumulates, displaying a wide variety of dip orientations including convolute-style layering (Volker & Upton, 1990). Across the ELI, there are also thick gabbroic sheets between some of the macro-rhythmic units (Bédard *et al*., 1988) and large gabbroic intrusive bodies in the CI. The entire complex is bisected by the Long Loch Fault which runs north-south through the Island, through the pre-Palaeogene rocks, and is the presumed feeder for the layered intrusion (Emeleus *et al*., 1996). The

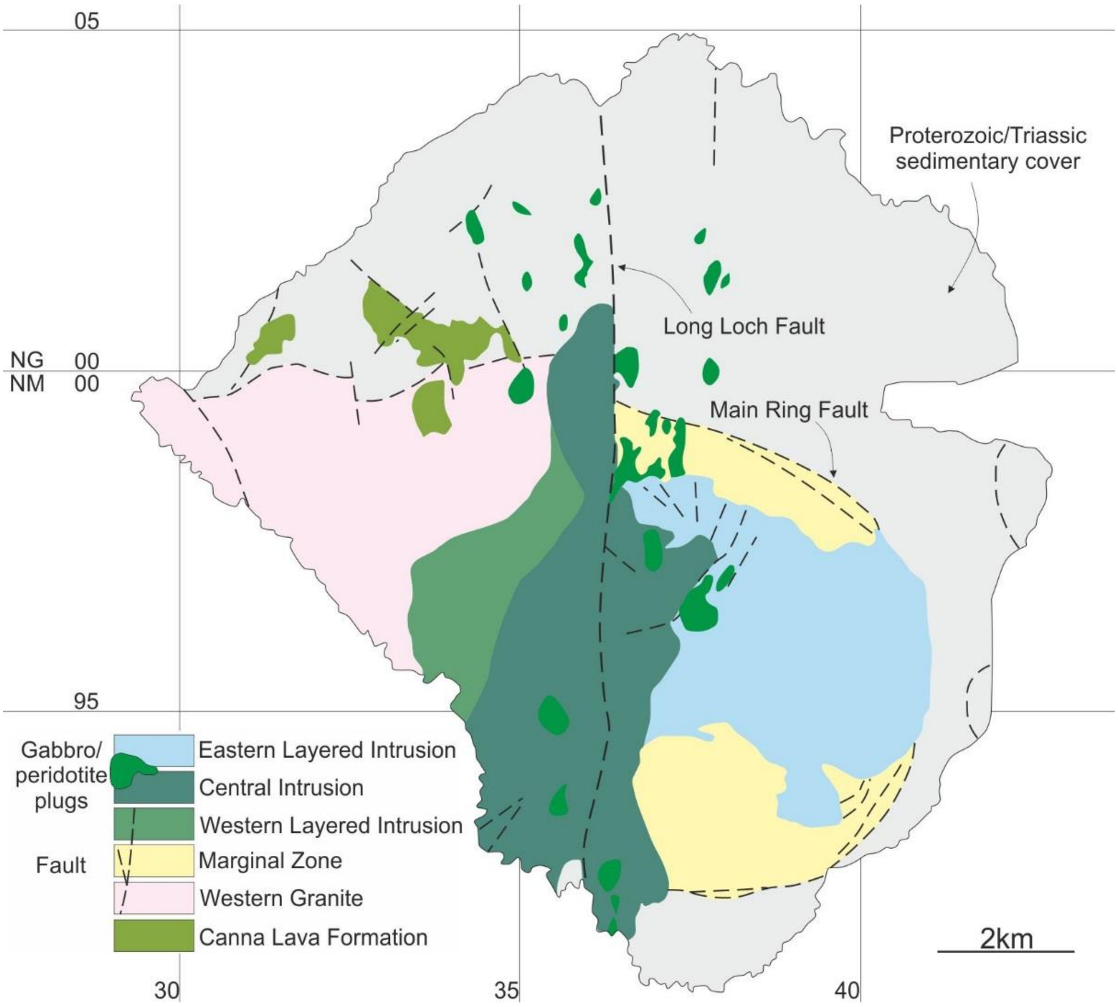

FIGURE 1.5: Simplified geological map of the Isle of Rum, adapted from Emeleus (1994)

parental magma to the Rum complex has been under much debate, with compositions required to explain the wide variety of mafic to ultramafic cumulates, but there is a consensus that the primary melt was picritic, carrying a variable olivine cargo (Greenwood, 1990; Upton *et al*., 2002; Leuthold *et al*., 2015). There is no record of mafic effusive products linked to the layered intrusion, with lava flows on Rum and the surrounding Small Isles instead linked to the lava fields of Skye and Mull (Worrell, 2002).

1.3 AIMS & OBJECTIVES

Aim 1: What controls the formation of granular-textured peridotite and harrisite within layered peridotites in the Rum ELI and WLI?

Objective 1.1	Produce high resolution field maps (including detailed structural observations) and/or logged sections through selected portions of the Rum ELI (Unit 10), and across the WLI, paying careful attention to the texture of olivine within harrisite.
Objective 1.2	Carefully evaluate the petrography of all peridotite types. Within the WLI, evaluate mineralogical and textural differences between the three members described by Wadsworth (1961).
Objective 1.3	Characterise mineral chemistry of component mineralogy within peridotites (olivine, plagioclase, clinopyroxene), including comparison mineral chemical analysis of constituent members of the WLI.

Aim 2: What does the spatial relationship between harrisite and Cr-spinel seams imply about Cr-spinel petrogenesis, and associated PGE-enrichment mechanisms?

Objective 2.1	Catalogue field relationships of Cr-spinel seams and peridotite types from high resolution logging of Aim 1 [Objective 1.1] and conduct careful petrographic analysis of seams.
Objective 2.2	Utilising quantitative textural analysis, including crystal size distribution and spatial distribution analysis methods, quantify and examine the range of textures from peridotite hosted Cr-spinel seams.
Objective 2.3	Characterise Cr-spinel mineral chemistry across the range of textures ascertained in Objective 2.2, including high resolution vertical traverses through the heights of seams.

Aim 3: If evidence of multiple replenishment is found, how does this affect post-cumulus crystallisations conditions within the crystal mush?

Objective 3.1	Characterise the mineral chemical variation of zoned intercumulus plagioclase, with careful determination of Ti and Sr composition using electron-microprobe.
Objective 3.2	Analyse the Sr-isotope variability between compositional contrasting plagioclase zones using micro-milling, and isotope-dilution thermal-ionising mass spectrometry.

Aim 4: Is the traditional 'magma chamber' model for the construction of the Rum Layered Suite still valid?

Objective 4.1	In additional to the compilation of evidence from previous aims, catalogue features associated with other portions of the RLS to assess the applicability of models presented to wider layered intrusion studies.

1.4 THESIS OUTLINE

CHAPTER 1 – INTRODUCTION

The introduction provides an overview of the key concepts of layered intrusion petrology and the generation of associated oxide-horizons, and justification for the study. A brief introduction to the geology of Rum is also included, as well as the study aims and objectives, and thesis outline.

CHAPTER 2 – UNIT 10, EASTERN LAYERED INTRUSION

This chapter serves to discuss the construction of the Unit 10 peridotite in the Rum ELI, combining detailed field work, mineral chemistry, textural analysis to propose the peridotite body was built of multiple, small volume replenishment events into the crystal mush, with Cr-spinel seams also occurring by the same process, with special focus on the physical mechanism of intrusion into the crystal mush and the effect of sill emplacement to the chemical disequilibrium within the crystal mush. Data from this chapter has been published as a research article in *Journal of Petrology* entitled: 'Incremental Construction of the Unit 10 Peridotite, Rum Eastern Layered Intrusion, NW Scotland'.

The chapter was produced in collaboration with Dr. Brian O'Driscoll, Dr. Ralf Gertisser, Prof. Stephen Daly, and Dr. Henry Emeleus, with a writing contribution by Luke Hepworth to the manuscript of 80%. Field, textural, and mineral chemical data was collected by Luke Hepworth from 2014 to 2016. QEMSCAN© image analysis performed by Dr. Alan Butcher and Hazel Horsch.

Chapter 3 – REACTIVE MELT FLOW AS A DRIVER FOR PRECIOUS METAL MINERALISATION IN MAFIC MAGMATIC SYSTEMS

Chapter 3 comprises a detailed mineral chemical and Sr-isotope study focusing on the intercumulus mineralogy from Unit 10 peridotite of Chapter 2. The purpose of the study is to record intracrystalline chemical and isotopic heterogeneity in plagioclase and clinopyroxene oikocrysts to identify markers for melt-rock reaction and reactive melt flow within the crystal mush. This data is intrincially linked to platinum-enriched Cr-spinel seams, in which the data suggests these both form from cumulate assimilation and through-flow of reactive melt along laterally oriented planes within the crystal mush. New diffusion modelling is performed using the Sr-isotope data to quantify the crystallisation and cooling timescales of the crystal. The conclusion of this model suggests, much like granitic intrusions, much of the Unit 10 existed in cold-storage, constantly rejuvenated by fresh intrusion of sills. This data is currently being prepared for submission to *Nature Communications/Geology*, in collaboration with Dr. Brian O'Driscoll, Prof. Stephen Daly, Dr. Ralf Gertisser, Dr. Chris Johnson, and Dr. Henry Emeleus. Field, petrographic, and mineral chemical data was collected by Luke Hepworth, with Sr-isotope analysis carried out by Luke Hepworth and Prof Stephen Daly, with a writing contribution of 70%.

CHAPTER 4 – THE WESTERN LAYERED INTRUSION

Chapter 4 consists of a detailed investigation into the Rum Western Layered Intrusion, combining detailed field, textural, and chemical analysis of the entire layered sequence, with a focus on the formation of harrisite and the petrogenesis of associated Cr-spinel seams in order to test the hypothesis that the layering style is formed from sill emplacement like Unit 10 (Chapter 2) and propose that Cr-spinel seams represent discrete melt-channels within the crystal mush, where textures, mineral chemistry, and PGE-mineralisation is controlled by melt flux. The peridotite and seams are suggested to form from the same fundamental sill emplacement process as harrisite. The abundance of harrisite in the WLI allows for a simple thermo-chronological approach to sill emplacement using olivine morphology as a proxy for temperature and coupled with an investigation of the lower peridotite units, provides a new model for the build-up of the WLI as a sill complex. This chapter has been accepted for publication in *Journal of Petrology*, with the article entitled 'Linking *in situ* crystallisation and magma replenishment *via* sill intrusion in the Rum Western Layered Intrusion, NW Scotland'. The paper was produced in collaboration with Dr. Brian O'Driscoll, Dr. Ralf Gertisser, Prof. Stephen Daly, and Dr. Henry Emeleus. Field, textural, and chemical data was collected by Luke Hepworth with a writing contribution to the manuscript of 80%.

CHAPTER 5 – THE CONSTRUCTION OF LAYERED CUMULATE BODIES: THE EVIDENCE AND IMPLICATIONS OF SILL EMPLACEMENT

The synthesis to the thesis is presented in Chapter 5, where the key findings of the previous chapters are discussed in a broader context, particularly to discuss the wider implications of the study and define new areas for future work, including some new observations from the Stillwater Complex, USA. The details of sill emplacement emphased in this thesis are outlined here, with criterion and hypotheses applied to the peridotite portions of Unit 7, 8, and 9 in the ELI. These new observations are used to make key inferences about the major mode of construction for the RLS, bringing in all previous chapters work and previously published work in a new conceptual model. The data included as part of this section is currently being prepared for publication in *Contributions to Mineralogy and Petrology* in collaboration with Dr Ralf Gertisser and Dr Brian O'Driscoll.

CHAPTER 6 – CONCLUSIONS

The conclusions of the work carried out within this thesis are summarised in this chapter, with key concepts and implications arising from this work highlighted.

CHAPTER 2 – UNIT 10, RUM EASTERN LAYERED INTRUSION

2.1 INTRODUCTION

Layered mafic-ultramafic intrusions offer excellent opportunities to study magma solidification processes in sub-volcanic systems, including the accumulation of the crystal mush and late-stage post-cumulus processes (e.g., Wager & Deer, 1939; Sparks *et al*., 1985; Holness, 2007; O'Driscoll *et al*., 2007a; Namur & Charlier, 2012; Latypov *et al*., 2015). Aside from their relevance to improving our understanding of magma differentiation and phase petrology, a handful of layered intrusions are associated with economically important base and precious metal mineralisation. Enhancing our understanding of the magma chamber processes responsible for the formation of various types of cumulate rocks thus has the potential to improve our knowledge of important ore-forming systems. The comparatively small size and young age of the Rum Eastern Layered Intrusion (ELI) provides an opportunity to see past some of the effects of post-cumulus textural and mineral chemical equilibration that are common in some larger and older layered mafic-ultramafic intrusions, and study the discrete effects of magma chamber dynamics and magma replenishment in open-system layered intrusions, as well as investigate the mineralisation associated with magma replenishment.

The focus of this chapter is the Unit 10 peridotite portion of the ELI of the Rum Layered Suite (RLS), NW Scotland, presenting new field and petrographic observations on this body of cumulate, including the important observation that numerous Cr-spinel seams exist throughout a significant proportion of its thickness. Previously reported Cr-spinel seams on Rum are mostly restricted to the boundaries between feldspathic and peridotitic cumulate (Henderson & Suddaby, 1971; O'Driscoll *et al*., 2010). Although models for the formation of stratiform Cr-spinel seams in layered intrusions are debated in the literature, they mostly call on the intrusion of new magma into the chamber (e.g., Campbell & Murck, 1993; Cawthorn, 2005; Mondal & Mathez, 2007; O'Driscoll *et al*., 2010). This leads us to consider that the Unit 10 peridotite may be formed from multiple replenishment events. Another common feature amongst many of the models for Cr-spinel seam formation is that seams are typically supposed to form at the magma-crystal mush interface (e.g., Irvine, 1977; Spandler *et al*., 2005; Mondal & Mathez, 2007; O'Driscoll *et al*., 2010; Junge *et al*., 2014). However, so-called ‘subsidiary’ Cr-spinel seams occur several centimetres beneath several of the ELI unit boundaries (O’Driscoll *et al.*, 2009a) suggesting that some of these may form within the crystal mush. In addition, sill-like protrusions beneath the platiniferous Merensky Reef in the Bushveld Complex that are rimmed with Cr-spinel also suggest a process operating within the crystal mush (Ballhaus, 1988; Latypov *et al*., 2015), and also indicate that Cr-spinel seams in layered intrusions can form *in situ* (O’Driscoll *et al*., 2010; Latypov *et al*., 2015).

Detailed field observations and petrography, as well as quantitative textural and mineral chemical data for rocks of the Unit 10 peridotite are presented. A model is proposed that argues that this body was incrementally built up of multiple, small volume replenishment events. The features of the Unit 10 peridotite also suggest emplacement of magma into the crystal mush, rather than at the magma-crystal mush interface. The peridotite-hosted Cr-spinels seams also formed *in situ* during these replenishment events. The data presented here strongly suggest that crystal settling is not a viable mechanism for cumulate formation on Rum and supports the growing body of evidence that *in situ* crystallisation may be a far more common process in layered intrusions (Bédard *et al*., 1988; O’Driscoll *et al*., 2010; Latypov *et al*., 2015). In particular, the importance of *in situ* crystallisation for Cr-spinel seam petrogenesis and associated PGE mineralisation is emphasised here (*cf*. Butcher *et al*., 1999; O’Driscoll *et al*., 2009b).

2.2 THE RUM LAYERED SUITE

The RLS has long been considered to represent a classic example of an open-system magma chamber which formed at ~60 ±1.3 Ma (Hamilton *et al*., 1998) as part of the British Palaeogene Igneous Province (Emeleus & Bell, 2005; Emeleus & Troll, 2014). The RLS is the type locality of ‘harrisite’ (Harker, 1908), a variety of peridotite comprising coarse, branching and skeletal olivine crystals, which also includes hopper olivine morphologies (*cf*. Donaldson, 1976; O’Driscoll *et al*., 2007a). The RLS is subdivided into the Eastern Layered Intrusion (ELI), Western Layered Intrusion (WLI), and Central Intrusion (CI) (Fig. 2.1). The ELI typifies the open-system magmatic behaviour of the intrusion as a whole, with each new major influx of magma represented by a coupled peridotite-troctolite ± olivine gabbro macro-rhythmic unit (Brown, 1956), of which there are 16 in total (Volker & Upton, 1990). Traditional models of cumulate formation for the ELI centred on the fractionation of each batch of magma via crystal (gravity) settling of successive liquidus phases to account for the transition of peridotite to more felsic cumulate. This interpretation has since been challenged with some units considered to have formed from multiple magma batches (e.g., Units 12 and 14; Renner & Palacz, 1987; Holness & Winpenny, 2008) and the peridotitic portions of some units postulated to be intrusive bodies (Bédard *et al.*, 1988; Holness, 2005; Holness *et al.*, 2007). Unit 10, Brown's (1956) type unit for batch fractionation comprises the thickest peridotite layer in the ELI. Increasing Fe-content of cumulus olivine with stratigraphic height through the peridotite was taken to support this simplistic batch fractionation interpretation (Dunham & Wadsworth, 1978), with a similar argument made by Tait (1985) but invoking two separate magma replenishments instead.

2.3 FIELD RELATIONSHIPS

The Unit 10 peridotite is well exposed between Hallival and Barkeval (Fig. 2.1), with less well exposed outcrops around Askival and Atlantic Corrie. Figure 2.2 illustrates logged sections through the Unit 10 peridotite at four locations between Hallival and Barkeval (Fig. 2.2; with grid references for the base of each log provided in the high-resolution figure in Appendix 1.1). The contact between the underlying Unit 9 feldspathic cumulates is only observed at the Barkeval locality but can be inferred at the Hallival locality (Fig. 2.3a). On the basis of previous studies (Tait, 1985; Palacz & Tait, 1987) the ~65 m Unit 10 peridotite can be divided into a lower peridotite (LP; ~40 m) and an upper peridotite (UP; ~25 m). The relative thicknesses of the LP and UP vary slightly between the four logged sequences. The boundary between the LP and UP is sharp, with a ubiquitous 0.2–2.5 m harrisite layer separating them (Fig. 2.2).

2.3.1 The Lower Peridotite

Granular-textured peridotite is the dominant type of peridotite in the LP and comprises layered peridotite orthocumulates. Layer thickness is variable (i.e., 0.2–1 m); layering at the finer scale (2–

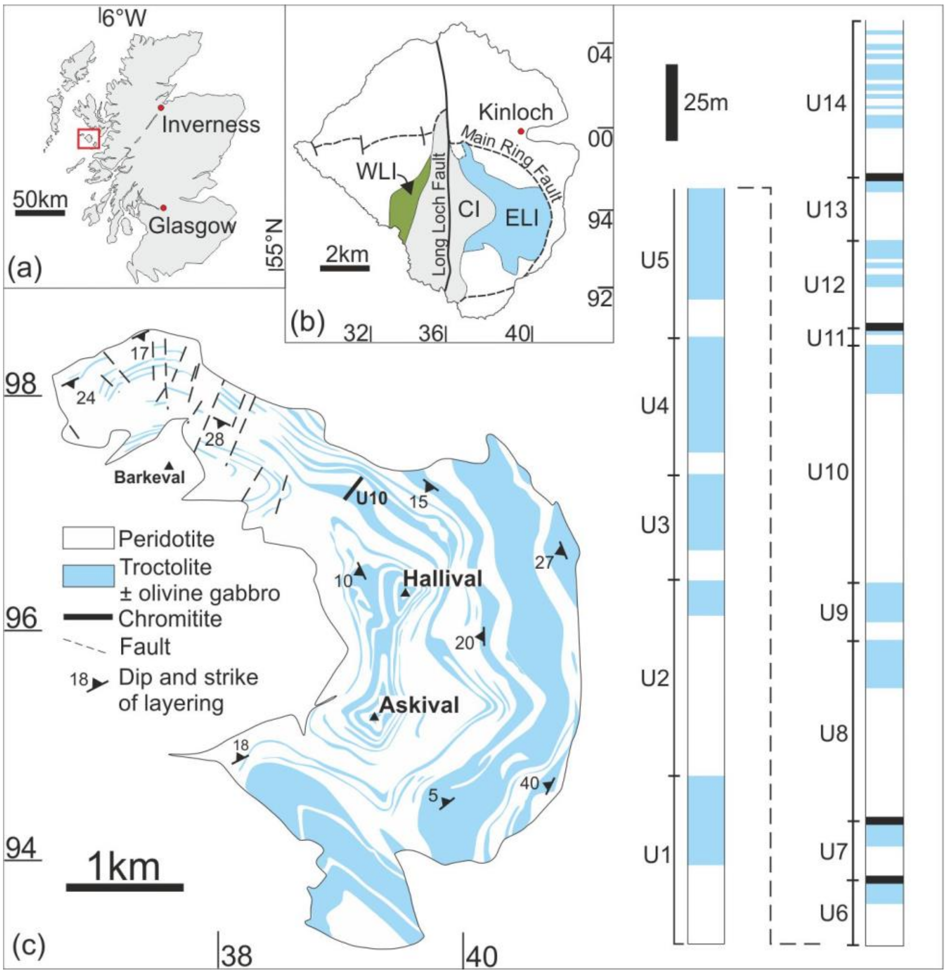

FIGURE 2.1: (a) Location map of the Isle of Rum in Scotland. (b) Location of the Rum Layered Suite with the Eastern Layered Intrusion (ELI) highlighted in blue, and the Western Layered Intrusion (WLI) in green, CI = Central Intrusion (c) Geological map (after Emeleus, 1994) of the Eastern Layered Intrusion showing the position of Unit 10 (black bar) and a schematic log showing the major boundary chromitites (black bands, modified after Emeleus *et al*., 1996).

3 cm) is defined by the positions of Cr-spinel seams and subtle variations in the abundance of intercumulus plagioclase or clinopyroxene. Small-scale structures are observed in the layering, e.g., at the Barkeval location (Fig. 2.3a) where pronounced undulations occur in fine-scale layering directly above harrisite layers that have extremely irregular contacts. Layer-parallel foliation defined by tabular cumulus olivine crystals in granular-textured peridotite is common throughout the LP, most obvious (and strongest) in close proximity to harrisite layers. No lineation of olivine crystals was observed. Large (~40 cm) irregularly-shaped troctolite autoliths rimmed with diffuse Cr-spinel selvedges occur in granular-textured peridotite at the Barkeval location (Figure 2.3a; 2.4a, b; ~2 m above the Unit 9-10 boundary).

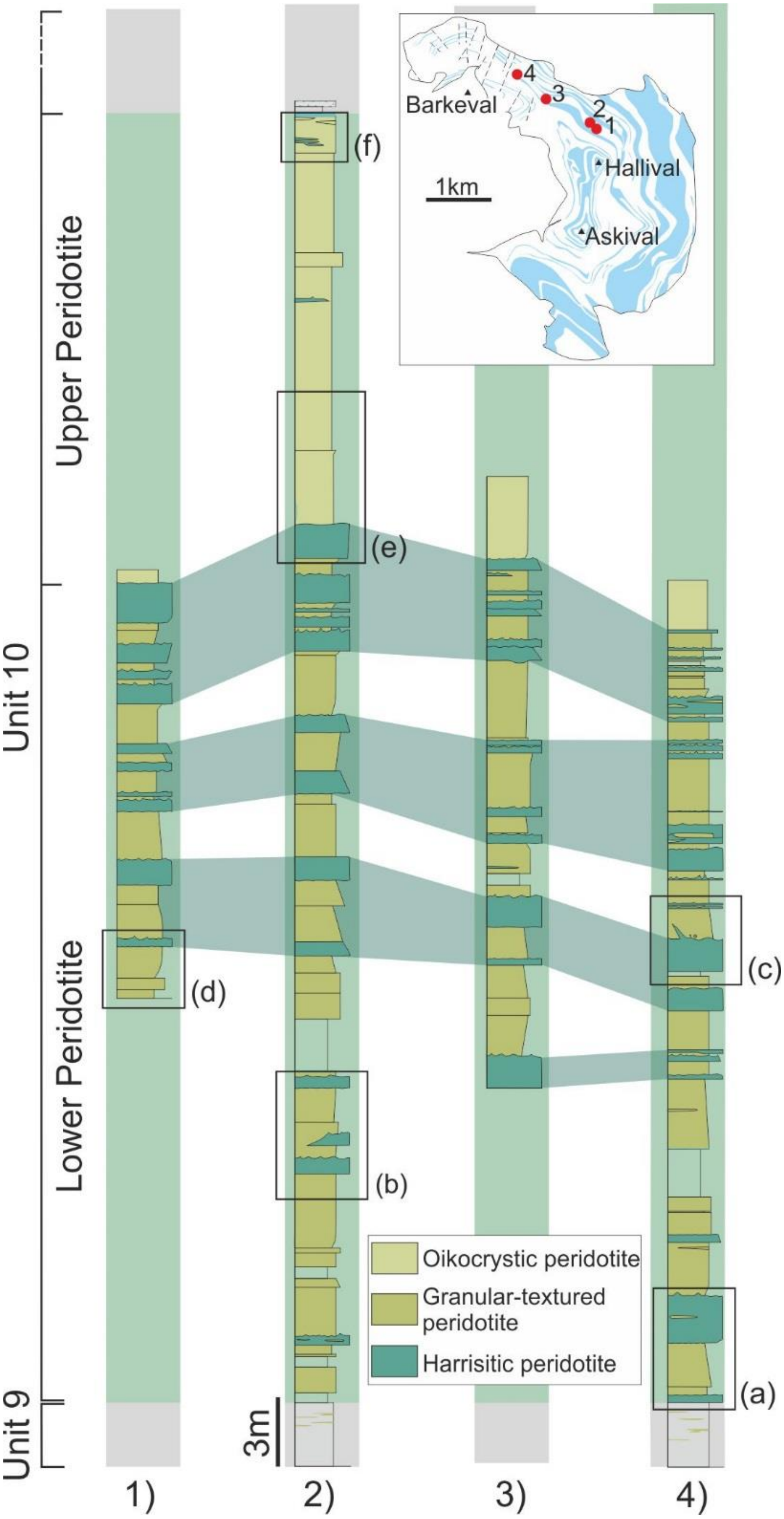

FIGURE 2.2: Simplified graphic logs through the Unit 10 peridotite with the four logged sections indicated on the ELI map (red numbered dots). Harrisitic peridotite layers can potentially be correlated (medium green bands) across the four localities in packages of similar stratigraphic position and layer characteristics. Note the abundance of thinner layers in location and 4 compared to 1, with some harrisite layers thickening towards location 1 (with distance from the Long Loch Fault feeder zone).

Harrisite layers are abundant throughout the LP. These typically have a very high proportion of intercumulus material (~40–50 vol. %), comprising plagioclase and clinopyroxene, often with cm-sized skeletal olivine visible at outcrop (Fig. 2.5a; h). Textural variation of harrisite is also evident in the field, in the form of patchy layers composed of varying grain sizes of skeletal harrisitic olivine (Fig. 2.3a; 2.5b). Contrary to previous work on harrisites (e.g., Donaldson, 1974; O'Driscoll *et al*, 2007a) the long axes of skeletal olivine are rarely perpendicular to the top and base of the layer and are randomly arranged. Packages of harrisite layers can be correlated from one log to the next (see Fig. 2.2), but the correlation of certain layers is not possible due to the bifurcation, tapering and complete lateral termination of some layers along strike (Fig. 2.2; 2.3b). Where the layers do not terminate, harrisite layers can be often be traced tens of metres across the entire length of the outcrop. The thickness of harrisite layers is highly variable (0.2–4 m) and based on field observations and the logged sections, it is tentatively suggested that some layers (and packages of layers) increase in thickness away from the postulated feeder zone for the intrusion, the Long Loch Fault (Emeleus *et al*., 1996; Fig. 2.2). Harrisite layers have flat-to-broadly undulose bases while their tops range from being flat-to-extremely irregular (Fig. 2.3c). The upper contacts of harrisite layers exhibit irregularities on their upper surfaces, with more pronounced examples of such apophyses evident around Barkeval (Fig. 2.3c; 2.5c). Less extreme irregularities in the upper and lower contacts of peridotite layers occur with distance away from the Long Loch Fault (Fig 2.5d). Harrisite layers taper and terminate against granular peridotite, still with irregular upper surfaces (Fig. 2.5e; h). Variably sized (10–30 cm) granular-textured peridotite autoliths are recorded in some thicker (>1 m) harrisite layers. Olivine grain size is significantly reduced in the granular-textured peridotite autoliths (~1 mm), with a noticeable accompanying reduction in the proportion of intercumulus minerals (≤10 vol. %).

Cr-spinel seams are extremely abundant within the LP, occurring in both granular-textured peridotite and harrisite. The occurrence of Cr-spinel seams is typically accompanied by a relative increase in the proportion of intercumulus plagioclase within the seam. Individual seams are not laterally extensive and can rarely be traced over more than several tens of metres. Seam thickness

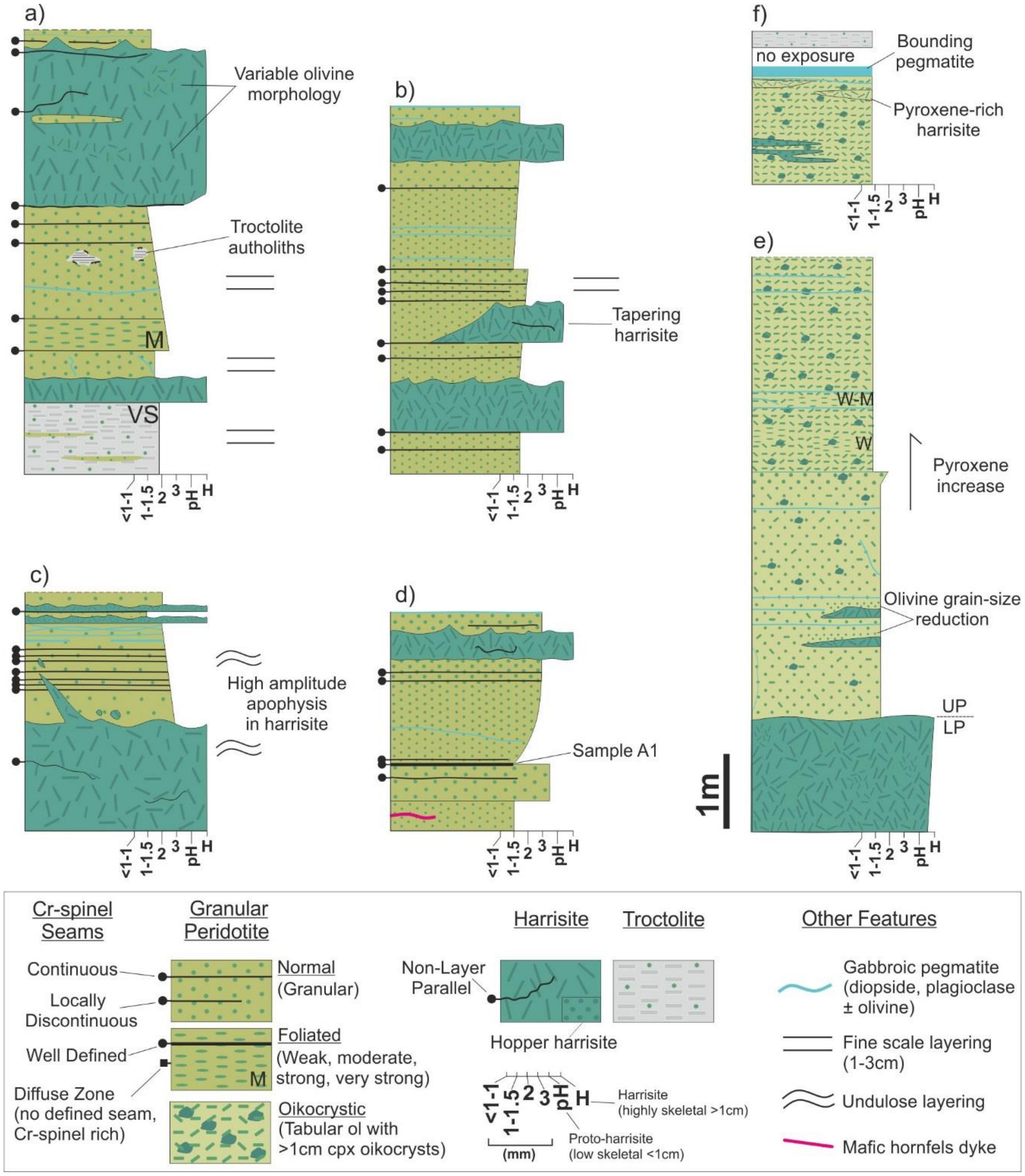

FIGURE 2.3: Selected stratigraphic sections of the Unit 10 peridotite referenced in Figure 2.2. (a) Base of the Unit 10 peridotite with troctolite autoliths incorporated into the granular-textured peridotite. Thick harrisite layer also contains a granular-textured peridotite lenses, and variable olivine morphologies. (b) Tapering harrisite layer with associated Cr-spinel seams also featured in Figure 2.5. Cr-spinel seams occur commonly in proximity to the tapering harrisite (c) Harrisite apophyses and layer deformation with a harrisite layer at the source-proximal Barkeval locality, also shown in Figure 2.4d. (d) Variable grain sizes of granular-textured peridotite layers with well-defined Cr-spinel seam above coarse granular-textured peridotite. Note the fining of olivine just above the seam also seen in Figure 2.7d. (e) Upper and lower peridotite contact. Pyroxene increase with height and rare tapering harrisite layers with associated external olivine grain size reduction. (f) Top of the UP, with pyroxene rich harrisite layers and bounding pegmatite between the peridotite and feldspathic cumulate. See Appendix 1.1 for full high resolution graphic logs, with location grid references and stratigraphic sample locations used in this chapter.

is highly variable (2–20 mm), with an average thickness of 4–5 mm. The textures of the Cr-spinel seams are comparable to peridotite-hosted seams observed in the Unit 12 peridotite (*cf.* O'Driscoll *et al*., 2010), which were described by those authors as 'chain-textured' where the Cr-spinel occurs in intercumulus plagioclase and surrounds cumulus olivine crystals. The texture of the seams is consistent irrespective of peridotite lithology. Only one of the seams studied here is not chain-textured, and no cumulus olivine was observed within the upper and lower limits of the seam (Fig. 2.3c; 2.4c). This seam also exhibits irregularities (depressions and culminations) along strike (Fig 2.4c). Significant undulations, even apparent discontinuities, of Cr-spinel seams can occur above harrisite layers (Fig. 2.4b).

It is important to specify that many of the Cr-spinel seams referred to here are not chromitite, *sensu stricto*, i.e., they often contain <<60 vol. % Cr-spinel. They are referred to here as 'Cr-spinel seams' because the Cr-spinel is often more diffusely disseminated than in some of the other well-known Rum seams (*cf.* O'Driscoll *et al*., 2010). However, the Cr-spinel seams are still considered to represent clearly delineated 'events' (horizons) within the cumulate pile. The Cr-spinel seams studied here can be broadly divided into four groups based on their lithological relationships to surrounding peridotite: granular-textured peridotite-hosted seams, boundary seams, harrisite-hosted seams, and foliated peridotite-hosted seams. Granular-textured peridotite-hosted seams occur with no obvious textural or mineralogical variation above or below the seam (Fig. 2.4e). Boundary seams occur with obvious textural (or mineralogical) variation in the peridotite above and below the seam, such as Cr-spinel seams that occur between harrisitic and granular-textured peridotite (Fig. 2.4f). Harrisite-hosted seams occur within individual harrisite layers. These seams are the most discontinuous and are also not layer-parallel but have an undulose character. While harrisite-hosted seams are often not layer-parallel, no vertically-oriented Cr-spinel seams were found in the Unit 10 peridotite. Foliated peridotite-hosted seams occur locally where the cumulus olivine is tabular or elongated (including harrisitic olivine) and defines a foliation within the upper and lower confines of the Cr-spinel seam. The character (i.e., type) of Cr-spinel seam can also change along the lateral extent of a given seam, particularly where harrisite layers terminate, but their associated seams continue laterally (Fig. 2.5f).

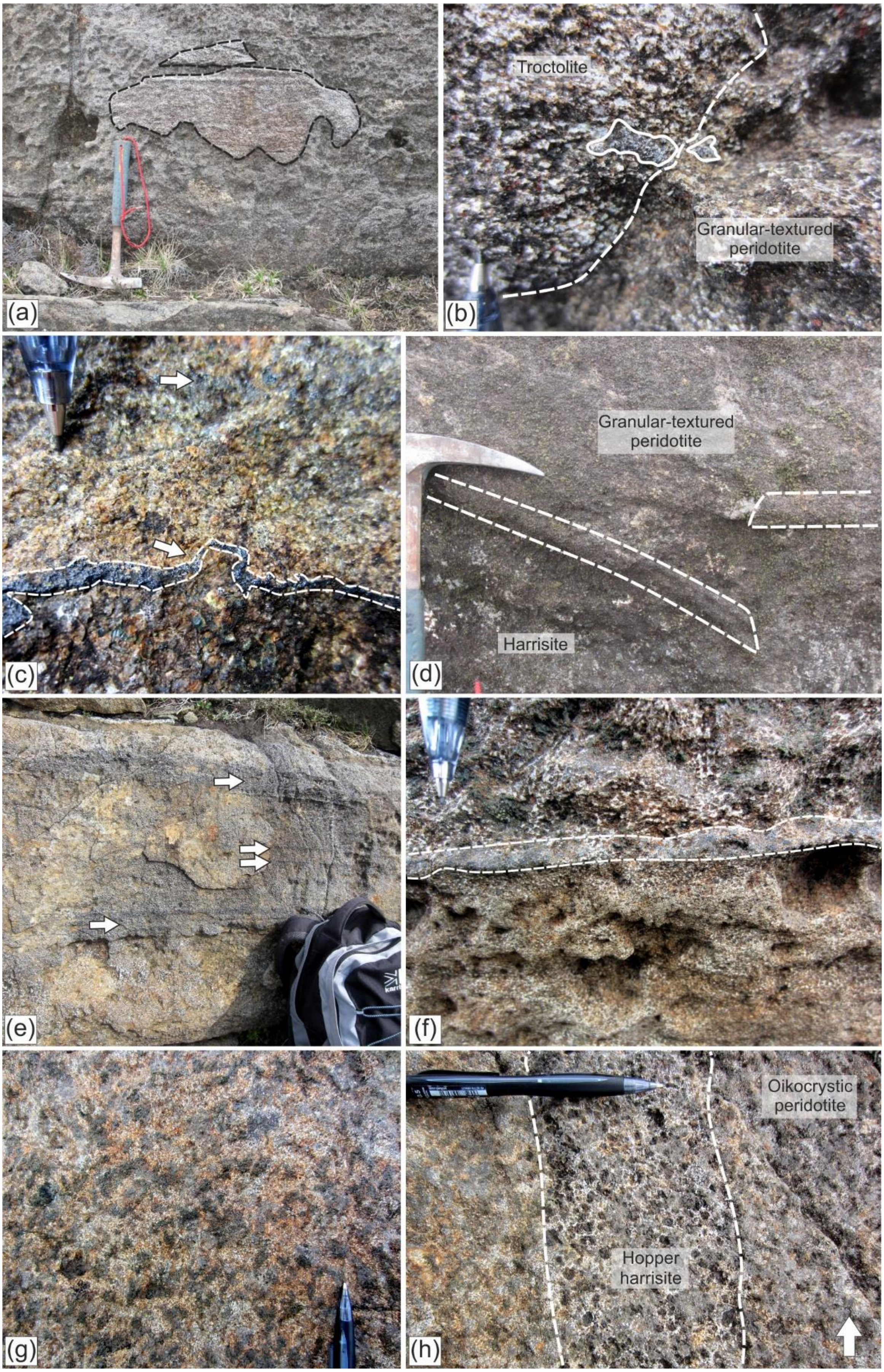
(a)
Troctolite
Granular-textured peridotite
(b)
(c)
Granular-textured peridotite
Harrisite
(d)
(e)
(f)
(g)
Oikocrystic peridotite
Hopper harrisite
(h)

◄FIGURE 2.4: Field features of the Unit 10 lower peridotite. (a) Troctolite autolith (outlined) in granular-textured peridotite ~ 2m from the Unit 9–10 boundary. Note the irregular shape with layering parallel to host peridotite. (b) Close of the edge of the troctolite autolith in ‘a’ with chromitite clot outlined between the two lithologies. (c) Clearly defined Cr-spinel seam on the top surface of a very coarse granular-textured peridotite, with overlying very fine grained low intercumulus volume granular-textured peridotite. Note the loop-like culmination in the centre of the Cr-spinel seam outlined and also chain-textured seam ~2 cm above well-defined seam (arrowed). (d) Broken Cr-spinel seam (outlined) above harrisite with minor upwelling of harrisite between the break in the seam. (e) Multiple, cm-thick Cr-spinel seams (arrowed) in varying lithologies. The uppermost and lowermost arrowed seams occur above and below a harrisite, respectively, with the central seams occurring in granular-textured peridotite. (f) Boundary-type Cr-spinel seam (outlined) at the base of high intercumulus harrisite. (g) Clinopyroxene-oikocrystic peridotite from the upper peridotite. Note the high abundance of rounded–elongated dark-green diopside oikocrysts. (h) Vertical oriented ‘hopper-harrisitic’ peridotite from the upper peridotite (outlined). Note the large, rounded, dark olivine crystals in the hopper-harrisite. Way up indicated by arrow.

2.3.2 The Upper Peridotite

The UP is best exposed in the two Hallival logged sections (Fig. 2.2), where there is near continuous outcrop into the overlying feldspathic cumulates. The UP is relatively homogenous, comprising a texturally distinctive clinopyroxene-oikocrystic peridotite (Fig. 4g). However, the lowest ~3 m of the UP is distinctly less pyroxene-rich (Fig. 2.3e). The UP is predominantly massive, with layering locally defined by harrisite layers toward the top (Fig. 2.2; 2.3e, f). These harrisite layers contain clinopyroxene oikocrysts like the surrounding granular-textured peridotite. Other harrisite layers in the UP have ‘hopper-textured’ olivine crystals (see Donaldson, 1976), and share similar morphological characteristics to harrisite layers within the LP, with flat bases and variably irregular top surfaces. Harrisite layers in the UP can occur as discordant (sub-vertical) sheets (Fig. 2.4h), as well as layer-parallel sheets. Cr-spinel seams are absent from the UP. Gabbroic pegmatite veins are common throughout the UP, composed of ≤2 cm euhedral clinopyroxene and subhedral plagioclase crystals, with rarer ~5 mm equant olivine crystals. These pegmatites become extremely common towards the top of the UP, where they occur as ≤10 cm thick vertical sheets. The boundary between the UP and overlying feldspathic cumulate is marked by a ~20 cm thick gabbroic pegmatite layer (Fig. 2.3e).

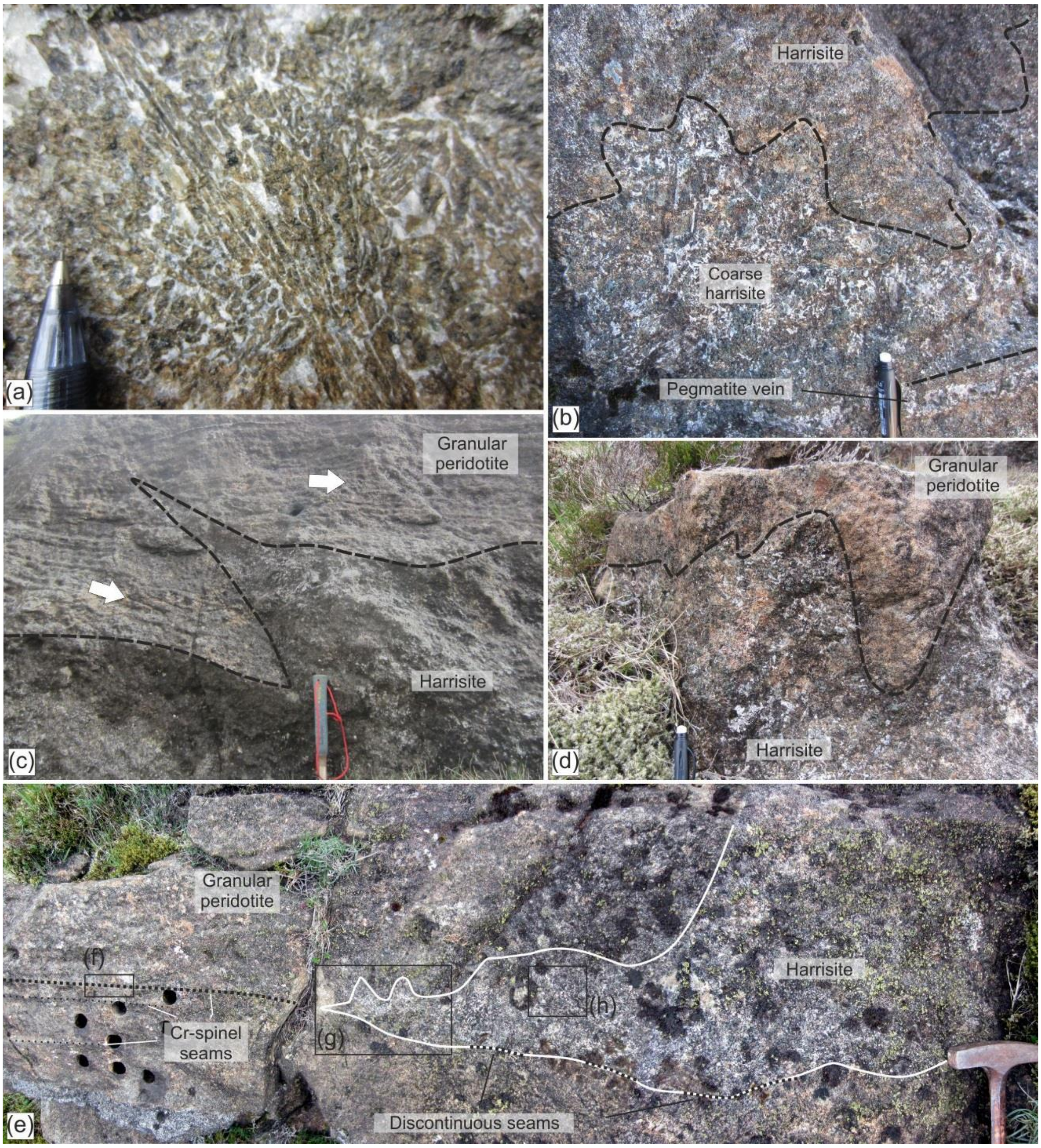

FIGURE 2.5: Harrisite features of the lower peridotite. (a) Highly skeletal olivine crystals in harrisite layer up to several cm long. (b) Internal textural variation of harrisite layer. Coarse skeletal patch within finer skeletal harrisite layer. (c) High amplitude harrisite apophyses from the Barkeval locality protruding into well-layered granular-textured peridotite above. Note the brittle-like disturbance of well-layered peridotite left of the apophyses, now dipping variably from the layers above. (d) Low amplitude irregularities in the upper surface of harrisite layer around Hallival. (e) Tapering harrisite layer around Hallival (outlined) with irregular upper surface, discontinuous Cr-spinel seams along the base including chain-textured Cr-spinel seam which continues into granular-textured peridotite to the left as the harrisite terminates.

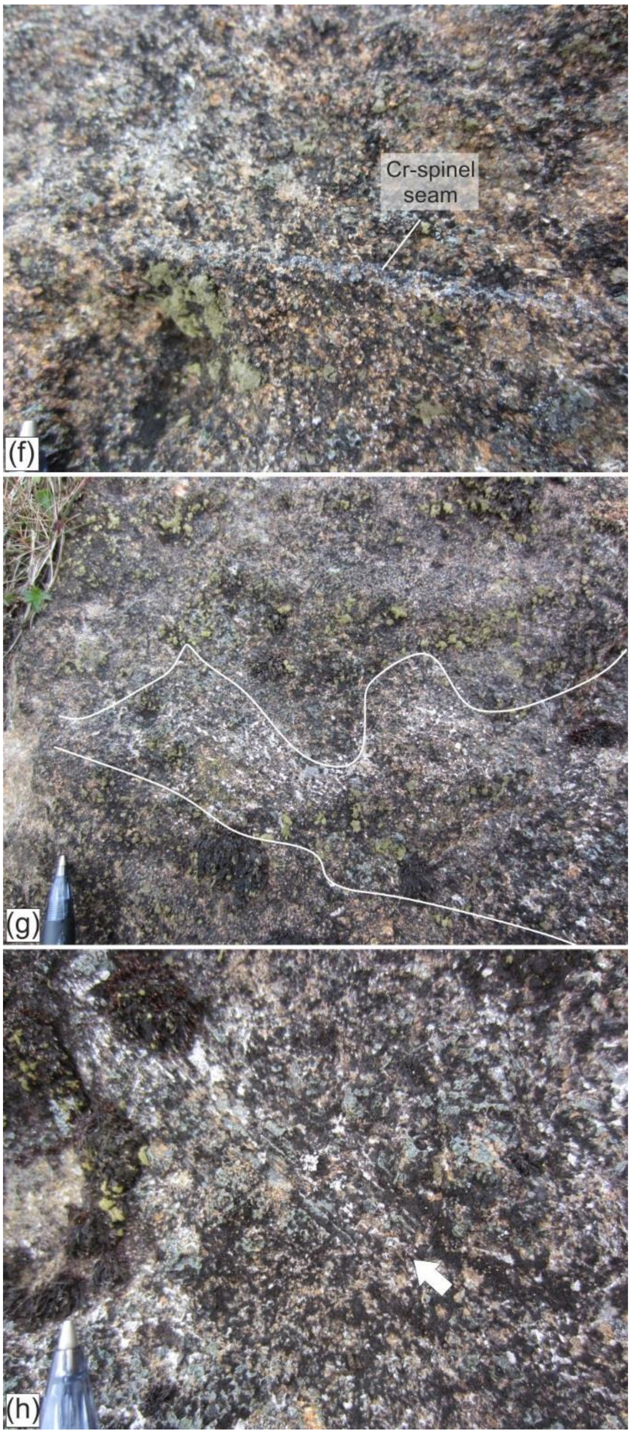

FIGURE 2.5 CONTINUED: Black outlines in (e) show locations of (f) chain-textured Cr-spinel seam in granular-textured peridotite ahead of tapering harrisite layer, (g) irregular upper contacts of harrisite at layer toe. Note also the variation in intercumulus abundance within the harrisite (outlined) and granular-textured peridotite around, and (h) centimetre-sized skeletal olivine within harrisite layer.

2.4 PETROGRAPHY

2.4.1 The Lower Peridotite

The cumulus mineralogy of the granular-textured peridotite is dominated by rounded, euhedral (~0.5–3 mm) olivine crystals. Small numbers of crystals with tabular (elongate) and hopper crystal morphologies (~3–5 mm) occur in most samples; with increased abundances of the latter in coarser-grained granular-textured peridotites. Olivine crystals close to Cr-spinel seams often show a reduction in grain size and abundance of apparent triple junctions with 120° dihedral angles (e.g., Figure 2.6d). Euhedral Cr-spinel crystals (~0.3 mm) occur outside of Cr-spinel seams in accessory proportions (~1 vol. %). Noticeably finer-grained (~0.1 mm) Cr-spinel inclusions occur within some olivine crystals, but these are comparatively rare. The volume proportion of intercumulus material varies between 10–25%. The intercumulus mineralogy is dominated (≥85%) by plagioclase oikocrysts (0.5–5 mm), with subordinate diopside oikocrysts. Zoning of the intercumulus plagioclase is visible under the petrographic microscope, including rare oscillatory zoning (Fig. 2.6a; 2.6b, see also Fig. 2.15). As noted above, foliation is common, defined by elongate or tabular olivine crystals (Fig. 2.6c). Apatite, biotite, serpentine, chlorite, calcite, epidote and kaersutite/titano-pargasite occur as accessory phases, typically in the interstices of the olivine framework.

Harrisite in the LP consists of approximately equal-to-subequal proportions of cumulus and intercumulus minerals. Olivine crystal morphologies in harrisite are dominated by very coarse-grained hopper and highly skeletal olivine crystals. The most elongate crystals can be up to several centimetres long. The intercumulus mineralogy comprises very coarse-grained (≤ 3 cm diameter) plagioclase and diopside oikocrysts, with average overall proportions of 70:30, respectively. Trace amounts of serpentine, chlorite, calcite, epidote, biotite and amphibole also occur.

Cr-spinel seams in the Unit 10 peridotite are chain-textured (with the exception of one sample; Fig. 2.3, 2.6d). The constituent Cr-spinel crystals occur in the intercumulus minerals between and around cumulus olivine crystals (Fig. 2.6e). The Cr-spinel crystals are euhedral and have a consistent grain size range of 0.05–0.3 mm, with an average crystal size of ~0.2 mm. The average crystal size in harrisite tends to be ~0.3 mm. Polygonal Cr-spinel crystal aggregates are locally observed, resulting in subhedral-euhedral crystal shapes and a corresponding grain size increase that can be detected via reflected light microscopy. Cr-spinel is enclosed by intercumulus plagioclase oikocrysts, and more rarely by intercumulus clinopyroxene, with deformation twinning common in plagioclase. Cr-spinel is common adjacent to embayments in cumulus olivine crystals (Fig. 2.6e). Ilmenite exsolution lamellae occur in Cr-spinel, but typically in crystals that do not occur in seams.

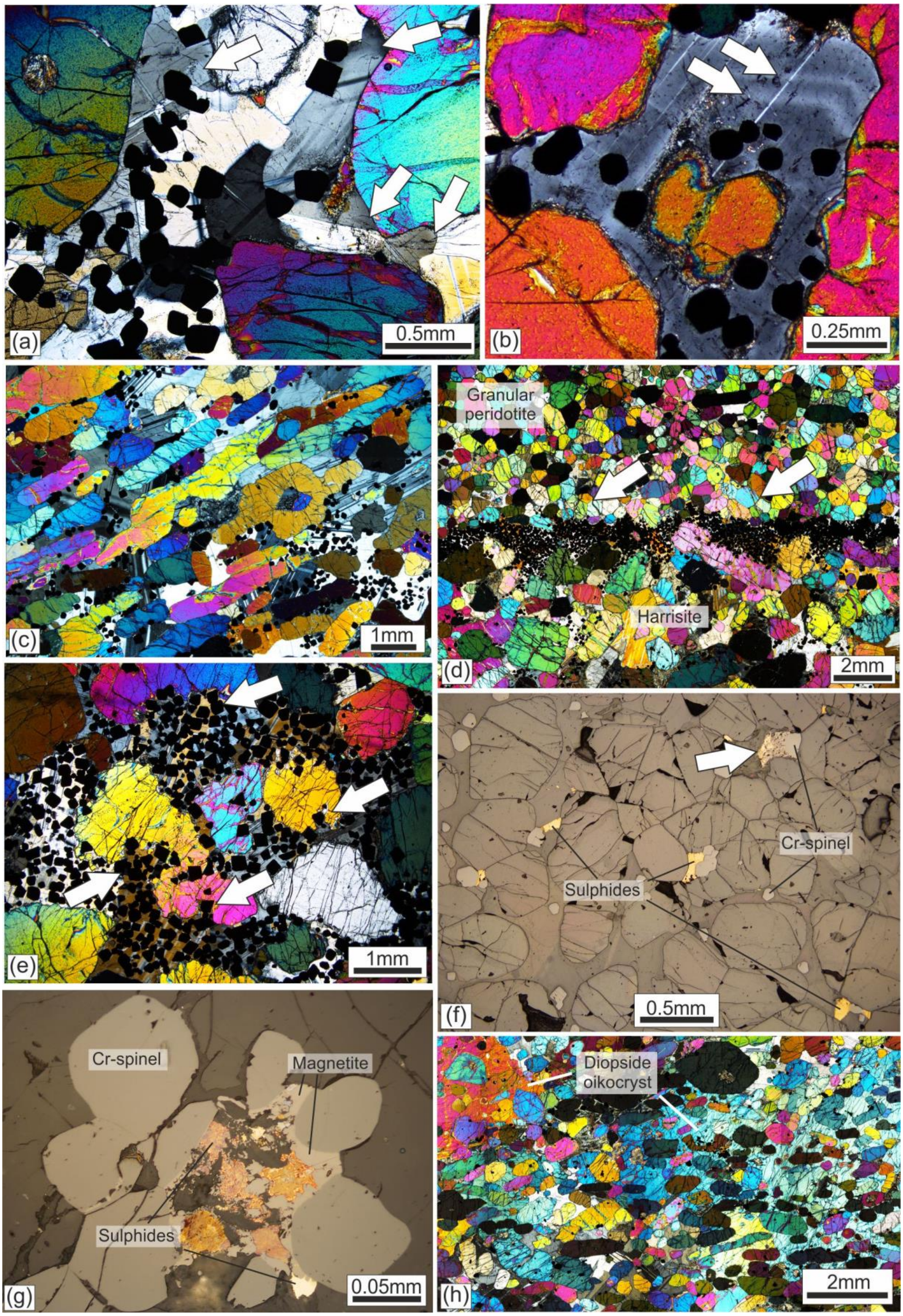
(a)
0.5mm
(b)
0.25mm
Granular peridotite
Harrisite
(c)
1mm
(d)
2mm
(e)
1mm
Cr-spinel
Sulphides
(f)
0.5mm
Cr-spinel
Magnetite
Sulphides
(g)
0.05mm
Diopside oikocryst
(h)
2mm

◄FIGURE 2.6: Petrography of the Unit 10 peridotite. (a) Optical zonation of intercumulus plagioclase crystals (examples arrowed) several mm above a boundary-type Cr-spinel seam from the lower peridotite. Note also the preferential placement of Cr-spinel at plagioclase/plagioclase grain boundaries in patches of finer-grained intercumulus plagioclase. (b) Oscillatory zoning in plagioclase oikocryst from a diffuse Cr-spinel seams of the lower peridotite. (c) Strong layer parallel foliation in harrisite from the lower peridotite. (d) Well-defined Cr-spinel seam above very coarse grained–harrisite. A reduction in intercumulus volume is observed immediately above the seam, and the development of high angle triple grain boundaries between granular olivine crystals (arrowed). (e) Example of 'chain-textured' Cr-spinel seam with cumulus olivine crystals within the limits of the seam. The olivine crystals have many (potentially deep) embayments now occupied by Cr-spinel (arrowed). (f) Reflective-light photomicrograph showing multiple high reflectivity sulphide crystals closely associated with Cr-spinel from a very diffuse seam in the lower peridotite. (g) Reflective-light photomicrograph of various Cu-Ni sulphides with magnetite attached to Cr-spinel. (h) Typical clinopyroxene-oikocrystic peridotite from the upper peridotite with large, clinopyroxene crystals occupying significant intercumulus volume. Note also the larger hopper olivine grain in the top centre of the image.

Base-metal (Ni-Cu) sulphides also occur very closely associated with Cr-spinel (Fig. 2.6f), often moulded onto or touching Cr-spinel grains. Where sulphide grains occur, magnetite is also present, seemingly attached to the Cr-spinel crystals (Fig. 2.6g). Platinum-group minerals (PGM) including Pt-arsenides/tellurides, Pd-antimonides, Ru-Ir alloys and Pt-Ir sulphosalts, as well as electrum (Au-Ag) grains, occur closely associated with these sulphides (Fig. 2.7; 2.8).

2.4.2 The Upper Peridotite

Cumulus olivine crystals in the UP have a heterogeneous texture, consisting of granular-textured (equant) olivine as well as elongate/tabular olivine (~2 mm long) with subordinate, coarser-grained (~4 mm) hopper and skeletal olivine (see Fig. 2.6h). Cr-spinel occurs between cumulus olivine, enclosed by intercumulus clinopyroxene and plagioclase. Disseminated Cr-spinel is more abundant in the UP than in the LP (i.e., up to 5 vol. %). The proportion of intercumulus minerals accounts for 15–25 vol. % of the rock, and these comprise plagioclase oikocrysts (1–2 mm diameter) and larger (5–20 mm) rounded-elongate oikocrysts of diopside. The volume percentage proportion of intercumulus plagioclase to diopside is 60:40, respectively. Compositional zonation is also optically apparent in intercumulus plagioclase, as observed in the LP. A non-pervasive foliation of variable strength, carried by the tabular olivine crystals, is common throughout the UP, oriented approximately parallel to layering.

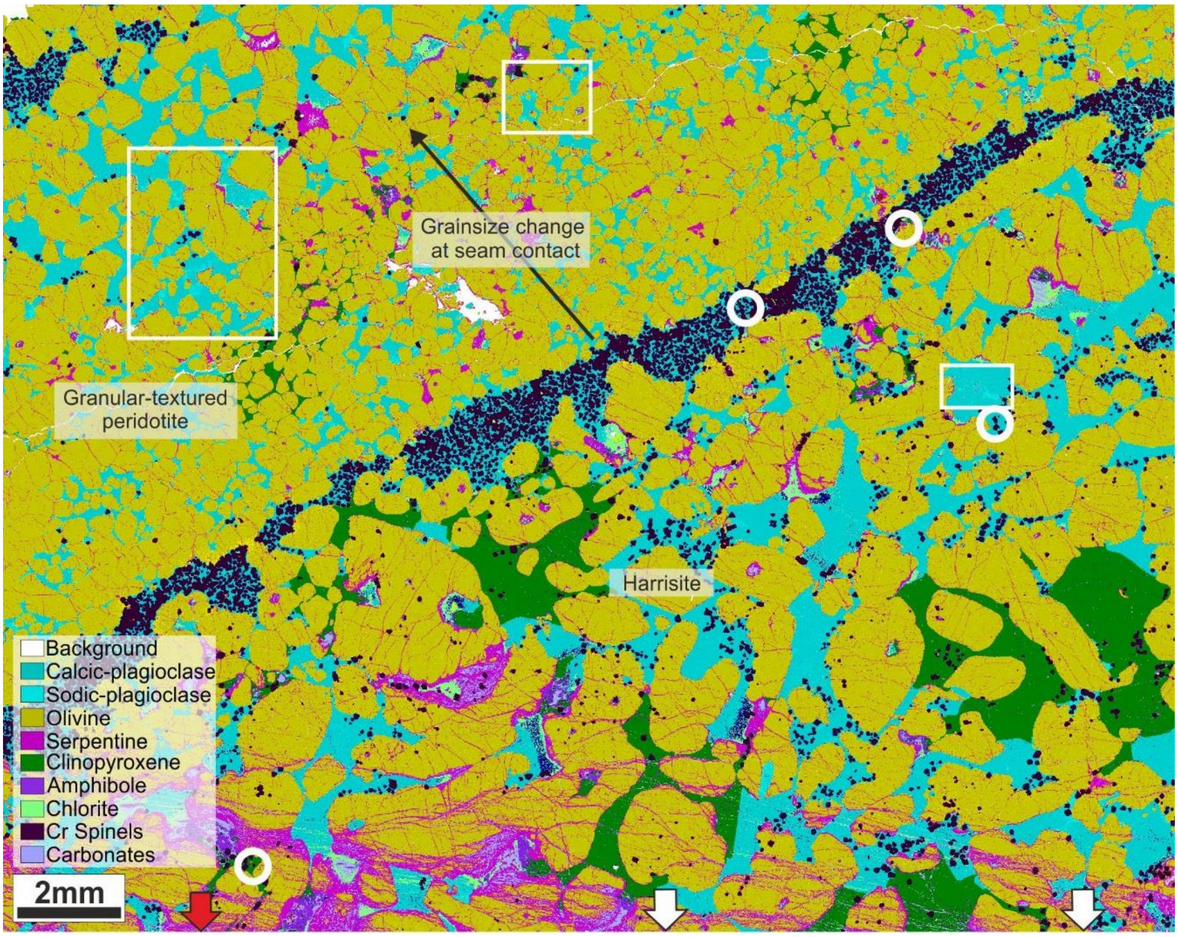

FIGURE 2.7: QEMSCAN® image of well-defined Cr-spinel seam featured in Figure 2.4f and 2.6d, adapted from O'Driscoll *et al*. (2014). White circles indicate the position of detected PGM grains, with white arrows at the base indicating PGMs just beyond the view of the image. Red arrows at the base indicate the position of electrum (Au-Ag alloy) grains just beyond the image. Note also the 'patchy' zonation of intercumulus plagioclase (varied blue shade) highlighted in the white boxes.

2.5 CRYSTAL SIZE DISTRIBUTION ANALYSIS

2.5.1 Method

Crystal Size Distribution (CSD) analysis provides a quantitative means of measuring the grain size and number of crystals within a defined area of a sample of interest. As crystal size carries important information on cooling and nucleation rates within igneous rocks, CSDs have been used to infer crystallisation kinetics in magmatic systems independent of experimental or thermodynamic approaches (e.g., Cashman & Marsh, 1988; Marsh, 1998; Boorman *et al*., 2004; Higgins, 2006). It has been argued that simple crystallisation within either an open-system (steady-state) or closed-system (batch) end-member environment produces straight (or log-linear) CSD profiles that simply represent the nucleation and growth of crystals as magma cools and solidifies

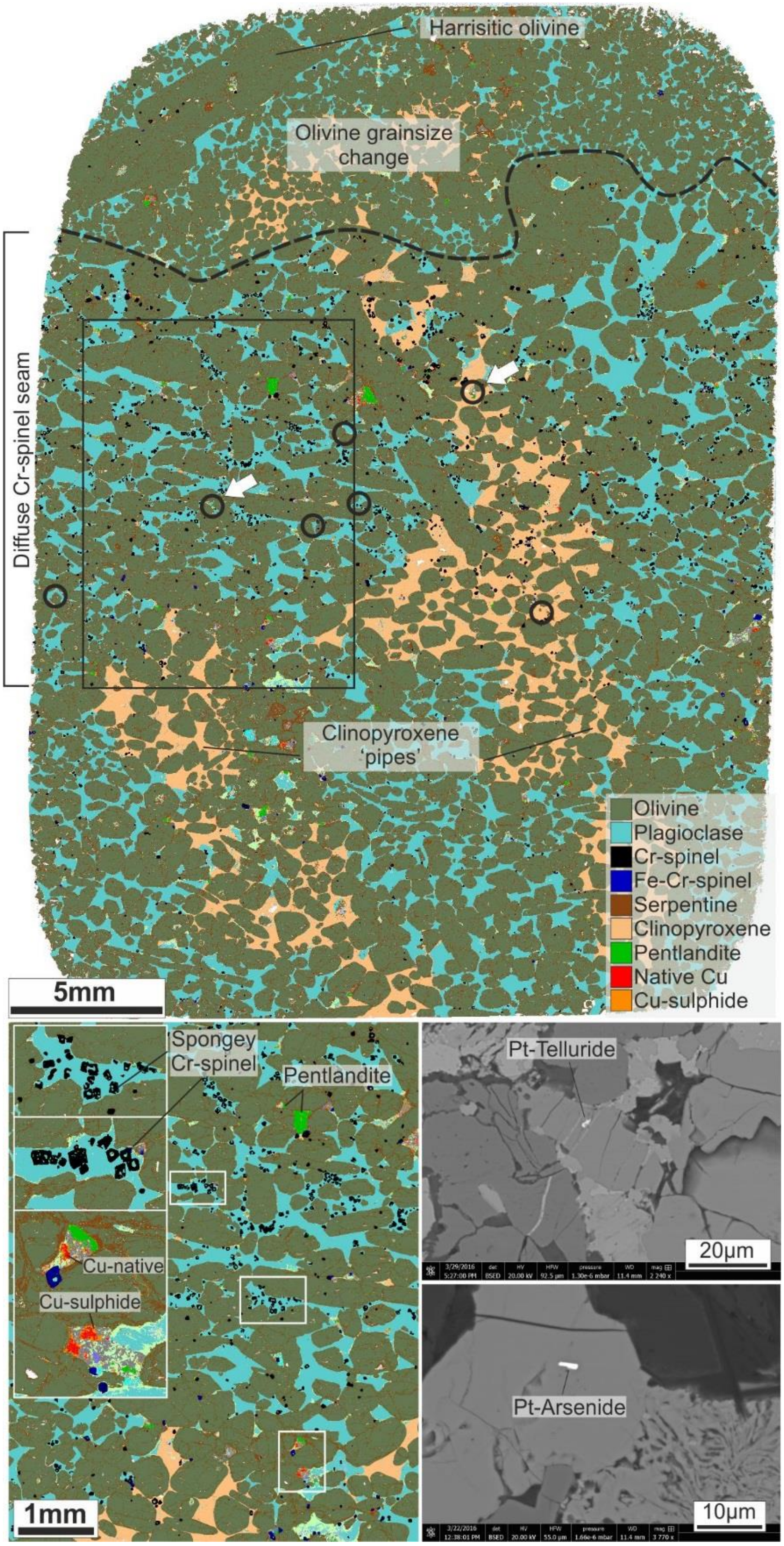

FIGURE 2.8: QEMSCAN® image of diffuse, PGM-rich, Cr-spinel seam (Sample U10I; see Appendix 1.1) from the LP, with close up image of boxed area highlighting the abundance of sulphide minerals. Black circles indicate the position of PGM grains, with BSE images of particular PGM grains highlighted by the arrowed circle. Note the unusual presence of clinopyroxene in long vertically oriented structures, and sharp grain size change of olivine in the top of the image.

(Marsh, 1998). Deviation from this log-linear shape (e.g. CSD kinking or curvature) has been attributed to various processes such as crystal accumulation and removal (Marsh, 1998), multiple crystal populations (Higgins, 1994; Marsh, 1998), post-cumulus crystal coarsening by annealing and Ostwald ripening, or compaction (Boorman *et al*., 2004; Higgins, 2002b). Log-linear CSDs can be further analysed by plotting derivative CSD parameters against one another (e.g., characteristic length versus intercept). Such parameters have been shown to have a relationship irrespective of the modal abundance of the mineral of interest (Higgins, 2002a).

In this chapter, CSDs are employed to support the petrographic observations in determining the environment of crystallisation of Cr-spinel seams and to aid in ascertaining the relative importance of magmatic and post-cumulus processes during their formation. The CSDs were determined from thin sections and calculated following the methods outlined in Higgins (2000; using the program *CSDCorrections version 1.4*). The CSDs were calculated by manually digitising reflected light photomicrographs, recommended for opaque phases to avoid misidentification of annealed Cr-spinels (O'Driscoll *et al*., 2010; Vukmanovic *et al*., 2013). The digitised images were analysed using *ImageJ* image analysis software to determine the input parameters for *CSDCorrections*. Feret length, the length of a square with an area equal to that of the analysed crystal, has been employed as a crystal size parameter here, following the method of O'Driscoll *et al*. (2010). No preferred orientation of Cr-spinel crystals was observed. An aspect ratio of 1:1:1 and a roundness factor of 0.5 were input into *CSDCorrections*. In total, CSDs were produced for Cr-spinel seams from 16 samples, incorporating the different seam groups introduced above, as well as accounting for differences within the seam groups defined above (such as seam thickness). A minimum of 500 crystals was analysed in each sample where possible to obtain a statistically viable representation of each seam (Mock & Jerram, 2005). As the smallest crystals are easily visible in reflected light, the lower crystal size limit of 0.01 mm is taken to represent the true lower limit of the sample.

2.5.2 Results

Crystal Size Distribution plots are illustrated in Figure 2.9, with additional CSD output data in Appendix 1.2. Previously published CSD data for the Unit 11-12 main Cr-spinel seam and so-called

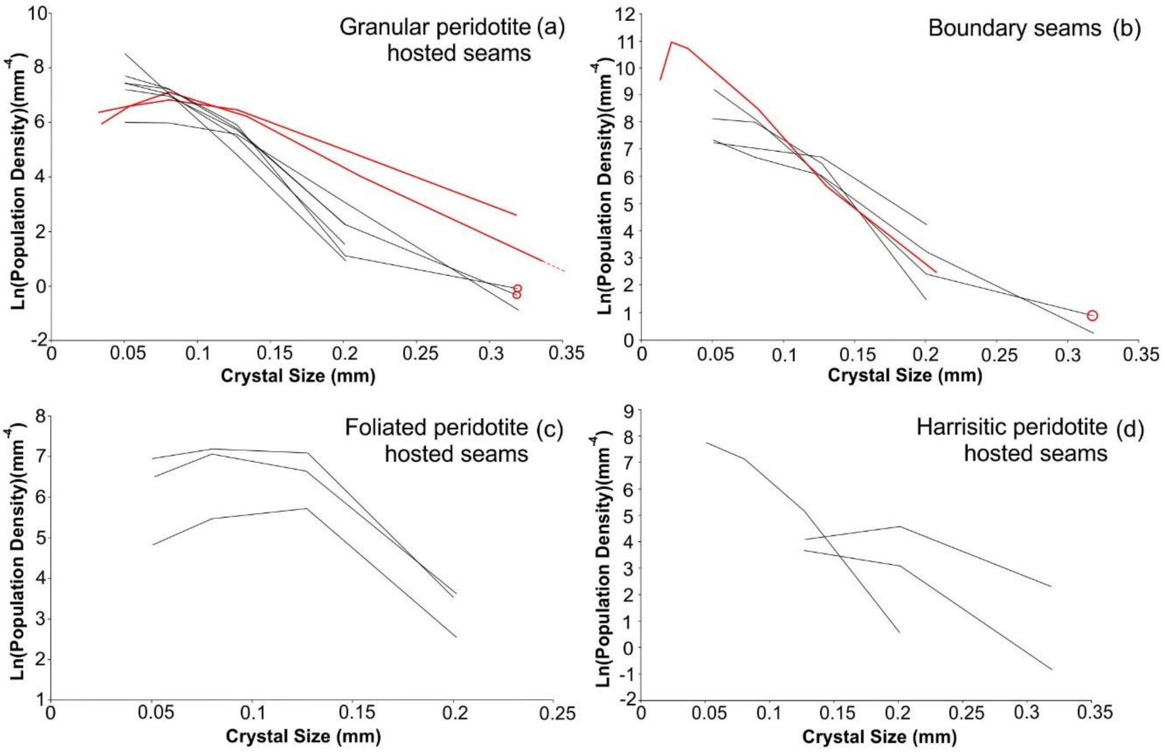

FIGURE 2.9: Crystal size distribution diagrams of the sixteen Cr-spinel seams analysed in this chapter, separated into the four seam groups discussed in the text. The Unit 11-12 main seam and two peridotite hosted Cr-spinel seams from the Unit 12 peridotite in red (O'Driscoll *et al*., 2010) are included for comparison. Red circles denote CSD bins with significant errors. All error data can be found in Appendix 1.2.

peridotite-hosted 'supra-seams' above the Unit 11-12 boundary (O'Driscoll *et al*., 2010) are included for comparison in Figure 2.9. All CSD plots display log-linear profiles at larger size fractions with perturbations in some of the profiles occurring for smaller size fractions. There is modest variation within the specific groupings of seams distinguished above (Fig. 2.9). For example, CSDs for granular-textured peridotite-hosted seams define a range of slope values from -55.0 to -21.2 mm^{-1}. The profiles are broadly log-linear, with shallowing of the CSD slope typical at smaller size fractions. Boundary seams show very similar profiles to those of the granular-textured peridotites, with slopes that range from -48.4 to -27.1 mm^{-1}, log-linear profiles, and a shallowing of slopes at the smallest size fractions. The harrisite-hosted seams have CSDs with similar slopes to the aforementioned groups (-55.1 to -19.5 mm^{-1}), with the shallowest slopes measured in this chapter. They also exhibit further shallowing at smaller size fractions. Seams hosted within foliated peridotites display similar slope values to those in previous groups, for the largest size fraction, but are characterised by broad overturns at the middle-to-smallest crystal size bins. Kinking of the CSD profiles is observed for

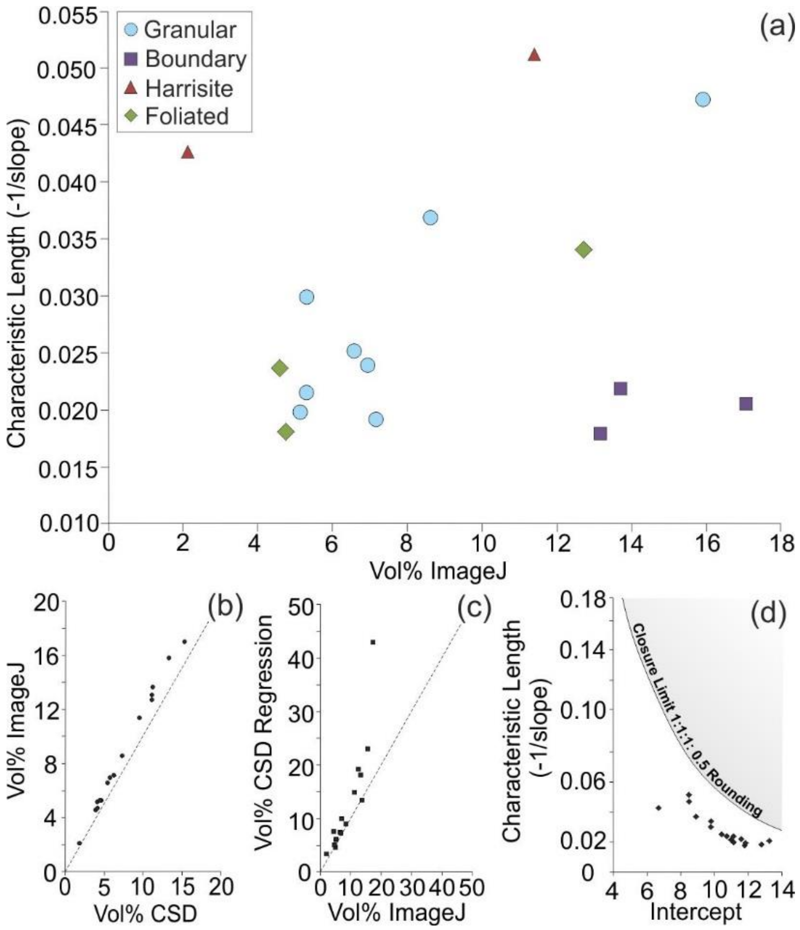

FIGURE 2.10: Crystal size distribution derivative diagrams for Cr-spinel seams analysed in this chapter. See text for explanation.

some granular-textured and boundary group seams. These size bins are typically associated with large uncertainties, and as such caution must be taken when interpreting the CSD profile.

A plot of characteristic length (-1/slope; see Higgins, 2002a) versus intercept (Fig. 2.10a) partly distinguishes the Cr-spinel seams groups previously recognised on field evidence (i.e., granular, boundary, harrisite-hosted). The foliated seam group does not produce a distinctive group. Instead, these data plot within the granular grouping irrespective of the peridotite host (i.e., harrisitic or granular). The volume percentage of Cr-spinel from both *ImageJ* and *CSDCorrections* show a strong correlation (Fig. 2.10b). A good correlation also exists between the measured volume phase proportion and the *CSDCorrections* regression (calculated in *CSDCorrections 1.4*; see Higgins, 2002a), supporting a true log-linear profile (Fig. 2.10c). Deviation from this 1:1 fit occurs in samples that have the strongest perturbations from a log-linear profile, such as foliated and harrisite-hosted samples where the changes in CSD slope occur at small size fractions. The CSD data fall below the closure limits defined by assuming 100 vol. %, of the mineral phase of interest (Higgins, 2002a; Fig. 2.10d) which is a useful indicator of the robustness of the CSD dataset.

2.6 WHOLE ROCK GEOCHEMISTRY

2.6.1 Methods

Major element analysis was performed by X-ray Fluorescence (XRF) at Bureau Veritas Minerals, in Vancouver, Canada. Centimetre-sized slabs of rock were prepared to remove altered and weathered surfaces before being cleaned with de-ionised water and dried at 50°c for several hours. Samples were then crushed to < 75 µm and fused with $Li_2B_4O_7$/$LiBO_2$ before being analysed by XRF. Repeat analysis of one sample was performed with reproducibility < 1%. Details on the detection limits and standards used in analysis can be found in Appendix 1.3.

2.6.2 Results

The major element geochemistry for samples in this chapter are summarised in Table 2.1 and Appendix 1.3. The samples display modest variation in their major element composition and can be broadly delineated into groups corresponding to lithology (Fig. 2.11). Harrisites have the lowest MgO and FeO_t contents (28.71–32.87, and 11.01–12.28 wt. %, respectively) and the highest Al_2O_3 abundance (7.41–8.43 wt. %). The harrisites are compositionally more similar to Sample M9, a porphyritic picritic dyke (Upton *et al*., 2002), than the granular-textured peridotites. Granular-textured peridotites have a range in MgO and FeOt of 34.91–35.53, and 13.08–13.32 wt. %, respectively, with sample Gra-2B, as a coarse-granular–harrisitic peridotite with intermediary MgO values (32.91 wt. %) between both groups. Cr_2O_3 wt. % between the sample groups is largely dependent on lithology (specifically Cr-spinel content; see coarse-grained peridotite in Fig. 2.11), with similar Cr_2O_3 values between peridotite types (Fig. 2.11). The UP sample is broadly similar to the lower peridotite, but contains elevated FeOt (14.37 wt. %), which is comparable to values presented by Tait (1985).

Table 2.1. Whole rock major element geochemistry for peridotite types and Cr-spinel seams from the Unit 10 peridotite. Plotted data normalised to LOI. Sample locations can be found in Appendix 1.1.

	Har-1	Har-2	Har-3	Gra-1	Gra-2A	Gra-2B	Gra-3	U10I	U10Q	U10O	M9
SiO_2	43.13	42.34	41.43	41.41	41.21	40.20	41.17	40.15	35.10	41.24	41.86
TiO_2	0.27	0.41	0.16	0.14	0.21	0.30	0.17	0.13	0.25	0.24	0.61
Al_2O_3	8.47	7.40	7.74	5.15	4.88	6.48	5.73	4.47	8.49	5.26	6.55
FeOt	11.37	12.27	11.07	13.18	13.38	13.28	13.38	12.17	14.69	14.49	10.86
MnO	0.16	0.17	0.15	0.18	0.18	0.17	0.18	0.16	0.17	0.20	0.16
MgO	29.30	28.68	33.05	36.28	35.80	32.95	35.11	37.52	34.03	34.10	31.67
CaO	6.76	7.11	4.75	4.12	4.14	4.84	4.26	3.56	2.89	4.61	5.22
Na_2O	0.80	0.72	0.65	0.44	0.47	0.53	0.47	0.33	0.31	0.47	0.99
K_2O	0.05	0.05	0.04	0.02	0.03	0.03	0.02	0.01	0.01	0.02	0.07
P_2O_5	0.03	0.03	0.02	0.02	0.02	0.02	0.02	0.02	0.02	0.02	0.06
Cr_2O_3	0.15	0.72	0.24	0.50	0.65	1.73	0.66	0.64	5.03	0.49	0.29
SrO	0.01	0.01	0.01	0.01	0.01	0.01	0.01	0.00	0.01	0.01	0.01
SO_3	0.03	0.02	0.01	0.01	0.01	0.01	0.01	0.25	0.07	0.02	0.05
LOI	-0.06	-0.03	1.23	-0.69	-0.49	-0.44	-0.61	0.95	-0.48	-0.35	0.94
Total	100.53	99.92	99.32	101.46	100.99	100.55	101.19	99.41	101.07	101.17	98.39

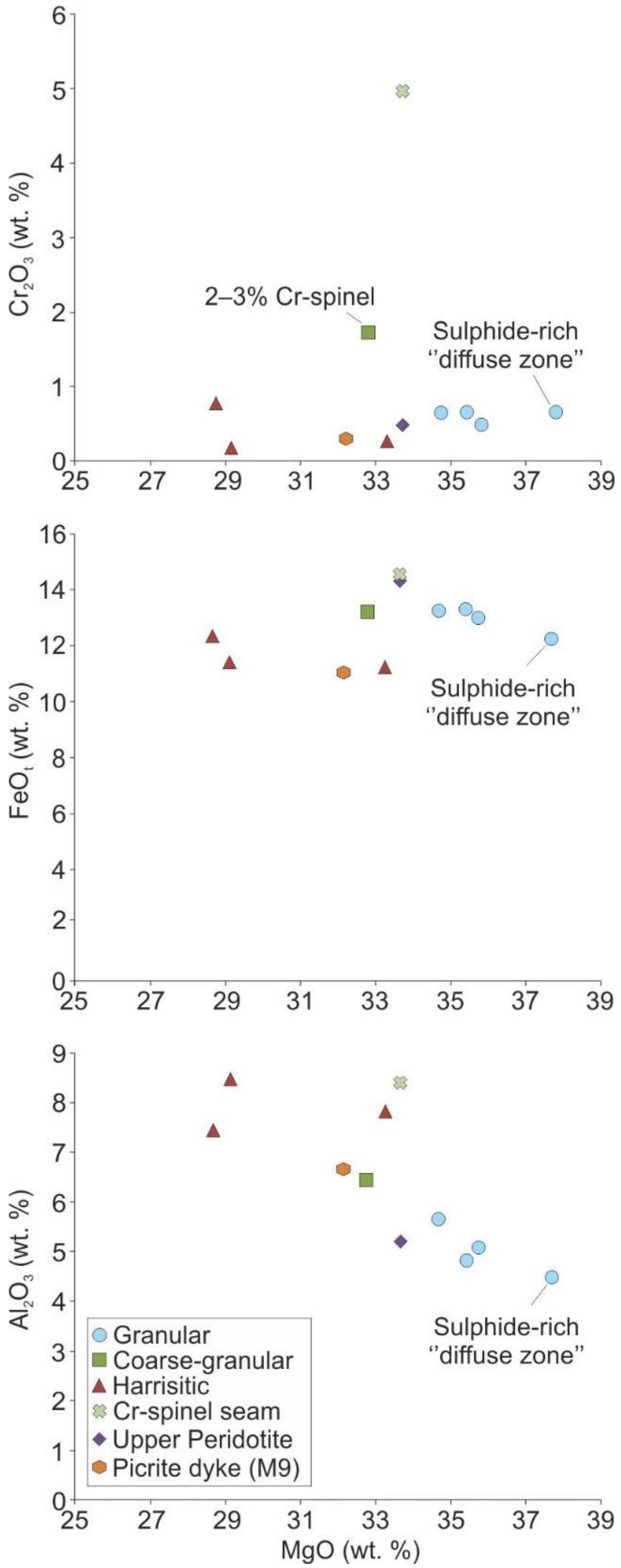

FIGURE 2.11 Selected Fenner diagrams for whole rock analyses of Cr_2O_3, FeO_t, and Al_2O_3 for peridotites in Unit 10. ''M9'' analysed as part of this chapter is the same picritic dyke as discussed in Upton *et al*. (2002). Note the moderate segregation of harrisite and granular-textured peridotite types.

2.7 MINERAL CHEMISTRY

2.7.1 Methods

Mineral chemical data were obtained using a JEOL JXA-8900RL electron microprobe at the Department of Geochemistry, Geowissenschaftliches Zentrum der Universität Göttingen (GZG) in 2014. The Cr-spinel compositions were obtained using an acceleration voltage of 20 kV with a beam current of ~20 nA and a typical beam diameter of ~1 µm. Cr-spinel count times on peak and background for Mg, Al, Cr, Fe and Si were 15s and 5s, respectively, and for V, Ti, Mn, Ni, Zn were 30s and 15s, respectively. Olivine compositions were obtained using an acceleration voltage of 15 kV, with a beam current of ~15 nA and a typical beam diameter of ~5 µm. Olivine count times on peak and background for Si, Mg, Al were 15 s and 5 s, respectively, for Fe, Mn, Ni were 30 s and 15 s, and 60 s and 30 s for Ca. Element maps of Na concentration were carried out on three samples where optical zonation of intercumulus plagioclase was observed under the petrographic microscope within the LP. One Cr map was also collected on a sample of a large clinopyroxene oikocryst from the UP. Sample locations can be found in Appendix 1.1. Element maps were obtained using an acceleration voltage of 20 kV, with a beam current of ~60 nA, a beam diameter of 2 µm and a dwell time of 50 ms.

Cr-spinel compositions were measured from 11 Cr-spinel seams; the measurements were made along three vertical traverses for each seam, with an average of 15 Cr-spinel crystals analysed per traverse. The traverses were approximately equidistant from one another (5–7 mm) along strike. Each traverse typically included several peridotite-hosted Cr-spinel crystals for comparison, above and below the seam. All of the Cr-spinel crystals analysed were hosted in plagioclase oikocrysts. Disseminated Cr-spinel were analysed in the UP, which lacks discrete seams. The ferric iron content of Cr-spinel was calculated following Droop (1987), which assumes that the spinel composition is stoichiometric. As such, Cr-spinel compositions rich in a ferric iron component should be treated with caution (*cf*. Quintiliani *et al*., 2006; O'Driscoll *et al.*, 2010).

2.7.2 Results

2.7.2.1 Olivine

The olivine chemical data discussed here are tabulated in Appendix 1.4. Olivine compositions in the Unit 10 peridotite have high-Fo values, with a narrow range between Fo 82–88 mol. %. Nickel concentrations range between 1832–3029 ppm (Fig. 2.12). There are no discernible differences in olivine compositions from the different LP peridotite types (granular-textured, harrisitic etc; Fig. 2.12). However, olivine from the UP has a generally lower Fo content than the LP olivines (Fo 82–84), with similar Ni concentrations of 1951–2556 ppm.

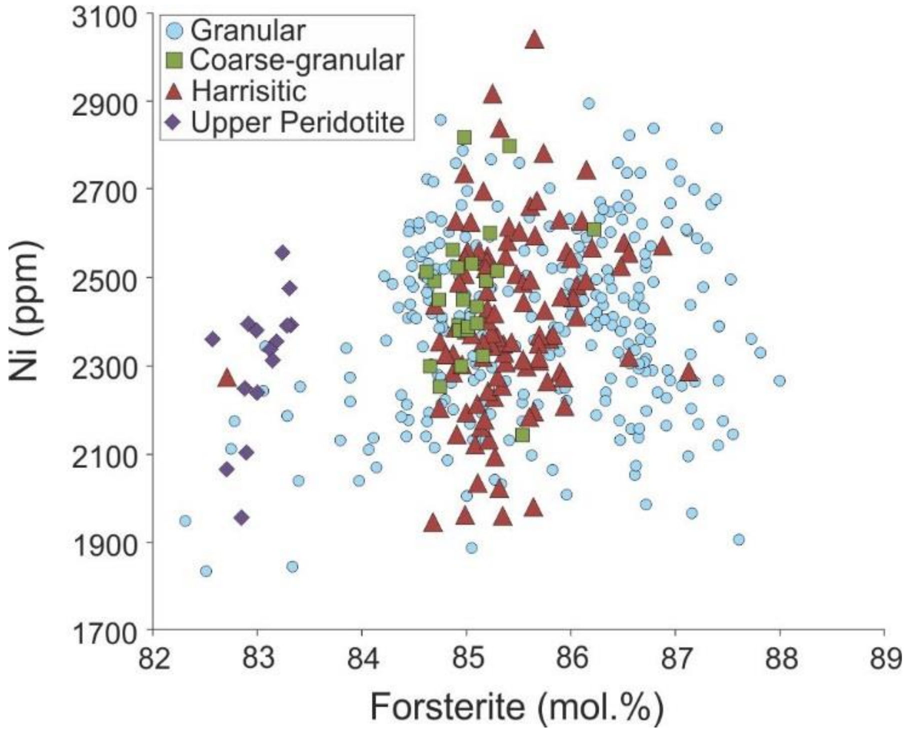

FIGURE 2.12: Ni (ppm) versus Forserite abundance (mol. %) of olivines from the Unit 10 peridotite. Note the significant overlap of all peridotite types of the lower peridotite. Upper peridotite olivine has lower Fo-values than lower peridotite olivines.

2.7.2.2 Cr-spinel

The full Cr-spinel chemical dataset discussed below is presented in Appendix 1.5. Cr-spinel chemistry is highly variable between samples, but no well-defined groups can be delineated. Previously published data for peridotite-hosted Cr-spinel from the RLS has been included for comparison (Upton *et al*., 2002; O'Driscoll *et al*., 2009a; Holness *et al*., 2007; Fig. 2.13a). Chromium number (Cr#; [$Cr^{3+}/(Cr^{3+}+Al^{3+})$]) values are similar for Cr-spinel between peridotite types but vary within and outside the seams. Magnesium number (Mg#; [$Mg^{2+}/(Mg^{2+}+Fe^{2+})$]) values for Cr-spinel within the seams varies between 16 and 59. There is no distinct chemical variation between the granular, boundary and foliated seam groups (Fig. 2.13b). However, harrisite-hosted Cr-spinel crystals are generally characterised by higher Cr# values (corresponding to lower Al_2O_3), and higher Fe_2O_3 (~17 wt. %) values, compared with ~14 wt. % Fe_2O_3 for granular, boundary and foliated seam types. Cr-spinel compositions in peridotite above and below the seams are also typically higher in Fe_2O_3 (Fig. 2.13b) and TiO_2- the latter varies from 0.71 to 5.80 wt. %. Cr-spinel compositions analysed from the UP differ significantly from those in the LP. Specifically, Cr_2O_3 content in the UP is considerably lower (25–32 wt. %), Fe_2O_3 content is higher ~23 wt. %, and TiO_2 contents are typically > 3 wt. %.

Cr-spinel from seams in Unit 10 exhibit compositional variation across individual traverses at the mm-scale. Similar patterns are observed from one seam to the next (Fig. 2.14). For example, Cr# is lower within seams, compared to higher Cr# values of Cr-spinel above and below the seams. This reflects an increase in Al_2O_3 within seams, with a concomitant increase in Fe_2O_3 away from the seam (see also Fig. 2.13b). TiO_2 is particularly low within seams but increases significantly (up to 5.8 wt. %) with distance away from the seam and into the surrounding peridotite. This is shown particularly well in Sample U10M (Fig. 2.14). This sample contains a relatively thick seam and a secondary diffuse seam several millimetres above the former. The TiO_2 values increase away from the thick seam but decrease again as the diffuse seam is approached. Additional detail on Cr-spinel chemical variation across these traverses can be found in Appendix 1.5.

2.7.2.3 Element Maps

Na maps of optically-zoned intercumulus plagioclase from the Cr-spinel seams show both normal and reverse compositional zoning (Fig 2.15), as well as an example of well-developed oscillatory zoning (Fig. 2.15a). Sample U10A, from a granular-textured seam displays well-developed oscillatory zoning (Fig. 2.15a). Sample U10R, from a foliated-type seam, exhibits patchy reverse zoning of the intercumulus plagioclase (Fig. 2.15b). Sample U10B displays normal zoning located <5 mm above a boundary seam that occurs on the top of a harrisite layer (Fig. 2.15c). Here, the cores

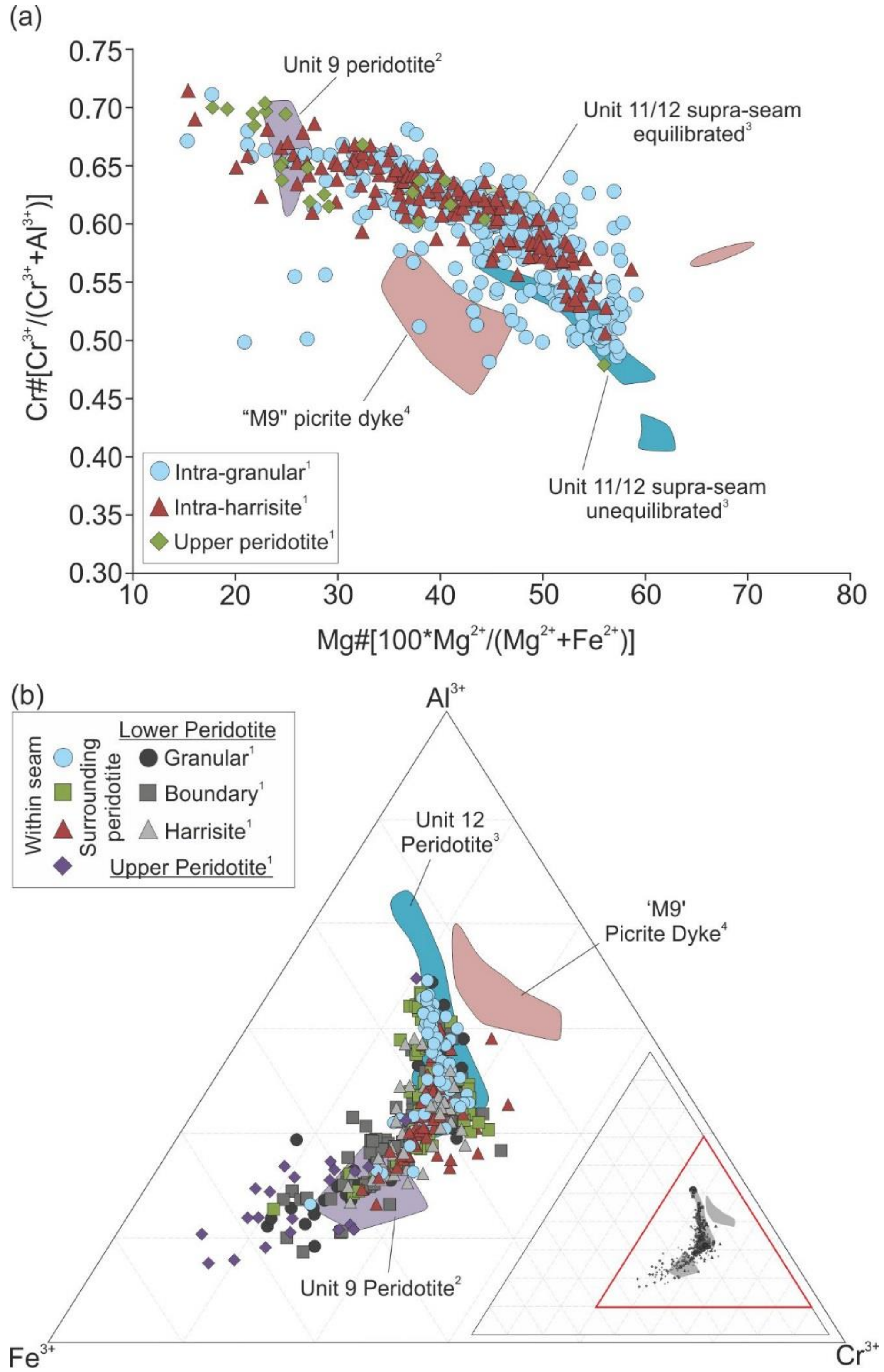

FIGURE 2.13: (a) Cr# vs Mg# diagram for Unit 10 Cr-spinel data analyses from Rum, divided into host peridotite lithology, compared with other peridotite-hosted Cr-spinels from the RLS, 1 = Unit 10 (this chapter), 2 = Unit 9, disseminated Cr-spinel (Holness *et al.*, 2007), 3 = Unit 12 'supra-seams' (O'Driscoll *et al.*, 2010), 4 = ''M9'' picrite disseminated Cr-spinel (Upton *et al.*, 2002; O'Driscoll *et al.*, 2010). (b) Cr-spinel trivalent cation ternary diagram (Al^{3+} - Cr^{3+} - Fe^{3+}) for spinels from the Unit 10 peridotite (1). Peridotite hosted Cr-spinel from other sections of the RLS are included for comparison (as above). These all cluster relatively close to the Unit 10 data, with the Unit 12 seams being the most aluminous. Note the Fe^{3+} and Al^{3+} variation between Cr-spinel within seams, and within the surrounding peridotite. See text for discussion.

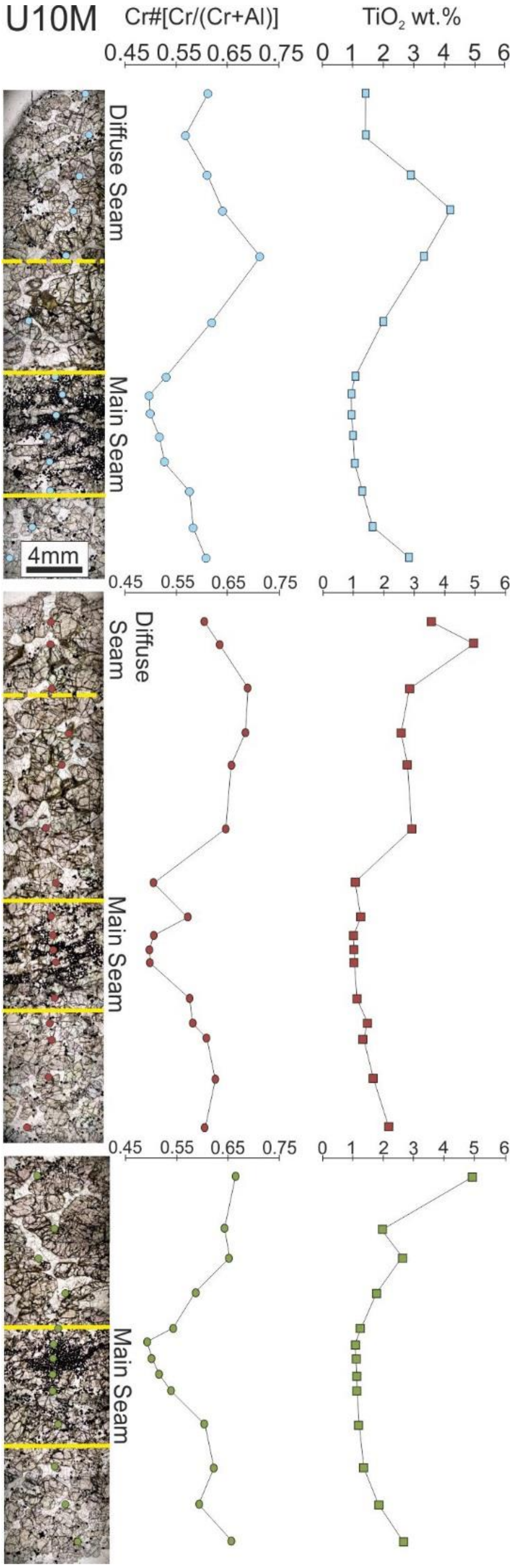
U10M
Cr#[Cr/(Cr+Al)]
TiO$_2$ wt.%
0.45 0.55 0.65 0.75
0 1 2 3 4 5 6
Diffuse Seam
Main Seam
4mm
0.45 0.55 0.65 0.75
0 1 2 3 4 5 6
Diffuse Seam
Main Seam
0.45 0.55 0.65 0.75
0 1 2 3 4 5 6
Main Seam

◄FIGURE 2.14: Chemical traverses of Cr#[$Cr^{3+}/(Cr^{3+}+Al^{3+})$] and TiO_2 wt. % across a Cr-spinel seam from the lower peridotite, with harrisite above the seam and granular-textured peridotite beneath it. A decrease in Cr# corresponds to an increase in Al^{3+}. The position of the seam on each sample has been highlighted for clarity. An increase in TiO_2 with a decrease in Cr# is typically occurs in Cr-spinel outside the limits of the seam. Additional traverses can be found in Appendix 1.5

of some of the intercumulus plagioclase crystals are markedly rectilinear, with seemingly rounded or subhedral rims. Zonation of intercumulus plagioclase is also apparent in the QEMSCAN® images (Fig. 2.7). While quantitative analyses of the mapped plagioclase crystals are not available, published and unpublished mineral chemical data for zoned cumulus and intercumulus plagioclase crystals from the Rum ELI indicate that variation of ~An_{83}–$An_{74,}$ and ~An_{74}–An_{63} occurs (O'Driscoll *et al*., 2009a; Hepworth, unpublished data). Element mapping on a clinopyroxene oikocryst from the UP reveals patchy zoning of Cr (Fig. 2.15d), similar to that reported in Unit 9 (Leuthold *et al*., 2014).

2.8 DISCUSSION

2.8.1 Intrusive Replenishment in the Rum Layered Suite

Harker (1908) originally considered the peridotite portions of the ELI rhythmic units to be intrusive. However, subsequent work on the ELI by Brown (1956) that was almost certainly influenced by studies of the Skaergaard Intrusion (Greenland), invoked fractional crystallisation and gravity (crystal) settling instead (Wager & Deer, 1939). Bédard *et al*. (1988) first challenged this model and instead suggested, like Harker (1908), that the peridotites of the ELI intruded into a pre-existing troctolitic crystal mush. Bédard *et al*. (1988) suggested that it was possible that all of the peridotite bodies of the ELI could be intrusive. More recently, detailed textural and geochemical studies of the Unit 9 peridotite, in particular, have demonstrated the intrusive nature of this body and shown that it modified (texturally and chemically) the feldspathic cumulate above and below it (Holness *et al*., 2007; Leuthold *et al*., 2014). Whilst the importance of open-system magma chamber systematics has been emphasised for the RLS in general (Renner & Palacz, 1987; O'Driscoll *et al*., 2007a; 2007b; Holness & Winpenny, 2008), further evidence of intrusive peridotites has not specifically been mentioned in the ELI. Here, it is argued that the Unit 10 peridotite is composed of multiple small volume intrusive replenishment events.

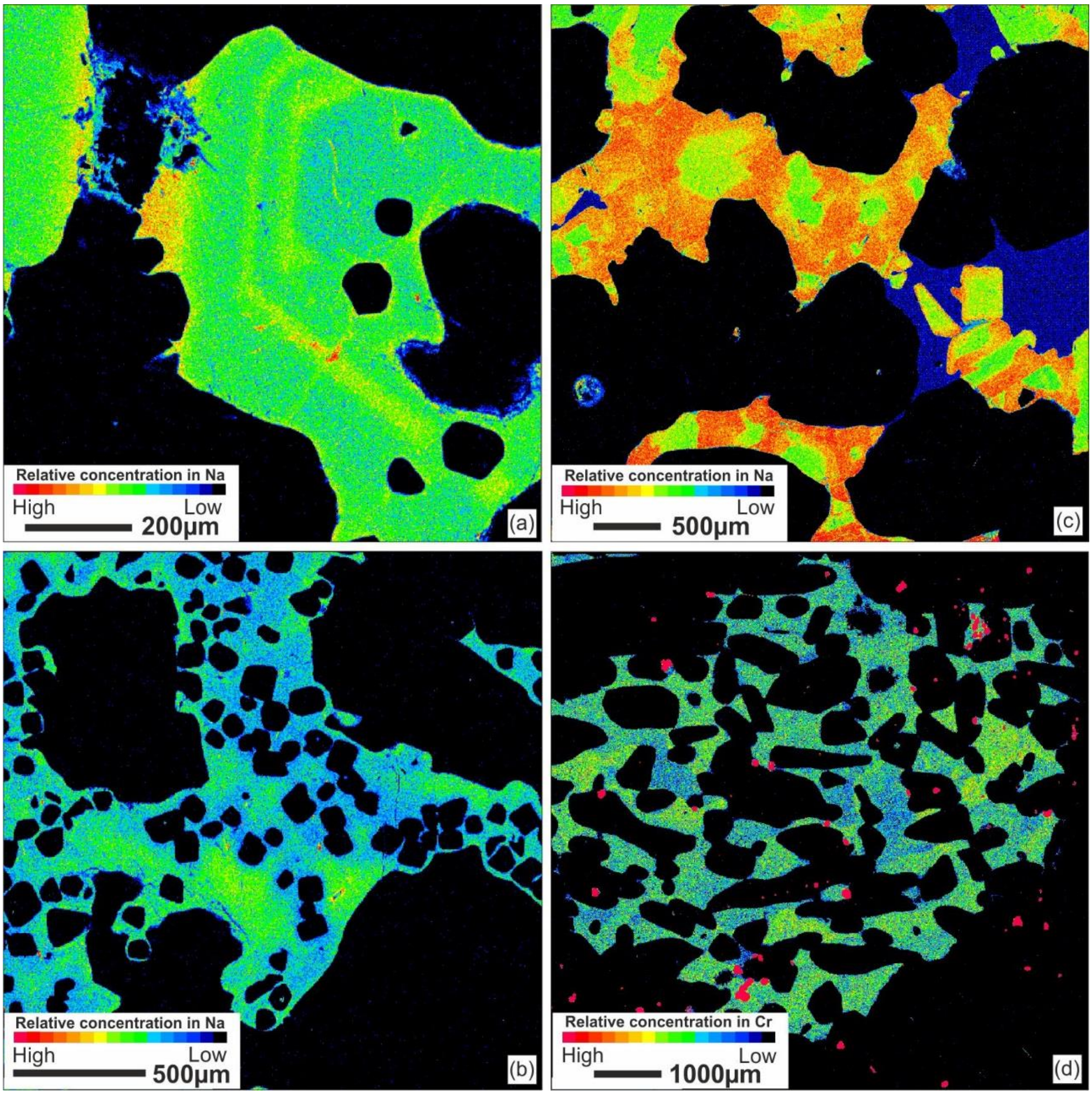

FIGURE 2.15: Mineral composition element maps from the lower peridotite (three samples a–c, see text for detailed location description) showing varied intercumulus plagioclase zonation in Na, and patchy zoning of Cr in a clinopyroxene oikocryst from the upper peridotite (d).

2.8.2 Intrusive harrisite

The Rum harrisites are a type example of crescumulate; containing large, often skeletal crystals growing perpendicular to the layer plane, as defined by Wager *et al*. (1960). The authors envisaged dendritic and skeletal olivine crystals growing upward from the contemporary magma chamber floor. As such, these rocks have become an important example of *in situ* crystallisation in layered intrusions. While the model of Wager *et al*. (1960) accounts for those olivine crystals that demonstrably grew upwards from a substrate, Donaldson (1974; 1975) highlighted the problems of the model in explaining apparently downward growing harrisitic olivine, or crystals with stellate morphologies that also frequently occur in these layers. Experimental studies that reproduced harrisitic olivine textures indicate that these rocks probably form relatively rapidly, under enhanced undercooling of picritic magma (Donaldson, 1975; Lofgren & Donaldson, 1975; O'Driscoll *et al.*, 2007a). Upton *et al.* (2002) further highlighted the important role picrite played as a parental magma to the RLS. O'Driscoll *et al.* (2007a) suggested that the enhanced undercooling that gave rise to harrisitic texture occurred in thin sheets of newly emplaced picrite at the base of the magma chamber. One implication of this idea is that the WLI (Fig. 2.1), where most of the Rum harrisite occurs, was built up of numerous small volume replenishments.

Multiple features of the Unit 10 harrisite layers are not consistent with processes that occurred at the magma-crystal mush interface (e.g., Fig. 2.2; 2.5c). Irregular upper surfaces, tapering and termination of harrisite layers have been reported from harrisites in the WLI, where they were considered to represent ponded intercumulus liquid from layers above or below the harrisite in question (Donaldson, 1982). This is significant, as it suggests that harrisite might form within the crystal mush. However, the lateral correlation of packages of harrisitic layers across hundreds of metres of Unit 10 stratigraphy (as suggested in Fig. 2.2) is not consistent with ponding of intercumulus liquid, especially as these layers also change in thickness, and may even cut across surrounding layers (Fig. 2.2). The tapering, bifurcation and complete termination of harrisite layers in Unit 10 pose problems for a model invoking ponding of intercumulus melt or magma chamber floor processes. Instead, it is suggested that these layers represent sill-like intrusions of picritic magma emplaced directly into the crystal mush as semi-stratiform intrusive bodies, similar to interpretations made by Bédard *et al.* (1988) in the ELI, and also to sill-like injections of komatiites observed in lava piles by Houlé *et al.* (2009). It is also suggested that large amplitude (> 50 cm) irregularities (Fig. 2.5c; d) on the upper surfaces of harrisite layers are best considered as features associated with intrusive sheets. It is not considered likely that structures such as that illustrated in Figure 2.5c could have been preserved on the magma chamber floor without collapsing. Instead, loading of a newly intruded and rapidly crystallising picritic sheet by the overlying crystal mush might explain such apophyses (Fig. 2.5c; d; see discussion below). There is a suggestion in Figure

2.2 that harrisite layers (and packages of layers) thicken with distance away from the feeder zone (Long Loch Fault), an observation that might be explained by considering the competency of the crystal mush. Further from the feeder zone, the crystal mush may have been cooler and more rheologically competent, such that thicker harrisite layers (associated with greater degrees of undercooling) could intrude. Finally, the granular-textured peridotite on either side of some harrisite layers exhibits extreme reductions in porosity (i.e., intercumulus mineral fraction) and well-developed textural equilibration. In the latter, the 2D apparent triple junctions of polygonal olivine grains approach 120° (see Fig. 2.6d), suggesting a degree of thermal maturation (*cf.* Holness, 2007a), which might indicate a contact metamorphic effect on either side of the intrusive harrisite sheets. To what extent the host (granular-textured) peridotite was solidified in each instance of harrisite emplacement (i.e., exactly how much intercumulus melt remained in the host) is difficult to estimate but may have been variable for different layers.

An important premise of harrisite formation is that the replenishing magma is aphyric (Donaldson, 1974; 1975; O'Driscoll *et al.*, 2007a). Higher degrees of undercooling with homogeneous nucleation of olivine led to the extremely large (>1 m long) dendritic olivine crystals that are observed in the WLI. The degree of undercooling (and supersaturation in olivine) has been experimentally shown to have a control on olivine morphology (Donaldson, 1974; 1976; Faure *et al.*, 2003; Welsch *et al.*, 2014), suggesting that the different harrisite layers of the WLI formed from different degrees of undercooling. This is not surprising, given that the multiple replenishments that fed the Rum intrusion are likely to have varied in volume (*cf.* O'Driscoll *et al.*, 2007a). In the case of the Unit 10 peridotite, however, the abscence of extremely coarse-grained dendritic crystals and the relative abundance of hopper olivine crystal morphologies suggest that the degrees of undercooling may have been comparatively lower than in parts of the WLI. The whole rock chemistry suggests harrisites are slightly more compositionally evolved than the granular-textured peridotites, with lower MgO (Fig. 2.10). However, lower FeO_t contents than granular-textured peridotites point towards a more evolved composition (with lower Mg#), while Cr_2O_3 contents remain broadly similar between peridotite types. The mineral chemistry of olivine and plagioclase in each peridotite type strongly suggest they crystallised from the same magma, with no variation in olivine compositions between different rock types (Fig. 2.12). The strong modal variation in mineralogy (i.e., harrisite contains a greater modal abundance of feldspar) explains this variation in whole rock chemistry and supports the argument for the two peridotite types crystallising from the same magma, but under different conditions. There are several possible reasons for the difference in crystallisation conditions. One might be that the parental melt batches that formed the Unit 10 peridotite may not have arrived at the level of the magma chamber in a completely aphyric state. Donaldson (1976) suggested that the presence of pre-existing nuclei may decrease the growth rate of spontaneously nucleating nuclei, ultimately suppressing the degree of supersaturation and forming less skeletal olivine morphologies. This might imply that peridotites forming the Unit 10 peridotite formed from a mixture of relatively aphyric and phyric magmas, now represented by harrisitic and granular-textured peridotite, respectively. With respect to the WLI, it might be expected that the ELI did not form from magmas that were as primitive (or superheated with respect to olivine). By the time the structurally higher ELI formed, the RLS was a well-established (thermally mature) system, compared to the WLI which lies towards the base of the intrusion and whose parental melts might have encountered a much steeper thermal gradient on entry to the magma chamber. O’Driscoll *et al.* (2007a; 2010) argued that the melts that formed the WLI were likely to have been aphyric, and also that features at some ELI unit boundaries (e.g., Unit 7-8) suggested emplacement of high-temperature aphyric picrites. By contrast, the textural study of Worrell (2002) found evidence of multiple crystal populations in the WLI and suggested that the granular-textured peridotites there formed from phenocryst-rich magmas. The model of O’Driscoll *et al.* (2007a) for harrisite formation might also be adapted for the Unit 10 peridotite, where the intruding picrite instead comes into contact with relatively cold cumulate or crystal mush, enhancing undercooling. This is supported by the presence of brittle deformation of layers above harrisite apophyses and the lack of cross-cutting of these apophyses by other peridotites types.

The physical state of the host crystal mush is an important factor in explaining the relationships at the boundaries between harrisites and granular-textured peridotites. In particular, it is possible that some of the complexity at harrisite upper surfaces arises as a result of the rheological contrast between the ‘orthocumulate’ harrisite and the more mesocumulate-like granular-textured peridotite.

Because of its greater volume of interstitial melt (as represented by intercumulus plagioclase), harrisite might remain ‘mushy’ longer than the peridotites above and below. Indeed, the greater volume of plagioclase in harrisite might therefore be expected to have lower solidus temperatures. The movement of interstitial melt from the intruded harrisite layers following emplacement could explain the irregularities and apophyses observed, as well as the associated deformation of layering that occurs adjacent to harrisite layers (e.g., Fig. 2.5c). However, this would be expected to result in distinctly olivine-poor apophyses, which are not present. In fact, harrisitic textures in the apophyses are similar to those in the main layered from which they are assumed to have originated. From this, it is suggested that the apophyses represent primary intrusion features at the boundaries of the conduits that facilitated harrisite emplacement, perhaps forming at points where the host cumulate was less well solidified or where brittle deformation opened fractures in the wall rock.

It is therefore argued that most, if not all, of the harrisite sheets in the Unit 10 peridotite are intrusive (i.e., emplaced as sills into the developing crystal mush). There is evidence that the granular-textured peridotite may also be intrusive, i.e., where Cr-spinel seams bound layers of such rock. It is emphasised that the physical properties of the resident crystal mush, the phenocryst content of the intrusive magma, or a combination of both played a critical role in the development of the different peridotite types in Unit 10.

2.8.2 *In situ* Cr-spinel seam formation within a crystal mush

The processes by which stratiform Cr-spinel seams form in layered intrusions is contentious, and a wide range of models have been proposed to explain their occurrence, including pressure changes, magma mixing, cumulate and wall-rock assimilation, emplacement as crystal cargos, accumulation by crystal settling and formation from a stratified magma column (Henderson & Suddaby, 1971; Irvine, 1977; Lipin, 1993; Spandler *et al*., 2005; Mondal & Mathez, 2007; O’Driscoll *et al*., 2009a; 2010; Junge *et al*., 2014). Many of the above models rest on the observation that Cr-spinel seams occur at levels of the intrusion stratigraphy associated with the introduction of new magma (i.e., replenishment, in an open-system magma chamber). The Unit 10 peridotite contains dozens of Cr-spinel seams, and the most likely explanation for this is that the peridotite body represents multiple replenishment events. Many of the published models for Cr-spinel seam formation assume that the horizon is formed at the magma-mush interface on the magma chamber floor, with a few exceptions (e.g., Voordouw *et al*., 2009). This presents a problem when considering the close spatial relationship of the Unit 10 Cr-spinel seams with intrusive harrisite and other peridotite layers. However, the possibility that Cr-spinel seams can form within the crystal mush has previously been suggested for the Bushveld Complex by Ballhaus (1988) and later by Latypov *et al*. (2015), where sill-like harzburgite protrusions that are rimmed with Cr-spinel occur beneath the platiniferous Merensky Reef. In addition, the felsic cumulates beneath the Unit 7-8 and 11-12 boundaries in the Rum ELI contain 'subsidiary' seams, which have been attributed to formation within the crystal mush by O'Driscoll *et al*. (2009a; 2010). It is proposed here that the Unit 10 peridotite seams form *in situ*, a notion that has previously been suggested for other chromitite seams within the RLS (O'Driscoll *et al*., 2009a; 2010, Latypov *et al*., 2013), and other intrusions (e.g., Barnes & Jones, 2013).

Previously reported observations that the Cr-spinel seams in the ELI follow culminations and depressions (and even overhangs), without changing thickness, show that crystal settling is not a likely mechanism for accumulation of the Cr-spinel (O'Driscoll *et al*., 2010; Latypov *et al*., 2013). It is shown here that Cr-spinel seams can have a close relationship with the interior, upper, and basal surfaces of intrusive harrisite sheets. The CSD data presented here for the Cr-spinel seams provide further support for crystallisation *in situ* (Fig. 2.9). Most of the Unit 10 Cr-spinel seams CSDs have a log-linear profile for most crystal sizes, suggesting a relatively simple relationship between nucleation and growth. The lack of a dominance of larger crystal sizes, or evidence of size-dependent mechanical sorting (Marsh, 1998; Higgins, 2002b), argues against crystal settling. Similar CSD profiles are observed from other Cr-spinel seams in the ELI (O'Driscoll *et al*., 2009a; 2010), and the Coobina Layered Intrusion in Western Australia (Barnes & Jones, 2013) where *in situ* crystallisation has also been invoked. However, the smallest and largest crystal size bins of some of the CSDs show additional complexity. Shallow slopes and downturns at the smallest crystal size fraction likely reflect post-cumulus coarsening or annealing (i.e., Ostwald ripening). The CSD profiles for boundary seams and granular-textured peridotite-hosted seams have relatively similar slopes. However, harrisite-hosted Cr-spinel seams typically display shallower profiles and are dominated by larger crystal sizes overall. This is attributed to interaction with the large interstitial melt component that the harrisitic mush contained, evidenced by the large proportion of intercumulus material. Conversely, in boundary seams and granular-textured peridotite-hosted seams the intercumulus component is much lower, suggesting a greatly reduced potential for interaction and post-cumulus modification of Cr-spinel with intercumulus melts. The CSD data suggest that the Cr-spinels from the foliated peridotites may have also undergone a form of Ostwald ripening. It is possible that the formation of the foliation affected the Cr-spinel texture, perhaps by loss of smaller nuclei and crystals during compaction-related expulsion of intercumulus melt (Higgins, 2002b).

The chemistry of the Cr-spinel across seam types (and textures) is generally overlapping, suggesting similar processes operating during petrogenesis. The exception to this may be harrisite-hosted Cr-spinels which display slightly more Fe_2O_3 rich compositions, consistent with their interaction with intercumulus liquid in the porous harrisitic crystal mush (e.g., O'Driscoll *et al*., 2009a; Leuthold *et al*., 2014). Compared to previously reported peridotite hosted Cr-spinel compositions in the ELI, the Unit 10 Cr-spinel spans much of the range of previous analyses. The consistency of chemical composition of Cr-spinel within peridotites alludes to a potentially significant control of host lithology/mineralogy on Cr-spinel composition, whereas in feldspathic hosts Cr-spinel can show either extreme Al-enrichment (O'Driscoll *et al*., 2010) or Fe-enrichment (Henderson, 1975; O'Driscoll *et al*., 2009a; Lenaz *et al*., 2011; Leuthold *et al*., 2014).

Chemical traverses through the seams and surrounding peridotite reveal mirrored trends in Cr# and TiO_2 (Fig. 2.14). There is an increase in Cr# with distance, above and below the seam, implying that the Cr-spinels in the seam have the highest Al_2O_3 contents. Following Bell & Claydon (1992) and O'Driscoll *et al*., (2009a; 2010) the latter Cr-spinel compositions are considered the closest to those originally crystallised from magma, a suggestion further supported by recent experimental data reported by Leuthold *et al*. (2015). Away from the seam, the increase in Cr# and concomitant increase in Fe_2O_3 suggest a greater degree of interaction with intercumulus melt in the host peridotite. This is observed in all datasets where Cr-spinel occurs outside the limits of a given seam (Fig. 2.13b). The lack of modification within the seam possibly results from a buffering effect of the liquid after Cr-spinel crystallisation or from the effect of reducing porosity once Cr-spinel has crystallised, reducing the ability of liquids to penetrate the seam, or from a combination of both. Notably, TiO_2 also increases with distance from the seams (Fig. 2.14). Maximum TiO_2 contents of up to 5.8 wt. % are observed in many instances, suggesting a degree of interaction with a trapped interstitial liquid, due to the incompatible behaviour of Ti^{4+} in these systems (Roeder & Campbell, 1985; Scowen *et al*., 1991; Barnes & Roeder, 2001; Wijbrans *et al*., 2015). The unit boundary (7-8 and 11-12) seams described by O'Driscoll *et al*. (2010) also have Cr-spinel with low TiO_2 contents (< 1 wt. %), with higher concentrations observed in accessory Cr-spinel in anorthosite and troctolite that were interpreted as reflecting a trapped liquid effect (see also Lenaz *et al*., 2011). This lends support to the mineral compositional patterns illustrated in Figure 2.14 being imposed at the post-cumulus stage, suggesting at least some mobility of interstitial melt in the crystal mush.

2.8.3 Preferential assimilation of a peridotite cumulate

The chemistry of the Cr-spinel seams and textural analysis suggest that seams formed *in situ* within a crystal mush. The spatial relationship of Cr-spinel seams with intrusive harrisite also strongly suggests a co-genetic relationship, i.e., the intrusion of picrite caused a seam-forming reaction with the host cumulate. This is not a new concept as the interaction of picritic liquid and a more evolved component (cumulate or liquid) has been used to explain the formation of Cr-spinel horizons in many layered intrusions (e.g., Muskox; Irvine, 1977; Rum; O'Driscoll *et al*., 2010; Bushveld; Latypov *et al*., 2015). The presence and field relations of potholes, culminations, and cumulate autoliths led O'Driscoll *et al*. (2010) to suggest that Cr-spinel seams occurring between Unit 7-8 and 11-12 of the Rum ELI formed from the assimilation of feldspathic cumulate floor by the influx of picritic magma, creating a hybrid liquid capable of crystallising abundant Cr-spinel. Similar interpretations exist for the Merensky Reef of the Bushveld Complex (Ballhaus & Sylvester, 2000; Latypov *et al*., 2015).

The presence of troctolite and granular-textured peridotite autoliths in the Unit 10 peridotite (e.g., Fig. 2.4a) suggest that the replenishing magma was capable of reworking (i.e., assimilating) cumulate. However, the lack of feldspathic cumulate within the Unit 10 peridotite poses a problem for the application of exactly the same model to explain chromitite seams here. Previous studies (referred to above) on the Rum chromitites invoke the almost total assimilation of cumulate adjacent to the replenished magma (O'Driscoll *et al*., 2010; Latypov *et al*., 2015). However, it is not immediately obvious that this should be the outcome where picrite is emplaced into a peridotitic host. The critical point, as outlined below, is that the rocks that have traditionally been referred to as peridotite on Rum can contain up to 50 vol.% plagioclase feldspar, so are effectively melatroctolites.

In Figure 2.16, the invading magma (M_1) is taken as the Rum parental magma of Upton *et al*. (2002) and Holness *et al*. (2007), equivalent to an aphyric 'M9' picrite. The assimilation of > 60% troctolite (T_1) as suggested by O'Driscoll *et al*. (2009a), labelled T_1, results in a binary mixing line with the liquid entering the spinel field thus crystallising abundant Cr-spinel. However, there is no evidence that troctolite was ever abundant enough within the Unit 10 peridotite to account for the number of seams present. The total assimilation of feldspathic peridotite of Unit 10, one of the composition of a typical granular-textured peridotite with >70% olivine, 25% plagioclase, and 5% clinopyroxene (P_1), and a second harrisitic peridotite with 50% olivine, 45% plagioclase, and 5% clinopyroxene (P_2), by the M_1 picrite, even if possible, would fail to reach the spinel field as the percentage of olivine is too high in the assimilant. Mixing of picrite with an evolved liquid was proposed in the Muskox Intrusion by Irvine (1977). To facilitate such a mixing model on Rum, the picritic liquid would have to hybridise with the intercumulus liquid between cumulus olivine crystals in the peridotite mush. The liquid, having crystallised olivine as it cools, will lie on the An-Fo cotectic, or potentially at the An-Fo-Di eutectic (E). However, the hybridization of the picritic liquid and evolved intercumulus liquid on a simple binary mixing line will not move it into the spinel field, so it is difficult to see how a seam will form. To satisfy the phase relations, it is proposed that the invading liquid reacts with the feldspathic peridotite, dissolving out plagioclase and removing only minor amounts of olivine. Such a reaction would saturate the liquid in Fo + An and place it on the An-Fo cotectic. Continued dissolution of olivine and plagioclase might lead to the liquid attaining the peritectic point (P) at about 1317 °C (Morse, 1980), such that the reaction Fo + An produces Sp + L. The liquid may then leave the Fo-An-Di plane completely, toward SiO_2, producing spinel as it does so. The process describe above is consistent with petrographic observations, where cores of relatively sodic plagioclase crystals exist within anorthitic plagioclase oikocrysts (Fig. 2.15b), and corroded olivine embayments are filled with Cr-spinel (Fig. 2.6e), suggesting stronger dissolution of plagioclase than olivine within the mush. The Cr required to form abundant Cr-spinel during this reaction can potentially be sourced from the invading picrite with ~2400 ppm Cr (O'Driscoll *et al*., 2009b). The Cr-spinel forming reaction is broadly isenthalpic (*cf*. Kelemen, 1990), though the temperature difference between fresh picrite magma and of that of a peridotite mush that has already crystallised abundant plagioclase will likely result in a net reduction in temperature. This net reduction may drive the hybrid liquid into the spinel field, permitting abundant Cr-spinel crystallisation, without the need to subsequently cool the superheated magma on hybridization (Latypov *et al*., 2015). As the Cr-spinel seams typically contain plagioclase as the intercumulus phase, the liquid path can be estimated to have descended onto the An + Sp cotectic and not the Fo + Sp cotectic (O'Driscoll *et al*., 2009a; 2010; Latypov *et al*., 2015). If the latter was the case, corroded cumulus olivine might be expected to recrystallise and new growth on olivine rims might act to 'heal' olivine crystal embayments observed ubiquitously within the Cr-spinel seams. It is also worth noting in this regard that olivine occurs interstitially to Cr-spinel seam hosted in troctolite or anorthosite (e.g., the subsidiary Cr-spinel seams at the Unit 7-8 boundary (O'Driscoll *et al*., 2007a). Finally, it should be noted that the Cr abundance has been shown to affect the spinel stability field (Irvine,

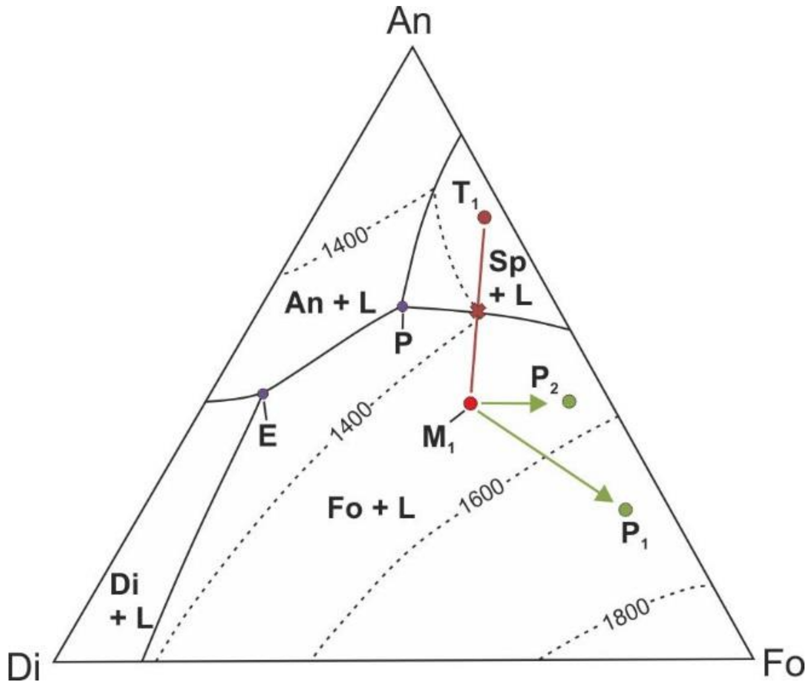

FIGURE 2.16: Pseudo-ternary phase diagram for the system olivine-plagioclase-clinopyroxene + spinel denoted Fo-An-Di-Sp, respectively, after Morse (1980), depicting the reactions involved in Cr-spinel petrogenesis for the Unit 10 peridotite, as discussed in the text.

1977), and that the use of the An-Fo-Di ternary diagram is simply a visual aid to illustrate the proposed reaction.

The preferential dissolution of phases in harzburgite has been used to explain the presence of dunitic bodies within the upper mantle sections of ophiolites (Quick, 1981; Kelemen, 1990; Kelemen *et al*., 1995; Morgan & Liang, 2005). Picritic/basaltic liquid saturated in olivine successively dissolves clino- and orthopyroxene in lherzolites and harzburgites, crystallising olivine to produce dunite residue with similar Mg# of olivine to the surrounding harzburgite (Quick, 1981; Kelemen, 1990; Kelemen *et al*., 1995). Processes invoking the removal of lower temperature phases by magma have also been proposed for the Rum ELI to produce cpx-poor troctolite from gabbroic rocks (Holness *et al*., 2007; Leuthold *et al*., 2014). Furthermore, this process has also been linked to the formation of chromitites found in dunites within the upper mantle (see Gonzaléz-Jiménez *et al*., 2014). Experimental work by Donaldson (1985) on the dissolution rates of common minerals within basaltic magmas showed that plagioclase will dissolve out of the rock faster than olivine at a rate of ~86 µm/hour. The dominant control of this process is the requirement for the dissolving magma to be undersaturated in the mineral being dissolved (Donaldson, 1985). It seems possible therefore that the picritic magma intruded into the crystal mush is more than capable of preferentially dissolving intercumulus plagioclase, producing a hybrid liquid able to crystallise abundant Cr-spinel within an existing crystal framework of olivine, without removing significant portions of olivine.

2.8.4 Hot tearing of the crystal mush as a mechanism for harrisite intrusion and Cr-spinel seam formation

Hot tearing is a metallurgic phenomenon that occurs during the casting of Al-alloys, where tears open as a result of thermal contraction parallel to the walls of the mould and to the solidification front that fill with the inter-crystalline liquid. This process of ductile fracturing is an intergranular or interdendritic process occurring above the solidus, i.e., in a semi-solid state (Lahaie & Bouchard, 2001; Eskin *et al*., 2004). Hot tearing has been shown to operate when the alloy consists of a touching framework of crystals and an interstitial liquid at high solid fractions, up to 85–95% (Eskin *et al*., 2004). Many of fundamental features of hot tearing are applicable to natural silicate crystal mushes and have been used to describe the origins of a variety of preferentially oriented segregation structures in flood basalt feeders (Phillpotts *et al*., 1996), dykes and sills (Geshi, 2001; Marsh, 2002), migmatites and granitic melts (Vigneresse *et al*., 1996), and layered mafic intrusions (Humphreys & Holness, 2010; Namur *et al*., 2013). In these studies, the crystal mush is ‘torn’ by local stresses produced by compaction, differential cooling, gravitational sagging, or localised shear, forming tears that allow the accumulation of liquid. Once the dilation has opened, liquid is preferentially drawn to the lower stress tears where it crystallises, producing texturally distinct schlieren or pods. Humphreys & Holness (2010) proposed that this process occurred in crystal mushes in the Marginal Border Series of the Skaergaard Intrusion, Greenland. The solidification front of the Marginal Border Series was vertically-oriented, and the crystal mush was essentially unsupported towards the centre of the magma chamber; this produced a strong lateral pulling stress (σ_3), with little to no vertical (i.e., compaction) stress (σ_1) as the crystal mush was effectively pulled towards the main magma body from the sidewall of the chamber. The gravitational stress on the mush facilitated shearing, opening tears in highly crystalline mushy rocks that filled with liquid drawn in from the main magma body, producing textural and chemically variable segregations oriented parallel to the shearing direction.

2.8.4.1 Shearing and hot tearing in the Unit 10 peridotite

Gravitational collapse or sagging of crystal mush as a mechanism to form hot tears might be important in the RLS, given the abundant evidence for deformation there (e.g., Volker & Upton, 1990; Emeleus *et al*., 1996; O’Driscoll *et al*., 2007b; Emeleus & Troll, 2014). The RLS has a roughly bowl-shaped structure, with the layers dipping variably towards the Long Loch Fault feeder zone (Fig. 2.1). Significant syn-magmatic deformation structures with proximity to this feeder zone suggest contemporaneous deformation and ‘sagging’ of the mush into the feeder zone (Volker & Upton, 1990; Emeleus *et al*., 1996; Emeleus & Troll, 2014). Magnetic fabrics within the ELI, including the Unit 10 peridotite, support this view (O’Driscoll *et al*., 2007b). Fundamentally, this sagging may have resulted in a significant $\sigma_3 > \sigma_1$ stress that strengthened towards the Long Loch Fault, where evidence for deformation is greatest (e.g., Volker & Upton, 1990). This strong σ_3 pulling stress has the potential to create shearing of the mush, and if the crystallinity is high, can open dilations and hot tears, allowing magma to be drawn up to low stress regions.

Peridotites in Unit 10 are largely classic orthocumulates (Wager *et al*., 1960) and resemble the ideal intergranular semi-solid configuration of Lahaie & Bouchard (2001), with a loosely touching crystal framework surrounded by a film of liquid (i.e., plagioclase-clinopyroxene normative liquid). The olivine framework is assumed to have been present at the time of intrusion (see earlier discussion), providing a minimum crystallinity (ϕ) estimate of 75–85% (calculated from *ImageJ*). Relic plagioclase crystals contributes < 1% to the assumed crystallinity at the time of intrusion, however, if Cr-spinel is taken to reflect the presence of pre-existing plagioclase of the crystal mush (which has been assimilated) crystallinity could be as high as ~95%. It is important to note that the process of hot tearing requires only a thin film of liquid to exist around crystals to operate (Lahaie & Bouchard, 2001), and that at high crystallinities in orthocumulates would not immediately constitute a rigid framework, particularly where the crystals are equant. The quantification of tensile strength of the crystal mush and the potential for hot tearing is poorly constrained by the paucity of experimental data for the mechanical properties of mushy crystalline rocks. Marsh (2002) proposed a quantitative estimate of the tensile strength of molten-to-solidified basaltic rock approximated as a function of crystallinity (ϕ):

$$\sigma_s = \sigma_0 \left[\frac{\sigma_f}{\sigma_0}\right]^{((\Phi-\Phi_0)/(1-\Phi_0))}$$

where σ_0 is the tensile strength at ϕ_0 and σ_f is the tensile strength on the solidus, where ϕ is 1. Marsh (2002) proposed a region of tearing and instability of a crystal mush with ϕ=65%, at a tensile strength of ~1 bar for a basaltic sill (Fig. 2.17). Higher crystallinities and high modal olivine within proposed sills in the Unit 10 peridotite would point to a greater tensile strength of the mush, suggesting the region proposed is potentially a minimum estimate, with tearing occurring into higher crystallinities (Fig. 2.17). The common feature of hot tearing models is the requirement for high crystallinities, greater than ~60% when the mush gains competency (Lahaie & Bouchard, 2001; Marsh, 2002; Eskin *et al*., 2004; Marsh, 2013). The RLS was emplaced at < 1 km depth which approximates to 150 ±50 bar (Holness, 1999), suggesting only negligible vertical stress (σ_1) from lithostatic pressure and a relatively thin cumulate pile above Unit 10 (~100 m,) that would have been significantly less than the lateral stress produced by the sagging of up to 95 m thick Unit 10 crystal mush across a distance of ~6 km towards the Long Loch feeder. As the mush is unlikely to be solidifying at a constant rate (particularly if being intruded repeatedly by picrite), it will produce a largely random intrusive pattern, and not a bottom to top pattern as is commonly assumed for layered intrusions. The concept of a variable solidification rate throughout is important for shear localisation between more rigid and mushy cumulate (Geshi, 2001). Localised shear zones at the boundaries of two rheologically contrasting materials may generate foliation, which is commonly observed at the boundaries between variable peridotite types and Cr-spinel seams in the Unit 10 peridotite (e.g., Fig. 2.6c). Indeed, the generation of non-equant crystal habits (e.g., elongate crystals in Unit 10) aids rigidity and susceptibility to tearing (Vigneresse *et al*., 1996), which could help to explain the close spatial relationship between stronger olivine foliations and intrusive peridotites (and Cr-spinel seams). The fundamental requirements for this type of tearing to occur in the Unit 10 peridotite are qualitatively met and point to a potentially prevalent process during the incremental development of

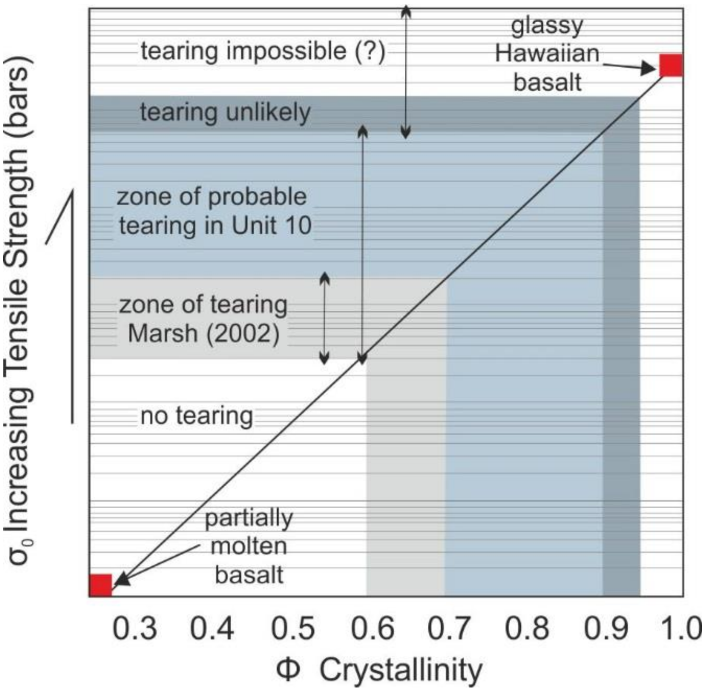

FIGURE 2.17: Qualitative illustration of tensile strength of a mush with increasing crystallinity, adapted from Marsh (2002). Zones of likely (and unlikely) tearing highlighted. See text for discussion.

the crystal mush, with important implications for the formation of harrisite layers and their associated Cr-spinel seams.

2.8.4.2 Conceptual Model

The key processes in the formation of the Unit 10 peridotite discussed in this section are summarised in Figure 2.18. A scenario in which a strong $\sigma_3 > \sigma_1$ stress-field is envisaged, promoted by sagging of the crystal mush towards the Long Loch Fault feeder zone caused gravitational collapse and 'hot tearing' parallel to $\sigma_{3.}$ This shearing stress of the crystal mush created intergranular dilations and shear zones, facilitating the migration of magma to zones of lower stress, producing peridotite layers (particularly harrisite) and Cr-spinel seams within the mush. These dilations likely amalgamated during the formation (akin to fault formation), producing extended pathways for invading magma (as evidenced by the intrusion-scale lateral correlation of harrisite layers; Figure 2.2), and providing the means to feed magma deep (laterally) into the mush. On entering the crystal mush along the numerous tears and dilations (Fig. 2.18a), the picrite magma locally assimilated feldspathic material from the mush, producing the various seam types discussed in this chapter. Granular-textured peridotite hosted seams therefore represent the injection of picrite into the mush where the intruded picrite did not inflate into a definitive sill (Fig. 2.18b), while boundary type seams represent intrusion of picrite which has inflated into a sill (e.g., harrisites; Fig. 2.18c). Intra-harrisite seams are interpreted to represent continued through-flow of picrite in a conduit, or perhaps multiple generations of through-flow, assimilating feldspathic material in the same way as in the previous examples (Fig. 2.18c).

2.8.5 Reactive liquid flow within the crystal mush: compositional disequilibrium of intercumulus plagioclase

An important consequence of the repeated injection of primitive magma into a crystal mush is the potential for the displacement of existing intercumulus liquids and/or the partial removal, via dissolution, of cumulus and intercumulus solids. The ubiquitous occurrence of zoning in intercumulus plagioclase oikocrysts reported in this chapter strongly supports the movement of reactive liquids in the Unit 10 peridotite, resulting in local compositional disequilibrium within the crystal mush. Published work on chemical and isotopic zoning in cumulate rocks has generally focused on cumulus plagioclase in feldspathic cumulates, with variable mechanisms used to explain the chemical disequilibrium, such as compaction and liquid migration (Humphreys, 2009; Namur & Charlier, 2012), diffusion-controlled redox and electrochemical gradients (Veksler *et al.*, 2015), or reworking and redeposition of crystals of different origins in density currents or plumes (Tepley & Davidson, 2003). Recent studies of reactive melt flow caused by the intrusion of the Unit 9 peridotite in the ELI suggest that chemical disequilibrium can be induced by migrating melts and can be recorded in zoning of clinopyroxene oikocrysts (Leuthold *et al*., 2014). Because intercumulus phases represent crystallised interstitial melt, zoning in these crystals is likely to be a function of processes operating within the crystal mush. The Unit 10 peridotite commonly displays compositional zonation of intercumulus plagioclase, especially close to Cr-spinel seams (Fig. 2.6a, b; 2.7; 2.15). The zoning patterns may be normal, reverse, or oscillatory. Normal zoning of intercumulus plagioclase has also been reported from peridotites in Unit 9, 12 and 14 (Holness, 2005; Holness *et al*., 2007; Holness & Winpenny, 2008).

The Unit 9 intrusive model is a useful analogy for the interpretation of the Unit 10 peridotite presented here. For example, the idea that reactive intercumulus melts can be displaced into the overlying crystal mush has already been proposed for Rum (Holness *et al*., 2007; Leuthold *et al*., 2014). Reversely-zoned intercumulus plagioclase oikocrysts within Cr-spinel seams can be explained by the injection of picritic magma, assimilation of existing plagioclase in the peridotite host, and subsequent recrystallization of more calcic plagioclase together with Cr-spinel around the olivine framework. Low-anorthite plagioclase cores remain where assimilation was incomplete (Fig. 2.15b). Normally-zoned plagioclase in intercumulus plagioclase is found just above the limits of a Cr-spinel seam located on the upper surface of a harrisite layer (Fig 2.15c). The injection of picritic magma may have locally displaced evolved intercumulus liquid into the overlying mush, producing low-anorthite rims onto the crystallising plagioclase. The evidence provided by the coupled occurrence of Cr-spinel seams and zoned intercumulus plagioclase (incl. oscillatory zoning) indicates that this process was repeated throughout the formation of the Unit 10 peridotite (see Fig. 2.18c).

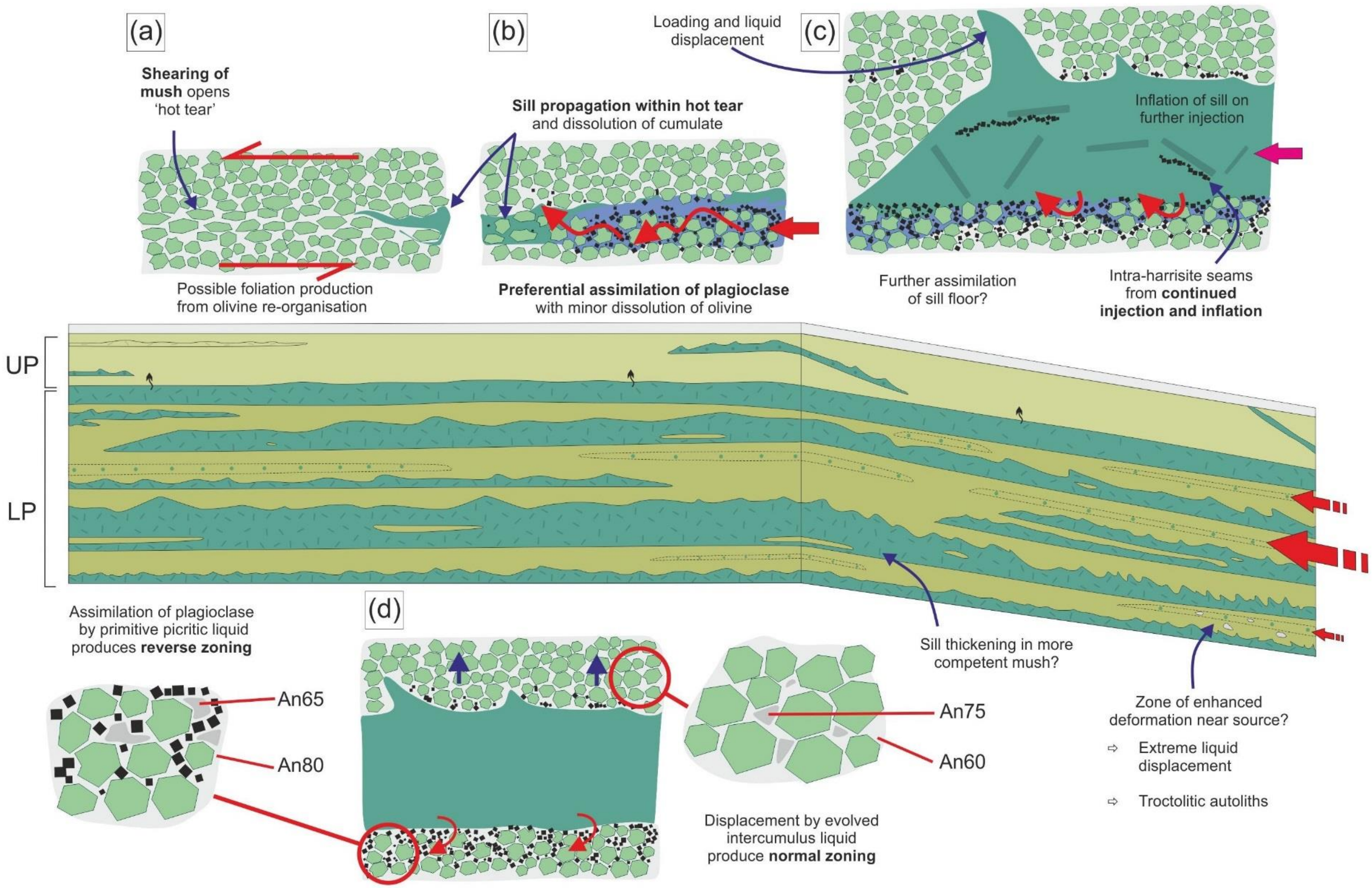
(a)
Shearing of mush opens 'hot tear'
Possible foliation production from olivine re-organisation
(b)
Sill propagation within hot tear and dissolution of cumulate
Preferential assimilation of plagioclase with minor dissolution of olivine
Loading and liquid displacement
(c)
Inflation of sill on further injection
Further assimilation of sill floor?
Intra-harrisite seams from **continued injection and inflation**
UP
LP
Assimilation of plagioclase by primitive picritic liquid produces **reverse zoning**
An65
An80
(d)
An75
An60
Displacement by evolved intercumulus liquid produce **normal zoning**
Sill thickening in more competent mush?
Zone of enhanced deformation near source?
⇨ Extreme liquid displacement
⇨ Troctolitic autoliths

◄FIGURE 2.18: Conceptual model for magmatic processes operating during the incremental construction of the Unit 10 peridotite, with insets illustrating processes in Cr-spinel seam petrogenesis (a–c) Shearing caused by sagging of the mush causes hot tearing, creating linear zones of weakness which is infiltrated by picritic magma. Foliation may be produced here. Picrite intrudes the tear, causing preferential dissolution of plagioclase increasing permeability of the mush as it dissolves plagioclase with minor olivine (e.g. Quick, 1981; Kelemen, 1990). The dissolution reaction produces a hybrid Cr-spinel saturated liquid (blue) that will migrate through the tear, crystallising abundant Cr-spinel *in situ*. If no sill forms, a granular-type seam will form from the Cr-spinel saturated liquid *in situ*, e.g. (b). If the picrite continues to flow within the tear it will inflate into a sill, forming boundary-type Cr-spinel seams, e.g. (c). Continued flow within a rapidly crystallising harrisite sill will produce harrisite-type seams from the dissolution of intercumulus plagioclase within harrisite. These seams will be locally unconstrained by shear and are not necessarily layer-parallel. (d) Displacement and assimilation processes of host mineralogy/liquid on injection of picritic magma into the crystal mush producing variable plagioclase zoning types. Reverse zoning formed during assimilation of pre-existing plagioclase, with precipitation of high-anorthite rims of plagioclase at the site of Cr-spinel formation. Above the sill, normal zoning forming by the displacement of host liquid on intrusive replenishment of picrite, producing low-anorthite rims on crystallising plagioclase

2.8.6 The Upper Peridotite: a pre-existing crystal mush?

As described above, the Unit 10 peridotite can be subdivided into two texturally and chemically distinct portions (Fig. 2.2). Palacz & Tait (1985) were the first to recognise the two (upper and lower) peridotite bodies and initially separated them at ~40 m based on an abrupt textural change. The detailed logging carried out in this chapter has confirmed the same textural change at this stratigraphic height, matching the previous authors' original demarcation well. Palacz & Tait (1985) and Tait (1985) reported more Fe-rich olivine in the UP than in the LP (>Fo_{85} versus $Fo_{80–83}$, respectively) which is also found here. They also noted a textural change in olivine, to more tabular crystals and a distinct increase in the abundance of intercumulus clinopyroxene. Palacz & Tait (1985) also noted a change in $^{87}Sr/^{86}Sr$ ratios (Fig 2.19), with the UP being more radiogenic than the LP (average values ~0.7050 and ~0.7031, respectively). They attributed these changes, particularly the distinct isotopic difference between the UP and LP, to crystallisation from two separate parental magma bodies.

The boundary between the LP to the UP is marked by a harrisite layer, a textural change in olivine, an increase in intercumulus proportion, and clinopyroxene oikocrysts that also become more abundant. However, the appearance of clinopyroxene across the LP-UP boundary is gradational, and the lowermost three metres of the UP has much lower clinopyroxene modal abundances than above this point, ~10% versus 30%, respectively (Fig. 2.3e). The compositions of disseminated Cr-spinel also change significantly, as compared with the LP, with the most Fe^{3+} enriched compositions and consistently high TiO_2 values found in the UP (Fig. 2.14). This is consistent with Cr-spinel compositions that are more modified from the primary Al-rich Cr-spinel (O'Driscoll *et al*., 2009a; 2010; Leuthold *et al*., 2015).

Holness *et al*. (2007) argued that the intrusion of the Unit 9 peridotite created a metasomatic marker horizon where a gabbroic crystal mush was partially melted, removing pyroxene from this section and recrystallizing it further up section. Leuthold *et al*. (2014) showed a similar relationship, showing that the displaced intercumulus melt was capable of further metasomatic alteration of the mush, creating highly pyroxene-rich gabbros in the final stage of this 'reactive liquid flow'. The observed change in clinopyroxene abundance and compositional modification of Cr-spinel fit with this model very well, suggesting that the intrusion of the LP potentially caused partial melting of the lowermost UP, removing pyroxene and causing significant modification of Cr-spinel by reaction with interstitial liquids. This bears lots of similarities to recent interpretations of the Unit 9 peridotite (Holness *et al*., 2007; Leuthold *et al*., 2014). Zoning of intercumulus plagioclase is also observed in the UP, suggesting a form of infiltration metasomatism or reactive liquid flow was capable of causing localised compositional disequilibrium similar to what has been found the LP. The clinopyroxene oikocrysts of the Unit 10 UP are also compositionally zoned (Fig. 2.15d), a feature reported by Leuthold *et al.* (2014) from within the Unit 9 feldspathic cumulate and attributed to reactive melt flow in the crystal mush.

The Sr isotopic variation found by Palacz & Tait (1985) further support these points. The lowermost portion of the UP is isotopically ($^{87}Sr/^{86}Sr$) similar to the LP (Fig. 2.19), and as Sr is hosted almost entirely in intercumulus plagioclase and clinopyroxene (Tepley & Davidson, 2003), partial melting of these phases by less radiogenic liquid from the intrusion of the LP would drastically alter the $^{87}Sr/^{86}Sr$ ratios of the UP mineralogy, an idea also discussed for parts of the Unit 9 feldspathic cumulate (Leuthold *et al*., 2014). The stepped isotopic variation manifested at the boundary between the LP and the UP (Fig. 2.19) precludes their formation via fractionation of the same source magma, as suggested already by Palacz & Tait (1985). It seems clear that the Unit 10 feldspathic cumulate is

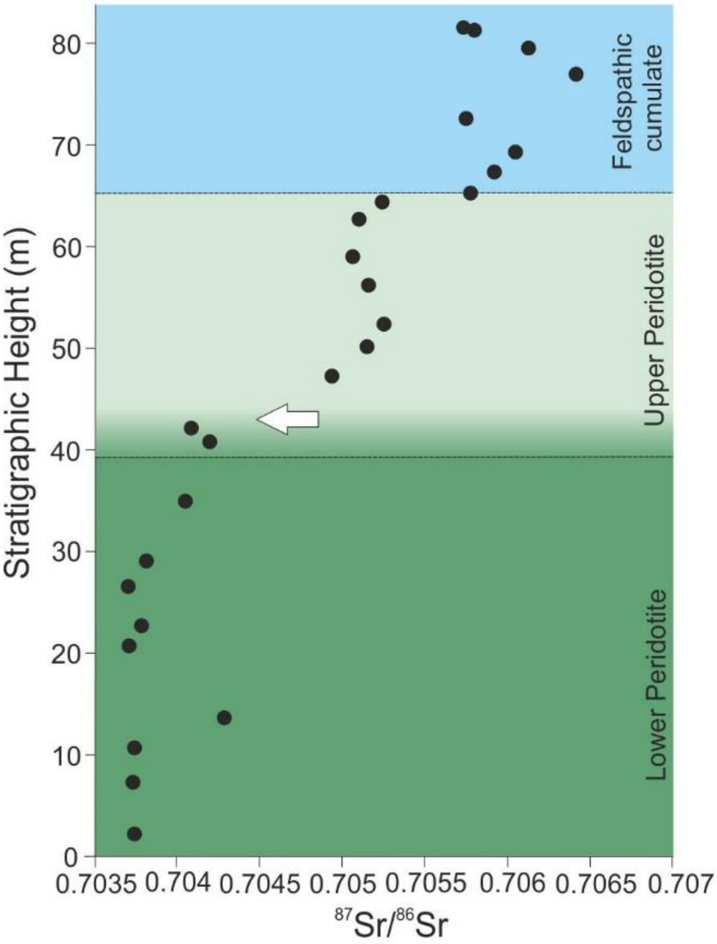

Figure 2.19 Whole rock ^{87}Sr/^{86}Sr ratios through the Unit 10 peridotite (from Palacz & Tait, 1985; uncertainties smaller than symbol size), with graphical separation of the lower and upper peridotite and feldspathic cumulate based on this chapter. Zone of proposed partial melting arrowed (see text).

formed from a magma containing much more radiogenic Sr than anything observed in the LP (Palacz, 1984). The removal of clinopyroxene from the crystal mush implies almost complete crystallisation of the protolith as this phase is a eutectic crystallisation product (Fig. 2.16). Harrisite is rare in the UP, but ‘hopper harrisite’ layers are present, occurring as non-layer parallel sheets (Fig. 2.4h), and pegmatites are markedly more abundant than in the LP, also occurring as non-layer parallel sheets. Non-planarity of layers points to a crystal mush that is also almost completely solidified, where shearing was limited or absent due to the rigidity of the mush, producing no easy pathway for infiltrating magma to migrate along (Fig. 2.18).

While the timing of emplacement between the UP and overlying feldspathic cumulate is not certain, the discussion above could be used to make the case for the UP being present at the time of emplacement of the LP. This would add further support to the argument for Unit 10 as an incrementally developed crystal mush and would also imply that layered intrusion cumulate sequences do not have to be constructed from the bottom-up.

2.8.7 Platinum-group element (PGE) enrichment

Cr-spinel seams in the Unit 10 peridotite contain base-metal sulphides, which are ubiquitously associated with a diverse array of PGM and Au-Ag grains (e.g., Fig. 2.7; 2.8). The Unit 10 Cr-spinel seams exhibit PGE enrichment up to 130 ppb Pd and 100 ppb Pt (O'Driscoll unpublished data), compared to values <1 ppb in mid-ocean ridge basalts (e.g., Bézos *et al*., 2005). Like the formation of Cr-spinel seams, PGE enrichment raises a mass-balance problem, as the thickness of many harrisite layers (< 1 m) is insufficient to account for the Cr concentrations in the seams and of 100's ppb levels of PGE-enrichment. To account for this problem in much larger layered intrusions, models have been forwarded that envisage the PGE being scavenged from a thick column of magma (Campbell *et al*., 1983; Cawthorn, 2005). Where *in situ* crystallisation of the PGM has been proposed, vigorous convection of a standing body of magma was invoked to allow the base-metal sulphides to scavenge PGE from the melt as it convects over the magma-crystal mush interface (Latypov *et al*., 2013). Many of the harrisite sheets are probably not thick enough to allow for vigorous convection (*cf.* O'Driscoll *et al*., 2010; Latypov *et al*., 2013; Latypov *et al*., 2015). However, the mass-balance issue can be solved by continual lateral through-flow within picrite sills where many times the volume of magma has passed through the sill than is currently represented by the solidified harrisite. This has important economic implications for comparatively thin cumulate bodies that are anomalously rich in PGEs and other precious metal mineralisation in other layered intrusions. Examples include the Cr-spinel lined peridotite sills below the platiniferous Merensky Reef of the Bushveld Complex (Ballhaus, 1988; Latypov *et al*., 2015), where replenishment and PGE-enrichment have plausibly occurred within the crystal mush. Similarities between textures of Rum peridotite-hosted Cr-spinel seams and the PGE-bearing peridotite-hosted chromitites of the Ultramafic Series of the Stillwater Complex (see Jackson, 1961) are also a potential analogue, where the ideas proposed here could be applied.

2.9 CONCLUSIONS

Recent work on the RLS, particularly the ELI has found growing evidence that argues against traditional models of crystal settling for fractionating discrete magma batches. Following the classic work of Brown (1956), it was suggested as early as 1988 (Bédard *et al*., 1988) that many of the peridotite layers that make up the ELI formed by injection of magma into a pre-existing crystal mush. In this chapter, further evidence to support this view was presented, with a conclusion that the Unit 10 peridotite was developed incrementally by numerous, small volume replenishment events into a pre-existing, and partially consolidated crystal mush undergoing significant shear stress by gravitational sagging toward the feeder. The importance of this conclusion is highlighted by the fact that Unit 10 has stood as the type example of batch fractionation on Rum for more than 50 years. The repeated intrusive replenishment of picritic magma crystallised harrisitic and granular-textured peridotite, the former generating significant liquid displacement structures. Closely associated diffuse Cr-spinel seams that occur along the base, top, and interior of these peridotites crystallised *in situ* on intrusion of this magma as a product of a preferential assimilation reaction with peridotitic cumulate. Repeated intrusion of picritic magma into the crystal mush generated localised compositional disequilibrium in silicate phases adjacent to Cr-spinel seams by the displacement and replacement of intercumulus liquids and solids. This model has important local implications for other Cr-spinel seam bearing peridotite bodies such as Units 8 and 12 (Henderson, 1975; O’Driscoll *et al*., 2010), where the peridotite may have undergone small volume intrusive replenishment.

As the Rum Western Layered Intrusion contains the greatest abundance of harrisite and also numerous Cr-spinel seams (Wadsworth, 1961), the applicability of the model presented here has relevance for other portions of the RLS. There is also scope to draw parallels with much larger layered intrusions such as the Ultramafic Series of the Stillwater Complex (Montana), where thick and similarly-textured Cr-spinel seams occur hosted within peridotite (Jackson, 1961). Finally, given that the Unit 10 Cr-spinel seams contain PGE, there is economic implications for world class PGE ore deposits in layered intrusions such as the Bushveld Complex, South Africa, where models of intrusive replenishment have not yet been fully explored.

CHAPTER 3 – REACTIVE MELT FLOW AS A DRIVER FOR PRECIOUS METAL MINERALISATION IN MAFIC MAGMATIC SYSTEMS

3.1 INTRODUCTION

The solidified remnants of basalt magmatic systems host the greatest concentrations of platinum-group metals on Earth. A small number of mafic-ultramafic intrusive systems, so-called layered intrusions, are responsible for supplying most of society's Pt, Pd and Rh (Naldrett & Duke, 1980; Naldrett, 2004; Cawthorn *et al*., 2005). A wealth of field, petrological and geochemical information exists for precious metal deposits in economically significant layered intrusions such as the ~2 Ga Bushveld Complex (South Africa; Naldrett, 2004; Eales & Cawthorn, 1996; Godel, 2015). However, uncertainty persists with respect to the mechanisms that concentrate the precious metals in centimetre-metre thick layers in these intrusions (Cawthorn *et al*., 2005; Mungall & Naldrett, 2008). Some models call for ore-forming processes that occurred at or close to the putative magma chamber floor (Campbell & Naldrett, 1979; Naldrett *et al*., 1986; Mungall & Naldrett, 2008), whereas others invoke relatively low-temperature fluid-rock interactions operating on partly-to-completely solidified assemblages (Mungall & Naldrett, 2008; Boudreau & McCallum, 1992; Boudreau, 1999). This disparity means that there may be broad ranges of temperature and rheology in solidifying magma chambers over which the platinum-group elements (PGE) become concentrated.

Improving our understanding of the dynamic behaviour of solidifying crystal mushes is therefore central to advancing our knowledge of precious metal enrichment in crustal magmatic systems. Studies of layered intrusions have equipped us with a broad physiochemical framework for understanding how crystal mushes form, as cumulates, and how they may be modified at the postcumulus stage (Holness *et al*., 2012; Namur *et al*., 2015). Physical processes such as melt percolation, reactive flow, melt segregation and mush compaction might all play important roles in solidifying crystal mushes (Cashman *et al*., 2017). However, there remain critical gaps in our understanding of the length- and time-scales over which these processes occur. The timescales over which crystal mushes cool and solidify are also not well known, this is especially important in the case in open systems where rejuvenation of crystal mushes can occur by input of relatively hot primitive magma which may significantly increase mush permeability, and lead to reactive through-flow of melt, resulting in a more protracted solidification history (Annen *et al*., 2006; Claiborne *et al*., 2010).

A novel dataset is presented demonstrating intracrystalline isotopic heterogeneity in PGE-rich cumulates of the classic Rum layered intrusion (NW Scotland). New microsampled plagioclase $^{87}Sr/^{86}Sr$ data unambiguously show that discrete levels of stratigraphy in the Rum crystal mush were subjected to small-volume reactive melt percolation events, and that this process is intrinsically linked to precious metal enrichment. The process of reactive melt percolation occurred mainly by porous through-flow of melt along diffuse cm-thick pathways. Melt percolation was predominantly focused laterally but continued melt through-flow may have eventually been accommodated by vertical melt escape into the overlying cumulate. The presence of up to 100 PGE-rich horizons in the ~60 m of cumulate stratigraphy attests to a process that was repeated numerous times. The preservation of Sr isotopic heterogeneities at length-scales of 10-100 μm constrains the cooling rates of the crystal mush in the Rum intrusion. It seems likely that each PGE-rich horizon was emplaced and closed to diffusive equilibration in a matter of several hundreds of years, a conclusion that lends strong support to the idea that basaltic intrusive systems may also exist in ‘cold storage’ and be rejuvenated by new magma input, like their granitic counterparts (Annen *et al*., 2006; Claiborne *et al*., 2010; Cooper & Kent, 2014).

3.2 THE MASS BALANCE PROBLEM IN PRECIOUS METAL ‘REEF’ FORMATION

Arguably, models for PGE enrichment in layered intrusions have been limited by the classic magma chamber paradigm. Traditional models of PGE enrichment invoke transport of the metals to the site of mineralisation from above (‘downers’) or below (‘uppers’) (Cawthorn *et al*., 2005; Mungall & Naldrett, 2008). In the former case, a common theme is the separation of base metal sulphides from the silicate melt following magma chamber replenishment. These sulphides go on to scavenge the PGE, before gravity-driven settling to the magma chamber floor and formation of the stratiform mineralised layer (or 'reef') (Campbell & Naldrett, 1979; Naldrett *et al*., 1986; Mungall & Naldrett, 2008). In the uppers model, halogen-rich fluids percolate upwards through solidified cumulate, stripping out the PGE and eventually depositing them at the site of mineralisation in an essentially metasomatic process (Boudreau & McCallum, 1992a; Boudreau, 1999). More recently, models have been proposed for the formation of PGE-reefs in layered intrusions that invoke in situ crystallisation at the magma chamber floor. The observation that PGE-reefs follow topographic irregularities in the floor, lining depressions and even overhangs, without changing thickness, rules out crystal settling and lends strong support to *in situ* crystallisation (O'Driscoll *et al*., 2010; Latypov *et al*., 2013; Latypov *et al*., 2015). With *in situ* crystallisation models, the trigger for sulphide saturation and unmixing is thermochemical assimilation of plagioclase-rich cumulate on the magma chamber floor.

A key issue that is addressed by these models is the mass balance problem. Namely, how do parental magmas with ppb levels of the PGE become enriched in concentrations four or five orders of magnitude higher to form reefs? Sulphide melt-silicate melt partition coefficients of 10^5–10^6 point to the strongly chalcophilic tendencies of the PGE (Mungall & Brenan, 2014), and so the question becomes one of allowing sulphide melt or sulphides to 'see' enough silicate melt to facilitate metal enrichment. This is resolved in the downers model by fluid dynamic considerations of plumes versus fountains in open-system magma chambers, quantified by R-factor calculations (Campbell & Naldrett, 1979; Naldrett, 2004). However, it has been well established that the downers model does not explain key features of many PGE-reefs (O'Driscoll *et al*., 2010; Latypov *et al*., 2013; Latypov *et al*., 2015), so another explanation is necessary. In addition, the downers model does not explain the observation that PGE-reefs are also enriched in base metals like Cr (i.e., chromitite seams) indicating that the mass balance issue must be resolved for these base metals as well. The recent investigation into Cr-spinel seam formation and PGE-enrichment within Unit 10 (Rum ELI) highlighted the potential for through-flow in solving mass-balance issues (Hepworth *et al*., 2017; Chapter 2), where more melt has passed through the rock than is represented by the observed volume of cumulate.

The Rum layered intrusion is a particularly valuable locality to interrogate these unresolved questions. Although not exploited for its PGE, it has 1–2 mm PGE-reefs that are exceptionally enriched in Pt and Pd (i.e., >1 ppm levels; O'Driscoll *et al*., 2009). It is small (~20 km^2) and young compared to the layered intrusions that host the world's economically significant PGE-reefs (e.g., the Archaean Stillwater Complex and the Proterozoic Bushveld Complex; Emeleus *et al*., 1996; O'Driscoll *et al*., 2010). This means that it may preserve primary textural and mineral chemical variations which have not survived in the aforementioned intrusions. For example, Tepley and Davidson (2003) reported intra-crystal (plagioclase) Sr isotope heterogeneities in gabbroic cumulates from Rum that they attributed to growth of cumulus crystals in a region of the magma chamber undergoing crustal contamination, before dynamic accumulation in a different part of the reservoir. The PGE mineralisation on Rum also occurs within lithologies that are remarkably similar to those of the Merensky and UG-2 Reefs in the Bushveld intrusion: namely, within chromitite seams that are underlain by anorthosite and overlain by mafic orthocumulate rocks. Rum therefore offers valuable insights into PGE-reef formation, with important implications for mineralisation in other layered intrusions.

3.3 BATCH FRACTIONATION VERSUS OPEN SYSTEM PROCESSES IN THE RUM INTRUSION

The Rum layered intrusion is a cornerstone for understanding open-system magmatic and sub-volcanic processes (Brown, 1956; Emeleus *et al*., 1996). It was emplaced at ~60 Ma during opening of the Northeast Atlantic, at a crustal depth of <2 km, and is part of the British and Irish Palaeogene Igneous Province (BIPIP). The eastern portion of the Rum intrusion is constructed of 16 macro-rhythmic units, each ~10–90m thick and composed of a peridotitic base and a troctolitic top, reflecting successive fractionation of olivine and then plagioclase from each new batch of basaltic or picritic magma. The ~80 m thick Unit 10 package has been held up as the archetypal example of batch fractionation and crystallisation of magma on Rum for >60 years (Brown, 1956). It is sub-divided into four sections as follows: the lower peridotite (~40 m), upper peridotite (~20 m), troctolite (~5 m) and olivine gabbro (~15 m; Brown, 1956; Palacz & Tait, 1985; Hepworth *et al*., 2017). The batch fractionation interpretation is consistent with broad trends in mineral chemistry (e.g., olivine Fo contents, which evolve towards more Fe-rich compositions from bottom to top of the unit; Palacz

& Tait, 1985). Bulk rock Sr isotope compositions are relatively uniform and unradiogenic at the base of the unit but change to much more radiogenic $^{87}Sr/^{86}Sr$ values in the upper peridotite and in the overlying feldspathic cumulates. This trend has been interpreted in the framework of the batch fractionation model, where the more radiogenic Sr values reflect progressively greater degrees of mixing between the incoming Unit 10 peridotite parental melt and a crustally-contaminated magma already resident in the magma chamber (Palacz & Tait, 1985).

More recently, the Unit 10 peridotite has been reinterpreted as resulting from incremental emplacement of small volume peridotite sill-like bodies (Hepworth *et al*., 2017; Chapter 2). In particular, the lower peridotite contains numerous 10–50 cm thick texturally distinct peridotite layers that exhibit intrusive relationships with the peridotite above and below. The presence of hundreds of mm-thick Cr-spinel seams has also been documented throughout the entire thickness of the lower peridotite (Hepworth *et al*., 2017; Chapter 2). For the most part, these Cr-spinel seams are several mm-cm thick and contain abundant base metal sulphides and a variety of platinum-group minerals. The Cr-spinel seams are predominantly diffuse, such that they comprise 0.5–1 cm thick layers of Cr-spinel in a chain-textured configuration surrounding the olivine crystal framework embedded in the intercumulus plagioclase (Fig. 4.1a). More rarely, discrete chromitite seams are present. Cr-spinel seams are stratiform, but not stratabound, and they locally branch bifurcate into two or more seams separated by <1 cm of peridotite. Olivine grain size is typically different often texturally variable on either side of a Cr-spinel seam. In close proximity, i.e., within a few cm on either side of Cr-spinel seams, intercumulus plagioclase crystals are ubiquitously compositionally zoned. The zoning can be normal, reverse or oscillatory in nature, but much more complex compositional zoning also occurs locally. In the upper peridotite, Cr-spinel seams are absent (Hepworth *et al*., 2017; Chapter 2). The upper peridotite is generally more homogeneous in appearance and is characterised by abundant and ubiquitous ~1 cm-sized oikocrysts of diopside. At the top of the upper peridotite, a ~20 cm thick pegmatite body occurs at the boundary with the overlying troctolite.

3.4 TARGET SAMPLING AND METHODOLOGY

3.4.1 Sampling

Intercumulus crystals form from the interstitial melt in the solidifying crystal mush, so they record evidence of postcumulus processes that operated after primary accumulation of the cumulus crystal framework. To investigate the compositional zoning in intercumulus plagioclase ubiquitously associated with the Cr-spinel seams (Fig. 3.1), three such seams were sampled from a 3 m interval in the middle of the lower peridotite (Appendix 1.1). One of these seams occurs along the contact with an intrusive peridotite, but the other two lack this association. Major element chemistry and compositional maps were collected on intercumulus plagioclase crystals using an electron microprobe at the Department of Geochemistry, Geowissenschaftliches Zentrum der Universität Göttingen, Germany, in 2015. Zoned intercumulus plagioclase crystals were then selected from the three seams for Sr isotopic analysis. One zoned clinopyroxene oikocryst from the upper peridotite as well as both plagioclase and clinopyroxene from the pegmatite body occurring between the upper peridotite and the troctolite unit were also analysed. Samples from the Unit 8 peridotite (*cf.* Henderson, 1975) and a harrisite from the WLI were also analysed for comparison.

3.4.2 Mineral Chemistry

Plagioclase mineral chemical data were obtained using a JEOL JXA-8900RL electron microprobe at the Department of Geochemistry, Geowissenschaftliches Zentrum der Universität Göttingen (GZG) in 2015. The plagioclase compositions were obtained using an acceleration voltage of 20 kV with a beam current of ~80 nA and a typical beam diameter of 20–25µm. Plagioclase count times on peak and background for Si, Ca, Al, Na, K were 15s and 5s, respectively, for Fe were 30s and 15s, for Sr and Ba were 360s and 180s, respectively, and for Ti were 300s and 150s. Element maps of Na and Ca-concentration were obtained of zoning types in plagioclase, and for Cr, Mg, Ti, Al-concentration of a clinopyroxene oikocryst from the Unit 10 peridotite (see Hepworth *et al.*, 2017; Chapter 2). Element maps were obtained using an acceleration voltage of 20 kV, with a beam current of ~60 nA, a beam diameter of 2 µm and a dwell time of 50 ms.

3.4.3 Sr-isotope analysis

Micro-milling targets were carefully selected based on criteria such as drill-bit diameter (75–200 µm), least potential mixing with other zones, and maximum possible sample excisable (with plagioclase ~400 ppm Sr; Fig. 3.2d). Once samples were selected, they were drilled using a New Wave Micromill at University College Dublin, Ireland following the methods of Davidson *et al*., (1998) and Charlier *et al*. (2006). Mixing between zones was avoided by careful sample selection and although some blending during drilling may have occurred, it is minimal based on the internal reproducibility between similar samples. Zones were drilled through a bead of 20µl of millipure water to produce a slurry, which was then collected into a clean beaker, before a further 10µl of millipure water was placed onto the sample site to collect any remaining sample. To digest the plagioclase residue, 0.8ml of HF and 0.2ml of HNO_3 was added to the beaker containing the sample which is then sealed and left on a hot plate overnight (>12 hrs). After digestion, the beakers are opened, and the acid solution is left to evaporate on the hot plate. The sample is then left to cool before adding 0.3ml of concentrated HNO_3 and evaporated again, with 0.3ml of concentrated HNO_3 and 0.1ml of millipure water added and evaporated. Once evaporated, 0.3ml of 1M HNO_3 is added to the sample beakers which is sealed and left to cool completely. Columns are prepared (washed with 0.05M HNO_3–8M HNO_3–0.05M HNO_3–1M HNO_3 prior to addition of sample). The sample solution is put onto the prepared Sr columns, and 1ml 1M HNO_3 is added and allowed to drip through fully, followed by 8M HNO_3 (to remove any detectable Ba). Clean collection beakers are placed beneath each column and 2ml of 0.05M HNO_3 is added to collect Sr. When Sr-solution is isolated, 0.05ml (50µl) is removed and placed into a vial and with 0.5 ml (500µl) of 3M HNO_3 and centrifuged prior to ICP-MS analysis to obtain absolute Sr-quantities (ng) of the sample (see Appendix 2). The Sr-solution is evaporated on the hotplate then sealed. For TIMS analysis on a Thermo-Scientific Triton thermal ionization mass spectrometer, 1µl of Ta-activator is put onto Re-filament with the sample dissolved in 1µl of 0.05M HNO_3 and put onto the filament and evaporated for use in the mass-spectrometer (Charlier *et al*., 2006). The full dataset including analytical uncertainties and standard analysis can be found in Appendix 2.

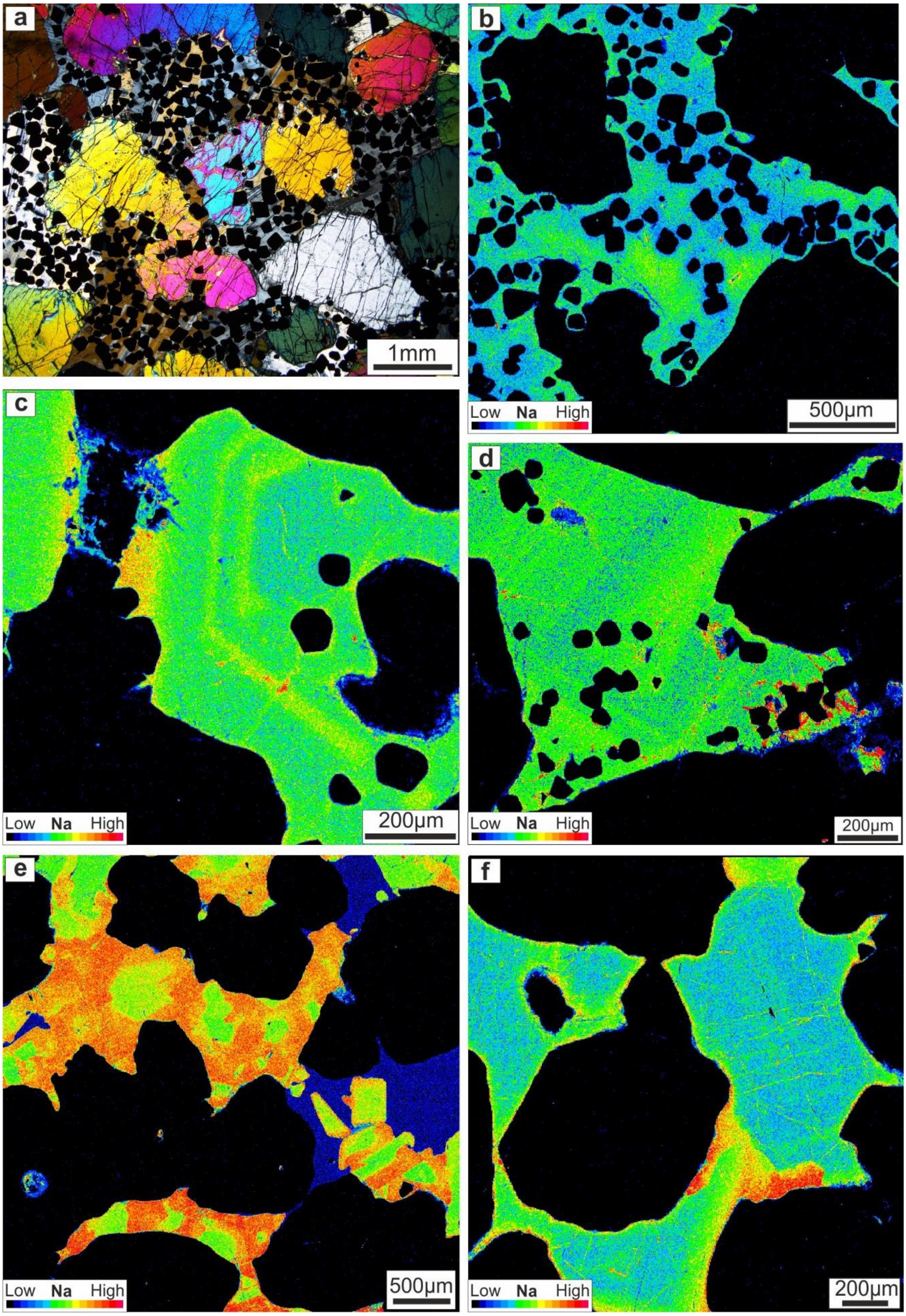

FIGURE 3.1: (a) Typical chain-textured Cr-spinel seam from the Unit 10 peridotite (see also Chapter 2). (b) Compositional map showing Na-content of reversely zoned plagioclase with irregular low Na cores. (c–d) Oscillatory zoning of Na-content within intercumulus plagioclase. (e–f) Normally zoned intercumulus plagioclase with high Na rims. Note the equant, low Na cores in (e).

3.5 RESULTS

3.5.1 Mineral Chemistry

The full mineral chemical can be found in the Appendix 3.1. The anhedral morphology of the plagioclase crystals and typically irregular zoning patterns means that distinguishing between crystal cores and rims in a conventional manner is not straightforward. Intercumulus plagioclase ranges in composition between labradorite and bytownite (An60–85). The K_2O and TiO_2 contents of intercumulus plagioclase negatively correlate with anorthite content, and plagioclase is ubiquitously more anorthitic where it contains Cr-spinel crystals. Plagioclase Sr concentrations mostly range between 350–500 ppm, and Ba concentrations are consistently <1 ppm. Electron microprobe element maps reveal that the clinopyroxene oikocryst from the upper peridotite contains complex, patchy zoning with a positive correlation between Cr_2O_3 and Al_2O_3 contents.

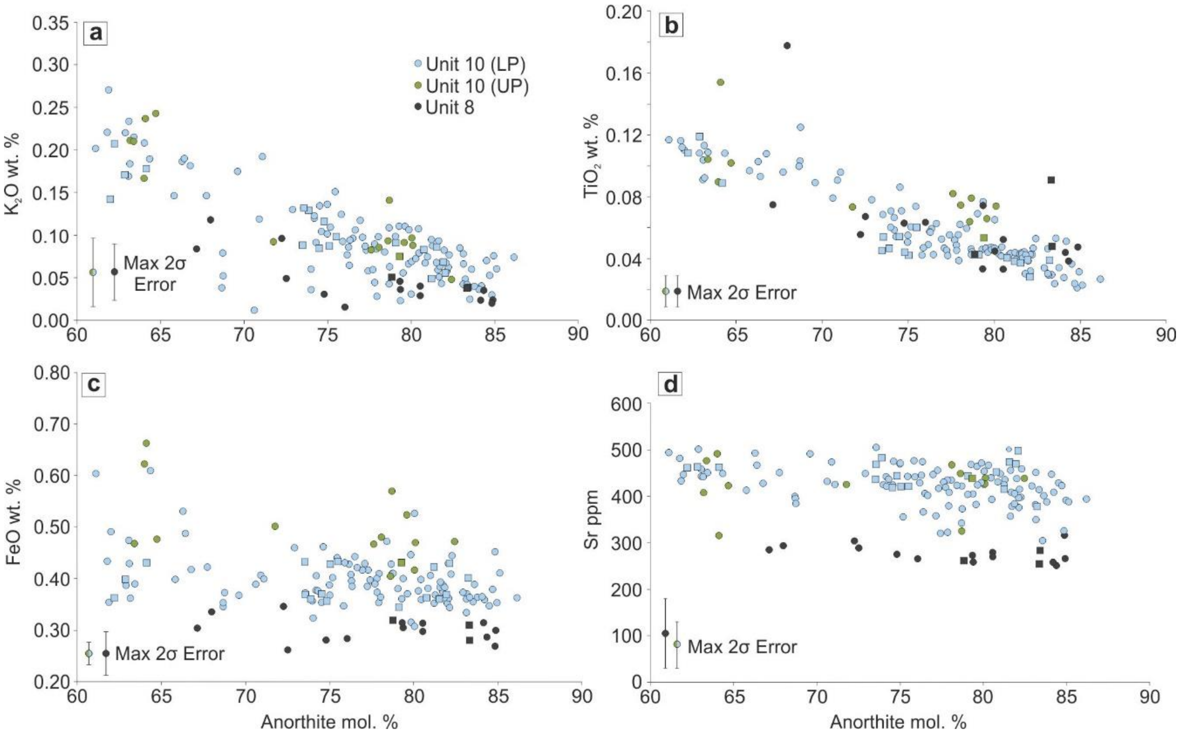

FIGURE 3.2: Mineral chemistry of intercumulus plagioclase from the Unit 10 and Unit 8 peridotite. (a) K_2O with pronounced negative correlation with anorthite. (b) TiO_2 with very strong negative correlation with anorthite content, indicative of oxide crystallisation (Humphreys, 2009) in the Skaergaard Intrusion. (c) FeO with no correlation, likely from sub-solidus exchange with olivine. (d) Sr (ppm) content of plagioclase from Unit 10 and Unit 8 peridotite. Note the lack of correlation with increasing anorthite content.

3.5.2 Sr-isotopes

The full Sr-isotope dataset can be found in Appendix 3.2. No age correction (for decay of ^{87}Rb) has been applied to the measured ^{87}Sr/^{86}Sr ratios and is not considered necessary due to low Rb concentrations (<100 ppm) and the relatively young age (60 Ma) of the intrusion. The Sr concentrations in the blanks were <0.02 ng and repeat measurements of SRM 987 yielded a mean ^{87}Sr/^{86}Sr value of 0.7102765 ±30 (n=13). Most of the analysed crystals reveal intracrystalline isotopic heterogeneity. The maximum range (with 2σ uncertainties) of ^{87}Sr/^{86}Sr is 0.704026 ±17–0.704591 ±8 in the Unit 10 plagioclase and 0.703533 ±23–0.704517 ±17 in clinopyroxene. Within a single, oscillatory-zoned plagioclase, three discrete zones yield 87Sr/86Sr values of 0.704337 ±20, 0.704095 ±20 and 0.704052 ±11 (Fig. 3.3a). The complex patchily-zoned clinopyroxene oikocryst yields a ^{87}Sr/^{86}Sr range of 0.703533±23–0.703894 ±23 (Fig. 3.3b). Isotopic disequilibrium is also observed within plagioclase, within clinopyroxene, and between both phases in the pegmatite unit (Fig. 4.4a). The isotopic variations measured correspond to major element variation in both plagioclase and clinopyroxene. In the case of plagioclase crystals, more anorthitic plagioclase is also characterised by more radiogenic ^{87}Sr/^{86}Sr values, although when the dataset from all crystals is plotted a broad trend of more unradiogenic ^{87}Sr/^{86}Sr with increasing anorthite is observed (Fig. 3.3b). In the clinopyroxene, low Al_2O_3 (and Cr_2O_3) domains within the oikocryst are characterised by more unradiogenic ^{87}Sr/^{86}Sr (Fig. 3.3b).

3.6 DISCUSSION

3.6.1 Reactive melt percolation and PGE enrichment in the Unit 10 crystal mush

It has been suggested that the Unit 10 lower peridotite was added by late-stage intrusion of aphyric (picritic) and olivine-phyric magmas while the upper peridotite predates this intrusive activity (Hepworth *et al.*, 2017; Chapter 2), displaying a metasomatic horizon indicative of partial melting (Holness *et al.*, 2007; Leuthold *et al.*, 2014). Several lines of evidence point against a crystal settling origin for the Cr-spinel seams. Firstly, the Cr- spinel:olivine ratio is too great for the seams to reflect

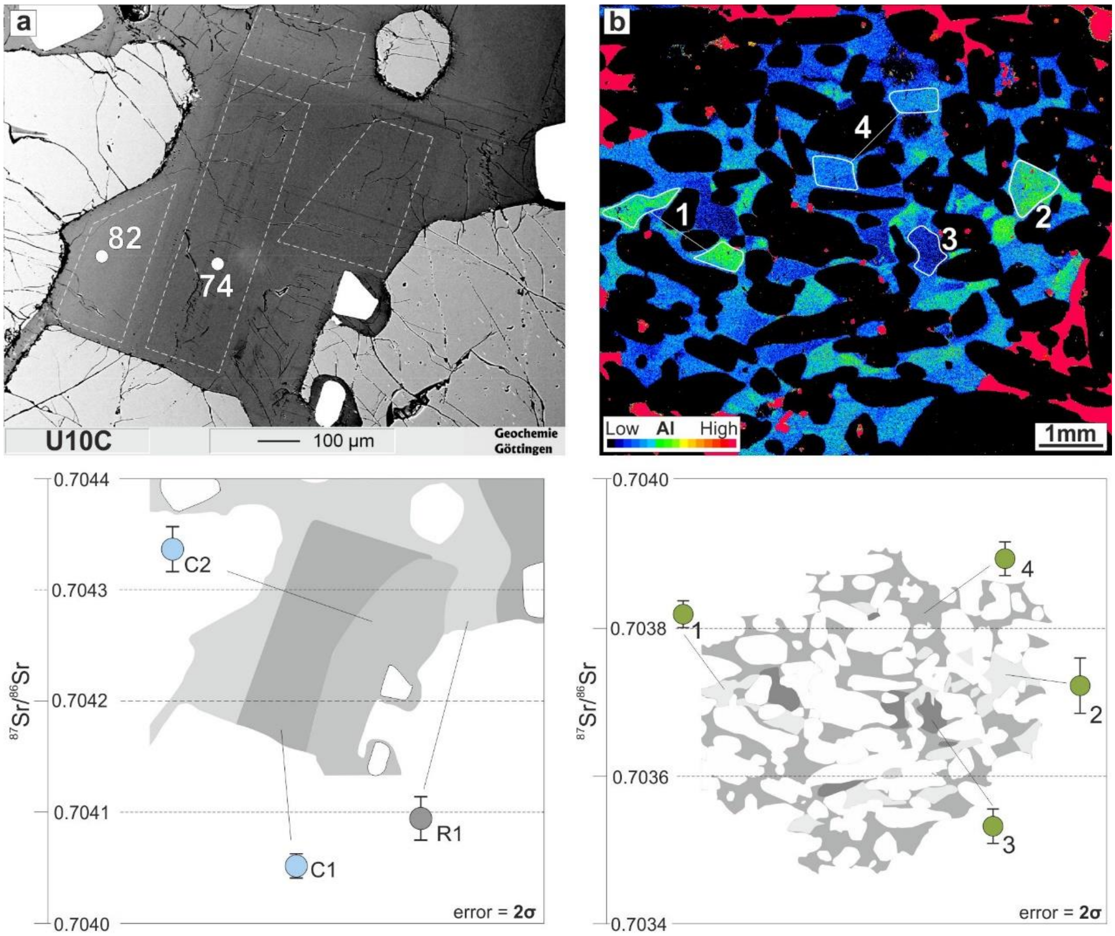

FIGURE 3.3: (a) Intracrystalline chemical and isotopic variation within a single plagioclase oikocryst from the Unit 10 lower peridotite. (b) Intracrystalline chemical and isotopic variation in a clinopyroxene oikocryst from the Unit 10 upper peridotite.

cotectic proportions of these minerals. The Cr-spinel seams are also undulose, following depressions and culminations without necessarily changing thickness. The textural and mineral chemical characteristics of the chain-textured Cr-spinel seams are therefore suggestive of *in situ* crystallisation during reactive melt flow (Fig. 3.1a). The coincidence of Cr-spinel with anorthitic plagioclase (An >75) in the interstitial areas of the seams, and absence of Cr-spinel from areas where the plagioclase is more sodic in composition (Fig. 3.1b–f), suggests that Cr-spinel crystallised during a peritectic reaction within the crystal mush. The strong correlation of plagioclase TiO_2 with anorthite content supports this (Fig. 4.2b; Humphreys, 2009); with the onset of crystallisation of Cr-spinel TiO_2 preferentially partitioned into that phase. Simultaneous dissolution of olivine and plagioclase during melting will lead to precipitation of spinel (plus anorthite or forsterite) at a temperature of ~1320°C (Morse, 1980). Picrite melts such as those considered to be the parental melts of the Rum intrusion are considered to have liquidus temperatures on the order of ~1350°C (Upton *et al*., 2002; O'Driscoll *et al.*, 2010), so the enthalpy budget was ample for driving the dissolution process.

The new intra-crystal plagioclase Sr isotope data span an equivalent range of Sr isotope compositions to the bulk rock data of Palacz and Tait (1985) from the lower peridotite (Fig. 3.4a), implying that there is a similar degree of heterogeneity present in ~3 m of peridotite cumulate as is present in the entire ~40 m lower peridotite thickness. The new data also provide strong confirmation of highly localised reactive melt flow at sites where Cr-spinel seams occur in the lower peridotite crystal mush. In a given crystal, the most anorthitic plagioclase zones are also characterised by a more radiogenic $^{87}Sr/^{86}Sr$ composition (Fig. 3.3a), supporting the suggestion that assimilation of feldspathic cumulate drove Cr-spinel crystallisation (O'Driscoll *et al*., 2010). The Unit 10 Cr-spinel seams have ~100 ppb Pt (Hepworth *et al*., 2017; Chapter 2), which is ~25 times the amount of Pt that could have been concentrated from a 1 mm layer of picrite melt. The previous authors suggested through-flow could solve this mass balance issue. The data reported here strongly support this model and finds clear evidence for multiple generations of melt within a single diffuse Cr-spinel seam, a feature which can only be answered by lateral through-flow within the crystal mush. The thickness of the Cr-spinel seams are therefore minimum estimates of the thickness of the percolation zones during crystallisation of each Cr-spinel seam.

3.6.2 Fluid dynamics and timescales of cooling

It is possible to place further constraints on the nature of the percolation zones in which each Cr-spinel seam formed. A critical observation is that many Unit 10 Cr-spinel seams extend laterally along strike for several tens of metres, without significant changes in thickness. The primary controls on reactive flow through a dissolvable matrix can be described by the Damköhler number (Da), which relates the amount of reaction that occurs to the flow rate, over a characteristic length scale (Spiegelman *et al*., 2001; Pec *et al*., 2015):

$$Da = \frac{\mathrm{R_{eff}}L}{\rho_{\mathrm{fluid}}\phi_0\omega_0}$$

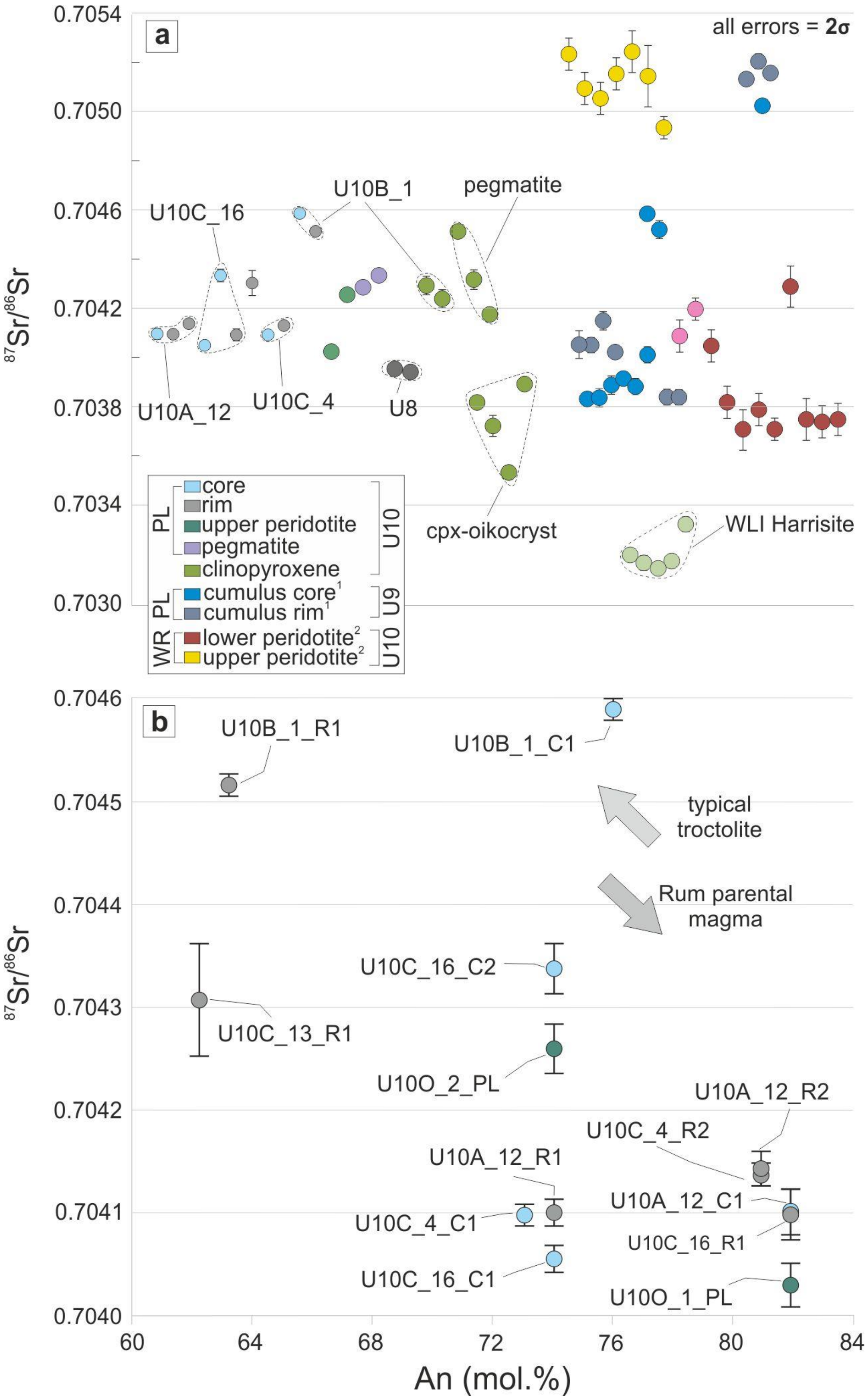

FIGURE 3.4: (a) $^{87}Sr/^{86}Sr$ for analysed plagioclase crystals. Data from micro-milled plagioclase from Unit 9 (Tepley & Davidson, 2003), and Unit 10 whole-rock analysis (Palacz & Tait, 1985) included for comparison. (b) $^{87}Sr/^{86}Sr$ versus anorthite content for plagioclase from the Unit 10 peridotite. Note the broadly negative correlation. Schematic arrows for typical mafic melts in the RLS, with more radiogenic (lower An) troctolites, and least radiogenic (higher An) picrite magmas, highlighting possible localised contamination of some plagioclase crystals.

The equilibration length (L_{eq}) describes how far the melt may advect before equilibrating with the host rock:

$$L_{eq} = \frac{\rho_{fluid} \phi_0 \omega_0}{R_{eff}}$$

R_{eff} is an effective reaction rate constant, L is the characteristic length scale, ρfluid is the density of the invading melt and $\omega0$ is the melt velocity at porosity $\phi0$. Values of R_{eff} can be calculated using the dissolution experiments of Donaldson (1985), and $\omega0$ using Darcy's law for melt flow through a porous matrix. Assuming a viscosity of 10 PaS for the invading picrite, the formation of percolation zones that extend 50–100 m along strike require Da of ~104 and L_{eq} of 2–3 mm. These values imply very high degrees of reaction relative to melt flux, and as well as underlining the requirement for through-flow of melt as outlined above, they highlight the importance of the relatively hot, aphyric picritic melts to the formation of Cr-spinel seams and associated PGE enrichment on Rum. Although it is likely that numerous percolation events are represented by the entire Unit 10 Cr-spinel seam population, not all of them formed at different times. However, if branched networks of percolation zones existed, separation of each zone by >10 cm of peridotite would have been required to allow disequilibrium transport, assuming no interchannel porosity.

Allowing for through-flow of reactive picrite, an open question concerns the fate of this melt. Hepworth *et al.* (2017) reported the presence of vertically-elongate clinopyroxene crystals in the lower peridotite (Fig. 2.8). The single clinopyroxene oikocryst analysed in this study has Sr isotope compositions that are more unradiogenic than any of the plagioclase analysed in this study, despite the bulk rock upper peridotite compositions being significantly more radiogenic than the lower peridotite bulk rocks. This observation is consistent with the clinopyroxene oikocrysts of the upper peridotite representing melt that escaped from the underlying cumulate pile prior to the emplacement of the lower peridotite. The melt is unlikely to be related to melt from the lower peridotite from evidence presented by Hepworth *et al* (2017) and the distinct ^{87}Sr/^{86}Sr compositions and might potentially represent an event related to the earlier emplacement of the upper peridotite (see Bédard *et al*., 1988; Leuthold *et al*., 2014). The pegmatite body from the top of the upper peridotite likely represents melts that ponded and solidified beneath

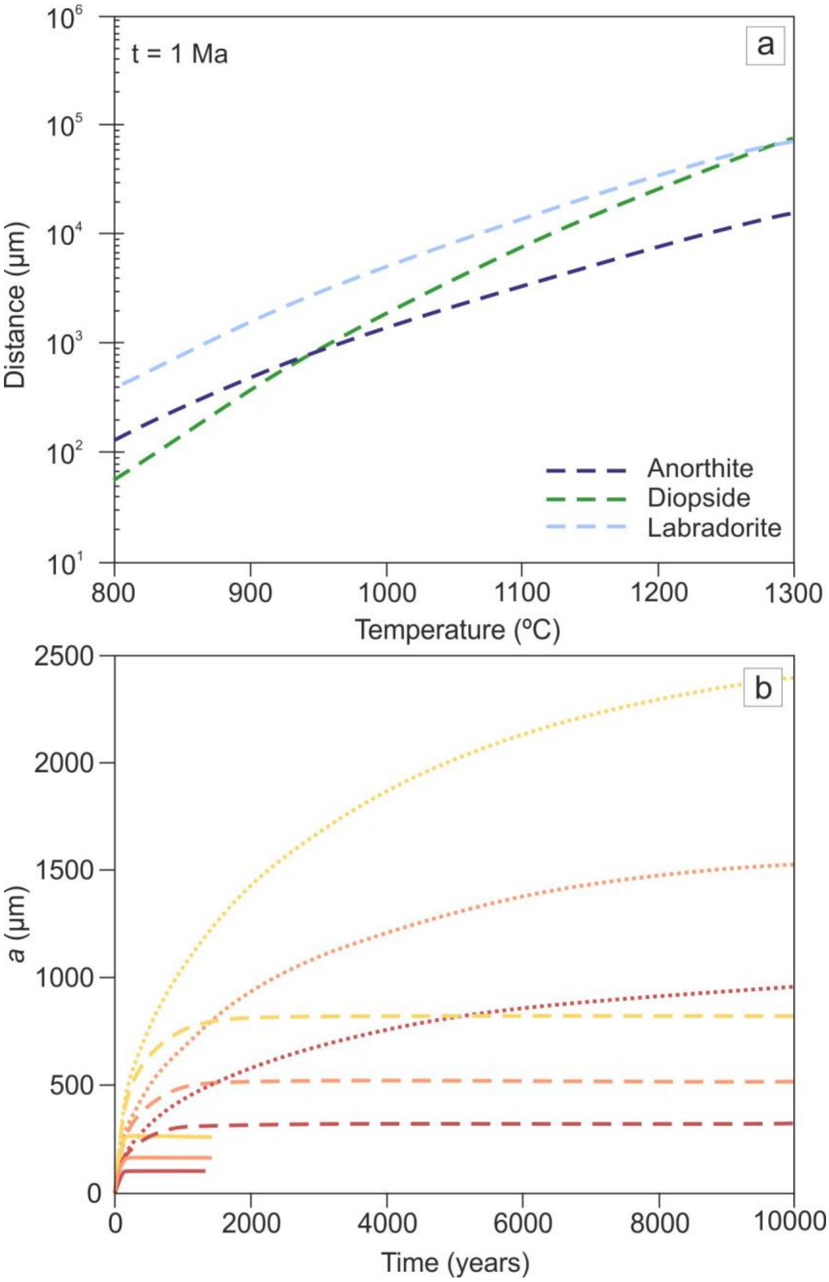

FIGURE 3.5: (a) Diffusion distance as a function of temperature over a duration of 1 million years for all three phases. (b) Cooling rate calculations for labradorite; these show 1°C/year (solid line), 0.1°C/year (dashed) and 0.01°C/year (dotted), for each of T0=1100°C (red), 1150°C (orange) 1200°C (yellow).

the overlying relatively impermeable cap represented by the feldspathic cumulate. The pegmatite contains plagioclase and clinopyroxene that are in isotopic disequilibrium (Fig. 3.4a), collectively exhibiting a similar range of ^{87}Sr/^{86}Sr compositions to the lower peridotite plagioclase. The preservation of intracrystalline Sr heterogeneity has implications for the timescales of cooling of the Unit 10 peridotite. Diffusion coefficients for Sr in plagioclase and clinopyroxene have been experimentally derived (Giletti & Casserly, 1994; Sneeringer *et al*., 1994), and it is possible to calculate diffusive equilibration times for Sr in anorthite, labradorite and clinopyroxene. Diffusion of Sr is fastest in clinopyroxene (Fig. 3.5a), but the heterogeneities observed in the oikocryst are on the order of mm apart (Fig. 3.3b). It is the Sr heterogeneities preserved in plagioclase, on the order of 10-100 µm, that point to short timescales for cooling in the Rum intrusion. Following Reddy *et al*. (1996) and subsequently Tepley & Davidson (2003), diffusivity can be calculated as a function of cooling rate. Figure 3.4a is the length-scale over which diffusion of Sr in labradorite can occur and is plotted against time for cooling rates of 1°C, 0.1°C and 0.01°C per year. Three possible starting temperatures are considered, 1100°C, 1150°C and 1200°C. Although the liquidus temperature of the incoming picrite was likely to have been higher initially, assimilation of feldspathic cumulate probably reduced this to temperatures in the range of those suggested. The calculations suggest that in order to achieve Sr heterogeneities over the length-scales observed, cooling rates were likely to have been in excess of 1°C per year, and cooling to below closure temperatures must have occurred within tens to hundreds of years, orders of magnitude faster than suggested by Tepley and Davidson (2003). These cooling rate estimates support the field evidence for the formation of the Cr-spinel seams by the development of cm-thick melt percolation zones through a largely or completely solidified crystal mush. The new Unit 10 Sr isotope data have thus established reactive melt flow as a mechanism for concentrating the PGE in high-temperature magmatic systems. Furthermore, the new data highlight the potential for partly-completely solidified mafic-ultramafic crystal mush zones existing in 'cold storage' to be rejuvenated by new magma input, as has been increasingly recognised in recent years for felsic magmatic systems (Claiborne *et al*., 2010; Cooper & Kent, 2014).

3.7 CONCLUSION

The recognition of intracrystalline Sr-isotope heterogeneity within mineral phases formed by *in situ* crystallisation (i.e., oikocrysts) has far reaching implications to outstanding petrological problems within mafic–ultramafic intrusions. The impact of this conclusion is enhanced by the fact any process forming these heterogeneities is occurring *within* crystal mush, a significant departure from previously observed isotopic variation. The issue of mass balance in critical metal deposits (e.g., Cr, V, PGE) is potentially solved by the advent of lateral through flow models, with key economic implications to much larger layered intrusions such as the Bushveld and Stillwater Complexes in South Africa and the USA, respectively. However, the identification of through flow, as recorded by intracrystalline Sr-isotope heterogeneity, also has the potential to solve outstanding petrological questions regarding the formation of adcumulates in cumulate systems. Many of the peridotites studied here have more modal olivine (>75%) than possible in thin sills (<1 m) by simple closed-system crystallisation. Furthermore, as this is occurring within the crystal mush (as sills), crystal settling is no longer viable (see Chapter 2), requiring a new mechanism allowing olivine to accumulate. It has already been shown that multiple generations of melt pass through the cumulate as thin as 1 mm, meaning that in larger sills, more melt is likely to flow through the cumulate, buffering not only the temperature but also the composition, allowing more protracted periods of crystallisation of certain phases (e.g., olivine). As such, many adcumulates could be tested for intracrystalline isotope heterogeneity to better understand role of through-flow in other cumulate systems, where cold-storage rejuvenation (i.e., partial melting and sill emplacement) is likely ubiquitous.

CHAPTER 4 – THE RUM WESTERN LAYERED INTRUSION

4.1 INTRODUCTION

Our understanding of the way that layered mafic-ultramafic intrusions are constructed is dominated by gravity-driven accumulation, where crystal settling from a column of magma produces a crystal pile at the magma chamber floor (Wager & Deer, 1939; Brown, 1956; Wager *et al*., 1960; Jackson, 1961; Wadsworth, 1961; Emeleus *et al*., 1996; Campbell, 1978; Sparks & Huppert, 1984; Huppert *et al*., 1986; McBirney & Nicolas, 1997; Holness, 2005; 2007; Tegner *et al*., 2009; Brandiss *et al*., 2014; Holness *et al*, 2017b). In open systems, replenishing magma enters the chamber at the interface between the resident magma and the crystal pile. Long-held views envisage the crystal mush at the floor of the magma chamber solidifying as a static mass, which may undergo chemical and thermal exchange with the magma above, but is kinematically immobile (see Maier *et al*., 2013). Alternative models for layered intrusion development by *in situ* crystallisation focus on a boundary layer at the magma chamber floor and around the intrusion margins as the zone where intrusion growth primarily occurs (e.g., McBirney & Noyes, 1979; O'Driscoll *et al*., 2010; Latypov *et al*., 2013; Latypov *et al*., 2015). Thus, there has been an emphasis on the magma-crystal mush interface, between the main magma reservoir and the crystal pile, which has significantly influenced our understanding of how layered intrusions are constructed, and how economically important platinum-group element (PGE) enriched horizons are formed within these bodies.

Models for PGE enrichment in layered intrusions largely call for the concentration of the precious metals at the magma chamber 'floor', whether through the competing uppers or downers models (see. Mungall & Naldrett, 2008), or by thermochemical erosion of the magma chamber floor (e.g., O'Driscoll *et al*., 2010; Latypov *et al*., 2013; Latypov *et al*., 2015). However, the recent identification of out-of-sequence layers in the Bushveld Complex (South Africa) by Mungall *et al.* (2016), as well as in the Stillwater Complex by Wall (2016), by applying high-precision U-Pb geochronology has cast doubt on the classic paradigm that layered intrusions are constructed from the bottom up. Mungall *et al.* (2016) suggest that the PGE-enriched horizons are associated with out-of-sequence layers, which develop due to sill-emplacement into semi- or completely solidified cumulate. Layered intrusion formation by sill emplacement, where magma replenishment occurs into the crystal mush, has been invoked for other layered intrusions based on detailed field evidence (e.g., Bédard *et al*., 1988; Tegner & Robins, 1996; Hepworth *et al*., 2017). The mechanisms of sill emplacement in layered intrusions require careful consideration of the physical and mechanical state of the crystal framework being intruded (Marsh, 2002; Holness *et al*., 2007; Humphreys & Holness, 2010; Namur *et al*., 2013; Hepworth *et al*., 2017). Enhancing our understanding of the behaviour of the crystal mush and the complex physical and chemical processes that may occur within a semi-solid framework during syn-magmatic intrusion is thus an important goal in further elucidating the mechanisms by which the precious-metal deposits typically associated with these layered mafic-ultramafic intrusions form, as well as the formation of layered intrusions more generally.

In this chapter, support for non-traditional models of layered intrusion construction (i.e., sill emplacement) is proposed. New field, petrographic and textural observations of the Rum Western Layered Intrusion (WLI; NW Scotland) are presented, and used to discuss the physical, thermal, and chemical processes occurring *within* the crystal mush that produced the WLI. A model for the petrogenesis of the abundant Cr-spinel seams that occur throughout the WLI is presented, whereby Cr-spinel seams represent melt channels along hot tears or shear zones that form within the crystal mush. There are important implications for PGE-mineralisation in these seams, which consequently must also form within the crystal mush. The combined field, textural and geochemical evidence is used to argue for a sequence of cumulate in the WLI that does not necessarily young upwards and suggests instead that the WLI represents a dynamic and incrementally developed crystal mush that was intruded repeatedly by picritic and basaltic magmas.

4.2 GEOLOGICAL SETTING

4.2.1 The Rum Layered Suite

The Rum Layered Suite (RLS) is a classic example of an open-system layered intrusion that formed at 60 ± 1.3 Ma (Hamilton *et al*., 1998) as part of the British and Irish Palaeogene Igneous Province (BIPIP; Emeleus *et al*., 1996; Emeleus & Bell, 2005; Emeleus & Troll, 2014). The RLS

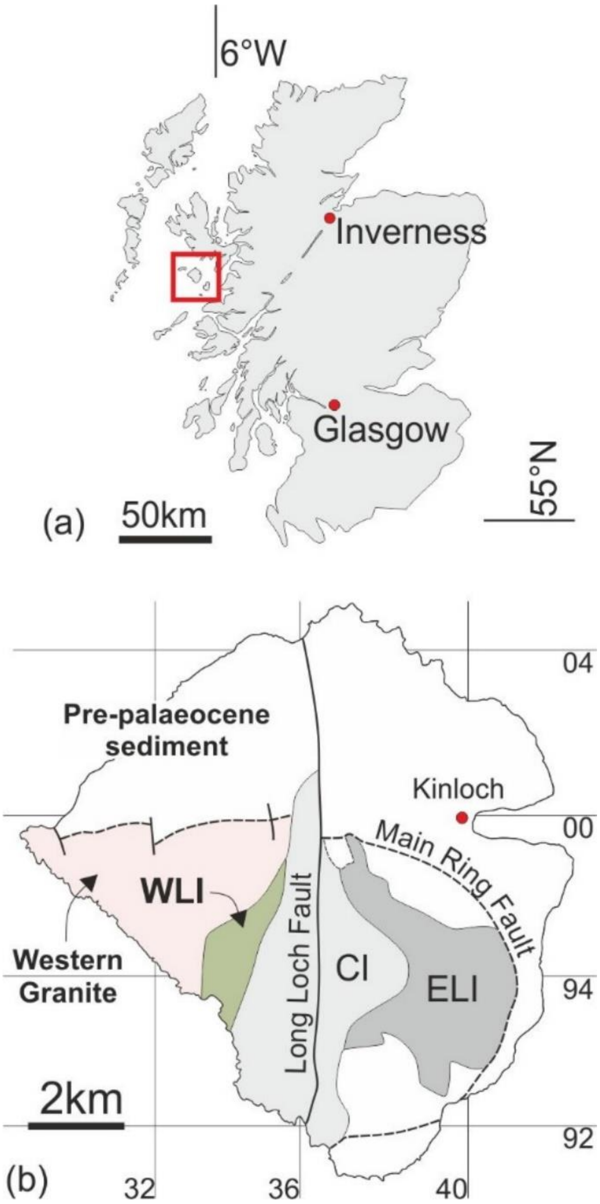

FIGURE 4.1: (a) Location of the Isle of Rum within Scotland. (b) Location of the Isle of Rum within Scotland. (b) Constituent intrusions of the Rum Layered Series (RLS): CI = Central Intrusion, WLI = Western Layered Series, ELI = Eastern Layered Intrusion (adapted from Emeleus, 1994).

can be divided into three distinct portions; the Eastern Layered Intrusion (ELI), the Central Intrusion (CI), and the Western Layered Intrusion (WLI; see below) (Fig. 4.1). The ELI is well-studied and has traditionally been held up as a type example of open-system magma chamber behaviour, with each major successive replenishment event represented by the sixteen-coupled peridotite-troctolite ± olivine gabbro macro-rhythmic units that comprise the intrusion (Brown, 1956; Volker & Upton, 1990). Early models invoked batch fractionation of successive cumulus phases and crystal settling to account for the transition from ultramafic to feldspathic cumulate, which was adapted where field observations pointed to multiple replenishment events within a single unit (e.g., Renner & Palacz, 1987; Holness *et al*., 2005; Holness & Winpenny, 2008). The construction of the ELI from the bottom up has been challenged for specific parts of its stratigraphy over the past ~30 years. Bédard *et al*. (1988) suggested that much of the upper portion of the ELI was emplaced as sills. Holness *et al*. (2005; 2007) focused on the Unit 9 peridotite and demonstrated that it was likely to have been emplaced into a pre-existing crystal mush, by documenting the effects of magma intrusion on the overlying cumulate. More recently, a detailed study of Unit 10 reported evidence that its peridotite portion formed incrementally, from numerous, small volume replenishment events within the crystal mush (Hepworth *et al*., 2017).

4.2.2 The Western Layered Intrusion

The WLI comprises the structurally lowest portion of the RLS and can be sub-divided into three composite parts (Fig. 4.2), from top to bottom as follows: the Ard Mheall Member (AMP), the Transitional Member (TSM), and the Harris Bay Member (HBM) (Wadsworth, 1961). Unlike the ELI, the WLI consists almost entirely of layered peridotite. The WLI (specifically 'Harris Bay') is the type locality of harrisite (Harker, 1908), an unusual variety of olivine cumulate comprising coarse, skeletal, branching and hopper olivine morphologies (Donaldson, 1974; O'Driscoll *et al*., 2007a). Harrisite is a key example of *in situ* crystallisation in layered intrusions, first documented by Wager *et al*. (1960). By comparison with the ELI, the WLI has lacked detailed attention for the past ~60 years. The most recent comprehensive description of the WLI is by Wadsworth (1961), whilst more recent research has focused on the petrogenesis of harrisite (e.g., Donaldson, 1974; 1976; 1982; O'Driscoll *et al*., 2007a). Wadsworth (1961) suggested that, much like the ELI, the WLI also represents an open-system, formed of multiple replenishment events. In absence of macro-rhythmic units, these replenishment events were recorded by harrisite layers, with so-called 'normal' or granular-textured peridotite representing periods between replenishment events, the latter formed by crystal settling of olivine from the overlying magma. Subsequently, the limited number of investigations into the formation of the WLI have broadly supported these ideas but have revealed more complexity in the variety of inferred magma chamber processes, such as invoking mobilisation of crystal slurries from unstable sidewalls (e.g., Worrell, 2002; O'Driscoll *et al*., 2007a). O'Driscoll *et al*. (2007a) supported some of the original concepts of Wadsworth (1961), highlighting the importance of the small volume replenishment events, and pointing to rapid crystallisation of harrisite from deeply undercooled picritic magma. The latter authors envisaged these processes operating on the magma chamber floor, with crystal settling or density current deposition considered the main process responsible for the formation of the granular-textured peridotite between picritic replenishment events.

4.3 FIELD RELATIONSHIPS

The WLI contains a variety of cumulate types such as harrisite and some granular-textured peridotites which are not true peridotites in that they contain <50 vol.% olivine. They are classified as olivine gabbro, troctolite, or melatroctolite in the scheme of Le Maitre (2002). However, for ease of comparison with the previous literature, WLI lithologies containing cumulus skeletal (or hopper) olivine crystals and intercumulus plagioclase ± clinopyroxene are referred to as harrisite, and cumulus granular olivine-textured rocks as 'peridotites', or as 'feldspathic peridotite' where particularly plagioclase-rich (>30 vol.%). Where clinopyroxene is a particularly prominent intercumulus phase (>30 vol.%), as in some of the Transitional Member rocks, the prefix 'wehrlitic' is applied, or 'dunitic' to distinguish particularly high (>90 vol.%) cumulus olivine contents. Thus, a 'wehrlitic peridotite' is a rock comprising abundant cumulus olivine plus intercumulus plagioclase, with >30 vol.% intercumulus clinopyroxene. Where gabbro (cumulus plagioclase) occurs (e.g., the HBM), normal Le Maitre (2002) terminology is used, such as melagabbro or leucogabbro reflecting the colour index.

4.3.1 The Western Layered Intrusion

The WLI was remapped as part of this study (Fig. 4.2). The new map is similar to Wadsworth (1961) and finds the same three distinct members, but a new sub-division of the Ard Mheall Member is proposed; the Ard Mheall Peridotite (AMP) and Upper Ard Mheall Peridotite (UAM). The exposed

WLI is a roughly ‘half-bowl’-shaped layered peridotite body that dips shallowly towards the Long Loch Fault (LLF) in the centre of the CI, the putative feeder zone to the RLS (Fig. 4.1). The dip of layering varies between the UAM/AMP, TSM and HBM. The dip of the layering across all parts of the WLI generally steepens with proximity to the LLF (to ~60°), with the AMP/UAM showing an average dip of ~20º to the east. Some layers within the UAM are noted to dip west at roughly 20º, a feature that is variable throughout the member. The TSM dips ~20º to the west like the overlying AMP. The HBM is much shallower, dipping ~10º to the west, and is horizontal with distance away from the LLF. Thickness estimates of the different members are consistent with those of Wadsworth (1961); the HBM is ~120 m thick, the TSM is ~53 m, and the AMP (incl. UAM) is ~245 m thick, totalling approximately 420 m of WLI peridotite cumulate (see Appendix 3.1). The contact between the AMP and TSM appears gradual over a vertical distance of a few metres, marked by a noticeable change in lithology (to wehrlitic-peridotite). The boundary between the TSM and HBM is exposed on the south eastern edge of the WLI, where there is a sharp change from olivine-gabbros to wehrlitic peridotite.

4.3.2 Ard Mheall Member

4.3.2.1 Ard Mheall Peridotite (AMP)

The AMP is the thickest peridotite body in the WLI, comprising approximately 245 m of well-layered peridotites, and hosting ubiquitous Cr-spinel seams throughout. It is well-exposed all around Ard Mheall Mountain, where the layering dips shallowly (10–15º) towards the CI (Fig. 4.2), with less exposure in the east where the dip of layering also become much steeper (40–60º). The AMP was logged in eight sections across the WLI; the high-resolution logs are accessible in Appendix 3.2. Correlation of individual layers or even packages of layers is not possible over distances of more than a few hundreds of metres; this is generally greater than the distance between many of the logs presented here. Petrological ‘facies’ have been identified in the logged sections, which describe the lithological variation, relationships between different types, and the range of occurrences of Cr-spinel seams. This is a useful way to reduce the complexity of textural and mineralogical variation observed, and the resultant classification is schematically illustrated in Figure 4.3.

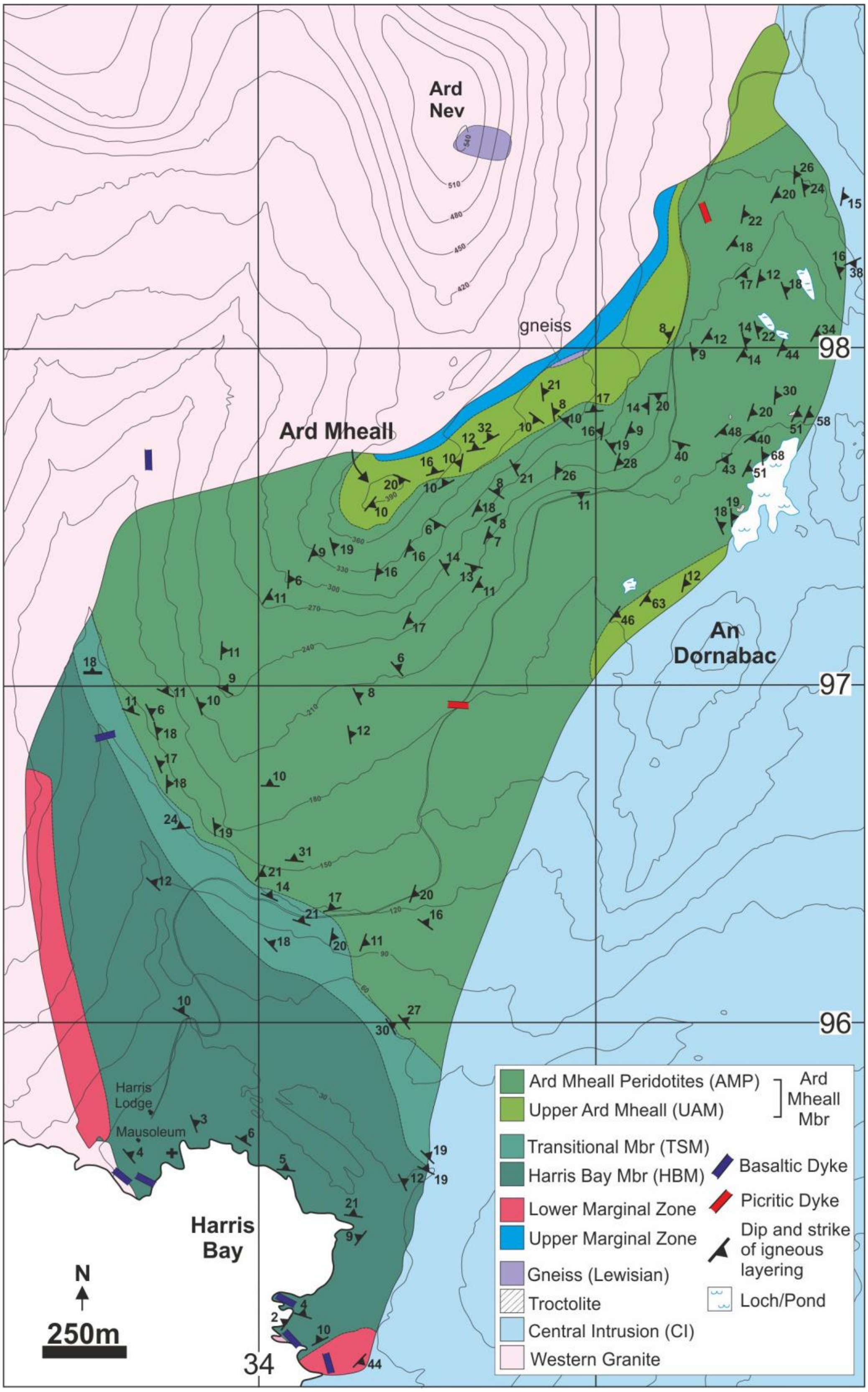

FIGURE 4.2: Geological map of the Western Layered Series (WLI) mapped as part of this study. Cross-sections of the WLI can be accessed in Appendix 3.1.

4.3.2.1.1 Harrisite

Harrisite is the most common peridotite in the AMP and comprises highly texturally-variable olivine crescumulate–orthocumulates (see Wager *et al*., 1960). Harrisite layer thicknesses range considerably (i.e., <0.1 m to >5 m). Individual harrisite layers may vary in thickness along strike as well as taper, bifurcate, and terminate (Facies A; Figs. 4.3;.4a). While harrisite layers are generally stratibound in nature and define the most obvious layering present in the WLI, the topology of the upper and lower surfaces of each layer can vary significantly (Fig. 4.4b–e). Harrisite layers can be flat on both bounding surfaces, or more commonly display prominent apophyses on their upper surfaces (Fig. 4.4b), undulose 'erosional' bases (Fig. 4.3; Facies B), and include rarer undercutting apophyses on their lower surfaces (Fig. 4.4d). The latter features are not mutually exclusive and can occur together in individual layers. The apophyses commonly found in harrisites in the WLI range in amplitude from several centimetres to several metres in height. In the latter case, they clearly crosscut existing magmatic layering in granular-textured peridotite (Figs 4.3: Facies C; 3.4e;). Dome-like protrusions of harrisite are also documented, that cross-cut 2–3 metres of overlying layering but extend for >10 m laterally (Fig. 4.3; Facies D). Relatively thick bodies (>1 m) of harrisite contain internal layering defined by variable olivine crystal morphology (Fig. 4.3; Facies E), giving them the appearance of being composite layers. Morphological variation in olivine forms can be significant between layers, although generally hopper morphologies predominate over branching and dendritic forms (Fig. 4.4f). There does not appear to be any consistent relationship between olivine morphology and layer thickness, but there is a general correlation of olivine morphology with structural height through the AMP, with the base containing the highest concentration of skeletal and branching olivine habits, while the central and upper portions of the AMP contain more finer grained hopper olivine forms. The morphologies of olivine crystals within individual layers (typically <1 mm) occasionally change at the base of the layer, with hopper varieties grading into more branching and skeletal varieties with height in the layer (Fig. 4.3; Facies F). Granular-textured peridotite autoliths are observed in harrisite layers throughout the AMP ranging from <5 cm to >1 m in diameter Fig. 4.3; Facies G). Foliation of olivine is observed at the outcrop-scale within harrisite. This foliation

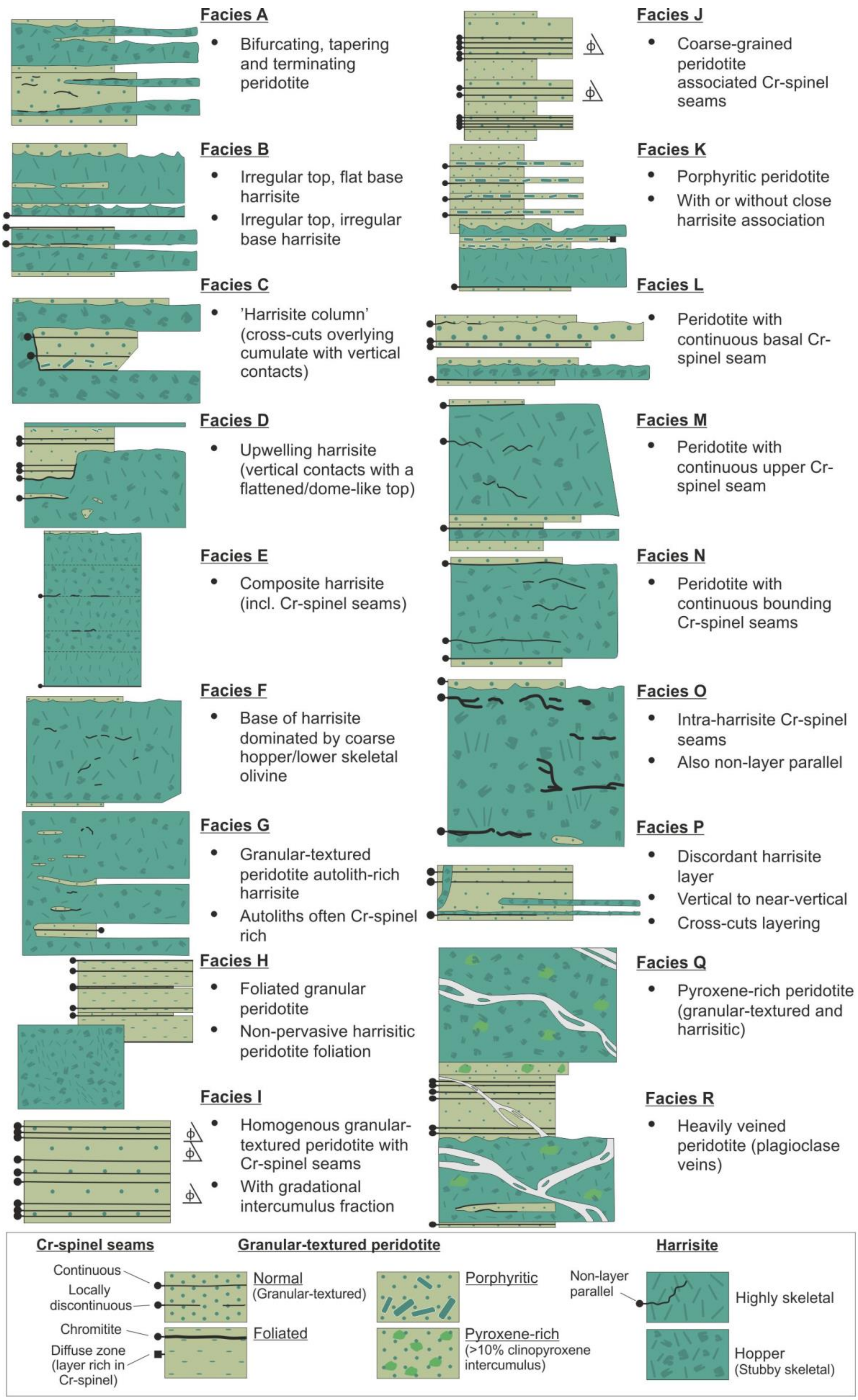

Facies A
- Bifurcating, tapering and terminating peridotite

Facies B
- Irregular top, flat base harrisite
- Irregular top, irregular base harrisite

Facies C
- 'Harrisite column' (cross-cuts overlying cumulate with vertical contacts)

Facies D
- Upwelling harrisite (vertical contacts with a flattened/dome-like top)

Facies E
- Composite harrisite (incl. Cr-spinel seams)

Facies F
- Base of harrisite dominated by coarse hopper/lower skeletal olivine

Facies G
- Granular-textured peridotite autolith-rich harrisite
- Autoliths often Cr-spinel rich

Facies H
- Foliated granular peridotite
- Non-pervasive harrisitic peridotite foliation

Facies I
- Homogenous granular-textured peridotite with Cr-spinel seams
- With gradational intercumulus fraction

Facies J
- Coarse-grained peridotite associated Cr-spinel seams

Facies K
- Porphyritic peridotite
- With or without close harrisite association

Facies L
- Peridotite with continuous basal Cr-spinel seam

Facies M
- Peridotite with continuous upper Cr-spinel seam

Facies N
- Peridotite with continuous bounding Cr-spinel seams

Facies O
- Intra-harrisite Cr-spinel seams
- Also non-layer parallel

Facies P
- Discordant harrisite layer
- Vertical to near-vertical
- Cross-cuts layering

Facies Q
- Pyroxene-rich peridotite (granular-textured and harrisitic)

Facies R
- Heavily veined peridotite (plagioclase veins)

◄FIGURE 4.3: Simplified ‘facies’ scheme depicting lithological relationships of peridotite (and Cr-spinel seams) through the AMP, see text for further description. High resolution graphic logs can be found in Appendix 3.2.

is non-pervasive but can trace out dome-like structures (Fig. 4.4g) from the alignment of elongate, branching olivine crystals (Figs. 4.3; Facies H; 3.5e). Veining by plagioclase is seen most commonly with height approaching the UAM. Clinopyroxene and gabbroic pegmatite veins occur more sparsely.

4.3.2.1.2 Granular-textured peridotite

Granular-textured peridotite is abundant throughout the AMP. It generally has significantly less intercumulus material (i.e., plagioclase and clinopyroxene) than harrisite (i.e., <15 vol.%). Packages of granular-textured peridotite are often internally layered, with a relatively limited range of layer thicknesses (5–20 cm). Layering is defined by changes in olivine grainsize or by the presence of Cr-spinel seams. Layering can also be defined by a gradational reduction in porosity (vol.% intercumulus proportion) towards the top of an individual layer, reversing sharply with the successive layer, often repeating several times in thicker sections of layered rock (Fig. 4.3; Facies I). Perturbations in fine-scale layering occur in close proximity to harrisite layers with high-amplitude apophyses, such as the upward flexure of layering adjacent to vertical harrisite contacts (Fig. 4.4e). Blocks of layered granular-textured peridotite are incorporated into harrisite, and from the random attitudes of the layering can be seen to have undergone some rotation by the host (Fig. 4.5c). Coarser-grained (~2–3 mm olivine) bodies of granular-textured peridotite taper and terminate like harrisite layers. Where lateral variations in layer thickness occur, irregular upper surfaces may also be present (Fig. 4.3; Facies A and L). An alternating relationship between coarse (~2 mm olivine) and fine (≤1 mm olivine) granular-textured peridotite is common, where fine-grained peridotite with a proportion of intercumulus material <10% occurs between coarser (and often Cr-spinel seam bearing) peridotite bodies (Fig. 4.3; Facies J). A similar relationship occurs between harrisite and granular-textured peridotite, where olivine grain-size and the volume proportion of intercumulus material is lower in the granular-textured peridotite. Layer-parallel foliation defined by the preferred alignment of tabular olivine crystals is common in granular-textured peridotites and is variably pervasive at the outcrop-scale (Fig. 4.5d). In both harrisite and granular-textured peridotite, clinopyroxene content broadly increases approaching the UAM (where it is >15 vol.%) though clinopyroxene abundance can still vary from layer to layer.

4.3.2.1.3 Porphyritic peridotite

A third distinct peridotite type can be identified in the AMP termed 'porphyritic peridotite'. This peridotite forms layers much like the granular-textured peridotite, but contains large, up to 7 cm long megacrysts of hopper and tabular olivine (Fig. 4.5e). The proportion of the olivine megacrysts varies significantly, sometimes comprising the bulk of thin peridotite layers or as low as 5 vol.% of a layer (Figs. 4.3; Facies K; 3.5e). The host material is always granular-textured peridotite and is consistently fine to medium-grained. Porphyritic-peridotite layers in which the olivine megacrysts comprise a significant proportion (i.e., >50 vol.%) of the layer, are ubiquitously thin (<5 cm), and often repeated in regular intervals (see Appendix 3.2). The occurrence of megacrysts is often linked to proximity to harrisite bodies, but this is not consistent throughout the AMP (Fig. 4.3; Facies K). Porphyritic peridotite bodies often exhibit a strong foliation, defined by the olivine megacrysts, though fine-grained olivine crystals in the groundmass may also contribute to the foliation in these cases (Fig. 4.5e). The individual megacrysts are generally display a rim of plagioclase (~1 mm thick). O'Driscoll *et al*. (2007a; 2015) reported imbrication-like structures in some of the olivine megacrystic layers. This feature was not confidently identified during this investigation.

4.3.2.1.4 Cr-spinel seams

Cr-spinel seams are extremely abundant in the AMP (see graphic logs in Appendix 3.2), occurring in all varieties of peridotite. Individual seams are not laterally extensive and can rarely be traced for more than several tens of metres along strike. The thickness of Cr-spinel seams is also highly variable, ranging from 2–30 mm. The thickness of individual seams can vary laterally over several metres, as can the modal abundance of Cr-spinel in seams. Discrete layers of granular-textured peridotite can be relatively enriched in Cr-spinel, creating diffuse seams up to 50 mm thick which

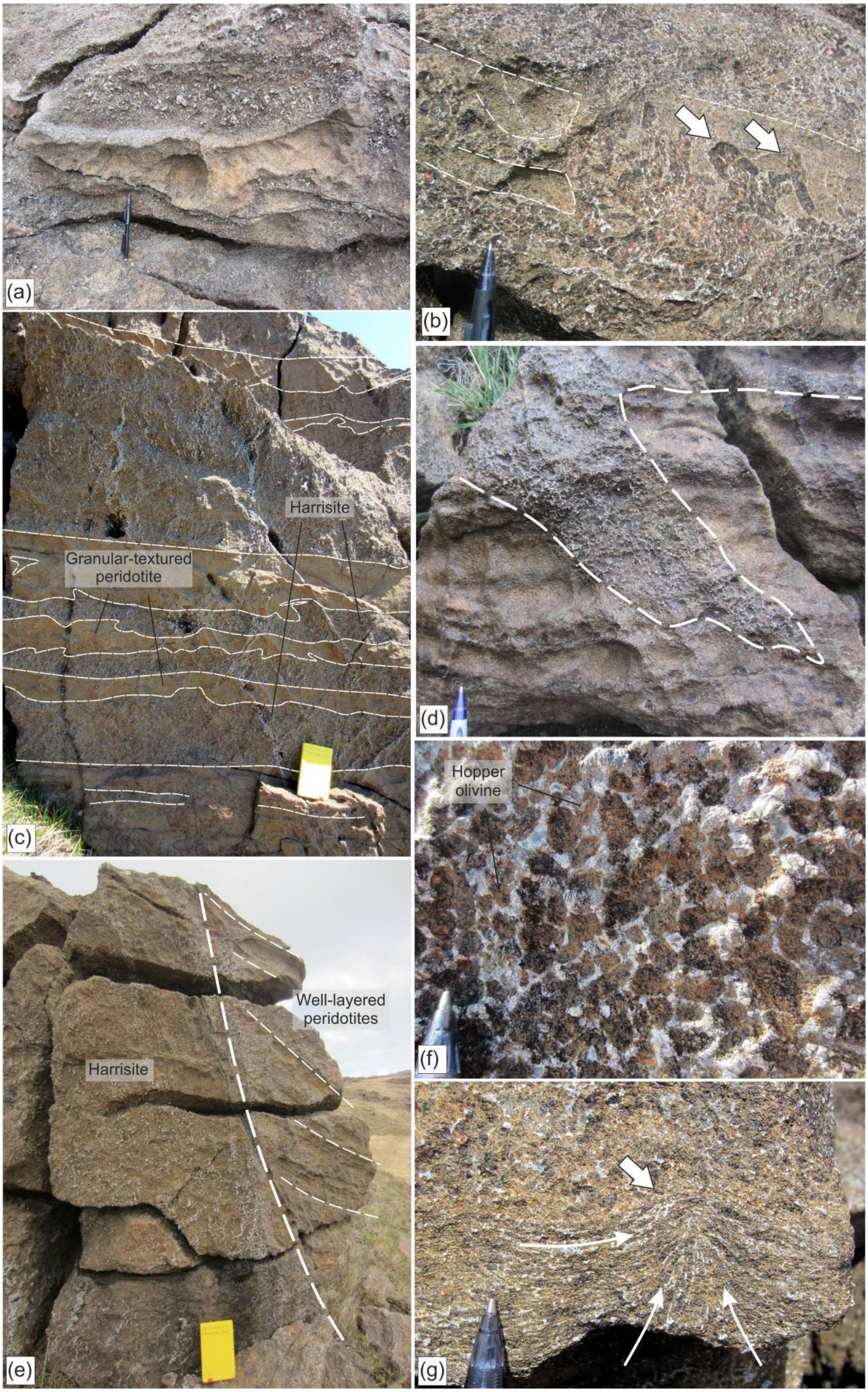
(a)
(b)
Harrisite
Granular-textured peridotite
(c)
(d)
Well-layered peridotites
Harrisite
(e)
Hopper olivine
(f)
(g)

◄FIGURE 4.4: Field relationships of peridotite in the AMP. (a) Bifurcating harrisite around fine grained granular-textured peridotite. Note the high intercumulus plagioclase fraction of granular-textured peridotite in contact with harrisite. (b) Irregular harrisite layer with upward oriented apophyses linked to the succeeding layer, see also the large branching olivine crystals (arrowed) protruding into the granular-textured peridotite. (c) Typical layering of harrisite and granular-textured peridotite, with irregular (upper) boundaries of harrisite. Note also the bifurcation in the top right, in the thickest harrisite layer. (d) Downward-oriented harrisite apophysis. Note faint continuation of plagioclase-rich layers through the apophysis. (e) 'Harrisite column' with metres high harrisite and deflected granular-textured peridotite. (f) Hopper dominated harrisite, with cm-sized rounded–hopper olivine crystals. (g) Strongly foliated harrisite with dome-like oriented elongated olivine crystals.

can be traced for several tens of metres. The textures of many of the Cr-spinel seams in the AMP (and WLI more broadly) are comparable to those in the Unit 12 and Unit 10 peridotite in the ELI, which were described as 'chain-textured' by O'Driscoll *et al.* (2010) and Hepworth *et al.* (2017). This texture is characterised by Cr-spinel forming chain-like aggregates around cumulus olivine crystals. The intercumulus silicate fraction comprises plagioclase with or without clinopyroxene, with deformation twinning commonly observed in plagioclase. Unlike Cr-spinel seams in the Unit 12 and 10 peridotites, seams in the WLI can also be formed of chromitite, containing little to no cumulus olivine at all. Thus, the AMP Cr-spinel seams can be divided into similar groups as those suggested for Unit 10 by Hepworth *et al.* (2017), based on their relationship to their host peridotite: granular-textured peridotite-hosted seams, boundary seams, harrisite-hosted seams, foliated peridotite-hosted seams, and an additional group of chromitite seams. Granular-textured peridotite-hosted seams exhibit no textural or mineralogical variation in the peridotite above or below the seam (Figs. 4.3; Facies I) and can be undulose (Figs. 4.5a; d; 4.6a). Boundary seams occur with a distinct textural or mineralogical variation in the peridotite on either side of the seam, e.g., a Cr-spinel seam between harrisite and granular-textured peridotite (Fig. 4.6b). Boundary Cr-spinel seams occur on the base (Fig. 4.3; Facies L), the top (Fig. 4.3; Facies M), or more rarely both surfaces of harrisite and granular-textured peridotite layers (Fig. 4.3; Facies N). Foliated peridotite (including harrisite)-hosted seams occur where cumulus olivine defines a foliation within (and less commonly outside) the upper and lower limits of the Cr-spinel seam. Harrisite- hosted seams occur within harrisite layers and contain Cr-spinel that is relatively coarse-grained (>1 mm in diameter). Chromitite seams have little or no cumulus olivine within the limits of the Cr-spinel seam and tend to be particularly thick

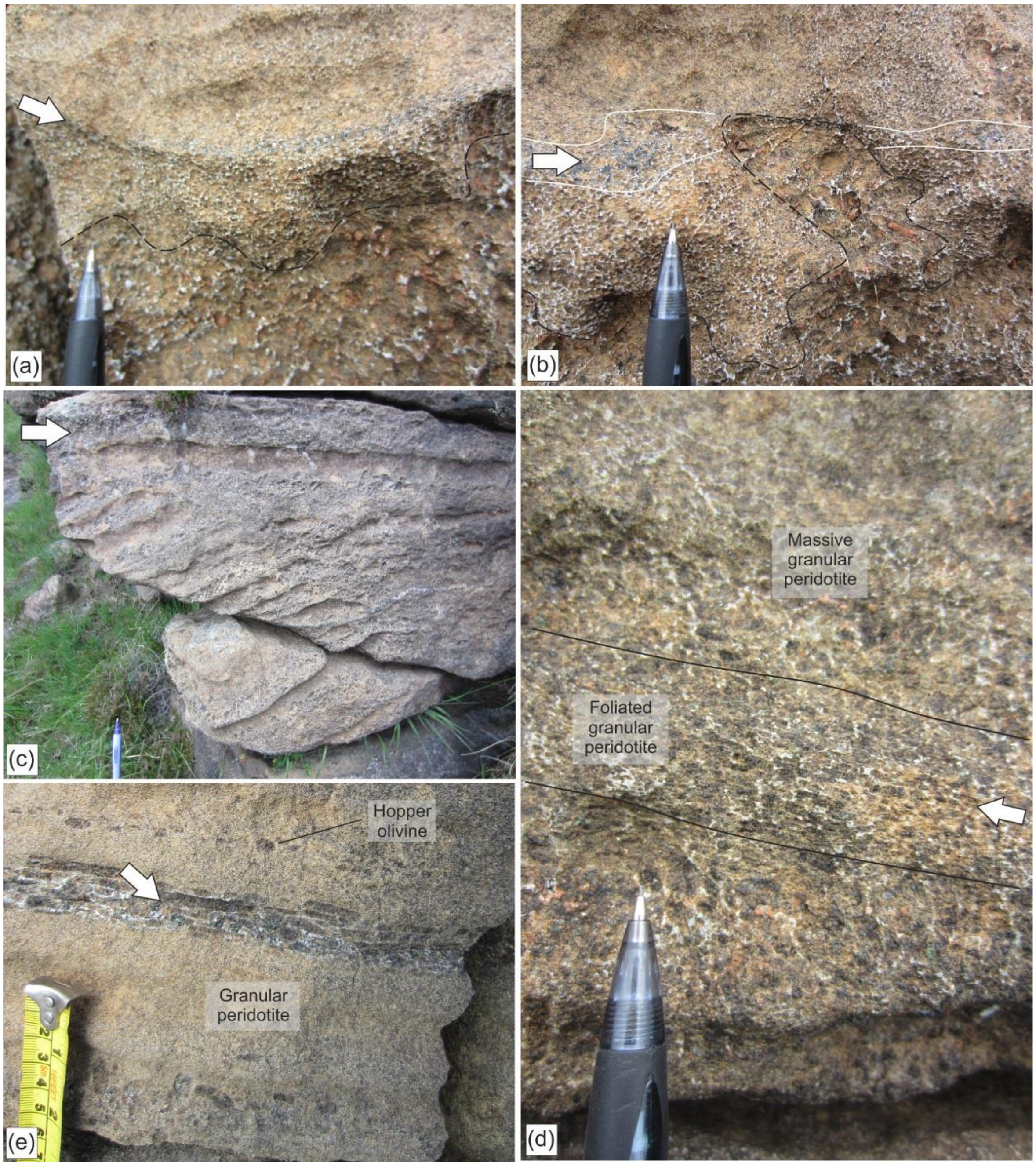

FIGURE 4.5: Field relationships of peridotite in the AMP. (a) Deflected Cr-spinel seam hosted within granular-textured peridotite above irregular harrisite (boundary shown by dashed line). (b) Cr-spinel seam along strike of (a) where Cr-spinel is cross-cut by an upward-oriented harrisite apophysis (seam outlined), close to which the Cr-spinel suddenly becomes disseminated (arrowed). (c) Block of layered granular peridotite, as shown by layering oriented ~45º from normal, within shallowly dipping harrisite (arrowed layer). (d) Strongly foliated zone within granular-textured peridotite (shown between black lines). (e) ‘Porphyritic peridotite’ layers within granular-textured peridotite. Arrowed example is composed almost entirely of strongly aligned cm-sized branching–elongate olivines.

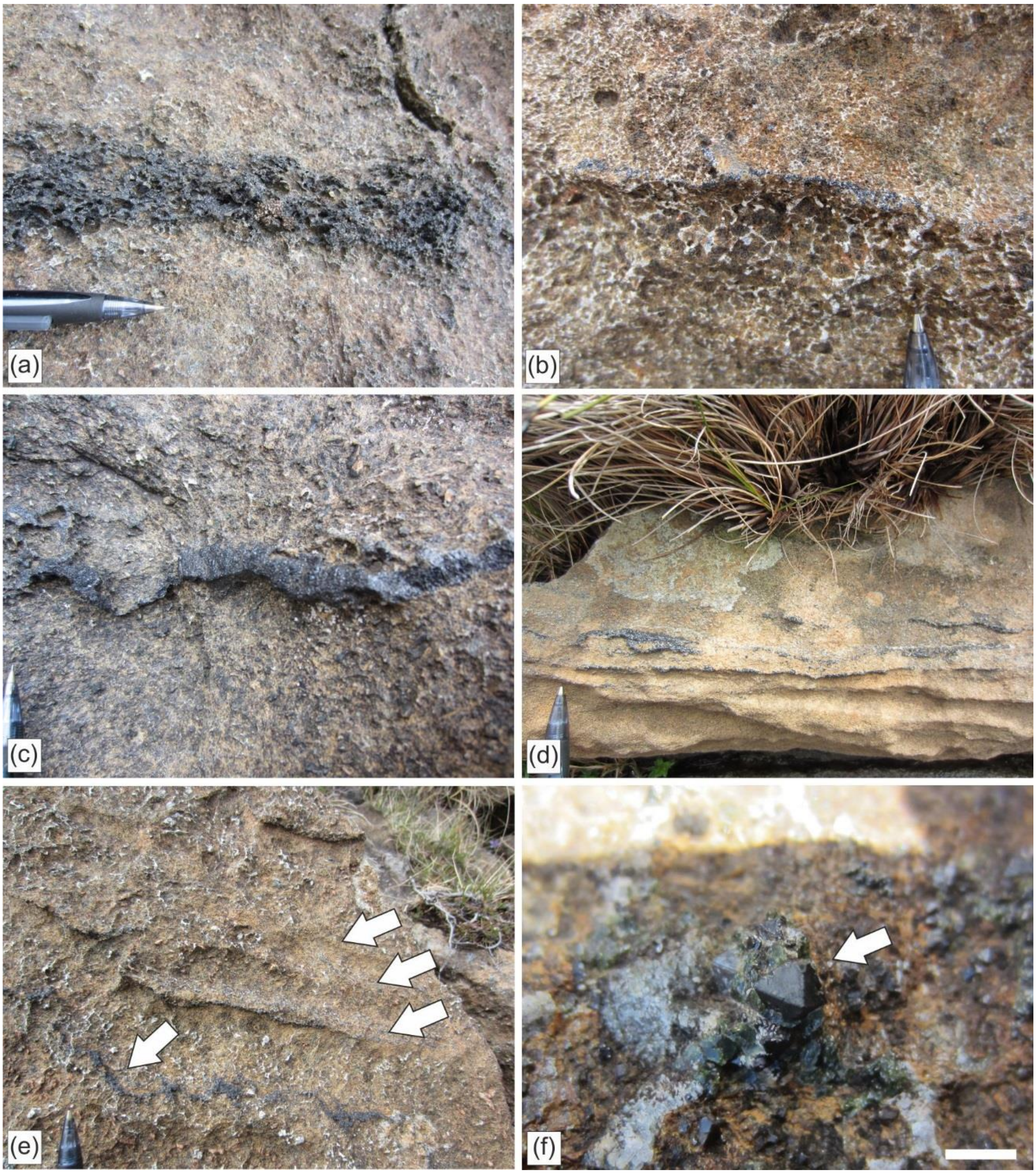

FIGURE 4.6: Cr-spinel seams in the AMP. (a) High concentration granular-type Cr-spinel seam in coarse-grained granular-textured peridotite. (b) Boundary-type Cr-spinel seam on the upper surface of coarse-grained granular-textured to hopper peridotite. (c) Chromitite seam within harrisite. Note the boundary irregularities along strike where Cr-spinel occupies intercumulus space around harrisitic olivine. (d) Anastomosing chromitite seam in fine-grained granular-textured peridotite. (e) Multiple-seams within harrisite layer (arrowed) with various concentrations of Cr-spinel. Note specifically the vertical orientation of seams towards the left (arrowed). (f) Very coarse Cr-spinel seam from a harrisite-hosted Cr-spinel seam, scale bar = 2 mm.

(>10 mm) (Fig. 4.6c). Chromitite seams are more commonly found within harrisite layers, but can also occur within granular-textured peridotite,developed laterally from another variety of Cr-spinel seam (Fig. 4.6d). Chromitite seams tend to be discontinuous and very irregular, with depressions and culminations along strike (Figs. 4.3; Facies O; 4.6e). They are effectively localised enhancements of Cr-spinel concentration. Harrisite-hosted (and chromitite) seams in the WLI may occur with vertical or sub-vertical orientations, so are not universally stratiform like those reported in Unit 10 of the ELI (Hepworth *et al.*, 2017). Cr-spinel seams in granular-textured peridotite are locally cross-cut by upward oriented harrisite apophyses (Fig. 4.5b). Cr-spinel seams are also cross-cut by plagioclase-rich veins.

4.3.2.2 Upper Ard Mheall Member (UAM)

The UAM is situated at the top of the WLI at Ard Mheall and in the same structural position on the eastern side of the WLI, where it contains layers that dip steeply toward the adjacent CI (Fig. 4.2). In both localities, the UAM has a minimum thickness of ~30 m. The boundary between the AMP and UAM appears to occur over 5–10 m, where mm–cm-sized intercumulus clinopyroxene oikocrysts are developed across the boundary. There is a change in outcrop colour from brown to grey, marking the transition into the UAM, caused by the increased abundance of intercumulus plagioclase and widespread plagioclase veining (Fig. 4.7a). The UAM is considerably less well-layered than the AMP peridotites and where layering does exist, it appears to be caused by the variation in abundance of intercumulus phases, particularly clinopyroxene. The dip of this layering is concordant, similar to that measured in the AMP, dipping shallowly to moderately toward the east. Stratabound mm–cm scale plagioclase veining also defines a layering structure in the UAM, which dips shallowly to the west (Fig. 4.7b). Harrisite is present in the UAM but is less common than in the AMP, and occurs as vertically-oriented sheets, crosscutting magmatic layering in the host rock (Figs. 4.3; Facies P; 4.7c). Broadly, an increase in the abundance of intercumulus clinopyroxene is the most distinctive feature of the UAM (Fig. 4.3; Facies Q) on Ard Mheall, where this mineral comprises up to 40 vol.% in wehrlitic peridotites (Fig. 4.7d, e). Abundant, vertically-oriented plagioclase veins

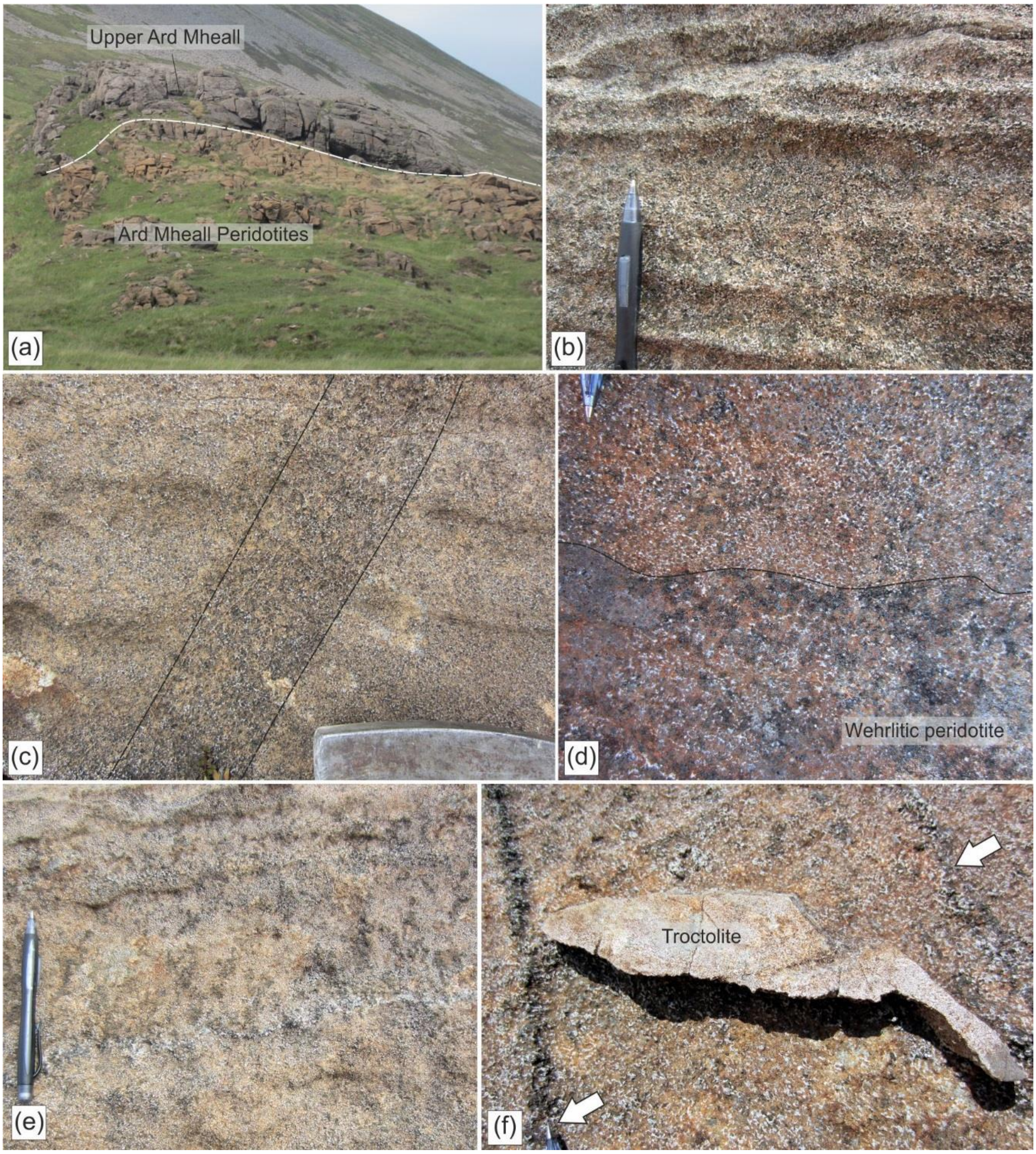

FIGURE 4.7: Field relationships of the UAM. (a) Boundary between the AMP and UAM with distinct grey colour change due to the increase of plagioclase abundance. (b) Layering defined by subtle changes in intercumulus volume. (c) Sub-vertically oriented hopper-harrisite dyke (marked by black dashed lines) cross-cutting layering. (d)Highly pyroxene-rich (wehrlitic) peridotite layer. (e) Typical pyroxene-rich (dark green oikocrysts) peridotite. (f) Trocolite autolith in UAM closest to the CI, with clinopyroxene-veins (arrowed).

locally cross-cut layering and are continuous at the outcrop-scale (Fig. 4.3; Facies R). Cr-spinel seams are apparently absent throughout the entire UAM. Exposures of the UAM to the east, in closer proximity to the CI, also contain abundant intercumulus clinopyroxene. Clinopyroxene veining is also present, in contrast to the Ard Mheall UAM exposures (Fig. 4.7f). Close to the boundary with the CI, irregularly shaped troctolite autoliths (<20 cm) occur in the UAM peridotites, a phenomenon not observed in the western UAM (Fig. 4.7f). Base-metal sulphides are unusually common in some of the eastern exposures of the UAM too.

4.3.3 The Transitional Member (TSM)

The TSM is a ~50 m thick layered peridotite body that crops out between the AMP and the HBM (see Appendix 3.2 for a high-resolution log). The layering has an average dip of ~20º towards the NE. The contact between the AMP and TSM is marked by a gradational transition downwards from layered feldspathic and dunitic-peridotites (AMP) to a red-weathered wehrlitic-peridotite (TSM) over <5 m from the AMP. The TSM is well-layered like the AMP and contains both harrisite and granular-textured peridotite types (Fig. 4.8a). The range of thicknesses of layers is similar to those in the AMP, though harrisite layers are generally thinner (i.e., typical range of 0.2–2 m). Fine-scale layering in the granular-textured peridotites occurs at the cm-scale, with layers defined by variations in intercumulus material and/or the presence of Cr-spinel seams (Fig. 4.8b). Features such as irregular tops and basal surfaces of harrisite layers occur in the TSM like they do in the AMP (Fig. 4.8c, d), though the amplitude of the apophyses observed is considerably less (<1 m) than in the AMP. Upward-oriented harrisite apophyses apparently connect with overlying harrisite layers (Fig. 4.8d). The harrisite layers in the TSM have different olivine morphologies to those in the AMP, with olivine crystal populations dominated by coarse-grained, bladed to branching shapes, often >10 cm in length (Fig. 4.8e). The TSM cumulates have noticeably more intercumulus material >20 vol.% than those in the AMP, and although feldspathic-peridotites exist within the member, wehrlitic peridotites are dominant. The wehrlitic peridotites have a high proportion of rounded, cm-sized clinopyroxene oikocrysts (Fig. 4.8f). Cr-spinel seams in the TSM are less common than in the AMP. They display similar lithological relationships, e.g., boundary-type seams between harrisite and granular-textured peridotite, or granular-textured peridotite-hosted seams (Fig. 4.8b). Feldspathic peridotite is only found in close proximity to Cr-spinel seams. The Cr-spinel seams are extremely discontinuous, rarely extending laterally for more than a few metres, but they can change significantly in thickness and

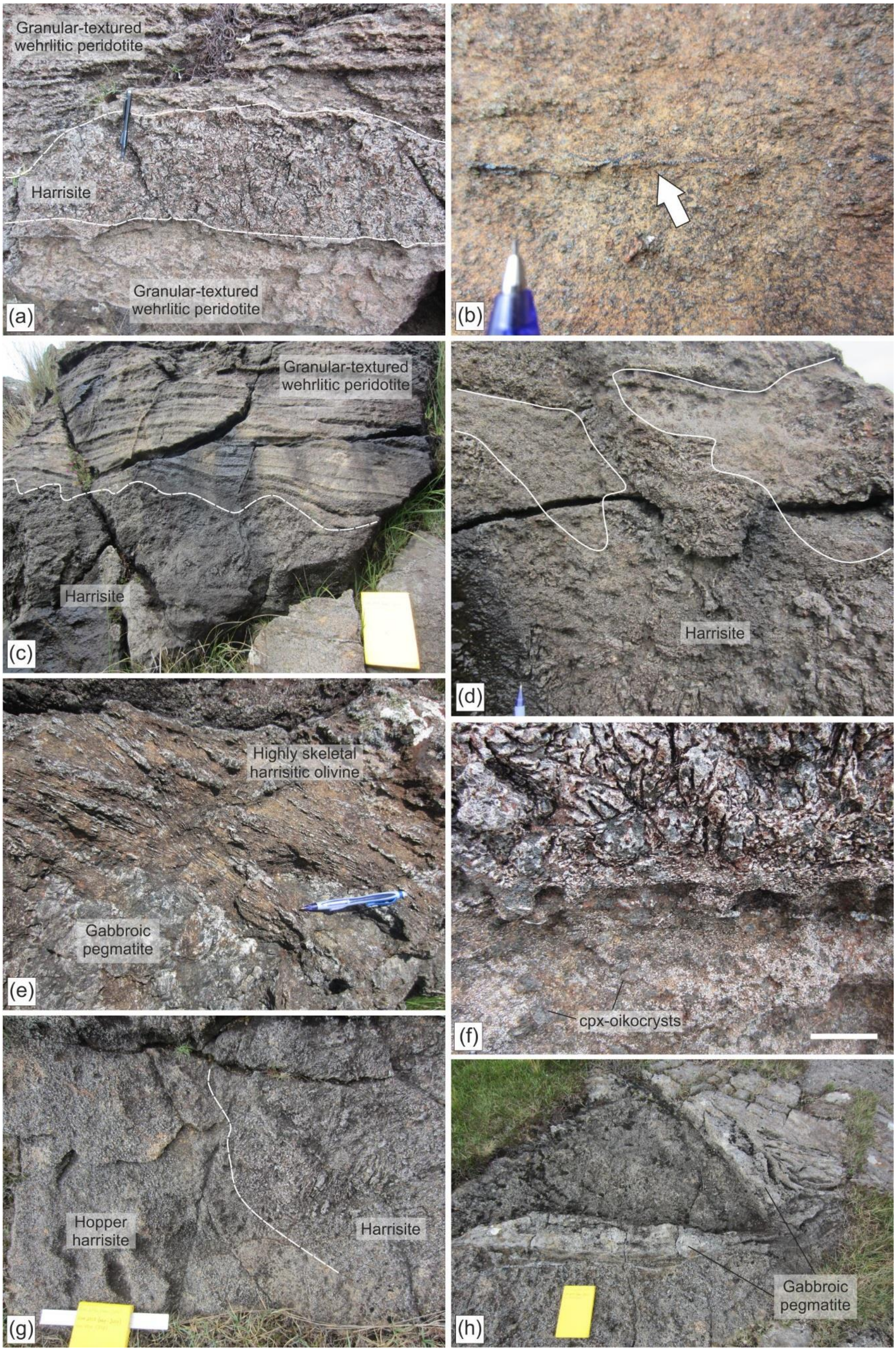
Granular-textured wehrlitic peridotite
Harrisite
Granular-textured wehrlitic peridotite
(a)
(b)
Granular-textured wehrlitic peridotite
Harrisite
(c)
Harrisite
(d)
Highly skeletal harrisitic olivine
Gabbroic pegmatite
(e)
cpx-oikocrysts
(f)
Hopper harrisite
Harrisite
(g)
Gabbroic pegmatite
(h)

◄FIGURE 4.8: Field relationships of the TSM. (a) Layering types. (b) Granular-type Cr-spinel seam. Note the highly discontinuous nature, even on a cm-scale. (c). Undulose upper surface of harrisite with well-layered granular-textured peridotite. (d) Upward-oriented apophysis linked between harrisite layers with granular-textured peridotite in between. (e) Very coarse, highly skeletal olivine. Note also the gabbroic pegmatite common in the upper TSM. (f) Pyroxene-rich 'wehrlitic' peridotite of both harrisite and granular-textured peridotite. Scale bar (in white) ~5 cm. (g) Complex harrisite in the upper TSM with hopper harrisite zones. (h) Gabbroic pegmatite veins in the upper TSM.

Cr-spinel concentration along strike like they do in the AMP. Harrisite bodies towards the top of the TSM are texturally heterogeneous, with clinopyroxene-poor layers containing large, irregular patches of hopper olivine, like morphologies in the AMP (Fig. 4.8g). Thick sheets (>10 cm) of gabbroic pegmatite are also common in the upper portion of the TSM (Fig. 4.8h).

4.3.4 The Harris Bay Member (HBM)

The HBM is approximately 120 m thick and comprises the structurally lowest exposed portion of the WLI (Fig. 4.2). The boundary with the overlying TSM is sharp, with a shallow dip <15^o toward the N–NE. In the lowermost part of the HBM, layering is horizontal. A schematic cross section through the WLI thus suggests onlap of the HBM by the overlying members (see Appendix 3.1). The contact of the HBM with the Western Granite is well-exposed at Harris Bay (Fig. 2), where the HBM clearly intrudes into the granite (Fig. 4.9a, b). Discrete sheet-like lobes of the HBM protrude into the granite, highlighting an irregular and complex boundary zone (Fig. 4.9c, d).

The HBM is well-layered, but unlike the overlying members, consists of a high proportion of feldspathic cumulates (e.g., olivine-gabbro). There is a noticeable increase in the proportion of this gabbroic cumulate towards the top of the member, such that the most olivine-rich lithologies crop out towards the base (at sea level). Layer thicknesses are relatively consistent throughout the member, with layers rarely exceeding 1 m, and on average are ~0.5 m thick. There is a broad decrease in the thickness that individual layers attain towards the top of the HBM, where layers are generally <0.5 m (Fig. 4.10a). Harrisite layers exhibit apophyses on their upper surfaces as reported for the overlying members, and large (up to 1 m long) olivine crystals are present in some outcrops (Fig. 4.10b). Individual harrisite layers also bifurcate, seen best on the coastal exposures at Harris Bay

FIGURE 4.9: Contact zone of the HBM and Western Granite. (a) Lobe of HBM into the Western Granite, with radial jointing around lobe (arrowed). (b) Intercalated nature of the HBM, also with position of the Lower Marginal Zone, backpack ~40cm high. (c) Thin tongue of HBM peridotite within the Western Granite. (d) Thick (~2 m) harrisitic peridotite sill (~2m thick), protruding the Western Granite with radial joints at the tip.

FIGURE 4.10: Field relationships in the HBM. (a) Typical layering within the upper portions of the HBM with harrisite and gabbro layers. (b) Very coarse, highly skeletal olivine (arrowed) in harrisite with irregular upper surface (shown by black dashed line). (c) Bifurcating, complex harrisite layer (boundaries shown by black dashed lines). (d) Strong foliation of granular-textured peridotite (arrowed) beneath harrisite layer. (e) Variation in gabbro textures in succession (arrowed) (f) Leucogabbro layer within olivine-gabbro.

(Fig. 4.10c). Granular-textured peridotite layers occur between harrisite layers that also display internal, finer-scale layering (1–2 cm thick). Cr-spinel seams are completely absent in the HBM, and layering is defined by relatively small changes in the intercumulus mineralogy, (i.e., abundance of clinopyroxene). Foliation of tabular olivine crystals is present, most commonly in close proximity to harrisite layers where it may be very strong (e.g., Fig. 4.10d). As noted above, the proportion of gabbroic layers is greater towards the upper section of the HBM, where layer thickness varies between 0.1–0.5 m thick (Fig. 4.10e). The layers are typically intercalated with harrisite but can form successions of several metres comprising gabbro alone. The HBM gabbro is variable in texture and mineralogy at the outcrop scale, defining individual layers of melagabbro, gabbro, and leucogabbro (Fig. 4.10f). Melagabbros are particularly coarse-grained (3–5 mm) whereas leucogabbros tend to be fine-grained (~1 mm) (Fig. 4.10e, f).

4.4 PETROGRAPHY

The term cumulus and intercumulus are used here purely as descriptive textural terms, the former describing primocryst/phenocryst phases (forming the cumulate framework), and the latter describing the material occurring in the interstices of the cumulus phases, with no implied genetic or timing implications.

3.4.1 Ard Mheall Member

4.4.1.1 Ard Mheall Peridotite

4.4.1.1.1 Harrisite

The cumulus mineral phase in harrisite is ubiquitously olivine, which varies in abundance depending on the dominant crystal morphology. Highly skeletal harrisites have a sub-equal proportion of cumulus and intercumulus material, while hopper olivine-dominated harrisite tends to have a lower intercumulus component (i.e., 10–30 vol.%). The morphology of olivine crystals in the AMP is variable but strongly dominated by hopper olivine crystal shapes (typical abundances >60 vol.%), with subordinate branching and skeletal forms. The crystal size of olivine in harrisite varies significantly in the AMP but has an approximate minimum crystal size (length) of 5 mm, including within lithologies containing both hopper and skeletal olivine. However, it is not uncommon for olivine crystals to greatly exceed 5 cm in length, particularly the highly skeletal and branching varieties. Hopper olivine crystals tend to be more restricted in size, with an average grainsize of ~1 cm. Euhedral Cr-spinel crystals are found outside Cr-spinel seams in accessory proportions (<1 vol.%). Accessory Cr-spinel in harrisites is often coarser-grained than in the other peridotite types, up to 1 mm in diameter (Fig. 4.6f). Finer grained (<0.1 mm) Cr-spinel occurs as rare inclusions in olivine. No skeletal Cr-spinel crystals were observed. The intercumulus mineralogy of the AMP harrisites is dominated by plagioclase, with clinopyroxene present in typical proportions of <10 vol.%. This is consistent across the range of harrisite morphologies. However, approaching the UAM, clinopyroxene content increases to >15 vol.%. Intercumulus plagioclase throughout the AMP comprises coarse-grained (1–3 cm) oikocrysts. Where present, subordinate intercumulus clinopyroxene occurs as similarly-sized oikocrysts. Plagioclase displays patchy optical zoning, particularly near Cr-spinel seams (Fig. 4.11a), and clinopyroxene can also be optically zoned, though this is rare (Fig. 4.11b). The olivine foliation observed at the outcrop-scale is also apparent in thin section, controlled by elongate and branching olivine crystals (Fig. 4.11c). Trace amounts of serpentine, chlorite, calcite, epidote and kaersutite occur in the interstices of the olivine framework.

4.4.1.1.2 Granular-textured peridotite

Granular-textured peridotites consist of ~70 vol.% rounded, euhedral (~0.5–3 mm) olivine crystals. A subordinate proportion of tabular and hopper olivine morphologies is present in most samples. A general observation is that the coarser-grained the peridotite, the greater the proportion of tabular and hopper olivine crystals. Euhedral Cr-spinel crystals occur in the interstitial areas and are also rarely present as inclusions in olivine. The intercumulus fraction typically comprises <15 vol.% of the granular-textured peridotites. For the most part, 1-5 mm plagioclase oikocrysts are dominant, though subordinate clinopyroxene oikocrysts of a similar size to the plagioclase also occur. Patchy compositional zoning is occasionally observed in both plagioclase and clinopyroxene oikocrysts (Fig. 4.11b). The volume proportion of intercumulus material can vary significantly between layers and can be as low as ~5 vol.%, where the rock is dunitic-peridotite. In such cases, the olivine triple-junctions have apparent dihedral angles approaching 120º (Fig. 4.11d). Such a texture is also common in granular-textured peridotite autoliths that occur within harrisite layers. The development of a foliation, carried by tabular olivine crystals, is common, especially adjacent to Cr-spinel seams (e.g., Fig. 4.11c). Trace amounts of serpentine, chlorite, epidote, calcite and kaersutite–titano-pargasite amphibole occur in the interstices of the olivine framework.

4.4.1.1.3 Porphyritic peridotite

The granular-textured peridotite that contains olivine megacrysts has a similar mineralogy and texture to granular-textured peridotite, except for the cm-sized (0.75–7 cm) euhedral olivine crystals that predominantly occur concentrated into layers throughout (Fig. 4.12a), as described above. The finer-grained granular-textured peridotite hosting the olivine megacrysts is dunitic, with a proportion of intercumulus plagioclase <10 vol. %. The olivine crystals in the granular-textured peridotite are fine-grained (~1 mm) and euhedral, commonly exhibiting apparent dihedral angles at olivine three-grain-junctions that approach 120º (Fig. 4.12b). Unlike the fine-grained olivine crystals, the megacrysts contain abundant crystallographically-constrained skeletal magnetite inclusions (Fig. 4.12a, b) (see also O'Driscoll *et al*., 2015). In the porphyritic peridotite, these inclusions only occur in the olivine megacrysts (i.e., they are absent in the fine-grained olivine in the granular-textured peridotite). However, it should be noted that magnetite inclusions are also observed in other harrisitic olivine crystals throughout the WLI (e.g., Fig. 4.12b, c).

4.4.1.1.4 Cr-spinel seams

Cr-spinel seams in the AMP exhibit a range of textures, but most are chain-textured, where the Cr-spinel crystals occur poikilitically enclosed in intercumulus plagioclase or clinopyroxene, distributed between and around cumulus olivine crystals (Fig. 4.11c). In chain-textured seams, Cr-spinel is often observed within embayments in cumulus olivine crystals (Fig. 4.11a, f). Chromitite seams, where little to no cumulus olivine occurs within the seam, are less common. Cr-spinel crystal morphologies in seams vary slightly, depending on their host peridotite. For example, in granular-textured

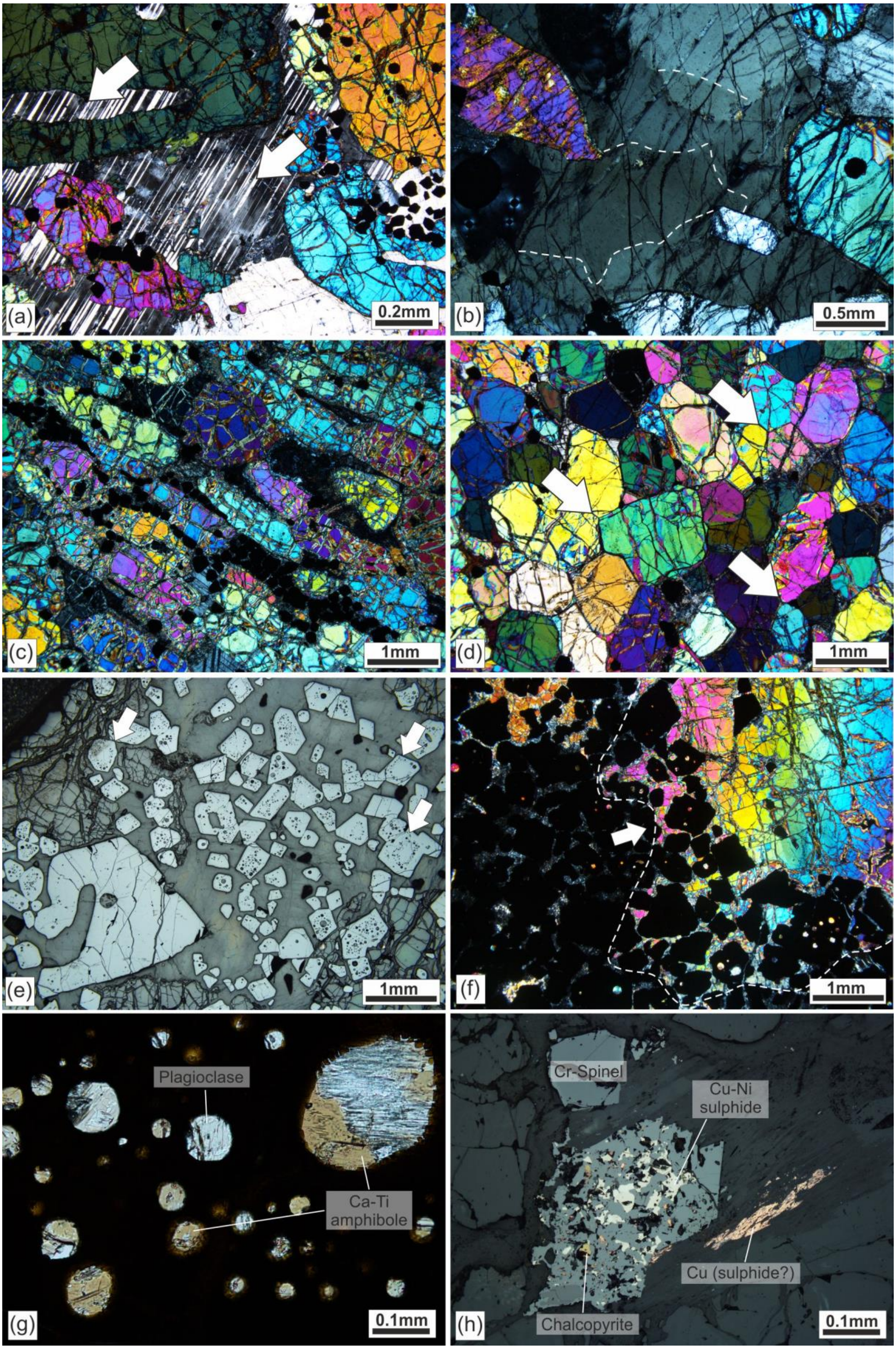
(a)
0.2mm
(b)
0.5mm
(c)
1mm
(d)
1mm
(e)
1mm
(f)
1mm
Plagioclase
Ca-Ti amphibole
(g)
0.1mm
Cr-Spinel
Cu-Ni sulphide
Cu (sulphide?)
Chalcopyrite
(h)
0.1mm

◄FIGURE 4.11: Petrography of the AMP. (a) Patchy zoning of plagioclase in proximity to Cr-spinel seam. (b) Possible patchy zoning in rare clinopyroxene oikocryst. (c) Foliated olivine within Cr-spinel seam. (d) 'Dunitic-peridotite' with polyhedral olivine arrangement with 120° triple-junctions (arrowed). (e) Reflected light image of coarse Cr-spinel with severe embayment, with inclusion rich Cr-spinel displaying zone-like patterns of the rounded inclusions (arrowed). (f) Cr-spinel seam cross-cutting large olivine crystal (outlined) across the top surface of a chromitite seam within harrisite. Note the high birefringence (olivine) inclusions in Cr-spinel close to the large olivine. (g) Typical mineralogy of rounded inclusions within Cr-spinel in plane-polarized light (h) Reflected light image with sulphide and metal phases associated with Cr-spinel, including replacement (sieve) texture of Cr-spinel by sulphide.

peridotite hosted Cr-spinel seams, Cr-spinel has a size range of 0.05–0.3 mm, while harrisite-hosted seams tend to be coarser-grained, with crystals up to ~0.8 mm in size, with an average size of 0.4 mm. Chromitite seams often host particularly coarse-grained (up to ~1.3 mm-sized) Cr-spinel crystals as well (Fig. 4.11e). Cr-spinel crystals in all seams are mostly euhedral. However, in some texturally distinct zones within composite chromitite seams, the crystals face are notably lobate. It should also be noted that this texturally distinct zone in composite chromitite seams is not a uniform thickness on seam margins (see Fig. 4.11e). Aggregates of Cr-spinel crystals occur in some samples, resulting in irregularly-shaped glomerocrysts. Within these, the constituent crystal boundaries can be resolved using reflected light microscopy. In chromitite seams, plagioclase is the only intercumulus phase (typically comprising ≤30 vol.% of the seam) and is often severely altered. In some instances, chromitite seams appear to cross-cut olivine crystals, such that a given olivine crystal is in optical continuity on either side of the seam, so is presumed to have predated formation of the seam (Fig. 4.11f). This phenomenon has previously been reported for Cr-spinel seams in the ELI Unit 12 peridotite by O'Driscoll *et al*. (2010). Well-rounded inclusions are very common in coarser-grained Cr-spinel crystals in harrisite-hosted and chromitite seams. The inclusions may define internal zones within Cr-spinel crystals or can be concentrated in crystal cores (Fig. 4.11e). The inclusions have a variety of compositions, including kaersutite, plagioclase, clinopyroxene, and base-metal sulphide (in one of the latter instances including a Pt-arsenide grain). Amphibole such as kaersutite is the most common type of inclusion (Fig. 4.11g). Ilmenite exsolution occurs in Cr-spinel crystals in the WLI but is much less a feature of Cr-spinel in seams, than accessory Cr-spinel in the various types of peridotite.

Base-metal sulphides, alloys and native metals are present in the AMP cumulates, especially in

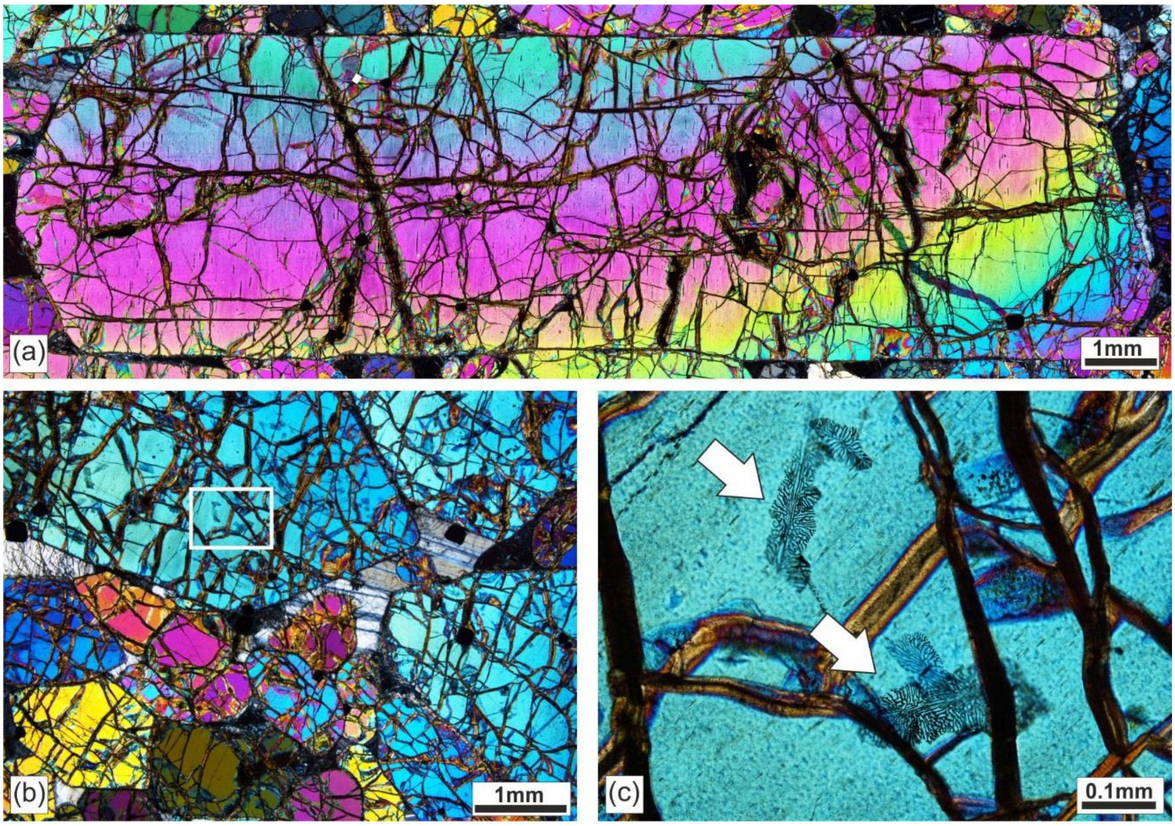

FIGURE 4.12: Porphyritic peridotite in the AMP. (a) Cm-sized blocky–elongate olivine crystal are part of porphyritic peridotite. Note the vertical, aligned magnetite inclusions. (b) large, blocky olivine crystals, with skeletal magnetite inclusions highlighted in (c).

close (mm–cm) proximity to Cr-spinel seams. Chromitite seams have a higher abundance of sulphides than chain-textured Cr-spinel seams. Common sulphide phases include chalcopyrite ($CuFeS_2$), pentlandite (Fe,Ni_9S_8), chalcocite (Cu_2S), heazlewoodite (Ni_3S_2), with less common bornite (Cu_5FeS_4), pyrrhotite (FeS) and native copper. The sulphides typically occur on Cr-spinel crystal faces, or at the triple junctions of touching Cr-spinel crystals. Where base-metal sulphides are in contact with Cr-spinel, the latter displays alteration to sieve-textured ferrian chromite (Fig. 4.11h). Platinum-group minerals (PGM; e.g., sperrylite), with upper grainsize limits of ~1 µm, can also be observed, closely associated with the base-metal sulphides described above.

4.4.1.2 Upper Ard Mheall Member (UAM)

The texture of the UAM peridotites resembles the granular-textured peridotites in the AMP, but with key mineralogical variations. Olivine is the dominant cumulus phase, with sparse cumulus Cr-spinel (also occurs as rare inclusions in olivine). Olivine crystals are equant (typically <3 mm), with less common tabular and hopper crystal morphologies. Rare harrisite layers are dominated by cm-sized hopper olivine crystal morphologies, as observed in the AMP. The volume proportion of intercumulus material in the granular-textured peridotite is higher than in the AMP (i.e., 15–25 vol.%). The intercumulus mineralogy is dominated by plagioclase but clinopyroxene is more abundant (15–40 vol.%) than in the AMP. Intercumulus plagioclase oikocrysts are coarse-grained, typically >5 mm, with clinopyroxene oikocrysts typically in the size range 0.5–1 cm, occasionally up to ~3 cm. While plagioclase oikocrysts tend to be equant, clinopyroxene-oikocrysts are both equant and elongate. Patchy compositional zoning is present in both intercumulus phases. A foliation, defined by olivine crystals, is locally developed.

4.4.2 The Transitional Member

The cumulus mineralogy of harrisites in the TSM comprises coarse-grained, skeletal and bladed olivine crystals, up to several cm in size. Sparse euhedral Cr-spinel (<0.2 mm) crystals are present between olivine crystals. Inclusions (<0.1 mm) of Cr-spinel are also found rarely within olivine. The intercumulus volume proportion constitutes >30 vol.% of TSM harrisites and is sometimes as much as 40–50 vol.%. The intercumulus proportion is made of coarse-grained plagioclase and clinopyroxene oikocrysts, typically as rounded crystal forms (0.5–2 cm in diameter). Plagioclase is slightly more abundant than clinopyroxene, typically making up 50–60 vol.% of the intercumulus fraction. Patchy compositional zoning is present in both intercumulus phases (Fig. 4.13a, b).

Olivine in wehrlitic peridotites has a very similar texture to that observed in the AMP granular-textured peridotites. In particular, 0.5–3 mm-sized rounded–equant olivine crystals, with subordinate hopper crystals, are dominant. Olivine crystals are smaller in size (≤0.5 mm) near or within some Cr-spinel seams. Clinopyroxene crystals that are apparently cumulus also occur rarely in the wehrlitic peridotites, displaying weakly developed exsolution lamellae (Fig. 4.13c). The proportion of intercumulus material is >20 vol.%, with plagioclase and clinopyroxene again the dominant phases again. Plagioclase is slightly more abundant than clinopyroxene (approximate ratio of 60:40). Both occur as 0.5–2 cm rounded oikocrysts, with some more irregular, elongate clinopyroxene oikocrysts also present. Both intercumulus phases display patchy compositional zoning, more commonly in the clinopyroxene (Fig. 4.13b).

Feldspathic peridotite in the TSM is dominated by intercumulus plagioclase, comprising >50 vol.% of the rock. This rock only occurs in close proximity to Cr-spinel seams in the TSM (Fig. 4.13d). Olivine is the only cumulus mineral, with a tendency to form elongate, skeletal forms <1 cm in length (Fig. 4.13a). Fine-grained Cr-spinel is present outside the seams, distributed around olivine crystals. Plagioclase oikocrysts are rounded–elongate, and 1–5 mm in diameter, and display patchy, irregular optical zoning (Fig. 4.13a). Intercumulus clinopyroxene is rare (≤5 vol.%) and has a similar size range of sizes to plagioclase but exhibits more irregular–rounded crystal shapes. Serpentine, chlorite, epidote and particularly kaersutite are present in greater quantities than in the AMP (i.e., 1–3 vol.%) in all peridotite types in the TSM.

Cr-spinel seams are rare in the TSM but share similar characteristics to those found elsewhere in the WLI, except that oikocrystic clinopyroxene is more often present in the seams. Cr-spinel seams in the TSM have higher proportions of intercumulus material, notably where clinopyroxene is the primary intercumulus phase (Fig. 4.13e), and plagioclase is almost absent (<5 vol.%). Olivine crystals poikilitically enclosed in intercumulus clinopyroxene are often significantly smaller and more rounded than olivines outside of the oikocrysts (Fig. 4.13f) and can define zones within the oikocryst where the olivine crystals remain in optical continuity with each other (Fig. 4.13f). Cr-spinel crystals in seams in the TSM are largely subhedral–anhedral and are typically 0.05–0.4 mm in diameter. There are larger numbers of fine-grained crystals (~ 0.05 mm), particularly where poikilitically enclosed by clinopyroxene. Irregularly-shaped aggregates of Cr-spinel are common, though grain boundaries can be resolved in reflected light. Cr-spinel is commonly present in cumulus olivine embayments. Base-metal sulphide minerals are more common in the TSM than in the AMP (Fig. 4.13g), and comprise chalcopyrite, pentlandite and abundant pyrrhotite. The pentlandite has a lower Ni:Fe ratio than pentlandite in the AMP, with noticeably lower Ni contents (see Appendix 3.4). Sulphides are particularly abundant in feldspathic peridotites but are also common in harrisites and wehrlitic-peridotites (Fig. 4.13g). The sulphides are often attached to or close to Cr-spinel crystals. As before, alteration of the Cr-spinel where close to base-metal sulphide is ubiquitous (Fig. 4.13g).

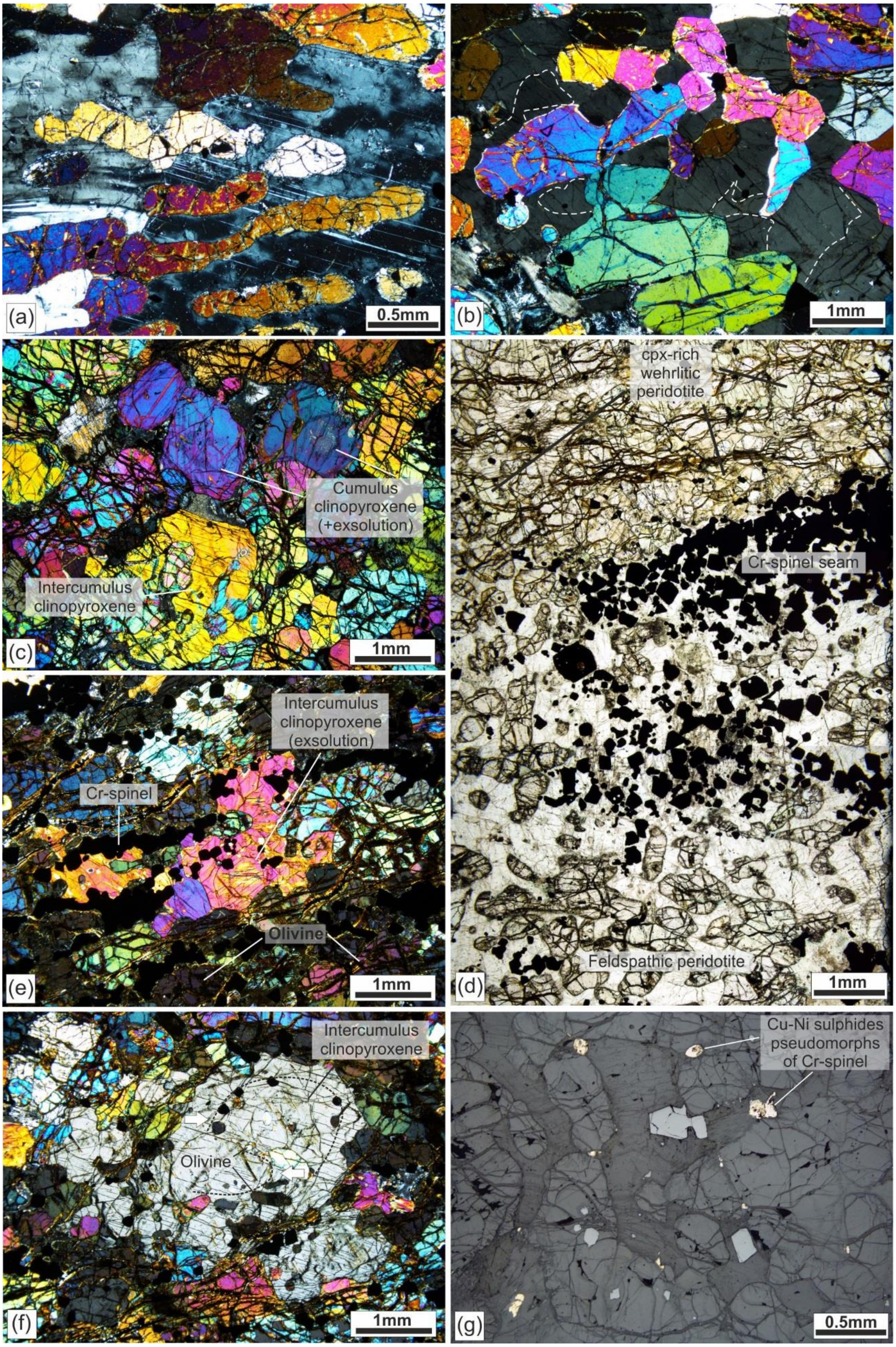
(a)
0.5mm
(b)
1mm
Cumulus clinopyroxene (+exsolution)
Intercumulus clinopyroxene
(c)
1mm
cpx-rich wehrlitic peridotite
Cr-spinel seam
Feldspathic peridotite
(d)
1mm
Intercumulus clinopyroxene (exsolution)
Cr-spinel
Olivine
(e)
1mm
Intercumulus clinopyroxene
Olivine
(f)
1mm
Cu-Ni sulphides pseudomorphs of Cr-spinel
(g)
0.5mm

◄FIGURE 4.13. Petrography of the TSM. (a) High abundance patchy zoning of intercumulus plagioclase, with highly skeletal, optically continuous harrisitic olivine. (b) Irregular zoning of clinopyroxene (outlined zones) (c) Cumulus and intercumulus (texture) clinopyroxene with exsolution lamellae. (d) Discontinuous Cr-spinel seam between wehrlitic and feldspathic peridotite. (e) Cr-spinel seam with intercumulus clinopyroxene, also displaying exsolution lamellae. Note the lack of plagioclase. (f) Large, intercumulus clinopyroxene with optically continuous, rounded olivine inclusions in circular arrangement. (g) Abundant sulphides, with spatially association with Cr-spinel and replacement texture in wehrlitic peridotite.

4.4.3 The Harris Bay Member

4.4.3.1 Peridotite

The cumulus mineralogy of harrisite in the HBM comprises olivine and plagioclase. Olivine typically occurs as coarse-grained (up to ~1 m long, in some cases, more commonly ~50 cm), skeletal and bladed crystals that do not appear to show any preferred orientation (Fig. 4.14a). Plagioclase also occurs as a cumulus phase, though rarely. Cumulus plagioclase crystals are coarse-grained (1–5 mm), euhedral–subhedral tabular crystals that commonly display optical zonation, including oscillatory zoning (Fig. 4.14b). Intercumulus plagioclase is abundant in harrisite occuring as anhedral oikocrysts, ~1–5 mm in diameter, though some larger (up to 10 mm) oikocrysts are also present. It sometimes displays optical zoning, though less common than in cumulus plagioclase, and is not observed as frequently as in the AMP and TSM. Intercumulus clinopyroxene comprises ~30–40 vol.% of the total intercumulus fraction, with very coarse ~5–20 mm, anhedral oikocrysts that locally display strong, patchy textures and zoning (e.g., Fig. 4.14c). Disseminated Cr-spinel crystals (<0.2 mm grainsize) occur throughout the harrisites, in the interstices of the silicate framework (i.e., hosted in intercumulus phases). Phlogopite and calcic amphibole are also present in quantities ranging between 1–3 vol.%, as well as occasional serpentine, chlorite, calcite and sparse apatite. Where present, the amphibole can also exhibit complex optical zoning (Fig. 4.14d).

Granular-textured peridotites in the HBM have mineral modes similar to those recorded in harrisite, though olivine is not as coarse-grained or skeletal (typically <5 mm), and the overall grainsize of plagioclase is also smaller (i.e., <2 mm). Olivine is ubiquitously cumulus, while plagioclase is intercumulus and rarely cumulus. Granular-textured peridotites in the HBM are often wehrlitic. Plagioclase (cumulus and intercumulus) and intercumulus clinopyroxene exhibit compositional zoning. Cr-spinel and magnetite are present as <0.2 mm euhedral–subhedral crystals, typically found in the interstices of the olivine framework but also as rare inclusions in olivine.

Slightly higher than trace abundances (typically 1–3 vol.%) of phlogopite, amphibole, serpentine, chlorite, calcite and apatite are also present.

4.4.3.2 Gabbro

The olivine-gabbros in the HBM contain olivine, plagioclase and clinopyroxene. There is significant variation in the textures between the melagabbros, olivine gabbros, and leucogabbros, although the textural configuration of olivine, plagioclase, and clinopyroxene is broadly the same in all gabbro types. In the melagabbros, olivine makes up ≤15 vol.% of the mineralogy, and exhibits distinctly anhedral, morphologies (0.25–3 mm in length). Olivine is often severely altered to serpentine and fine-grained iddingsite-chlorite mixtures. Plagioclase is abundant (>60 vol.%) and exhibits subhedral crystal shapes and crystal sizes ranging from 0.5–3 mm. Compositional zonation is ubiquitous in plagioclase, with oscillatory zoning rarely observed. Clinopyroxene is also abundant, as cumulus crystals ~2–3 mm in diameter and mm to cm-sized oikocrysts. Both intercumulus and cumulus pyroxenes are commonly zoned, with distinctly ‘spongy’ rims present on some cumulus crystals (Fig. 4.14g). The olivine-gabbro is mineralogically like the melagabbro, but exhibits a finer-grained texture, with olivine (<1 mm), plagioclase (<2 mm) and clinopyroxene (<3 mm) crystals all consistently smaller. Olivine and clinopyroxene are less abundant than in melagabbro, <10 vol.%, and <25 vol.%, respectively. Optical zoning is present in both plagioclase and clinopyroxene as in the melagabbros (Fig. 4.14e, g). Spinel (mostly magnetite) in the gabbros exhibits highly skeletal morphologies, forming elongated needles and blades (Fig. 4.14h). The leucogabbros are finer grained than the other gabbro types with olivine, plagioclase, and clinopyroxene having grainsizes ≤1 mm. Plagioclase is ubiquitously altered, exhibiting a ‘dusty’ appearance as a result of saussuritization (Fig. 4.14f). Olivine comprises <5 vol.% in the leucogabbros and is typically highly altered to iddingsite-chlorite mixtures. Clinopyroxene is cumulus in appearance, less altered than plagioclase and typically <1 mm in diameter. Cumulus crystals, and rarer intercumulus crystals, of perthitic alkali-feldspar (orthoclase) are present (Fig. 4.14f). Pockets of quartz are also found within the leucogabbros. Base metal sulphides (e.g., chalcopyrite and pyrrhotite) are also observed in close spatial association with spinel in all three gabbro types.

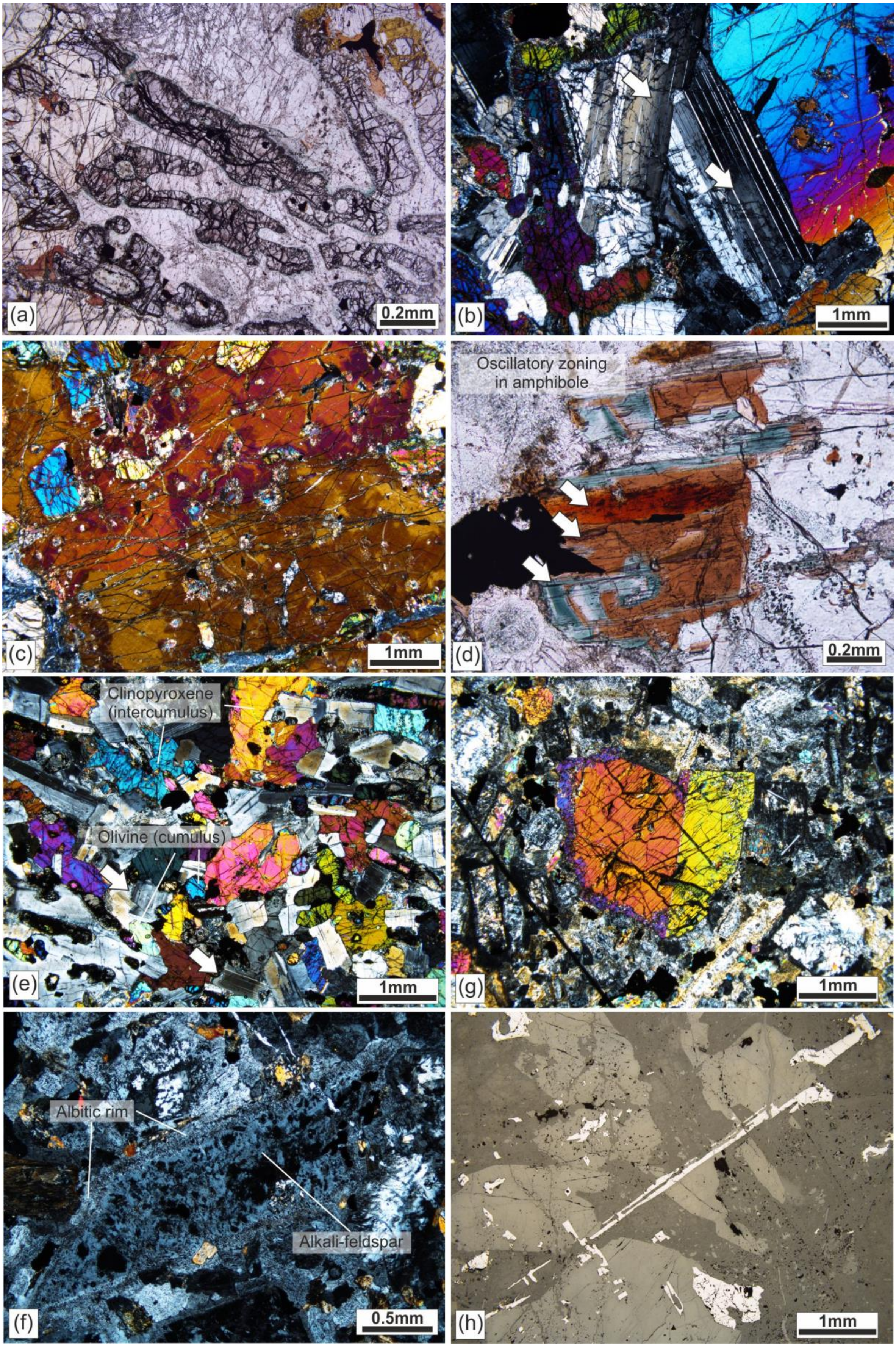
(a)
0.2mm
(b)
1mm
(c)
1mm
Oscillatory zoning in amphibole
(d)
0.2mm
Clinopyroxene (intercumulus)
Olivine (cumulus)
(e)
1mm
(g)
1mm
Albitic rim
Alkali-feldspar
(f)
0.5mm
(h)
1mm

◄FIGURE 4.14: Petrography of the HBM. (a) Thin skeletal olivine typical in the HBM. (b) Cumulus appearing zoned plagioclase (arrowed). (c) Extremely irregular zoning in coarse clinopyroxene oikocryst. (d) Oscillatory zoned amphibole with varying pleochroic rims (arrowed). (e) Typical gabbro from the HBM, with rounded cumulus olivine and abundant intercumulus pyroxene. Note the zoning in plagioclase (arrowed). (f) Cumulus (appearing) alkali-feldspar (orthoclase) with abundant albitic perthites and rim. (g) Simple twined clinopyroxene phenocryst with spongey outer rim of clinopyroxene. (h) Highly skeletal spinel (magnetite–Cr-magnetite) from HBM gabbro in reflected light.

4.5 QUANTITATIVE TEXTURAL ANALYSIS

4.5.1 Crystal Size Distribution Analysis (CSDs)

4.5.1.1 Method

Crystal Size Distribution (CSD) analysis provides a method to study the kinematics of crystal nucleation and growth in rocks, independent of experimental or thermodynamic methods (Cashman & Marsh, 1988; Marsh, 1998; Boorman *et al*., 2004). Simple crystallisation in open (steady-state)- or closed (batch)- magma system end-members should produce a straight (log-linear) CSD profile that reflects increasing nucleation of crystals as the magma solidifies (Marsh, 1998). Deviation from an ideal log-linear profile (e.g., kinking or curvature) has been attributed to a variety of magmatic processes such as crystal accumulation or removal (Marsh, 1998), coexistence of more than one crystal population (i.e., in crystal cargos or slurries; Higgins, 1994; Marsh, 1998), and post-cumulus processes such as crystal annealing, coarsening (e.g., Ostwald ripening) or physical compaction of crystal mushes (Higgins, 2002b; Boorman *et al*., 2004). Recent numerical modelling of crystal nucleation and the resultant CSDs by Špillar & Dolejš (2014) suggests that log-linear to concave-down profiles, the latter often proposed to be caused by crystal coarsening, can be formed by variable growth and nucleation rates. Concave-up CSD profiles, often attributed to be the result of mixing populations or crystal accumulation, can be produced by heterogeneous nucleation (Špillar & Dolejš, 2015a). CSD parameters such as characteristic length and intercept have been shown to share a relationship irrespective of the volume percentage of the mineral phase analysed (Higgins, 2002a). The consideration of closure in CSDs can reveal important information on the quality of CSD calculations and the degrees of freedom available to interpret CSD data; i.e., samples which are close to or on the closure limit cannot have undergone processes that significantly alter the volumetric phase proportions from one sample to the next, such as textural coarsening (Higgins, 2002a).

Conversely, if a population does not come close to its closure limits, more freedom to interpret changes in the volumetric abundance exists (Higgins, 2002a).

The CSDs reported in this study were determined from polished thin-sections and calculated following the approach of Higgins (2000; using *CSDCorrections version 1.4*). Cr-spinel and olivine crystals were manually digitised using reflected and cross-polarised light, respectively. Reflected light images were used for Cr-spinel to avoid misidentification of annealed opaque crystals in transmitted light (see O'Driscoll *et al*., 2010; Vukmanovic *et al*., 2013). The digitised images were then processed using *ImageJ* image analysis software to calculate the input parameters for *CSDCorrections*. For Cr-spinel in this study, 'feret-length', the length of a square with an area equal to the analysed crystal, is employed as the main size parameter, following O'Driscoll *et al*. (2010). No alignment of Cr-spinel is observed in any of the samples (i.e., a 'massive' fabric setting was used). An aspect ratio of 1:1:1 and roundness factor of 0.5 were input into *CSDCorrections*. In total, 37 CSDs were produced from various WLI Cr-spinel seams (see Fig. 4.15), covering the range of different Cr-spinel seam textural types described above. Data were produced for a minimum of 500 crystals in each sample, where possible, to produce a statistically robust representation of each seam (Mock & Jerram, 2005). As the smallest crystals are easily distinguishable using reflected light, the lower crystal size limit is taken as the true lower limit of the sample. The quantification of crystallinity used in some CSD derivative plots was calculated using *ImageJ*, with the R-value calculated within *CSDCorrections version 1.4* (see. Jerram *et al*., 1996; Higgins, 2006).

4.5.1.2 Results

The CSD plots are presented in Figure 3.15, with the raw CSD output data provided in Appendix 3.3. The different groupings of Cr-spinel seams established based on petrographic observations are generally not distinguishable in the CSD dataset. All CSDs display a log-linear profile at larger size portions, with deviation in some profiles at smaller size fractions, and reveal a range of slope values from -38.0 to -6.4 mm^{-1}. Granular-textured and boundary-type Cr-spinel seams (Figs. 4.15a, b) have very similar slope values (-37.8 to 17.1 mm^{-1}). Harrisite-hosted Cr-spinel seams have shallow CSD slopes (Fig. 4.15c) but can be distinguished based on the dominant olivine morphology of the host.

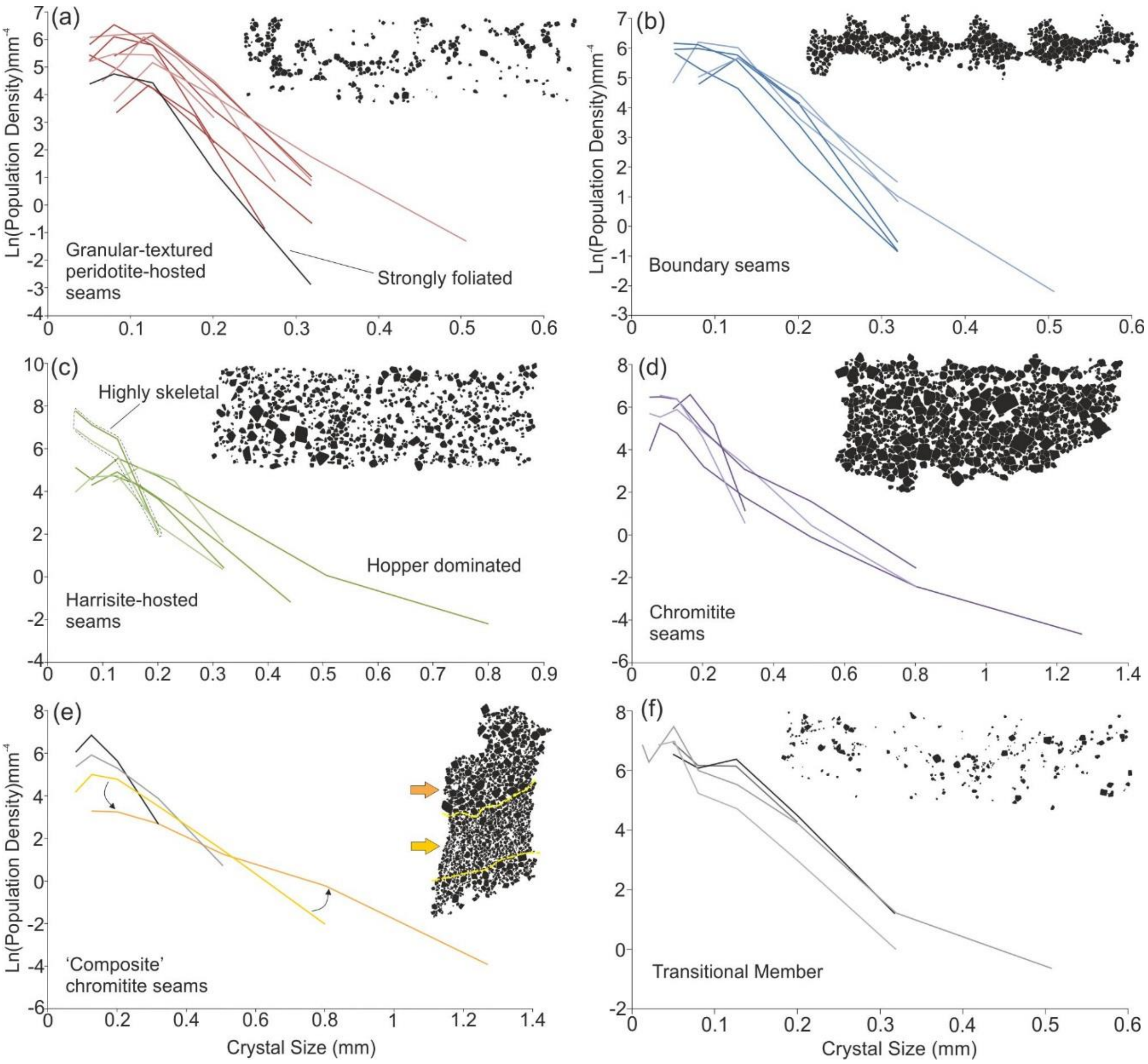

FIGURE 4.15: CSD profiles of Cr-spinel seams from the AMP and TSM of Cr-spinel types in this study, with representative texture maps of the seam-groups defined in this paper. Output data can be found in Appendix 3.3.

Specifically, skeletal olivine-dominated harrisite-hosted Cr-spinel seams have slope values between -38.0 and -32.0 mm^{-1}, whereas hopper olivine-dominated harrisite-hosted Cr-spinel have shallower slope values between -26.6 to -11.8 mm^{-1}. Chromitite seams have the shallowest slopes (i.e., ≤ -14 mm^{-1}; Fig. 4.15d). Composite chromitite seams display variable CSD profiles across the different textural zones, where coarser-grained zones have distinctly shallower slopes than the central finer-grained zone (Fig. 4.15e). Downturns at the smallest size fractions are observed in CSDs from Cr-spinel seam types, except for harrisite-hosted seams, in which the downturn is absent in skeletal olivine-dominated harrisite-hosted seams, but present in hopper olivine-dominated harrisite-hosted seams (Fig. 4.15c). Foliated peridotite-hosted seams have a distinctive CSD profile similar to those reported for the Unit 10 peridotite (Hepworth *et al*., 2017). They display a log-linear profile at the largest size portions but have a broadly ‘humped’ profile at the small size fraction. The TSM Cr-spinel seam CSD profiles show similar patterns to those in the AMP (Fig. 4.15f), with log-linear profiles at larger size portions, and some downturns at smaller size fractions. The data from the TSM and AMP show a comparatively restricted range of slope values between -16.3 and -24.1 mm^{-1}, which mainly represent the large size fractions of the CSDs. The TSM CSDs exhibit slightly higher population densities and complex profile shapes at the smaller size fractions, than the AMP (Fig. 4.15f)

CSD derivative diagrams can be found in Appendix 3.3, with selected plots illustrated in Figure 4.17. A characteristic length (CL) versus volumetric proportion plot distinguishes some of the Cr-spinel seam as outlined previously (Fig. 4.16a), such as the chromitite seam group, which plot with distinctly higher CL and a relatively high-volume proportion of Cr-spinel, and a harrisitic peridotite-hosted Cr-spinel seam outlier. The other seam groups cluster closely together with low CL and volumetric abundance. The volume percentage of Cr-spinel (calculated in *ImageJ*) was plotted against the crystallinity of each sample (vol.% olivine – assumed to be pre-existing; see Hepworth *et al*., 2017), with a good negative correlation ($R^2 = 0.77$; Fig. 4.16b) suggesting a correlation between the availability of space in the crystal framework and Cr-spinel abundance. Most samples plot well below the closure limits defined by 100% volumetric abundance. Spatial Distribution parameters, such as R-value (which quantifies the degree of clustering versus ordering of a grain population; see Jerram *et al*., 1996; 2003; Špillar & Dolejš, 2014; 2015a), plotted against the vol. % Cr-spinel reveal a strong positive correlation ($R^2 = 0.83$; Fig. 4.16c). Furthermore, an increase in crystallinity results in a moderate negative correlation with R-value (Fig. 4.16d), also highlighting a relationship between clustering, Cr-spinel abundance, and available space within the crystal mush (i.e., more Cr-spinel forms where more space is available).

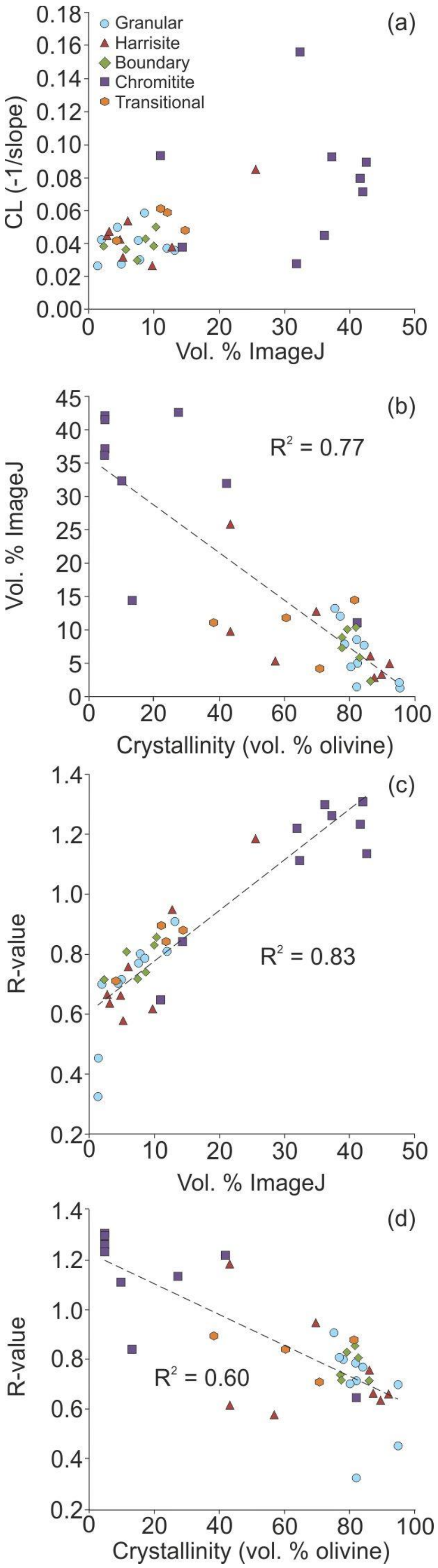

FIGURE 4.16: Selected CSD derivative plots for Cr-spinel seams in this study. (a) Characteristic length (CL) versus volumetric percentage. Note the separation of the chromitite seams. (b) Negative correlation ($R^2 = 0.77$) of volumetric percentage of Cr-spinel versus crystallinity for Cr-spinel seams with a similar separation of chromitite as in (a). (c) Good correlation between the vol.% abundance of Cr-spinel and R-value. (d) Correlation between crystallinity (vol. % olivine) and R-value, suggesting a strong relationship with available space and crystallisation of Cr-spinel

4.6 MINERAL CHEMISTRY

4.6.1 Methods

Mineral chemical data were obtained using a JEOL JXA-8900RL electron microprobe at the Department of Geochemistry, Geowissenschaftliches Zentrum der Universität Göttingen (GZG) in 2014 and 2015. The Cr-spinel compositions were obtained using an acceleration voltage of 20 kV with a beam current of ~20 nA and a typical beam diameter of 1 μm. Cr-spinel count times on peak and background for Mg, Al, Cr, Fe and Si were 15 s and 5 s, respectively, and for V, Ti, Mn, Ni and Zn were 30 s and 15 s, respectively. Plagioclase compositions were obtained with an acceleration voltage of 15 kV with a beam current of ~15 nA and a typical beam diameter of 20 µm. Plagioclase count times on peak and background for Si, Na, K, Ca, Fe and Al were 15 s and 5 s, respectively, and for Ba and Sr, were 30 s and 15 s, respectively. Clinopyroxene compositions were obtained with an acceleration voltage of 15 kV with a beam current of 15 nA and a typical beam diameter of 15 µm. Clinopyroxene count times on peak and background for Si, Na, K, Ti, Fe, Al, Mg, Ca and Mn were 15 s and 5 s, respectively, and for Cr and Ni, were 30 s and 15 s, respectively. The ferric iron content of Cr-spinel in this study was calculated following Droop (1987), assuming the spinel composition to be stoichiometric. Thus, small variations in ferric iron content of Cr-spinel should be treated with caution (Quintiliani *et al*., 2006; O'Driscoll *et al*., 2010).

Cr-spinel compositions in eighteen different seams from the AMP (16) and TSM (2) were measured in two vertical traverses across each seam, each traverse consisting of ~20 points and extending into the host peridotite above and below. In the HBM and UAM where no Cr-spinel seams occur, disseminated Cr-spinel crystals were analysed. Plagioclase and clinopyroxene mineral chemical data from the AMP, UAM, TSM, and HBM were obtained from selected samples where optically zoned and unzoned crystals were observed, to evaluate the maximum range of compositions of these phases present in the WLI. A minimum of one rim and one core was analysed per zoned crystal in each case, with unzoned crystals analysed as well. Mineral chemical analyses of plagioclase and clinopyroxene from the AMP (Worrell, 2002) have been plotted with the new data, for comparison.

4.6.2 Results

The full mineral chemical dataset discussed below can be accessed in Appendix 3.4.

4.6.2.1 Cr-spinel

The composition of Cr-spinel in the AMP is highly variable, with some of the most aluminous Cr-spinel yet documented from the RLS (up to 39 wt.% Al_2O_3; Cr# [$Cr^{3+}/(Cr^{3+}/Al^{3+})$] 0.29). Accessory Cr-spinel disseminated throughout the AMP peridotites typically has typically higher Cr# and lower Mg# [$Mg^{2+}/(Mg^{2+}/Fe^{2+})$] than Cr-spinel that occurs within seams, the latter corresponding to higher Al_2O_3 and MgO values (Figs. 4.17a). There is significant overlap in the Cr-spinel chemistry of boundary and granular-textured peridotite-hosted Cr-spinel seams. However, the chromitite seams have distinctly low Cr# and high Mg# (Fig. 4.18a). Some compositional variation is also present in harrisite-hosted Cr-spinel seams, where Cr-spinel has consistently higher Fe_2O_3 contents (~17.7 wt. %; Fig. 4.18) and elevated TiO_2 concentrations (typically ~3 wt. %, and as high at 7 wt. %; Fig. 4.17b). It is noteworthy that the Cr content of the Cr-spinel does not vary substantially between the different seam types (overall range is 34 to 38 wt.%; Fig. 4.18). Vertical traverses of Cr-spinel seams of all types reveals consistent variations in Cr# (and Mg#), Fe_2O_3 and TiO_2. Specifically, Cr# and Mg# typically increase towards the centres of Cr-spinel seams, while Fe_2O_3 increases towards seam margins (AM6; Fig. 4.20). In most seams, TiO_2 is constant throughout, except at the outer margins where it increases sharply (AM18; Fig. 4.20). Chromitite seams display constant Cr-spinel compositions within the seam, but these usually change dramatically above and below the seam (AM18; Fig. 4.20). In one relatively thick, texturally composite chromitite seam (AM18; Fig. 4.19), TiO_2 concentration remains constant, except at the internal textural boundary, across which a step-change of ~0.5 wt.% TiO_2 occurs (AM18; Fig. 4.19). Compositional zoning of coarse-grained Cr-spinel crystals occurs locally in some chromitite seams, e.g., in sample AM18 (Fig. 4.20) which exhibits an increase in TiO_2 and Fe_2O_3 towards the rim of the crystal.

The composition of Cr-spinel from the UAM shows modest differences to that in the AMP, with slightly elevated Cr# and lower Mg# (Fig. 4.17a). The ferric iron content of UAM Cr-spinel is higher, up to 19 wt. % (Fig. 4.18), whilst TiO_2 is similar to that in the AMP. Cr-spinel in the TSM exhibits

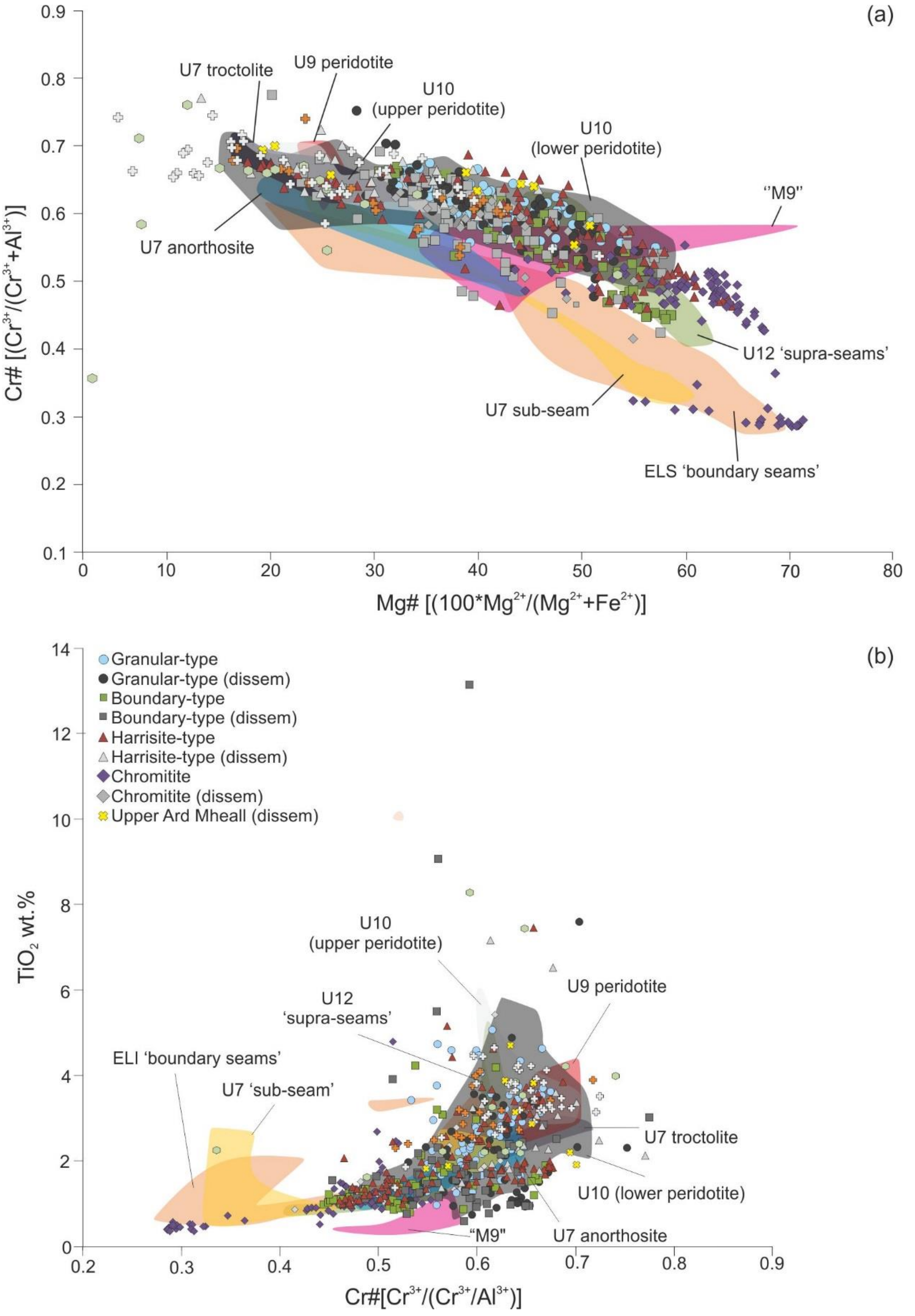

FIGURE 4.17: (a) Mg# vs Cr# and (b) Cr# vs TiO_2 wt. % plot for Cr-spinel seams from the WLI, including reference Cr-spinel from across the RLS. Unit 7, 8, 11, 12 data from O'Driscoll *et al.* (2009a; 2010). Unit 9 data from Holness *et al.* (2007), Unit 10 data from Hepworth *et al.* (2017), and M9 picrite dyke of Upton *et al.* (2002) from O'Driscoll *et al.* (2009a).

distinctly lower Mg# and higher Cr# values than the AMP, with disseminated Cr-spinel displaying some of the lowest Mg# values in the WLI (Figs. 4.17a, 4.18). The ferric iron content of Cr-spinel is considerably higher in the TSM, with Fe_2O_3 contents ~28 wt. %, and TiO_2 also consistently relatively high (~3 wt. %; Fig. 4.17b). Vertical traverses through Cr-spinel seams reveal similar trends to those observed in the AMP, with a broadly symmetrical pattern through the Cr-spinel seam with increasing Fe_2O_3 and Cr# towards the edges of and outside seams. However, TiO_2 contents remains comparatively constant through the seam traverse, increasing sharply into the overlying peridotite (TM1; Fig. 4.19). The TiO_2 content of all Cr-spinel in the TSM traverse is elevated compared to AMP traverses (~4 wt.%). Another traverse through a diffuse Cr-spinel seam in the TSM shows a broadly similar pattern to TM1 (Fig. 4.19) with an over-all TiO_2 enrichment, but a notable sharp increase crossing into wehrlitic peridotite. (see Appendix 3.4).

Cr-spinel in the HBM is disseminated throughout both peridotites and gabbros and no seams are present. The Cr-spinels generally have high Cr# and very low Mg# (Fig. 4.19), and exhibit significant Fe-enrichment, particularly Fe_2O_3, with values as high as 66% wt. %. The HBM Cr-spinels are poor in Al_2O_3, so overall, they are best classified as ferrian-chromite–Cr-magnetite (Fig. 4.18). Like the disseminated Cr-spinel in the other members of the WLI, TiO_2 is relatively elevated (>3 wt. %; Fig. 4.17b).

4.6.2.2 Clinopyroxene

Clinopyroxene in the AMP is predominantly diopside, with a limited Mg# range (84–90). Cr_2O_3 contents are typically ~1 wt. %, with TiO_2 consistently >1 wt.% (Figs. 4.21a, b). There is no correlation between Cr_2O_3 or TiO_2 with Mg#; instead a largely scattered array is observed that corresponds well to the data reported by Worrell (2002). Clinopyroxene oikocrysts in the UAM ubiquitously exhibit chemical zoning. Weak normal zoning with respect to Cr_2O_3 is observed, with rims containing lower values. TiO_2 content also varies significantly between the cores and rims of UAM oikocrysts, with the cores characterised by lower (<0.5 wt.%) contents, whilst the rims have similar values (~1 wt.%) to the unzoned clinopyroxene of the AMP (Fig. 4.21b).

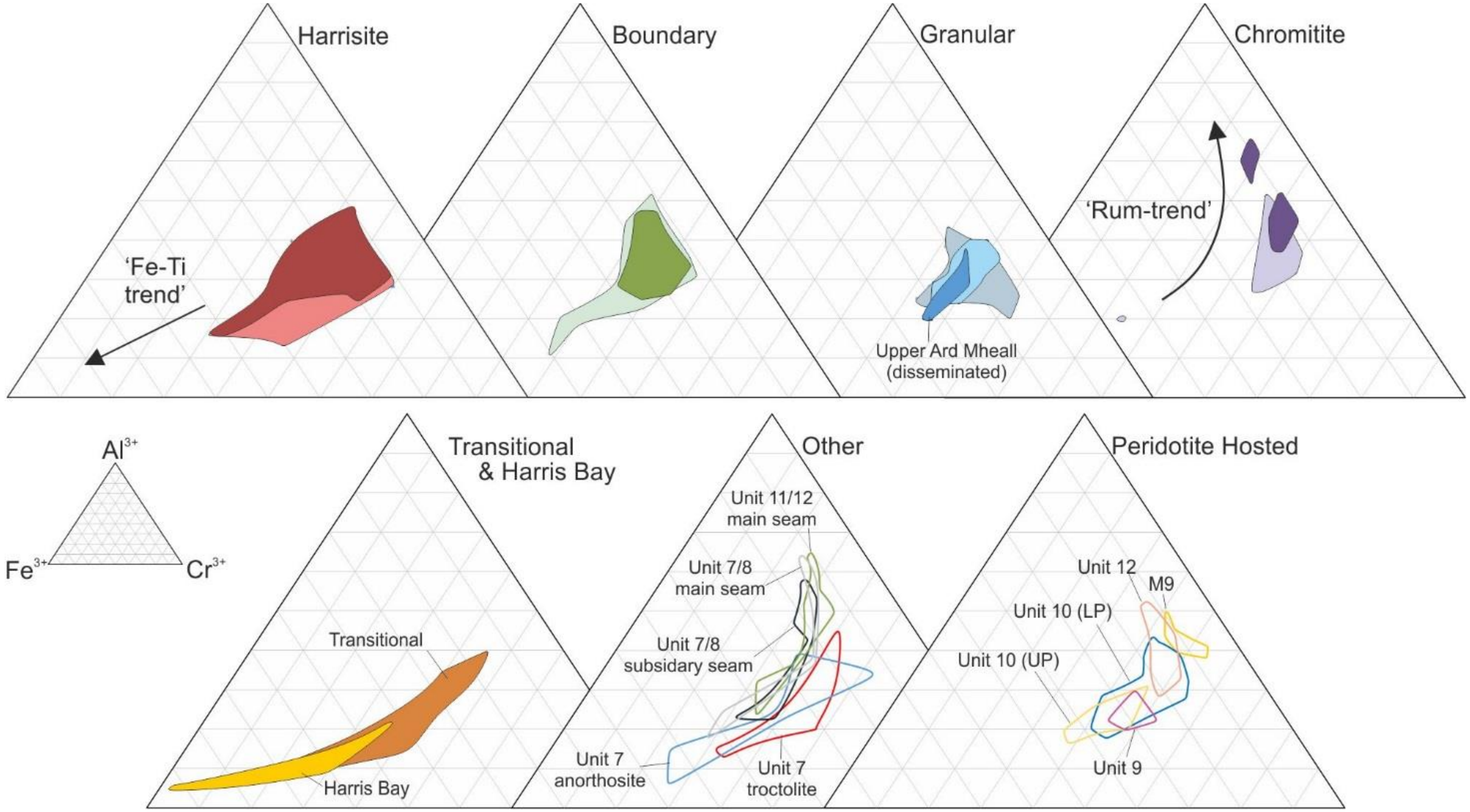
Harrisite
'Fe-Ti trend'
Boundary
Granular
Upper Ard Mheall (disseminated)
Chromitite
'Rum-trend'
Al^{3+}
Fe^{3+}
Cr^{3+}
Transitional & Harris Bay
Transitional
Harris Bay
Other
Unit 11/12 main seam
Unit 7/8 main seam
Unit 7/8 subsidary seam
Unit 7 anorthosite
Unit 7 troctolite
Peridotite Hosted
Unit 12
M9
Unit 10 (LP)
Unit 10 (UP)
Unit 9

◄FIGURE 4.18. Trivalent ternary plots for Cr-spinel from the WLI. Peridotite-hosted and other Cr-spinel seam data have been added for reference. Unit 7, 8, 11, 12 data from O'Driscoll *et al.* (2009a; 2010). Unit 9 data from Holness *et al.* (2007), Unit 10 data from Hepworth *et al.* (2017), and M9 picrite dyke of Upton *et al.* (2002) from O'Driscoll *et al.* (2009a).

Clinopyroxene in the TSM is also diopside, with lower Mg# (~83) than in the AMP. Normal zoning is rarely apparent, but where present is characterised by the variation of TiO_2 contents from cores to rims of ~0.5 to ~1 wt. %, respectively, up to a maximum rim value of ~1.8 wt. % (Fig. 4.21b). Clinopyroxene in the TSM is unzoned with respect to Cr_2O_3 content and reveals a scattered array of values between 0.72–1.19 wt.% (Fig. 4.21a). There is a weak positive correlation between Cr_2O_3 and Mg#, and a weak negative correlation with TiO_2 and Mg# (Fig. 4.21b).

Clinopyroxene in the HBM has a similar composition to that of the overlying members, but is most like clinopyroxene of the TSM, with relatively low Mg# and with similar trends in TiO_2 and Cr_2O_3 to the TSM (Figs. 4.21a, b). Clinopyroxene crystals in the HBM are abundantly and strongly normally-zoned with variation observed in both Cr_2O_3 and TiO_2 contents. The highest TiO_2, and thelowest Cr_2O_3 contents are measured in the rims. Mg# and TiO_2 are negatively correlated in HBM clinopyroxene, as also observed in the TSM (Fig. 4.21b).

4.6.2.3 Plagioclase

Plagioclase oikocrysts from the UAM consistently have a slightly lower An-content (~81 mol. %) and higher FeO contents (up to ~0.5 wt. %) than those in the AMP (Worrell, 2002; Fig. 4.21c). Plagioclase zoning is present, with lower An contents (~70 mol.%) measured.

Plagioclase in the TSM is typically normally zoned, though oscillatory zoning and reverse zoning are also present (Fig. 4.21c). Plagioclase cores have average An-contents ~84 ±2 mol. %, as in the AMP, while the rims are less calcic (~66 ±3 mol.%). The FeO content of plagioclase in the TSM is elevated (typically >0.4 wt.%) compared to plagioclase in the AMP (Worrell, 2002; Fig. 4.21c).

Plagioclase oikocrysts in one harrisite sample in the HBM are normally and oscillatory zoned. The An-content of cores is comparable to the other WLI members, with high anorthite values between 72–86 mol.%. Normally zoned rims have among the lowest An-contents (~56 mol.%) in the WLI.

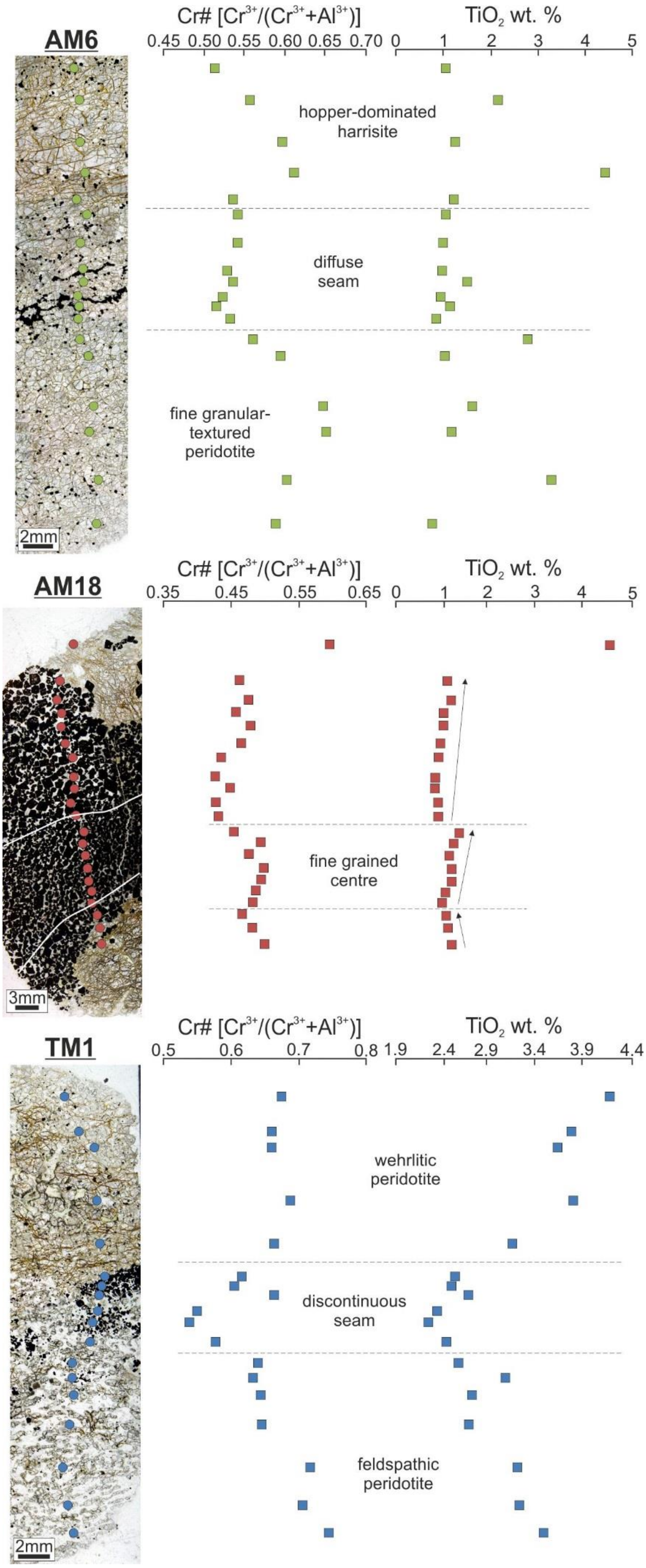
AM6
Cr# [Cr3+/(Cr3++Al3+)]
0.45 0.50 0.55 0.60 0.65 0.70
TiO2 wt. %
0 1 2 3 4 5
hopper-dominated harrisite
diffuse seam
fine granular-textured peridotite
2mm
AM18
Cr# [Cr3+/(Cr3++Al3+)]
0.35 0.45 0.55 0.65
TiO2 wt. %
0 1 2 3 4 5
fine grained centre
3mm
TM1
Cr# [Cr3+/(Cr3++Al3+)]
0.5 0.6 0.7 0.8
TiO2 wt. %
1.9 2.4 2.9 3.4 3.9 4.4
wehrlitic peridotite
discontinuous seam
feldspathic peridotite
2mm

◀FIGURE 4.19: Cr-spinel seam traverses through Cr-spinel seams from the WLI. AM6 is a diffuse, boundary-type seam, AM18 is a composite chromitite seam from the AMP, while TM1 is a laterally discontinuous Cr-spinel seam from the TSM. Note the mirrored trends in AM6 and TM1 on either side of the seam, with enhanced TiO_2 contents in TM1. Note also the kinks in a stable composition through AM18 (arrowed) where textural changes are observed (highlighted), with another potential kink within AM6 seam, where the Cr-spinel becomes more diffuse.

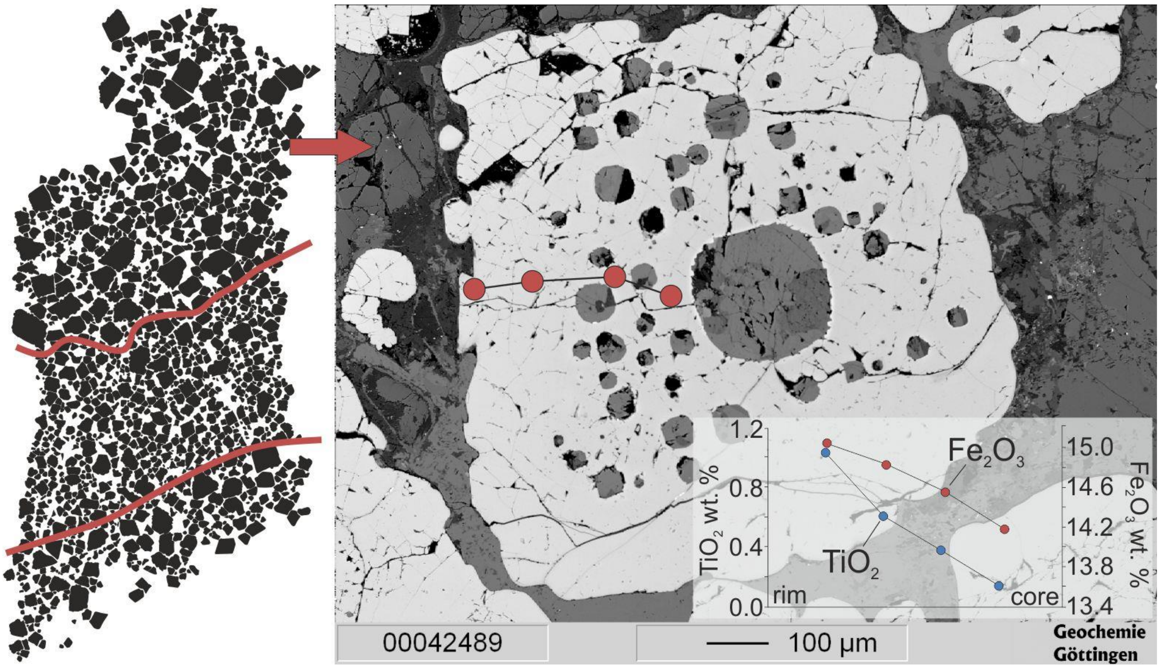

FIGURE 4.20: Single crystal traverse of Cr-spinel from coarse textural zone in composite chromitite seam (arrowed) in sample AM18, showing increases in TiO_2 and Fe_2O_3 towards the lobate rim. Note also the abundance of rounded inclusions (typically with amphibole, plagioclase ± sulphide) in the core.

The FeO content of all plagioclase is elevated (>0.3 wt.%) in comparison to the AMP, overlapping with the UAM and TSM.

4.7 DISCUSSION

4.7.1 Sill emplacement and Cr-spinel seam petrogenesis in the Western Layered Intrusion

4.7.1.1 Sill emplacement of harrisite

Harrisite is a type example of ‘crescumulate’, as defined by Wager *et al* (1960). These authors envisaged harrisitic olivine as having grown upwards from the magma chamber floor, so this texture also represents a key example of *in situ* crystallisation in layered intrusions. The presence of numerous harrisite layers throughout the WLI has been cited as evidence for multiple replenishment events in the WLI, with each harrisite taken as representative of a discrete influx of picritic magma (Wadsworth, 1961; O'Driscoll *et al*., 2007a). These studies considered magma replenishment to have occurred at the magma chamber floor, where the undercooled picrite crystallised harrisitic olivine on the substrate. The replenishment events were thought to have been separated by periods of crystal settling and density current (slurries) deposition, to produce the granular-textured peridotites (Worrell, 2002; O'Driscoll *et al*., 2007a). Donaldson (1981) pointed out that harrisite layers in the WLI locally terminate laterally and bifurcate and suggested that at least some harrisite could therefore form within the crystal mush from expelled intercumulus liquid. A similar idea was recently invoked for the Unit 10 peridotite of the ELI, where harrisite bodies with irregular contacts (e.g., apophyses on their upper surfaces) were highlighted as evidence for an intrusive origin (Hepworth *et al*., 2017). The latter authors suggested that harrisite bodies in Unit 10 represent apparently randomly distributed, sill-like intrusions of picrite. Harrisite layers from the WLI bear striking similarities to those in the Unit 10 peridotite, but with some important differences. In the HBM, the intercalation of harrisite bodies comprising single or multiple layers (Figs. 4.9a, b, c, d) into the Western Granite, strongly suggests sill emplacement of harrisite in WLI. The outcrop-scale features described by Donaldson (1982) and Hepworth *et al.* (2017) are observed ubiquitously in the WLI harrisite layers, such as bifurcation (Fig. 4.4a), and upward-oriented apophyses (Fig. 4.4c), including rarer undercutting apophyses (Fig. 4.4d). Harrisite apophyses in the WLI protrude into the overlying cumulate as dome-like structures, <1 m vertically, but over several metres laterally. Upward-oriented apophyses emanating from some WLI harrisite bodies can be several metres high and over a metre wide, forming 'harrisite columns' which cross-cut and deflect the layering in the host granular-textured peridotite (Fig. 4.4e). The texture of the harrisite, including olivine morphology and grainsize, the proportion of intercumulus material and overall mineral mode is unchanged from the layer to the apophyses (including the downward oriented apophyses), so the apophyses are considered to represent a primary magmatic feature, and not the result of late-stage filter-pressing of intercumulus liquid (Donaldson, 1982). Collectively, these observations point strongly to an intrusive origin, as sill-like bodies, for most if not all the harrisites in the WLI. The distribution of harrisite layers through the WLI appears random, with very little internal lateral correlation possible within

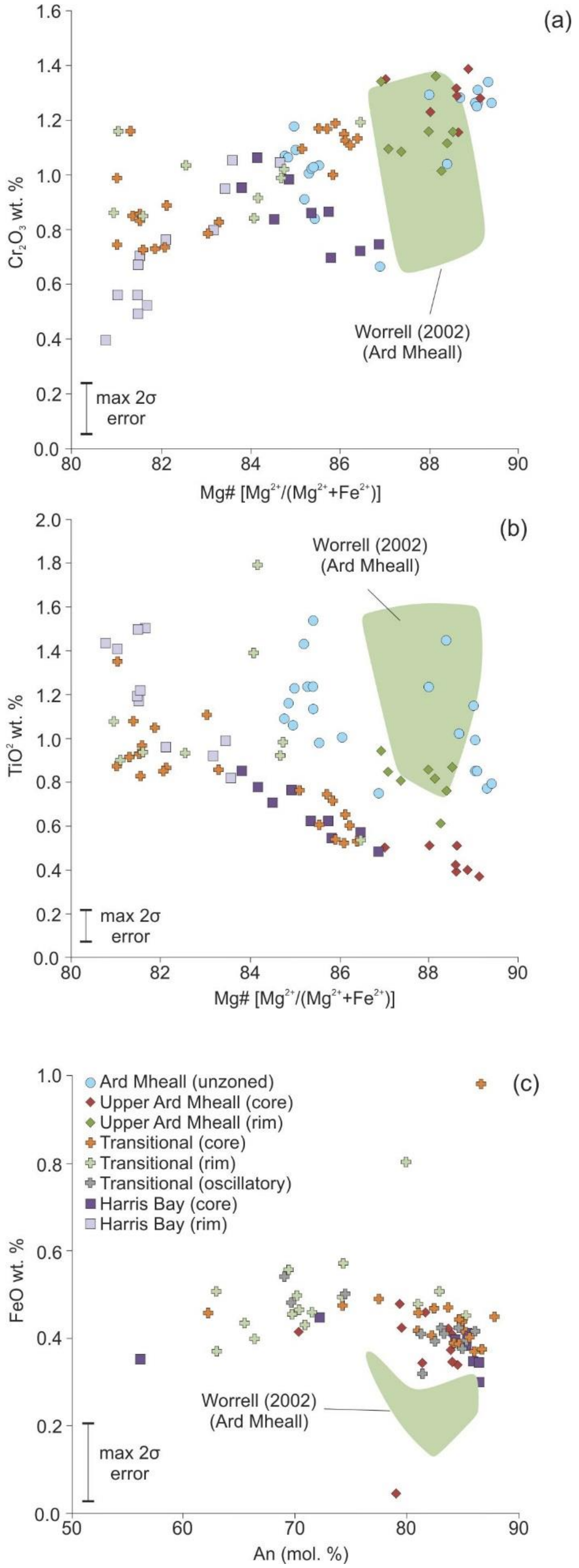

FIGURE 4.21: Clinopyroxene and plagioclase mineral chemistry from the WLI. (a) Cr_2O_3 wt. % versus Mg# plot for clinopyroxene. (b) TiO_2 versus Mg# plot for clinopyroxene. (c) FeO wt.% versus anorthite mol. % plot for plagioclase. Data from Worrell (2002) has been added for comparison. See text for discussion.

the different members of the intrusion (see Appendix 3.2). The source of most of the picrite (to form harrisite) is postulated to be the LLF to the east of the WLI (Fig. 4.1), in agreement with Emeleus *et al*. (1996). However, the observation that harrisite bodies form vertically-oriented domes and column-like structures, deforming the layering in the cumulate that they intrude (Figs. 4.4e), suggests that at least some harrisite could be linked to sub-vertically oriented syn-magmatic conduits within the WLI crystal mush (see Fig. 4.8d). Late-stage peridotite plugs, representing pipe-like magmatic conduits, are common in the RLS, cross-cutting the stratigraphy of the layered rocks, and are also well known to occur as satellites outside the margins of the RLS (Holness *et al*., 2012), suggesting this is not an unusual mode of magma emplacement on Rum.

4.7.1.2 Textural evidence for in situ crystallisation of Cr-spinel seams in the WLI

The petrogenesis of Cr-spinel seams (chromitites, *sensu lato*) in layered intrusions is contentious. A variety of mechanisms has been proposed to explain the concentration of Cr-spinel in different layered intrusions, such as pressure changes and roof-rock assimilation in the Stillwater Complex, USA (Lipin, 1993; Spandler *et al*., 2005), magma-mixing in the Muskox Intrusion in Canada (Irvine, 1977), and stratified magma columns, crystal slurries, and cumulate assimilation in the Bushveld Complex, South Africa (Mondal & Mathez, 2007; Junge *et al*., 2014; Latypov *et al*. 2015). There have also been several models proposed for the petrogenesis of the Cr-spinel seams found in the RLS, including crystal settling and felsic cumulate (magma chamber floor) assimilation by primitive magma (e.g., mixing; Irvine; 1975; Henderson & Suddaby, 1971; O’Driscoll *et al*., 2009a; 2010). Though quite different in many respects, the models above are similar in that they all call for chromitite formation at the magma chamber floor. The WLI contains hundreds, if not thousands of Cr-spinel seams, which suggests numerous replenishment events. An array of outcrop- to crystal-scale features point to crystallisation of Cr-spinel seams on Rum *in situ* (O’Driscoll *et al*., 2010; Latypov *et al*., 2013). The close spatial association of Cr-spinel with harrisite in the WLI, where the seams occur along the bases, tops, and interiors of harrisite layers, also points to the formation of the Cr-spinel seams by *in situ* crystallisation. The presence of near vertically-oriented Cr-spinel seams within harrisite bodies also argues against crystal settling (Fig. 4.6e). The textures of many Cr-spinel seams, in which Cr-spinel occurs in the intercumulus spaces around olivine crystals, also makes crystal settling difficult to envisage (Jackson, 1961), particularly as the olivine displays corroded and deeply embayed shapes (Fig. 4.11a, f), suggesting a reaction between the two phases (necessarily also involving the interstitial melt). The close association of Cr-spinel seams with harrisite also points to formation within the crystal mush, as it has been argued above that harrisite forms by intrusion of magma (see also Ballhaus, 1988; Latypov *et al*., 2015). This is particularly true for those seams found within, and on the upper surfaces of harrisite layers. Anastomosing Cr-spinel seams (Fig. 4.6d), as well as those that bifurcate, and exhibit braiding are also indicative of intra-mush processes. Similar features have been reported for chromitite seams in the Bushveld Complex (Voordouw *et al*., 2009), where intrusive chromitite has also been documented (Mukherjee *et al*., 2017). The petrographic observation that large, optically continuous, olivine crystals are cross-cut by Cr-spinel seams also constitutes evidence for seams forming within the crystal mush (Fig. 4.11f), as harrisitic olivine (which is cross-cut) requires near homogenous crystallisation conditions (Donaldson, 1974; 1976) so must pre-date the spinel and not represent overgrowth (see also Hepworth *et al*., 2017). This feature could not feasibly develop on the magma chamber floor.

The crystal size distribution (CSD) data presented here support the field and petrographic evidence; that the Cr-spinel seams formed by *in situ* crystallisation. The majority of CSD profiles for Cr-spinel seams in the WLI are log-linear at the larger size portions (Fig. 4.15), typical of a relatively simple relationship between nucleation and growth, without changing the crystallisation conditions (Marsh, 1998). There is a paucity of population densities of larger crystals, often cited as evidence of size-dependant sorting (Marsh, 1998; Higgins, 2002b), with similar profiles observed for Cr-spinel seams in the ELI (O’Driscoll *et al*., 2009a; 2010; Hepworth *et al*., 2017) and in the Coobina Layered Intrusion in Western Australia (Barnes & Jones, 2013), where *in situ* crystallisation has also been invoked. The general lack of complexity in the CSD profiles is a feature of all seam types (e.g., boundary, granular-textured), where even the population density of the CSD groups is very similar. Thus, despite the structural and lithological heterogeneity that is evident from the field observations of different Cr-spinel groups (e.g., continuity, host rock lithology, seam thickness, diffusiveness), the controls and limitations on Cr-spinel crystal nucleation and growth appear to be similar, suggesting a common petrogenetic origin.

At the smallest size fractions, many of the CSD profiles deviate from log linear behaviour and display humped profiles. This reduction in the smallest crystal size fraction could be a function of post-crystallisation coarsening or annealing (i.e., Ostwald ripening), resulting in a net loss of the smallest crystals with minor increases in the larger grain sizes (see Higgins, 2002b). However, there is a lack of fanning in the large size fractions among CSD groups (Fig. 4.15) so textural coarsening has not operated on all size fractions. The prevalence of sharp downturns in the CSDs at small crystal sizes has been attributed to filter-pressing in crystal mushes (Higgins, 2002b; 2006). However, compaction is not envisaged as having been an important process during the construction of the WLI. Although granular-textured and hopper olivine-textured peridotites comprise rounded olivine crystals, which will compact if interstitial melt is present (McKenzie, 1984), Worrell (2002) deemed the effects of compaction to be negligible in the WLI based on a comprehensive study of olivine CSDs. One obvious difference can be found in the skeletal olivine-textured harrisites that yield log-linear Cr-spinel CSDs with no downturn at small crystal sizes. The Cr-spinel crystal populations in these peridotites are fine-grained in contrast to the CSDs for the hopper olivine peridotite-hosted seams and are also characterised by much higher nucleation densities. The high nucleation density of Cr-spinel may be a primary feature of the seams in skeletal olivine-textured harrisite layers or suggest that the process responsible for removing the smallest crystal sizes operated more efficiently in skeletal frameworks. For example, the profile shape may be a result of variable through-flow, removing smaller crystals i.e., an elutriation effect.

4.7.1.3 Cr-spinel seam petrogenesis in focused zones of melt-rock reaction in the WLI cumulates

Textural, petrographic, and field observations suggest that the Cr-spinel seams in the WLI crystallised *in situ* from a process that occurred repeatedly. As noted above, the intimate association of Cr-spinel seams with harrisites, whether seams occur within harrisite bodies or along their upper/lower surfaces, strongly points to a genetic relationship between them. Furthermore, this evidence also points to a ubiquitous formation mechanism for all seam types. Cr-spinel compositions in the WLI are variable, essentially the entire range of major element (e.g., Mg#, Cr#) variation reported from the rest of the RLS is present within the WLI Cr-spinel (Fig. 4.17a). There is no clear geochemical distinction between boundary-type and granular-textured peridotite-hosted Cr-spinel seams (Figs. 4.17a, b, 18). However, in comparison with these, Cr-spinel in harrisite-hosted seams are enriched in Fe_2O_3, with lower Al_2O_3 contents. This relationship has been attributed to the reaction of Cr-spinel with a relatively evolved interstitial melt (O'Driscoll *et al.*, 2009a; Lenaz *et al.*, 2011; Leuthold *et al.*, 2014; 2015). The most compositionally distinct Cr-spinel population occurs in the chromitite seams. Here, Cr-spinel has the highest Al_2O_3 contents in the WLI (~39 wt.%), as well as in the RLS overall (Cr# 0.29, Mg# 71.4; Fig. 4.17a). High Mg#-low Cr# Cr-spinel characterises the so-called 'Rum-trend' (Henderson, 1975; Barnes & Roeder, 2001), and is typically present in Cr-spinels at the bases of the ELI unit boundary seams. O'Driscoll *et al.* (2010) suggested that these compositions represent the closest approximation to the hybrid magma (picrite plus troctolite) that crystallised the Cr-spinels, a conclusion also reached by Bell & Claydon (1992) for Cr-spinel in coeval peridotites of the Skye igneous centre. Titanium (Ti^{4+}) is incompatible in Cr-spinel and serves as a potentially useful indicator of magmatic environment (Roeder & Campbell, 1985; Scowen *et al.*, 1991; Barnes & Roeder, 2001; Wijbrans *et al.*, 2015). In the WLI, the TiO_2 content of Cr-spinel is typically ~2 wt. % but can be as high as ~7 wt. % in harrisite-hosted seams. Chromitite seams have the lowest TiO_2 contents (<1 wt. %); like those reported from the unit boundary seams in the ELI by O'Driscoll *et al*. (2010). These show a congruous decrease in TiO_2 with Cr# (Fig. 4.17b). Low initial TiO_2 in the parental melt of the Cr-spinel seam is a function of the activity of Al_2O_3 (Kamenetsky *et al*., 2001), which in turn is controlled by the assimilant that triggered Cr-spinel crystallisation. For example, assimilation of plagioclase (or a plagioclase-normative liquid) increases Al_2O_3 in the melt, reducing the potential for uptake of TiO_2 into enter Cr-spinel (O'Driscoll *et al*., 2009a; 2010). High TiO_2 values are therefore attributable to postcumulus processes, which are enhanced in the porous skeletal frameworks of harrisite where TiO_2 is consistently high. Conversely, it may be possible that TiO_2 activity is buffered in chromitites (<1 wt.% TiO_2), but not in other seam types. There is a linear relationship with decreasing TiO_2 as Al^{3+} increases through granular and harrisite, boundary, and chromitite (Fig. 4.17b). This corresponds more strongly with the abundance of Cr-spinel within the seam i.e., the more Cr-spinel per unit volume the more aluminous the spinel.

Electron microprobe traverses taken through seams reveal relatively constant Cr-spinel compositions, even in the thickest seams (up to 2cm), until above or below the limits of the seam, where Cr-spinel composition changes considerably (Fig. 4.19; see also Appendix 3.4). Above and below the seams, Cr-spinels are relatively enriched in Fe_2O_3 and TiO_2. In contrast, the composite chromitite seam (AM18; Fig. 4.19) exhibits an internal step-change in TiO_2 content, which matches the position of the textural boundary (see also Appendix 3.4). A similar phenomenon has been reported from the UG-2 chromitite in the Bushveld Complex of South Africa, where repeated step-changes in the TiO_2 content of Cr-spinel throughout the seam were interpreted as reflecting incremental, rather than instantaneous, construction of the chromitite (Junge *et al*., 2014). The outer edges of the AM18 seam are coarser-grained, and CSD profiles taken from different portions of the seam display fanning (Fig. 4.15e), suggesting textural coarsening of the marginal zones with respect to the inner portion. The Cr-spinel crystals in the coarse-grained marginal zones of AM18 have lobate grain boundaries (Fig. 4.20). Compositional zoning also occurs in individual crystals, with enrichments of TiO_2 and Fe_2O_3 towards the edges of the crystals (see Fig. 4.20). These observations indicate a crystal-melt disequilibrium reaction during the growth of these crystals. Thus, it seems likely that the coarse-grained marginal zones of the composite Cr-spinel seam are the result of a supra-solidus textural equilibration process (i.e., annealing). However, it is not immediately clear why the thickness of the upper marginal zone is significantly greater than the lower zone (Fig. 4.20), given that the texture of the peridotite is identical on either side. One explanation might be the tendency for melt to migrate upwards, particularly as this process is occurring within the crystal mush where small degrees of overpressure will occur. This suggestion would necessitate the trapping of melt within this seam (or melt channel), with little or no exchange with the adjacent cumulate.

Further support for a melt channel model is found from textural analysis. There is a strong correlation between spatial distribution and textural characteristics, which reveal a linear relationship between available space within the crystal mush (minimum crystallinity) and Cr-spinel abundance (Fig. 4.16b, c). Chromitite seams have the highest volumetric abundance of Cr-spinel, lowest crystallinity, and highest Al^{3+}compositions, suggesting there was more space for melt within the channel. Conversely, granular-types have a high crystallinity and lower volumetric abundance, something also mirrored in the clustering index (R-value; Fig. 4.16d), and therefore low Al^{3+} compositions. There is also a decrease in olivine abundance and a change from euhedral to anhedral crystals along this trend, with the most anhedral (and presumably corroded) olivine occurring in chromitites. Intermediary values also exist, forming a spectrum of textures and compositions, corresponding well to volumetric spinel abundance and crystallinity.

With the evidence presented above, notably of cross-cutting and anastomosing Cr-spinel seams (Figs. 4.6d; 11f), *in situ* crystallisation, and mineral chemistry, the Cr-spinel seams are best explained by progressive melt channel formation within the crystal mush. Each Cr-spinel seam preserves different degrees of melt through-flow, where granular-textured peridotite-hosted seams record the lowest volume of (porous) melt throughflow, while chromitite seams reflect the highest degree of (channelized) through-flow (see Fig. 4.22). The likelihood that melt might be able to flow through a semi-solid crystal mush over time-scales which fit the experimentally-derived dissolution rates of minerals such as plagioclase, considered here to be the critical assimilant that triggered Cr-spinel crystallisation (O'Driscoll *et al.*, 2010; 2009a; Latypov *et al.*, 2015; Hepworth *et al.*, 2017) is assessed. Using flow equations based on Darcy's law, the following equation can be determined:

$$q = \frac{(\varphi)(pB - pA)}{\mu}$$

where q is the flux within the channel, φ is the permeability of the matrix, pB is the bulk matrix density of the crystal mush (~3.049 g/cm^3, e.g., for a typical granular-textured peridotite modal mineralogy of 70% olivine, 20% plagioclase, 10% pyroxene), pA is the bulk density of the liquid of 2.66 g/cm^3 (Holness *et al.*, 2007), and μ is the viscosity of the liquid determined experimentally around ~1 Pa/s/m^2 by (Donaldson, 1976), with similar values used by Holness *et al*. (2007). From this, the velocity of melt (v) within the mush can be derived as:

$$v = \frac{q}{\Phi}$$

where *q* is the flux determined from equation (1), and ϕ is the porosity of the bulk matrix (the crystal mush). A range of permeability and porosity values are possible, as the degree to which crystal mush was solidified when magma injection occurred is not known (see below), but based on previously modelled estimates, Holness *et al.* (2007) used a permeability value of 10^{-10} m^2 and noted that Elliot *et al.* (1997) suggested an even higher permeability of 10^{-9} m^2. The typically orthocumulate texture of the WLI peridotites, with crystallinities typically in the range 90–40%, would have had a significant melt interstitial fraction. Furthermore, as the olivine crystal size in the WLI is typically > 1 mm, permeability could be higher still, i.e., > 10^{-8}–10^{-7} m^2 (von Bargen & Waff, 1986). At a permeability value of $10^{-8}m^2$, a bulk directional melt velocity of 0.099mm/hr is calculted. This value is of the same order magnitude as experimental calculations of plagioclase dissolution rates (~0.086 mm/hr; Donaldson, 1985) which might be dissolving at a similar rate to the melt flux to produce the Cr-spinel saturated liquid, allowing for steady propagation of the channel. The velocity of melt migration laterally through the crystal mush over length-scales of 1 m, even given the comparatively low porosities of 20% in the granular-textured peridotite, are comparable to crystallisation times of days and weeks for harrisitic olivine (O'Driscoll *et al*., 2007a). A minimum crystallinity of 5% in chromitite seams yields velocities of ~m^2/hr. It is suggested therefore that composite chromitite seams, such as AM18 (Fig. 4.19; 20), where melt through-flow was channelized (i.e., not porous), represent an end-member of this process, where flow of melt within the channel progressively decreased crystallinity (i.e., olivine) by melt-rock reaction during chromitite development. The rates of melt migration calculated above are all in agreement with crystallisation timescales of harrisite from months to hours suggested by O'Driscoll *et al.* (2007a), particularly as multiple sill-like intrusive events are suggested, which will keep the mush nearer to liquidus temperatures, facilitating the movement of melt within a hot, semi-solid crystal mush.

The transition from porous to channelized flow has been studied numerically in upper mantle peridotite bodies, including within ophiolites, and explains the formation of dunite bodies therein (e.g., Quick, 1981; Kelemen *et al*., 1995). Critically, this process produces a strong positive-feedback effect, whereby, as dissolution proceeds, permeability increases, thus allowing more melt through-flow, thereby increasing the rate of dissolution and porosity, and so on (Chadam *et al*., 1986; Ortoleva *et al*., 1987). This process was studied experimentally by Daines & Kolhstedt (1993; 1994) where the change from porous to channelized flow was achieved because of disequilibrium within the system (i.e., between the hybrid liquid and peridotite crystal mush), producing a porous reaction zone on the removal of phases (e.g., clinopyroxene and orthopyroxene). The combined petrographic, textural and chemical data presented here illustrate this continuum between porous (granular-type seams) and channelized flow (chromitite seams) of a Cr-spinel-saturated reactive melt though the crystal mush, where the continuum between these end members is a function of melt volume and dissolution rates, with an ultimate control on the composition and texture of Cr-spinel within the seams (Fig. 4.22). The seams form synchronously with harrisite (i.e., picrite sills) in the same hot tears and shear zones, with the spatial relationship between the two controlled by how far the sill migrates along the hot tear (see Hepworth *et al*. 2017). Intra-harrisite seams form from the continued flow of melt within the rapidly crystallising framework, with multiple generations of melt recorded within Cr-spinel seam melt channels (Fig. 4.22). Based on our discovery of the clinopyroxene-rich roof zone (UAM) to the WLI, the evolved components (interstitial melt) of these seam-forming reactions may have escaped upwards through the cumulate pile (see discussion below).

The model presented in Figure 4.22 helps to solve the long-standing mass balance problem implicit in concentrating so much Cr in the seams compared to parental melts with ~3000 ppm Cr (i.e., Upton *et al*., 2002), as more melt has moved through the channel than is represented by the net volume of the seam. Our model also helps to account for the elevated base-metal sulphide and PGM populations in the chromitites compared to granular-type seams (e.g., Butcher *et al*., 1999; O’Driscoll *et al*., 2009b; Hepworth *et al*., 2017). It may be that our model could also be readily applied to a variety of Cr-spinel seams (and chromitites) in much larger intrusions such as the Bushveld and Stillwater Complexes, where sill emplacement has been recently recognised around chromitite-bearing units (Mungall *et al*., 2016; Mukherjee *et al*., 2017; Wall *et al*., 2018). Furthermore, it may be of particular importance where this PGE-mineralisation is found in conjunction with ultramafic pegmatoids like harrisite (e.g., Cawthorn & Boerst, 2006; Mondal & Mathez, 2007; Wilson, 2015).

4.7.1.4 Initiating melt channel formation and conceptual model: shearing and hot-tearing of a crystal mush

Hepworth *et al.* (2017) proposed that hot tearing (and shearing) of a crystal mush under lateral shear stress formed ideal pathways for magma to migrate into the crystal mush of the Unit 10 peridotite in the ELI. Similar mechanisms have been invoked to explain melt concentrations within spatially restricted lenses or pods in natural silicate crystal mushes (Phillpotts *et al.*, 1996; Geshi, 2001; Humphreys & Holness, 2010; Namur *et al*., 2013). There are strong parallels between the field and petrographic observations in the WLI and those in the Unit 10 peridotite, including the evidence for deformation of layering, the lithological relationships and the compositions and textures of Cr-spinel seams, attesting to similar mechanism for magma emplacement into the crystal mush. As such, Cr-spinel seams (and therefore harrisite sills) in the WLI are formed from the lateral migration of melt through the crystal mush along hot tears or shear zones and present a schematic model in Figure 4.22.

To summarise, Cr-spinel seams form from the injection of picritic magma into the crystal mush along hot tears and shear zones, with Cr-spinel seams representing progressively developed melt channels which experienced variable amounts of through-flow, controlling the olivine texture, spatial distribution and chemistry of the Cr-spinel. These seams form syn-genetically with harrisite sills. Spatial relationships between the two are ultimately controlled by how far the harrisite parental melt migrates along the hot tear. Intra-harrisite seams, possibly protected from shear-stress by the skeletal framework form from the continued flow of melt within a rapidly crystallising framework, with multiple-generations of melt-flow recorded within Cr-spinel seam melt channels (Fig. 4.22).

4.7.2 The origin of olivine cumulates in the Western Layered Intrusion

4.7.2.1 Petrogenesis of harrisite and the thermal history of the WLI crystal mush

The WLI contains an extreme variety of olivine crystal sizes and morphologies for a comparatively small peridotite body, encompassing a range from mm-sized granular-textured (polygonal) olivine crystals to m-sized branching and skeletal varieties (Donaldson, 1974; O’Driscoll *et al*., 2007a). The conditions necessary to form the complex, skeletal and branching olivine crystals that comprise harrisite were studied experimentally by Donaldson (1974) where he proposed that harrisite represents picritic magma that underwent significant degrees of undercooling. The cause of this undercooling in the WLI is still uncertain. Donaldson (1974) speculated that volatile or water exsolution might have been responsible for lowering the liquidus of the parental magma, while O'Driscoll *et al.* (2007a) suggested the temperature difference between the replenishing picrite and resident magma in the chamber could have been sufficient. Hepworth *et al*. (2017) suggested that the Unit 10 harrisites formed from intrusive picrites that undercooled against the mostly solid crystal mush. Given the evidence presented here for an intrusive origin for harrisite in the WLI, the latter model may also be appropriate here. Harrisite in the WLI typically occurs within granular-textured peridotite. The field observations presented here show that no harrisite is visibly cross-cut by granular-textured peridotite. If the granular-textured peridotites represent an early (pre-harrisite) episode of crystallisation, they must have cooled significantly for the requisite undercooling to occur, so that picrite intrusions could form harrisites. The field relations reported here show that the rate of magma replenishment into the WLI was not necessarily constant and may have been linked to movements on the LLF (Volker & Upton, 1990; Emeleus *et al*., 1996). During periods of relative quiescence, cooling of the crystal pile likely occurred, such that a temperature gradient existed between new picrite replenishments and their host. The sharp unconformable boundary between the HBM and the TSM might indicate a particularly significant time-gap, given the clear change in composition of the parental magma to each.

A degree of volatile (including water) exsolution cannot be entirely ruled out, as amphibole and mica occur in trace (and slightly elevated ~1–2%) amounts in both harrisites and granular-textured peridotites. However, the amphibole is almost always texturally associated with serpentine and chlorite, which does not support it originating as a primary magma product. In this scenario, it might also be expected that harrisite would contain more hydrous minerals than granular-textured peridotite (as their parental melts presumably underwent greater undercooling), which is not the case, based on the petrographic evidence set out above.

Different members of the WLI are characterised by different olivine morphologies. The most complex (branching and skeletal) olivine morphologies occur in the lower TSM and HBM, while the

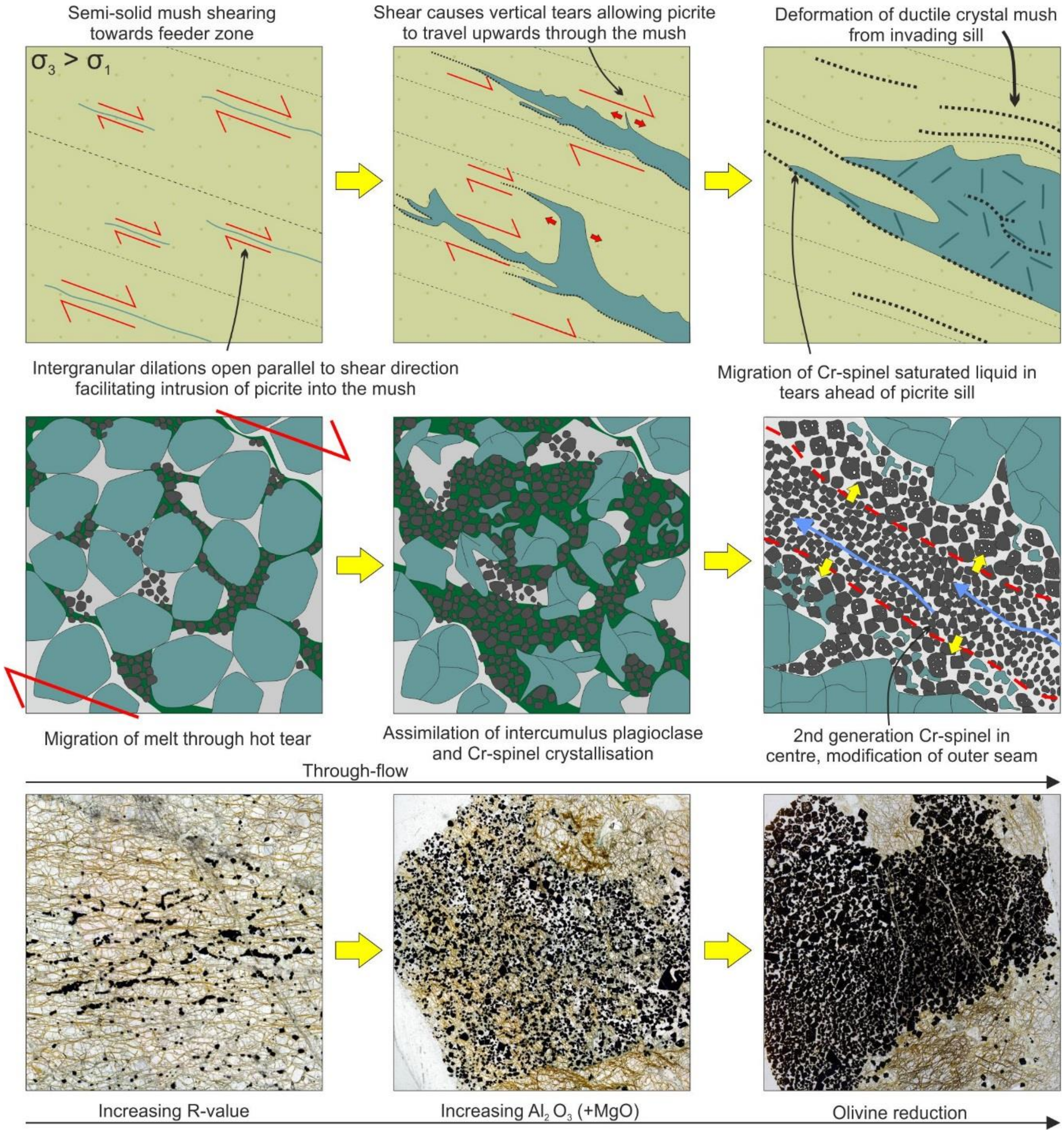

FIGURE 4.22: Conceptual model depicting the petrogenesis of harrisite and Cr-spinel within hot tears and melt channels within a layered, and deforming, peridotite crystal mush. See text for full description.

AMP is dominated by hopper and coarse-grained granular morphologies (Fig. 4.23). From experimental work carried out on olivine morphology (e.g., Donaldson, 1974; Lofgren & Donaldson, 1975; Donaldson, 1976; Faure *et al.*, 2003), it seems reasonable that the variation in olivine morphology both between individual peridotite-harrisite layers and between different members might have been caused by variable degrees of undercooling. A caveat to this is raised by the work of Means & Park (1994), who showed that given sufficient time at high subsolidus temperatures, complex crystal shapes (i.e., high surface area to volume ratio) may revert to more polyhedral shapes.

This is driven by textural equilibration, where the high interfacial energy in skeletal crystals is thermodynamically unstable and reduces to more stable, low surface area forms. Assuming no late stage mechanical remobilisation or disruption, it might be expected that the originally skeletal, now polyhedral crystals would remain in optical continuity in thin section. This is rare, and, where it is observed, can be explained by the cut effect of complex skeletal crystal forms. This is not to say that textural equilibration did not occur locally, but the intrusion-scale morphological variation of olivine in the WLI, from the HBM and TSM to the AMP, is considered as a primary magmatic feature.

The laboratory experiments of Donaldson (1976) on olivine morphology provide a useful gauge for crystallisation conditions in the WLI (Fig. 4.23). It can be speculated that the earliest episode of intrusion would have been characterised by the highest thermal gradient into the country rocks, but presumably ΔT°C did not exceed 250°C, or the replenishing magmas would have quenched (Donaldson, 1976). This would mean that the country rocks were already hot (>700°C) when the WLI began to form, which is supported by observed radial cooling joints around harrisite sills in the Western Granite (Figs. 4.9a, d). The HBM, containing the coarse-grained bladed–skeletal olivine crystals required the steepest thermal gradient (and a temperature difference ~200 ΔT°C), according to the study of Donaldson (1976), which might therefore indicate that the HBM represents the earliest stages of construction of the RLS (see also Greenwood, 1987; Greenwood *et al*., 1990). The morphology of olivine in the TSM (and the lowermost AMP) is generally coarse-grained and bladed–branching (Fig. 4.8e), suggesting a slightly reduced ΔT relative to the HBM of ~150–200°C, and pointing to crystal mush temperatures of ~900°C as the TSM and some AMP peridotites were being intruded. The AMP exhibits significantly greater variability in olivine texture than the other members. Overall, it is envisaged that the complex interplay between small volume replenishments, time, and undercooling resulted in the diverse array of olivine textures observed in the AMP peridotites. There is an abundance of layers of harrisite dominated by hopper olivine morphologies, suggesting degrees of undercooling ~50 ΔT°C and therefore a relatively hot crystal mush. However, there are less common examples of skeletal olivine-dominated harrisite in the AMP (see Appendix

3.2), suggesting that the crystal mush had the opportunity to cool significantly. These harrisites bodies may therefore represent some of the final magma emplacement events of the WLI (Fig. 4.24).

4.7.2.2 Syn-magmatic reworking of harrisite in deforming crystal mush

Some granular-textured peridotite layers contain megacrysts of harrisitic olivine, suggesting that at least some granular-textured peridotite formed contemporaneously with harrisite. Furthermore, the association of granular-textured peridotite with Cr-spinel seams (Fig. 4.3; Facies L) suggests a process like those proposed for harrisite formation, except that the intruding picrite may have carried an olivine cargo (Worrell, 2002), supressing harrisitic olivine growth (Donaldson, 1976).

A dynamic, high-crystallinity framework undergoing sufficient shear stress to form hot tears is not necessarily conducive to forming fragile skeletal olivine crystals in harrisites. High strain environments would likely deform and/or fragment these crystals, particularly as harrisites formed within the shear zones and hot tears, i.e., the areas of greatest stress. The WLI, specifically the AMP, contains layers of porphyritic peridotite (Fig. 4.5e, 4.12), consisting of abundant blocky–rounded, cm-sized olivine megacrysts, which are almost always strongly foliated parallel to layering (Fig. 4.5e, 4.12). The layers are typically thin (<5 cm thick), with a 'groundmass' of fine-grained granular-textured olivine. Porphyritic peridotite layers are often associated with Cr-spinel seams, usually along the layer bases (or more rarely tops). The porphyritic layers themselves are generally Cr-spinel rich (>5%). As noted above, the megacrysts have abundant inclusions of skeletal magnetite while the groundmass olivine is inclusion free (Fig. 4.12b, c). The different characteristics of the two olivine populations points to an autocrystic origin for the large olivine crystals, i.e., they represent 'clasts'. O'Driscoll *et al.* (2007a) reported an occurrence of these megacrysts that showed imbrication fabrics at the outcrop-scale, and consequently suggested they represented fragments of harrisitic olivine that were reworked on the magma chamber floor. The presence of the skeletal magnetite inclusions points to deeper undercooling of the magmas that crystallised the megacrysts (Barnes, 1985; Shore & Fowler, 1999; Godel *et al*., 2013). These inclusions are also observed in harrisitic olivine throughout the WLI.

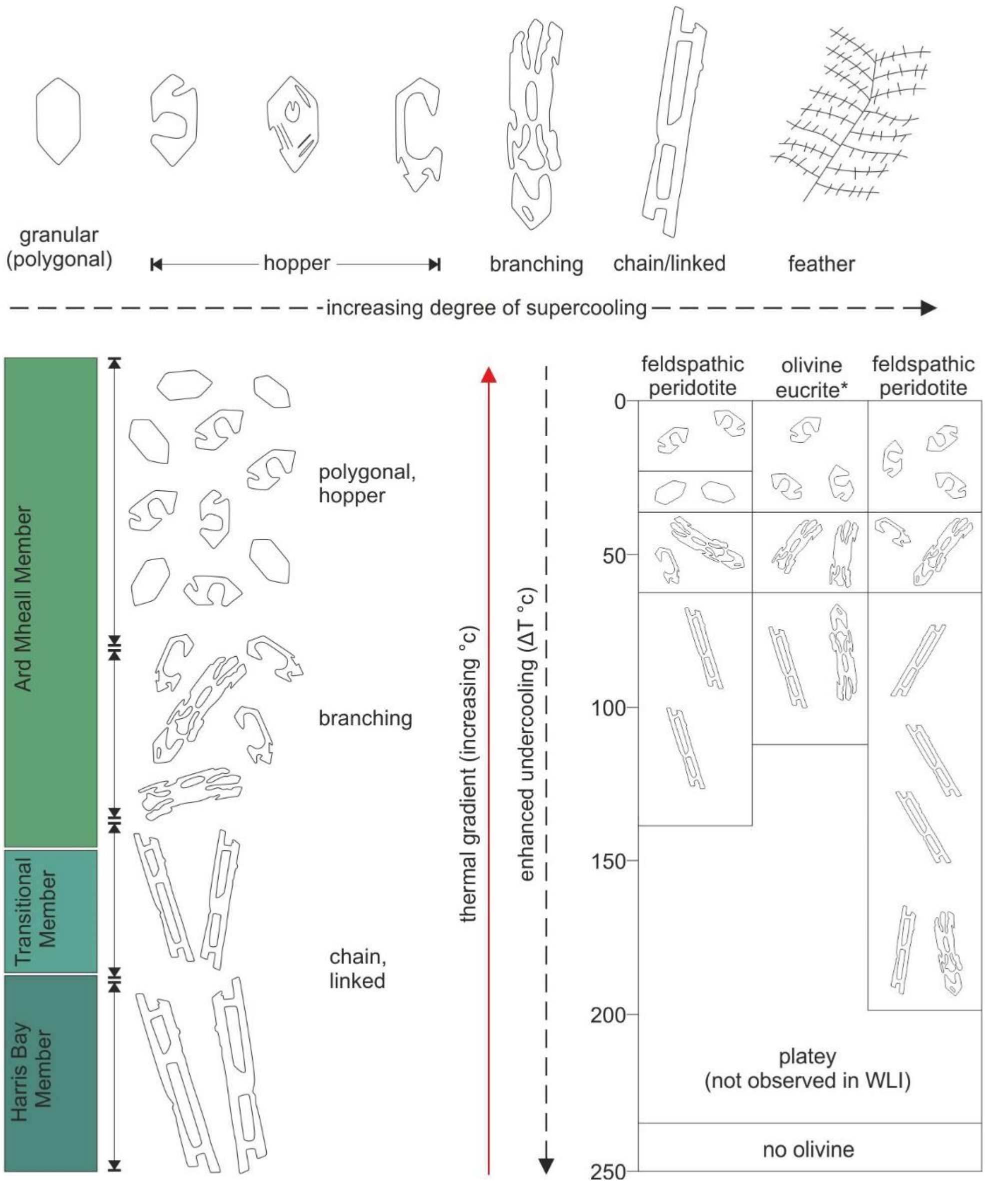

FIGURE 4.23: Simplified relationship of olivine morphology within the harrisites of all three members of the WLI, and experimental olivine morphology data adapted from Donaldson (1976) for harrisites in the WLI. Highlighted is the changing thermal gradient and degrees of undercooling depicted by olivine morphology throughout the crystal mush (*) Eucrite refers to the lithologies within the HBM (Harker, 1908).

Given that harrisite is suggested here to form within the crystal mush, a re-evaluation of the petrogenesis of the porphyritic peridotites is required. A model is proposed whereby the porphyritic-peridotite layers are harrisite sills that underwent shearing within the crystal mush, causing fragmentation of the large skeletal crystals within the hot tears and shear zones (see Hepworth *et al*., 2017), and producing the strong foliations that characterise both the megacrysts and groundmass olivine. It is worth noting that O'Driscoll *et al*. (2015) showed that the porphyritic peridotites also exhibit a well-developed olivine lineation, supporting the idea that a component of simple shear was involved in fabric development. The consistency of thickness of the porphyritic peridotite layers might mean that this process is only important where the sill is thin, where magma-static pressure is overcome by shear stress, possibly where the inflation rate (or flux rate) in the sill is too low. The thinness (<5 cm) of the layers also precludes formation by bed-load transport within sills, particularly as imbrication of olivine is not observed within harrisite layers (Fig. 4.3; see Appendix 3.2). The disruption and disarticulation of homogeneously crystallising harrisite would produce new nuclei for heterogeneous nucleation, suppressing the ability of the magma to undercool, and forming granular-textured olivine (Donaldson, 1976; Hepworth *et al*., 2017).

4.7.2.3 Infiltration metasomatism of crystal mushes in the WLI: The UAM and TSM members

Clinopyroxene is rare in the AMP, occurring in abundances <10 vol.% throughout most of the sequence until the top several tens of metres, where it increases to >20 vol.% across the AMP/UAM boundary (Fig. 4.7a, d, e). Compositional zoning in clinopyroxene crystals also becomes apparent at this interval. Plagioclase veins are very common in the UAM, which, coupled with the increase in clinopyroxene abundance, may point to the upward migration of more evolved interstitial melts. The mineral chemistry of the clinopyroxene is distinct from that in the underlying AMP, with distinct TiO_2 poor, high Mg# cores, and slightly lower Mg# and TiO_2-rich rims. Cr_2O_3 contents remain similar. The rim compositions overlap well with clinopyroxene from the underlying AMP, while the UAM clinopyroxene cores exhibit distinctly lower Cr_2O_3 and TiO_2 than other WLI clinopyroxene compositions (Figs. 4.22a, b). Plagioclase compositional variation is not large; the UAM plagioclase is more evolved (sodic) than that in the AMP, as reported by Worrell (2002), and the FeO content of the plagioclase is also marginally higher in the UAM than the AMP (Fig. 4.22c). The presence of more evolved mineral assemblages in the UAM supports a process involving the migration of an evolved clinopyroxene-saturated melt upwards through the crystal mush, promoting new rim growth onto pre-existing crystals and enriching the very top of the WLI mush, i.e., the UAM, in clinopyroxene. The evidence above therefore suggests that the UAM represents a metasomatised zone of cumulate. Such a process has been well-documented for clinopyroxene oikocryst-bearing cumulates in the ELI (Holness *et al*., 2007; Leuthold *et al*., 2014; Hepworth *et al*., 2017). It follows that the metasomatising agent came from the crystal pile beneath and that the clinopyroxene-rich zone comprising the UAM is the roof zone to the AMP, and hence the WLI. Such a model is inconsistent with there being a column of magma above the crystal mush, as an escaping clinopyroxene-rich melt would migrate into the chamber and presumably be mixed into the resident magma. This suggests instead that during solidification, the WLI crystal mush was directly roofed by country rock and the most westerly dipping layers in the UAM may record the orientation of the roof/cumulate boundary (i.e., the orientation of the contact with the Western Granite; Greenwood *et al*., 1987; Petronis *et al*., 2009).

The TSM is classified as 'transitional' because it represents a combination of features from the overlying and underlying members and was interpreted to represent an intermediary fractionation product of the WLI magma (Wadsworth, 1961). The TSM exhibits similarities to the overlying AMP, i.e., identical layering characteristics and lithologies (including Cr-spinel seams), but contains abundant clinopyroxene-oikocrysts, a feature more consistent with the underlying gabbroic HBM. There are differences in the compositions of the primary minerals in different members. For example, the AMP and TSM have very similar plagioclase (core) compositions (An ~80 mol. %), while the HBM is comparatively more evolved, with more Fe-rich olivine (<Fo 70 mol. %) and more albitic plagioclase (<70 mol. %) (Greenwood, 1987). Indeed, An-contents as low as 56 mol.% are revealed in the HBM (Fig. 4.22c). Normally-zoned rims of plagioclase from the TSM show a strong overlap with the plagioclase compositions from the HBM. No distinction in mineral chemistry between the HBM and the TSM is observed in clinopyroxene or Cr-spinel chemistry. Instead, the clinopyroxene compositions of the TSM and HBM overlap significantly, with similar trends observed between Mg# and TiO_2, while the AMP clinopyroxene compositions are scattered, tending to higher Mg# (Fig. 4.21b). The similarity in clinopyroxene chemistry between the HBM and TSM, and TSM plagioclase rim compositions with HBM plagioclase points to metasomatism of the TSM by evolved interstitial melt from the HBM. Cr-spinel chemistry in the TSM and HBM contain the most Fe_2O_3 and TiO_2-rich compositions, with crystals of ferrian-chromite and Cr-magnetite found alongside Cr-spinel in both members. Textural analysis of the Cr-spinel seams in the TSM suggests they have formed in a very similar environment to those in the AMP, with a significant overlap in CSD and SD characteristics (e.g., Figs. 4.15f; 3.17). However, Cr-spinel seams are not abundant in the TSM, and where present are extremely discontinuous (i.e., only traceable for a few centimetres), unlike those in the AMP. Cr-spinel in the TSM is also typically enclosed in clinopyroxene oikocrysts with little or no plagioclase present. This is an intriguing observation, as abundant Cr-spinel should not be able to co-crystallise in a clinopyroxene-saturated melt, as the excess SiO_2 should cause spinel to be re-dissolved (Morse, 1980). Perhaps this process has occurred and has been responsible for the extreme rarity of Cr-spinel seams in the TSM and heavily modified Cr-spinel compositions (Fig. 4.19; see Leuthold *et al*., 2014). The patchy zoning and intra-crystal resorption textures in intercumulus plagioclase in the TSM point to a dissolution process (Fig. 4.13a). Furthermore, large oikocrysts of clinopyroxene contain small, rounded and optically continuous olivine crystals inclusions (Fig. 4.13f), similar to textures observed by Barnes *et al.* (2016) in layered pyroxenites. Those authors suggested that this texture arises from infiltration of a comparatively siliceous melt, dissolving olivine and precipitating pyroxene (orthopyroxene in their case). The parental melts in the RLS were not silica-rich, so there is only very rare orthopyroxene present. However, clinopyroxene saturated melts have been shown to be particularly reactive, with the potential to dissolve or significantly modify the existing cumulate mineralogy (Holness *et al*., 2007; Leuthold *et al*., 2014), supporting mineral chemical observations that a reactive clinopyroxene-normative melt was present throughout the formation of the TSM.

Based on the above discussion, the TSM is suggested to represent another metasomatic horizon within the WLI (Fig. 4.24). The field observations (e.g., upward gradation of AMP/TSM boundary), and olivine morphological constraints discussed above suggest the TSM and AMP are petrogenetically related, sharing the same lithological and textural characteristics, while the HBM is distinctly gabbroic. The similarity of the TSM and HBM clinopyroxene chemistry and the high abundance of this phase in these members compared to the AMP suggest that the clinopyroxene-normative melt was sourced from the HBM. The infiltration metasomatic event saturated the crystal mush in clinopyroxene, forming large oikocrysts throughout the lowermost AMP (see Leuthold *et al*., 2014), and causing minor but pervasive dissolution of existing plagioclase (Fig. 4.13a), Cr-spinel, and olivine. This process accounts for the relic and reabsorption textures (Fig. 4.13f), and heavily

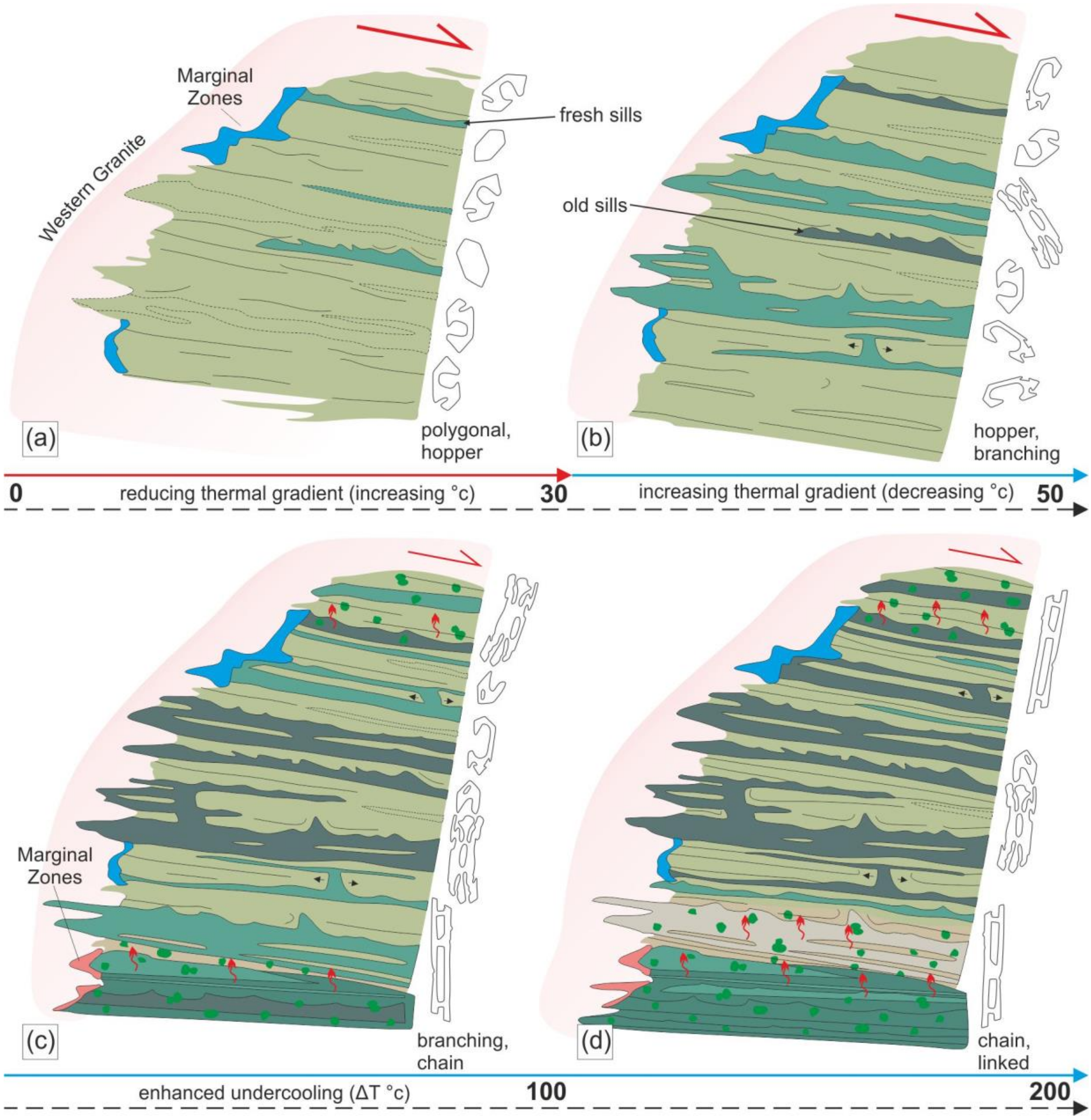

◄FIGURE 4.24: Conceptual model for the formation of the WLI, including simple thermal history depicted by olivine texture at each stage (see Donaldson, 1976). (a) Emplacement of the WLI and rapid increase in temperature of the crystal mush due to high intrusion rate, restricting the undercooling to incoming picrite sills, resulting in granular-textured peridotite (and some hopper dominated harrisite sills). (b) After a period of quiescence (or reduced magma flux), the crystal mush cools, such that the input of new sills undergo higher degrees of undercooling, producing more hopper and branching olivine forms (i.e., harrisite). During the process of sill emplacement, evolved cpx-rich melt will migrate to the top of the crystal mush, pooling to form the UAM. (c) As the crystal mush continues to cool with time, fresh sills undergo higher degrees of undercooling, forming more complex olivine morphologies. Here, the intrusion of the HBM occurred, with the most complex olivine forms, suggesting the highest degrees of undercooling (see Fig. 4.8b). (d) Emplacement of the HBM at the base of the WLI produces a metasomatic horizon by partially melting the overlying crystal mush, saturating it in clinopyroxene, forming the TSM. Any injection of new sills will form rarer, highly complex olivine morphologies due to high degrees of undercooling (found mostly within the HBM) modified Cr-spinel compositions (including Cr-magnetite; O'Driscoll *et al*., 2009a; Leuthold *et al*., 2014; 2015).

The interpretation described above highlights some of the complexity inherent in sill-emplacement models for layered intrusions. The HBM was capable of exchanging interstitial melt with the TSM, but the relative timing of this process to emplacement of either member is still uncertain. The sharp discordant boundary between the HBM and TSM signifies a time-gap between both. Historically, it has been considered that emplacement of the HBM predates that of the TSM and AMP, and there is no new unambiguous evidence in this study to suggest otherwise. However, either intrusion of the AMP magmas into/onto the HBM, or intrusion of the HBM into the AMP could equally trigger the upward-percolating fluids that metasomatised the TSM. A scenario where the HBM is the younger intrusion would not create problems for the undercooling model presented above, provided the time-gap across the unconformity between the HBM and TSM was sufficient to allow the requisite undercooling of ~200 ΔT°C to form the coarse-grained bladed–skeletal olivine crystals that characterise the HBM (Fig. 4.24). Considering recent work on out-of-sequence layering in other layered intrusions (e.g., Mungall *et al*., 2016; Wall, 2016), constraining the relative age of the HBM in the WLI represents an important avenue for future research.

4.8 CONCLUSIONS

Contrary to the well-established view of the RLS as a classic example of a layered intrusion; formed from upward-younging stratigraphy and gravity settling of crystals to form cumulates at the floor of the magma chamber (e.g., Wadsworth, 1961; Emeleus *et al*., 1996; Emeleus & Troll, 2014), it is concluded that the WLI originated as a series of sills into an incrementally developed crystal mush. Similar interpretations invoking sill emplacement have also been put forward for peridotite cumulates in the ELI (Bédard *et al*., 1988; Hepworth *et al*., 2017), highlighting the importance of this underlying construction process for cumulates across the RLS.

The results shown here provide evidence that Rum WLI was built-up of multiple, sill-like replenishment events into an incrementally developing crystal mush, where sills are best (but not exclusively) represented by harrisite. The emplacement of sills is facilitated by slow gravitational collapse of the high-crystallinity cumulate, producing hot tears and shear zones enabling magma injection (Humphreys & Holness, 2010; Namur *et al*., 2013; Hepworth *et al*., 2017) and contemporaneous reworking of some crystallising sills, emphasising the dynamic crystal mush.

The injection of new magma into the crystal mush formed Cr-spinel seams along the same tears and shear zones as invading sills in progressively developing (permeable to porous flow) melt channels, which given the high flux rates could have developed channelized flow (Daines & Kohlstedt, 1993; 1994). The associated PGE-enrichment must therefore have occurred *within* the crystal mush. This conclusion has significant implications for the formation (and mechanism of enrichment) of PGE-horizons more generally in layered intrusions, traditionally assumed to occur at the magma chamber floor (e.g., Bushveld; UG2 or Merensky Reef).

The evolution of the layered WLI crystal mush was likely highly chaotic, given its formation by the apparent spatially and temporally random juxtaposition of sills. However, because olivine is abundant, the undercooling (approximated from olivine morphology) can be used as a simple proxy for temperature (Donaldson, 1976), providing better insight into the WLI system, allowing a simplified timeline where sill-emplacement, Cr-spinel seam petrogenesis and metasomatic processes can be better understood. Lastly, the evidence for non-aggrading layered igneous bodies presented here has important implications to the build-up of other olivine-rich cumulates (i.e., peridotites) found at the base of many layered intrusions (see Jackson, 1961; Wilson, 2015), where the current structural level is not an unambiguous indicator of relative age.

CHAPTER 5 – THE CONSTRUCTION OF LAYERED CUMULATE BODIES: THE EVIDENCE AND IMPLICATIONS OF SILL EMPLACEMENT

Problems addressed in layered intrusions typically revolve around relatively small-scale or layer scale processes that form specific layers, concentrate mineral (and metal-enriched) horizons, or form micro-scale textures towards the last stages of crystallisation (e.g., Tepley & Davidson, 2003; Spandler *et al*., 2005; Holness *et al*., 2005; 2007; O'Driscoll *et al*., 2007a; 2009a; 2010; Holness *et al*., 2011; Latypov *et al*., 2013; Maier *et al*., 2013; Veksler *et al*., 2015; Lindhuber *et al*., 2015; Hunt *et al*., 2016; Forien *et al*., 2016, see also Namur *et al*., 2015). It is important to note that while these studies provide substantial understanding of magmatic processes operating during the activity of the intrusion, they are based on a conceptualisation of layered intrusion formation from a body of crystal poor, fractioning magma, where the crystal mush occurs primarily along the walls and floor of this magma chamber. Where evidence is found contrary to this paradigm, subsequent re-interpretation of the broad scale construction mechanism of layered intrusions can render many previous models incompatible, particularly where evidence against large-scale fractionation in layered intrusions highlights the importance of sill emplacement (e.g., Bédard *et al*., 1988; Mungall *et al*., 2016).

To assess the relative importance of the sill emplacement model proposed in the preceding chapters, criterion favouring sill emplacement are outlined and discussed, including the three-dimensional geometry and spatial distribution of cumulate layers, cross-cutting relationships, and pegmatoid horizons (i.e., harrisite). This basic framework is then applied to previously undocumented peridotite horizons from Unit 7, 8, and 9 of the Rum ELI, and peridotites from the Ultramafic Series and J-M Reef of the Stillwater Complex, USA. The aim of this framework is to provide means to unambiguously ascertain the presence of sill emplacement in layered intrusions, or question traditional perception of particular lithological associations, which may be better explained by the processes discussed in this thesis. Lastly, the new observations are combined with previous literature to produce a new conceptual model for the entire RLS, where the layered intrusion is considered a complex of peridotite sills emplaced incrementally into pre-existing feldspathic cumulate (i.e., gabbro). The model could then be applied to a wide variety of other layered intrusions, including the layering of syenitic complexes like Illimausaq in Greenland (Marks & Markl, 2015), where many features found throughout this study can be reproduced with significant implications to the broad construction of layered intrusions.

5.1 SOME CRITERION FOR SILL EMPLACEMENT IN LAYERED INTRUSIONS

Recent geochronological work on the Bushveld and Stillwater Complexes has revealed important evidence for sill emplacement by demonstrating out-of-sequence layers within cumulate sequences (Mungall *et al*., 2016; Wall *et al*., 2018). This work was supported by some basic field observation that were inconsistent with traditional upward forming layers. However, field evidence demonstrating sill emplacement in layered intrusions is uncommon, limited by studies based largely on drill core. Bédard *et al.* (1988) highlighted the cross-cutting relationships between the peridotite and feldspathic portion of Unit 9 in the Rum ELI and noted that the peridotite was discontinuous laterally. As such, it was suggested that the peridotite represented a sill, later corroborated by detailed textural and geochemical analysis (Holness *et al*., 2007). Tegner & Robins (1996) used the reactions between lithologies with careful field observation to infer sill emplacement within a Caledonian layered intrusion. Here, several criteria used to identify sill emplacement in this study are outlined. It is expected that these can be readily applied across layered intrusions not only to providing first order supporting evidence for sill emplacement but establish better targets for absolute dating methods and advanced analytical techniques.

5.1.1 The topology and spatial distribution of layering

The topology of the contact between cumulate layers is arguably the most important determining factor of sill emplacement. Bédard *et al* (1988) showed that the Unit 9 peridotite in the Rum ELI cross-cut the overlying feldspathic cumulate by several metres in a broad dome-like structure. From this very basic observation it could be shown that the peridotite was younger than the overlying cumulate. This meant a upward (aggrading) formation of the cumulate sequence could no longer be reconciled with the observations, leading the authors to invoke sill emplacement of the peridotite. In both Chapters 2 and 4, individual harrisite layers exhibit upward-oriented apophyses that cross-cut the overlying layers ≤1 m (Fig. 2.5c). Much larger (>1 m) apophyses of harrisite occur in the Rum WLI as so-called ‘harrisite columns’ that truncate and deform surrounding cumulate (Fig. 4.4e). Broader cross-cutting relationships of harrisite layers are also abundant in the WLI, where dome-like structures cross-cut overlying layers. As with the interpretation of the Unit 9 peridotite, these features were used as conclusive evidence for sill emplacement, where the topology of these structures would never survive on the magma chamber floor. The features instead resemble liquid escape structures from sediments only possible during intrusion (see Chapter 2).

Second to the topology of layers (or packages of layers) is the spatial distribution of layering, notably its lateral extent. Bédard *et al*. (1988) noted lateral discontinuities within the Unit 9 peridotite and used this to further support their argument for sill emplacement. If magma were to be replenished at the magma chamber floor, it should spread out evenly, and will not form lens or discontinuous cumulate. Instead, such a feature is much better explained by uneven sill propagation (i.e., as lobes). The lateral discontinuity of layers was noted in Unit 10 (Chapter 2) in harrisite layers, which would terminate laterally, change in thickness, and potentially transgress nearby cumulate (Figs. 2.2; 2.5e). Furthermore, the lateral bifurcation of layers was noted within the WLI (Fig. 4.4a; 4.9c), another feature exclusive to intrusive bodies. However, what was noted in WLI harrisite layers was the interconnected nature of some layers, which displayed bridge-like structures between the underlying and overlying layers without any change in texture (Fig. 4.8d). These features are an intriguing combination of cross-cutting relationships and spatial distributions as suggests layer coalescence (i.e., braiding); a feature which can only be explained by sill emplacement.

5.1.3 Metasomatic horizons

When a sill is emplaced into a pre-existing lithology, it has the potential to modify it, leaving behind distinct textural, geochemical, or isotopic markers which can be used infer localised sill emplacement. This is particularly relevant where the marker horizons occur above the suspected sill, highlighting the pre-existing nature of the overlying lithology. For example, the feldspathic portion of Unit 9 hosts a distinctly pyroxene-rich horizon ~1 m from the peridotite/feldspathic cumulate contact. The horizon, known locally as the ‘wavy horizon’ has been proposed to have formed by the partial melting of a pre-existing gabbro by the emplacement of the peridotite sill beneath, causing liberated pyroxene-rich melt to concentrate higher up in the cumulate pile (Holness *et al*., 2007; Leuthold *et al*., 2014). Similar sill-host reactions have also been used to infer the emplacement of picrite sills in Caledonian layered intrusions (Tegner & Robins, 1996). In Chapter 2, the Upper Peridotite of Unit 10 was argued to pre-date the Lower Peridotite. As the lowermost Upper Peridotite contained distinctly reduced clinopyroxene abundance, it was suggested the emplacement of the Lower Peridotite caused partial melting of the overlying cumulate. This was supported by the Sr-isotope analysis of Palacz & Tait (1985), which highlighted a mixed zone where this clinopyroxene-poor horizon occurred. Within the WLI, the Transitional Member was suggested to represent a metasomatic horizon, formed from the emplacement of the Harris Bay Member, partially melting the overlying peridotite and saturating it with clinopyroxene-rich melt from the underlying HBM.

A common theme among these models is the presence of unusually clinopyroxene-rich lithologies, where the clinopyroxene occurs as large (cm-sized) oikocrysts (Fig. 2.4g). In many examples, this poikilitic layer is spatially associated with nearby ultramafic cumulate (olivine and/or orthopyroxene), with a clinopyroxene-poor lithology in between (see Holness *et al*., 2007). However, even if a distinct, spatially restricted marker does not exist as with Unit 9, a sudden change in clinopyroxene content (decreasing or increasing) could signify partial melting as with Unit 10 (Chapter 2), or infiltration metasomatism (Chapter 4), pointing towards sill emplacement, especially if associated with underlying ultramafic layers. These partially melted marker horizons are likely to occur beneath emplaced sills, but the tendency of liquid to move upwards (and laterally) due to overpressure will make infiltration metasomatism more likely to occur *above* the sill. Furthermore, the changes in mineralogy should not be restricted only to pyroxene, but also plagioclase, which is likely to be modified by hot, primitive magma (see O'Driscoll *et* al., 2009a). Based on the work here, these horizons, often few and far between in the literature, could become a useful tool for the identification of sill emplacement in layered intrusions, and help interpret diverse sequences of cumulates.

5.1.4 Pegmatoidal markers

The importance of harrisite has been emphasised in this study, where it is used as evidence for incremental sill emplacement across the RLS, based largely upon the topology of individual layers (see also Donaldson, 1982). However, the implications of this conclusion require an alternative mechanism for the undercooling mechanism that causes harrisitic olivine to form. Donaldson (1974) assumed a variety of mechanisms, including the role of volatiles such as water, which might lower the liquidus temperature and promote undercooling. However, there has been no supporting evidence for the role of volatile exsolution produced (i.e., prominence of hydrous mineral phases). As such, O'Driscoll *et al*. (2007a) put forward an alternative mechanism; a chilling effect between the picrite and resident magma. The evidence for sill emplacement of harrisite presented in Chapter 2 meant this model needed to be adapted, instead assuming the chilling effect occurred upon contact with a lower temperature crystal mush, promoting coarse-grained (and skeletal) crystal growth without significant volumes of water (see Chapter 2; Hepworth *et al*., 2017).Indeed, the net reduction in temperature during gabbro assimilation proposed by Renna *et al*. (2016) for ophiolitic harrisite also points to the important control of host temperature during crystallisation of anhydrous, coarse-grained crystals. This was used more extensively in the WLI, where a systematic change of olivine morphology could be used to reconstruct a simple thermal history during crystal mush development. Harrisite has been used extensively as evidence for processes such as sill emplacement and *in situ* crystallisation in the RLS, but the wider applicability of these concepts is currently unknown due to the seeming rarity of harrisite-type peridotites within other layered intrusions.

Harrisite was first recognised as a pegmatite by Harker (1908), but this classification is not utilised in favour of its type-name, despite representing a pegmatite (or pegmatoid) texturally (crystal size >1 cm). Coarse-grained, pegmatoidal layers, consisting of cm-sized crystals, are common in layered intrusions. Olivine-rich pegmatoids in the Stillwater Complex are associated with chromitite and PGE-deposits (Campbell & Murck, 1993; Boudreau, 2016; Fig. 5.1), with olivine and orthopyroxene-rich varieties in the Bushveld Complex also associated with major chromitite (and PGE) deposits (Cawthorn & Boerst, 2006; Mondal & Mathez, 2007; Wilson, 2015), and gabbroic pegmatoids in the Skaergaard Intrusion (Larsen & Brooks, 1994). Unlike typical pegmatites, hydrous phases are not a major component in mafic–ultramafic pegmatoids. The lithologies all have similar attributes to

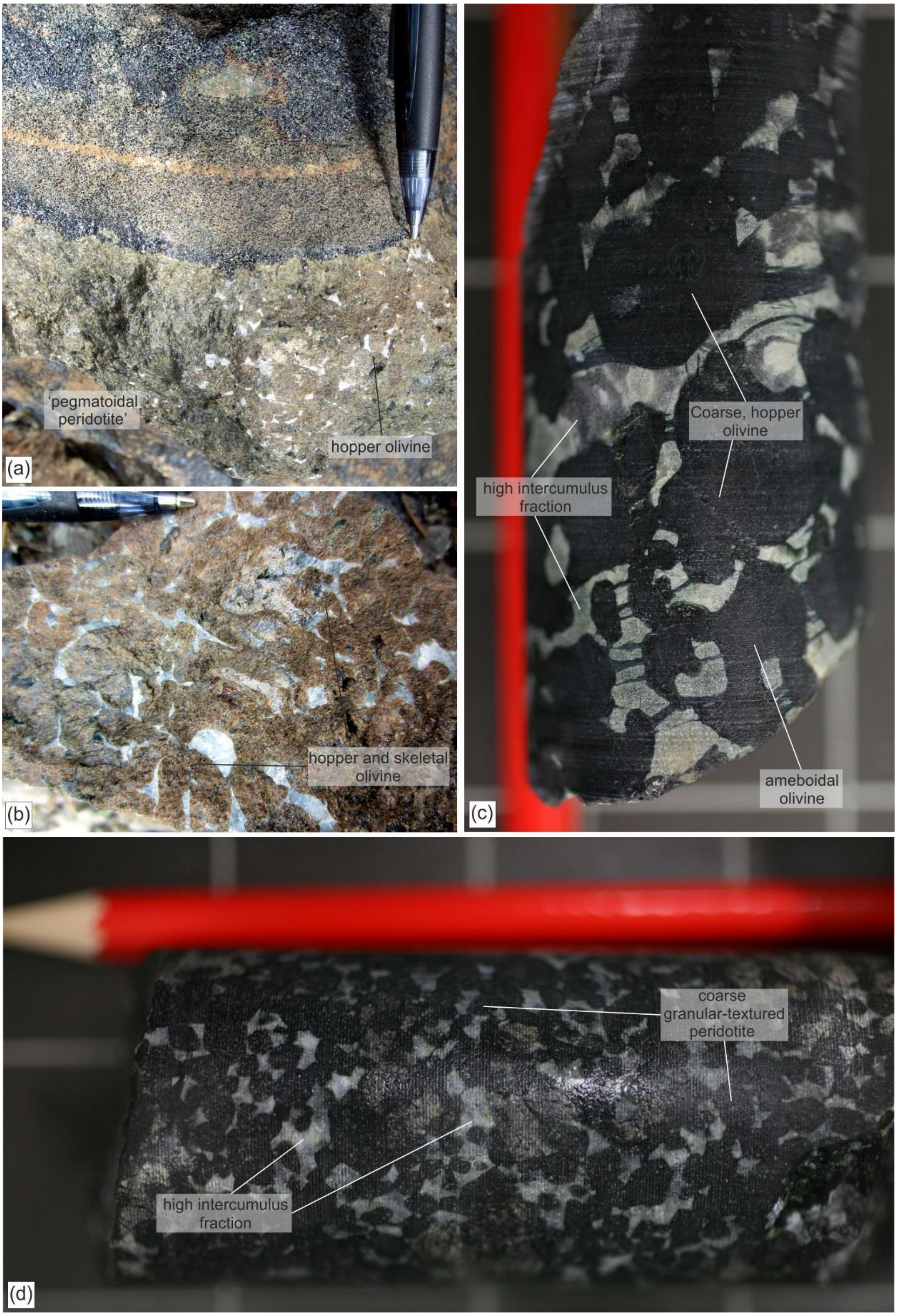

FIGURE 5.1: Pegmatoidal lithologies in the Stillwater Complex, Montana, USA. (a) Very coarse (> 1cm) hopper olivine from the Ultramafic Series. (b) Close up of hopper and skeletal olivine morphologies in ‘pegmatotidal peridotite from the Ultramafic Series. (c, d) Ameboidal and hopper olivines, and coarse-grained granular layers, respectively, from the J-M Reef, Middle Banded Series. Note also the high-intercumulus volume across samples.

harrisite found on Rum, with coarse, skeletal and/or hopper (ameboidal) morphologies are common. The intercumulus (interstitial) crystals are also very coarse. Olivine studied from samples collected in 2016 from the ‘pegmatoidal peridotites’ in the Ultramafic Series and J-M Reef of the Stillwater Complex (USA) are texturally comparable to olivine crystals found in harrisite discussed throughout the RLS (Fig. 5.1), where hopper and ameboidal morphologies dominant cumulus crystals (Fig. 5.1a, b, c), notably bounded by chromitite (Fig. 5.1a). Layered coarse-grained granular-textured morphologies also occur in layers within the J-M Reef PGE-deposit (Fig. 5.1d). Furthermore, olivine and pyroxene crystals from the Merensky Reef and UG2 pegmatoids (Bushveld Complex) have similar morphologies to harrisite (e.g., Cawthorn & Boerst, 2006; Mondal & Mathez, 2007; Latypov *et al*., 2017), particularly to the complex variety of olivine crystals (e.g., hopper varieties) in the WLI in Chapter 4.

The crystals, irrespective of their composition, have grown exponentially larger than surrounding layers, apparently without the significant volume water typical of pegmatites (e.g., Donaldson, 1974). Indeed, the textures of pegmatoidal crystals across layered intrusions are very similar to crystals within harrisites in the RLS, and may point to a common origin, where the sill (and chill) emplacement mechanism proposed here for the petrogenesis of coarse-grained lithologies is not necessarily limited to olivine, but applicable to pyroxene and feldspar (Donaldson *et al*., 1973). Where mafic–ultramafic pegmatoids in layered intrusions are associated with high-grade ore deposits (e.g., Merensky Reef, UG2, and J-M Reef), the consequence of a sill emplacement model implied by associated pegmatoids has significant implications for the concentration of precious metals, where careful quantitative comparison may potentially identify new markers for sill emplacement in layered intrusions (*cf*. Mungall *et al*., 2016). This identification criterion might be of importance where field study, and the identification of conclusive features, is not possible, but pegmatoidal, and other very coarse-grained lithologies occur as distinct layers in drill core.

5.2 SILLS IN THE RUM EASTERN LAYERED INTRUSION

Harrisite has been used as the main line of evidence for sill emplacement Unit 10 and the WLI (see above). The numerous harrisite layers found therein imply that the crystal mush was constructed incrementally, by numerous small volume replenishment events (*cf*. Wadsworth, 1961; O'Driscoll *et al*., 2007a). The conclusion asks the question as to how common harrisite is in the ELI (and wider RLS) and does this imply sill emplacement as it does in Unit 10 and WLI? The identification of sill emplacement with other macro-rhythmic units would require the classic cyclic model to be reconsidered, and potentially replaced formation via sill emplacement first suggested by Bédard *et al*. (1988), with the potential to expand the model across the RLS where evidence points to intrusion/sill emplacement of peridotite (Volker & Upton, 1990).

The peridotite portions of ELI units have not been well documented. Here, observations are documented on the peridotite portions of Unit 7, 8, and 9, with the aim to better catalogue any features of sill emplacement highlighted above and to provide insight into the broad construction of this classic layered complex. Figure 5.2 highlights the complexity of peridotite/feldspathic cumulate boundaries from Unit 7, 8, and 9. The Unit 7 boundary (Fig. 5.2b) protrudes the overlying troctolite, cross-cutting it by >1 m vertically and laterally. Smaller apophyses cutting into the troctolite also occur all along the boundary, typically <10 cm high (Fig. 5.2c). Harrisite is also abundant within the Unit 7 peridotite, with composite layers present (Fig. 5.3a). The Unit 8 peridotite has a similarly irregular boundary and is also laterally discontinuous (Fig. 5.2a), with portions seeming missing. Indeed, the thickness of Unit 8 also increased by ~20 m with proximity from the LLF. The peridotite of Unit 8 is very lithologically diverse (Fig. 5.2d), which are not ubiquitous laterally, with all four varieties present only with distance away from the LLF. Nearer to the LLF (i.e., Figure 5.1; Barkeval), only well-layered and harrisite-bearing peridotite is present showing upward-oriented apophyses cutting into the overlying peridotite (Figs. 5.3b; 4a). Unit 9 as shown in Figure 5.2a contains large domes of harrisite cross-cutting the overlying troctolite (including the 'wavy horizon') and into the base of the Unit 10 peridotite. In addition to this, the Unit 9 and 10 peridotites coalesce (Fig. 5.2e), with similar observations between Unit 8 and 9 (Fig. 5.2a). Unit 9, like Unit 10, contains very similar harrisite layers which terminate laterally, bifurcate, and display upward-oriented apophyses that protrude the overlying peridotite (Figs. 5.3c; 4d). Like Unit 10 (Chapter 2), all three peridotites contain at least two distinct peridotite types, an overlying poikilitic variety(cpx-oikocrysts) and an underlying well-layered (harrisite-bearing) variety. The poikilitic peridotite is absent in Figure 5.2a (nearer to the LLF) in all three Units but is present and often thicker with distance from the LLF (around Hallival). Both peridotite types display the features described above, with harrisite only present within the well-layered peridotite.

On first order observation, the two distinct peridotite types per unit suggest at least two replenishment events like Unit 10 (Tait, 1985; Palacz & Tait, 1985; Chapter 2). The fact both peridotite types display numerous features of sill emplacement outlined above, suggests they formed as sills into pre-existing cumulate, and not on the magma chamber floor. Indeed, as the well-layered peridotite is only find with proximity to the source, and the chronology outlined in Chapter (Hepworth *et al*., 2017), suggests the well-layered peridotite intruded later than the poikilitic peridotite. Previously undocumented occurrences of harrisite layers in Unit 7, 8 and 9 displaying upward-oriented apophyses, bifurcation and lateral termination points to an incremental, small volume replenishment process highlighted in Chapters 2 and 4. Another important conclusion that could be drawn from coalescence of many peridotite bodies close to the LLF is that many of the peridotite have a braided geometry, connecting with proximity to the source, and do not represent discrete ‘unit’ events, but instead a random juxtaposition of peridotites into troctolites and gabbros, with no genetic relationship (e.g., Palacz, 1984; 1985). That is to say the peridotites of Unit 9 and Unit 10 (or more) represent the same replenishment episode, separated only by pre-existing feldspathic cumulate, with no strictly defined construction pattern (i.e., bottom up). The ELI units proposed by Brown (1956) become less well defined, particularly where evidence suggests they are not products of fractionation, but spatially juxtaposed igneous intrusions.

5.3 FORMATION OF CR-SPINEL SEAMS BY INTRUSION INTO CRYSTAL MUSHES

Cr-spinel seams are an integral feature of the RLS peridotites. They are closely associated with harrisite, often occurring along the tops, bases, and interiors of these layers. As such, the seams must have formed *in situ* within the crystal mush, as harrisite best represents sill emplacement within the RLS. Evidence supporting this conclusion includes vertically-oriented or bifurcating Cr-spinel seams, where crystal settling is implausible (*cf*. Latypov *et al*., 2013). Furthermore, quantitative


Unit 8 peridotite?
(missing?)
Unit 10 peridotite
Unit 9 allivalite
Unit 9 peridotite
Harrisite
dome
Unit 9 allivalite
Unit 9 peridotite
Unit 10 peridotite
Unit 8 allivalite
Unit 7 allivalite
?
?
Unit 8 peridotite
(a)
Unit 7 allivalite
Unit 7 peridotite
(b)
Unit 7 allivalite
cross-cutting
Unit 7 peridotite
(c)
wehrlitic schlieren
feldspathic peridotite
poikilitic peridotite
(d)
No distinction between
Unit 9 and 10 peridotite
Unit 9 (allivalite)
Unit 10 (peridotite)
10?
9?
U9 peridotite
U9 allivalite
truncated by
peridotite
(e)

◀FIGURE 5.2 Field relationships of Unit 7, 8, and 9 in the ELI. Note that allivalite is used here to describe both troctolite and gabbro in the feldspathic cumulate (Harker, 1908). (a) Complex field relationships between peridotite and feldspathic cumulate (allivalite) east of Barkeval. (b) Small-scale apophyses in the Unit 7 peridotite, cross-cutting into the overlying feldspathic cumulate. (c) Metre-scale cross-cutting protrusion of the Unit 7 peridotite into the overlying cumulate. (d) Peridotite types in Unit 8. Note sharp (and undulose) reduction in clinopyroxene into the feldspathic peridotite. See also the brown, wehrlitic peridotite schlieren. (e) Field relationships in the Unit 9 peridotite around Barkeval, with cross-cutting

textural analysis across a range of seam textures reveals a markedly uniform, and simple crystallisation process *in situ*. The relationship between harrisite and Cr-spinel seam was suggested to occur syn-genetically with harrisite, where the injection of picrite produced a Cr-spinel seam from the dissolution of intercumulus plagioclase strongly supported by intracrystalline zoning patterns (Chapter 3). The spatial relationship between the sill and seam was therefore determined by the degree of sill propagation, with intra-harrisite Cr-spinel seams representing additional through flow and assimilation within the rapidly crystallising sill (O'Driscoll *et al*., 2007a). The spectrum of textural and mineral chemical characteristics within WLI Cr-spinel seams (Chapter 4) with the same harrisite association and simple, *in situ* crystallization conditions was expanded from the ideas in Chapter 2, where seams represent isolated melt channels. It was suggested the continuum of characteristics was best explained by the progressive development of these channels within the crystal mush, where chemistry and textural was determined by the degree of through flow of melt (see Fig. 4.22).

Beside those found within this study, peridotite-hosted Cr-spinel seams have been documented in two other peridotite bodies in the ELI. O'Driscoll *et al*. (2010) noted chain-textured seams in the Unit 12 peridotite, just above the main boundary chromitite. Further note of peridotite-hosted seams are from Unit 8, where cm-thick Cr-spinel seams occur (Henderson, 1975). Peridotite-hosted Cr-spinel stringers have also been recognised in the CI (Volker & Upton, 1990). As harrisite has been shown to be an almost ubiquitous feature of peridotites in the RLS, it is no surprise that Cr-spinel are just as common in Unit 7, 8 and 9. The identification of more seams, particularly if they are as abundant as those show in Unit 10 (and WLI), highlight the importance role of incremental construction in layered intrusion growth (see above), and provide new insight into the concentration of precious-metals associated with these types of mineralisation.

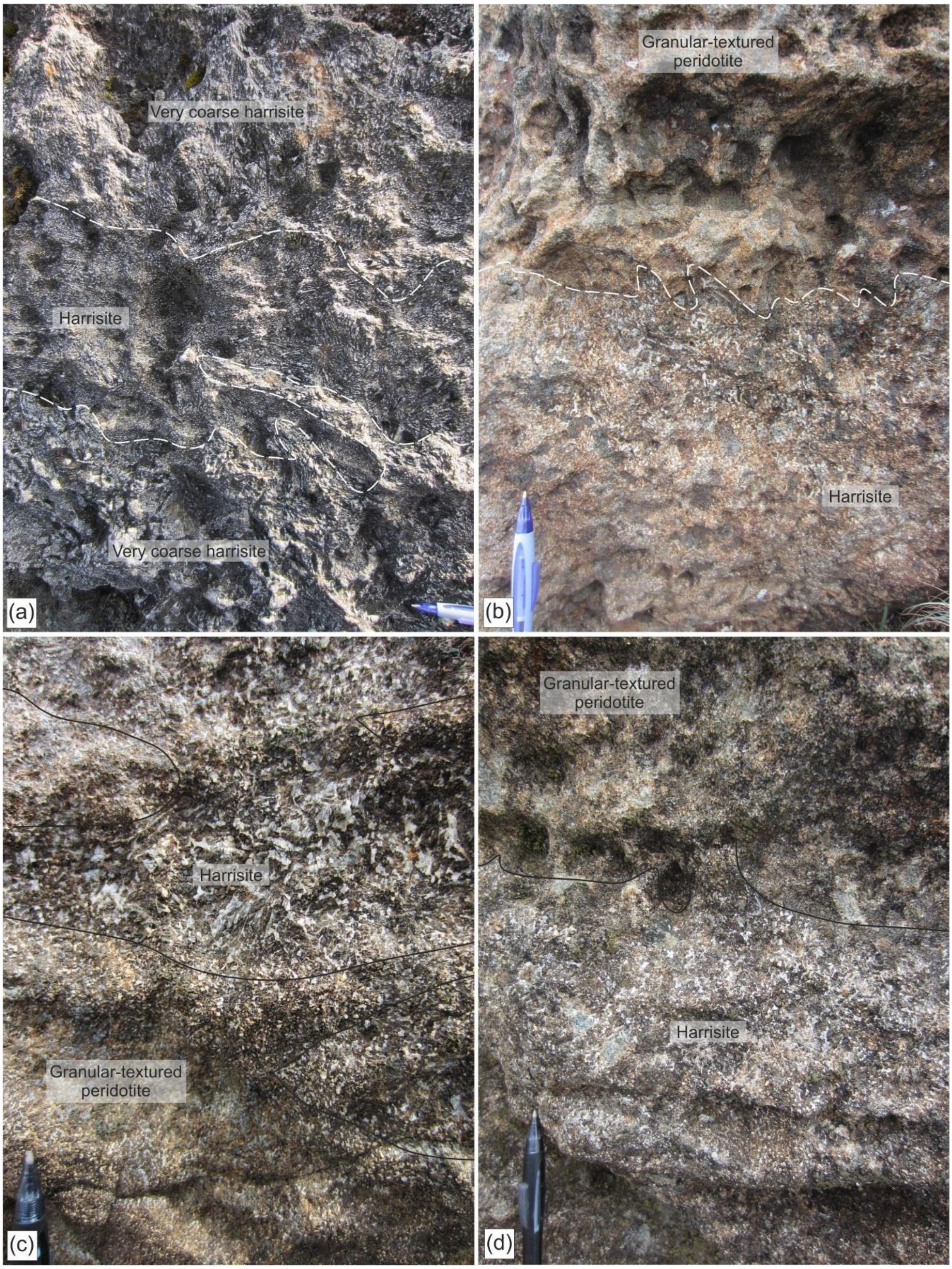

FIGURE 5.3: Harrisite from the ELI. (a) Composite harrisite layer in the Unit 7 peridotite. (b) Interlayered harrisite (with upward-oriented apophyses) and granular-textured peridotite in the lower Unit 8 peridotite with characteristic cm-sized cpx oikocrysts for Unit 8. (c) Irregular, bifurcating harrisite layer in the Unit 9 peridotite. (d) Harrisite with upward-oriented apophyses like (b) in Unit 9.

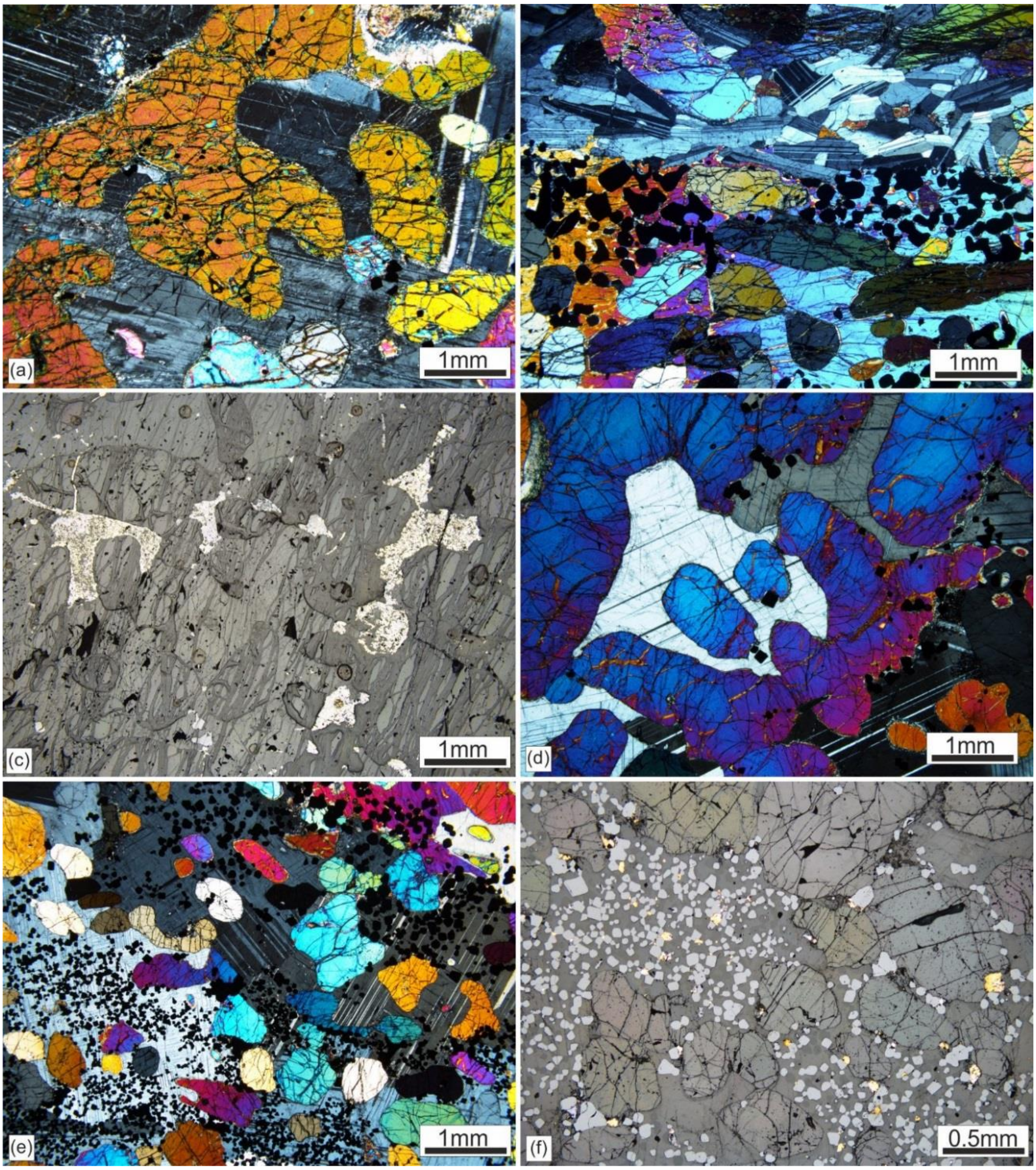

FIGURE 5.4: Petrographic features of the Unit 8 and 9 peridotites. (a) Harrisitic olivine from the 'feldspathic peridotite' in the Unit 8 peridotite (see Fig. 4.1d). (b) Cr-spinel seam in wehrlitic peridotite from Unit 8, note the single large cpx-oikocryst in the bottom half of the image, and anorthosite schlieren above the seam. (c) Reflected light image of large interstitial sulphides from wehrlitic peridotite in Unit 8. (d) Harrisitic olivine from the Unit 9 peridotite east of Barkeval. (e) Composite Cr-spinel seam with coarse upper portion from Unit 9. (f) Reflected light image of abundant sulphides from the Cr-spinel seam depicted in (e).

The Unit 7 well-layered peridotite contains numerous Cr-spinel seams, often defining layers in the peridotite, much in the same way illustrated in Chapters 2 and 4, with many of the seams hosted within in granular-textured peridotite (Fig. 5.5a). The seams typically < 5mm thick, and laterally continuous only for tens of metres, which display a chain-texture described by O'Driscoll *et al*. (2010). Two out of the four peridotite types in Unit 8 contain Cr-spinel (and chromitite) seams; the well-layered peridotite and the wehrlite (Fig. 5.4b;.5b). Seams found within the Unit 8 well-layered peridotite are unusually thick (up to 2 cm) and define the main mode of layering (Fig. 5.5e). Like other seams, they are chain-textured, with particularly high densities of Cr-spinel, with some classified as chromitites (>>60% vol. Cr-spinel). The second Cr-spinel seams occur within wehrlite schlieren at the very top of the Unit 8 peridotite. They are highly discontinuous, typically traceable for less than 1 m. Unlike other Cr-spinel seams, they are almost entirely enclosed by clinopyroxene with distinctly ameboidal Cr-spinel textures (Fig. 5.4b). The Cr-spinel seams within Unit 9 are akin to those found in other peridotites (e.g., Unit 10), with thin (<5 mm) seams associated with harrisites, or with granular-textured peridotites. However, seams within Unit 9 are particularly fine-grained (<0.1 mm; Fig. 5.6) with composite textured seams recognised. Patchy zoning of intercumulus plagioclase is particularly notable in Unit 9, but common in Unit 7 and 8 as well. Uniquely to Unit 8 (wehrlite) and 9, these seams are very sulphide-rich, often with mm-sized blebs occurring between the olivine framework or attached to Cr-spinel crystal faces (Figs. 5.4c, f). Lastly, the CI also hosts Cr-spinel and chromitite seams (and stringers), first noted by Volker & Upton (1990), but often oriented vertically or sub-vertically, typically hosted in coarse-grained peridotite or associated with large volumes of harrisite (Fig. 5.5f).

One important conclusion to be drawn from the discovery of abundant Cr-spinel seams in other peridotite bodies in the RLS is that it points to more replenishment events than even the number of harrisite layers suggest, supporting mush construction by incremental, small volume replenishment. The spatial association of Cr-spinel seams and harrisite (or coarse-grained peridotite) like those in previous chapters point to a co-genetic relationship. This means the Cr-spinel seams also formed within the crystal mush, supported by the intrusive evidence given previously on peridotites in Unit 7, 8, and 9. Furthermore, the harrisite association also points to crystallisation *in situ*. Preliminary

FIGURE 5.5: Cr-spinel seams from the RLS. (a). Layering in the Unit 7 peridotite defined by Cr-spinel seams. (b) Chromitite seam in wehrlitic peridotite from Unit 8. (c,d) Cr-spinel seams in the Unit 9 peridotite, note the proximity to the allivalite, including Wavy Horizon of Holness *et al.* (2007). (e) Thick Cr-spinel seams within coarse-grained granular-textured peridotite from the base of the Unit 8 peridotite. (f) Vertically-oriented Cr-spinel seam in peridotite from the CI.

textural analysis highlights a particularly simple crystallisation process discussed throughout the previous chapters to be a function of *in situ* crystallisation (Fig. 5.6). Post-cumulus modification in Unit 8 and composite seams in Unit 9, marked by the shallowing of the CSD slope, reveal additional complexity which could indicate processes such as infiltration metasomatism in the case of the cpx-hosted seams in Unit 8, or potential multiple generations of melt interaction in Unit 9 suggested in the WLI (Chapter 4). Indeed, the composite seams found in Unit 9, which given the abundance of sulphides, may indicate a similar melt channel process described in the WLI. The CI's abundance of vertically-oriented Cr-spinel seams further highlights the importance of *in situ* crystallisation for the formation of seams, where features presented here and in other peridotite bodies in the RLS might be explained by a comparatively simple melt-channel model (see Fig. 4.21), akin to processes operating in the ophiolitic mantle (González-Jiménez *et al*., 2014).

The applicability of this model is not necessarily limited to the RLS. Chromitite seams from the Ultramafic Series of the Stillwater Complex, USA, have the same association with the pegmatoidal peridotite (see above discussion) as Cr-spinel seams have with harrisite in the RLS. Many textures, such as anastomosing chromitite stringers are extremely similar to those in the WLI (Jackson, 1961; Fig. 5.3a), suggesting the discrete melt-channel model may be directly scaled up to much larger olivine-rich intrusions like Stillwater Complex. Furthermore, the geochronological work of Mungall *et al*. (2016) showed major chromitite horizons represent discrete events. This is a particularly important example, as the Bushveld Complex is the largest and most economically important source of platinum-group metals on Earth (Mungall & Naldrett, 2008); but where the petrogenesis of these deposits is still contentious. If the major chromitite horizons are discrete events, unrelated to the surrounding cumulate (Mungall *et al*., 2016), the melt channel model can easily account for the layer, despite the difference in scale. Replenishment events into the Bushveld Complex were undoubtedly vast, such that resultant layers will be particularly thick, scaled with volume replenished. The model might also be relevant where large-scale braiding occurs in chromitite layers, where intrusive or intra-mush petrogenesis has already been suggested (Voodouw *et al*., 2009; Mukherjee *et al*., 2017). The occurrence of pegmatoidal lithologies alongside many major chromitites in the Bushveld Complex (see Mondal & Mathez, 2007; Latypov *et al*., 2015) might further support this speculation,

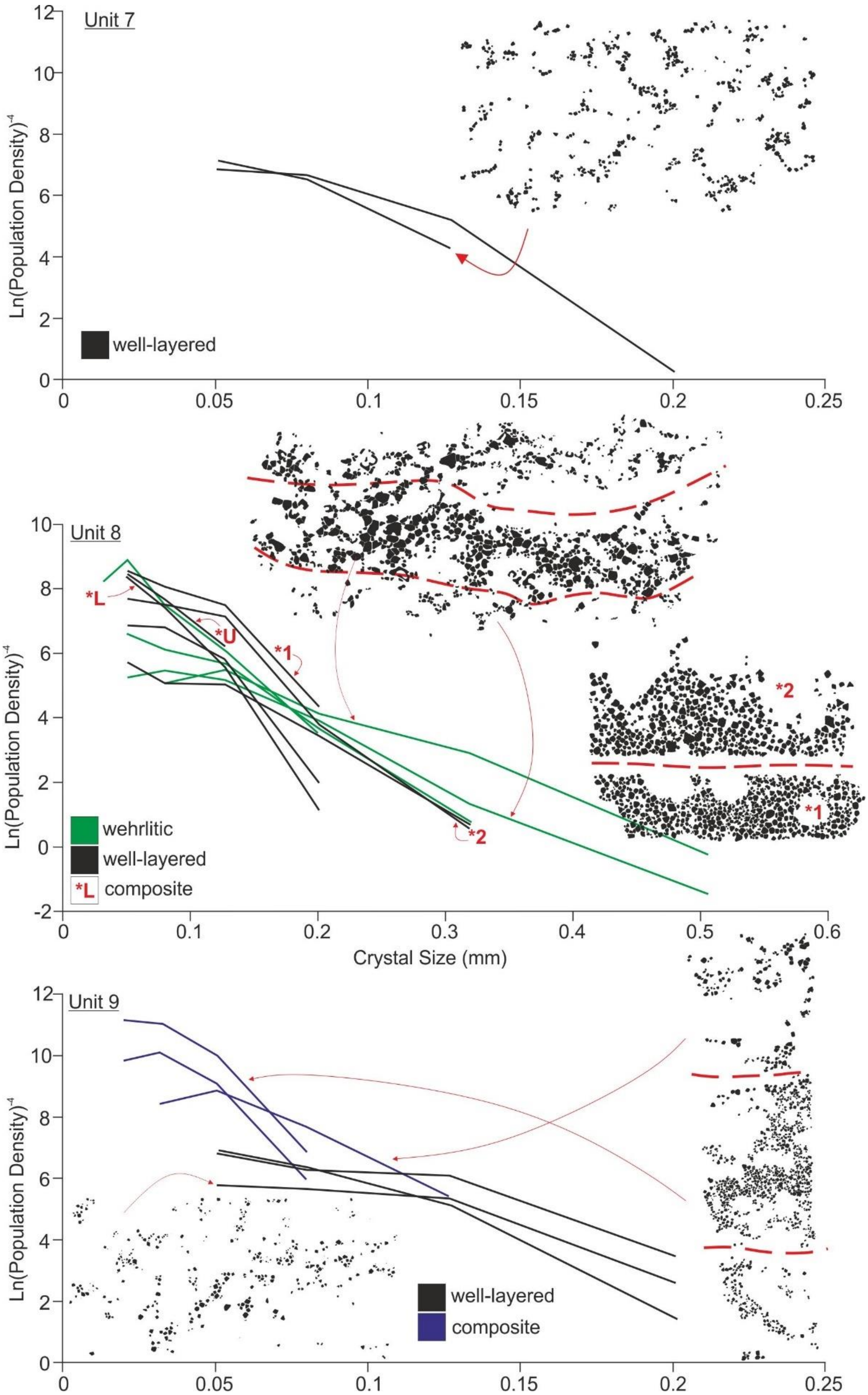

FIGURE 5.6: CSD profiles for Cr-spinel seams from the Unit 8 and 9 peridotites. The Unit 8 profiles are very shallow, suggestive of a coarsening effect (note that these are typically hosted in clinopyroxene). The Unit 9 profiles are considerably finer grained and steeper. Overall, the profiles are log-linear like those in previous chapters, pointing to a simple crystallisation process *in situ*.

where the importance of discrete, intra-mush modes of formation has yet to be explored fully, particularly where evidence *in situ* crystallisation is recognised (Latypov *et al*., 2017). The study of these important layers should be considered independent from one another, where superposition does not necessarily imply co-genesis, especially where evidence reveals unconformities of tens of thousands of years (Mungall *et al*., 2016; Wall *et al*., 2018). Lastly, the implications of a melt-channel model to precious-metal concentration within these spinel horizons are significant. The model points to metal enrichment *in situ* where the mass balance issue of generating such high R-factors can be accounted for by though flow within melt channels, where more melt has passed through the channel than is represented by the observed volume, an idea strongly supported by the Sr-isotope evidence presented in Chapter 3.

5.4 HOT TEARING AND THE DEFORMATION OF CRYSTAL MUSHES

If harrisite and Cr-spinel seams are entering the mush via the same process the strict parallelism of the two features must be accounted for. Well-oriented segregations and schlieren have been noted in both extrusive and intrusive igneous rocks, including layered intrusions, where they are formed via the mechanical deformation (e.g., shearing) of the crystal mush under gravitational stress (e.g., Marsh, 2002; Humphreys & Holness, 2010; Namur *et al*., 2013). An adaptation of this process, known as 'hot tearing,' was suggested for the Unit 10 peridotite (Chapter 2; Hepworth *et al*., 2017). The gravitational shearing of the crystal mush caused interconnected weakness (akin to fault formation) which allowed magma into the crystal mush in order to crystallise Cr-spinel seams and harrisite sills. The stress acting on the crystal mush, sagging towards the feeder zone will have imparted a strict (though not necessarily intense) stress regime, resulting in pervasive layer parallelism between any intruding magma and related reaction products (e.g., Cr-spinel seams). To facilitate hot tearing, crystal mushes require high-crystallinity frameworks (up to 90%; Marsh, 2002; Chapter 2; Hepworth *et al*., 2017) such that solid-state (sub-solidus) processes might begin to become important. The process of hot tearing (and shearing) of crystal mushes is poorly understood, with very limited experimental data, or data from natural examples (Marsh, 2002). However, the wellordered structure in layered intrusions, such as distinct schlieren or lenses (or layers themselves) are structurally comparable to banding in many metamorphic rocks (e.g., Lucas & St-Onge, 1995; Glazner & Boudreau, 2011). The nature of active crystal mushes (i.e., their crystallinity) is uncertain, but many features such as those highlighted here and in Humphreys & Holness (2010) attest to a pervasive control akin to shearing, which cannot be accounted for at crystallinities lower than 60% (Marsh, 2002), but potentially up to 90% (Chapter 2; Hepworth *et al*., 2017). As such, a particularly pertinent area for future study should be the structural analysis of cumulate rocks in the field, identifying the relationships of so-called ‘slump structures’ that may very well represent shearing, especially where strong outcrop-scale trends in features such as layering/banding, foliation, vergence, or slump/fold-axis are found. The combination of detailed field measurements with quantitative crystallographic studies might better highlight the importance of rheomorphic (post-cumulus) processes on the final texture of cumulates in layered intrusions. (e.g., Holness *et al*., 2017a).

5.5 THE ‘RUM SILL COMPLEX’

The conceptualisation of magma chambers as open bodies of crystal-poor magma is so deeply rooted in petrology that thick sheets of magma situated above crystal mushes are assumed to exist despite the absence of supporting evidence, an issue not isolated to the study of layered intrusions (*cf*. Cashman *et al*., 2017). However, this view is particularly prevalent in layered intrusions, where the discovery of the Skaergaard Intrusion in East Greenland significantly influenced the processes ascribed to the development (and conceptualisation) of magmatic bodies (Wager & Deer, 1939; Wager *et al*., 1960). There are important consequences for a pre-conceived conceptualisation when working in ‘natural laboratories’ for magma differentiation, leading to an overwhelming bias to the construction mechanisms and modes of magmatic differentiation commonly assumed to occur with height (e.g., Tepley & Davidson, 2003; Latypov *et al*., 2003; Tegner *et al*., 2009; Boudreau, 2016; Latypov *et al*., 2013; Holness *et al*., 2017b). As such, the intrusive model of the ELI by Bédard *et al*. (1988) still included a large open body of magma with this idea carried forward by Emeleus *et al*.

(1996) who provided the widely-used conceptualisation of the RLS where the crystal mush is overlain by a substantial thickness of crystal-free (or poor) magma (Fig. 1.1). Large igneous intrusions, such as granitic intrusions, or sub-arc magma systems, are generally not considered to form via simple large-scale replenishment or magma fluxes into the crust, as this produces a crustal accommodation issue, and are instead thought to form via an incremental process, with smaller sheets of magma slowly producing larger crystal mushes (e.g., Leuthold *et al*., 2012; Annen *et al*., 2015; Cashman *et al*., 2017).

It was argued here that the Unit 10 peridotite and WLI formed entirely by incremental sill emplacement, roofed by pre-existing cumulate as the Unit 10 allivalite, or the Western Granite in the WLI (Chapter 2 and 4, respectively), where filter-pressing has trapped liquid towards the top of the crystal mush (Chapter 4) or caused partial melting and metasomatic markers in the overlying cumulate (Chapter 2; Hepworth *et al*., 2017). This is strongly supported for the evidence for cold-storage style magmatism for Unit 10 in Chapter 3, where it was suggested crystallisation is extremely rapid (<100s years) once emplacement occurred. Furthermore, evidence has also been put forward to suggest Unit 7, 8, and 9 are formed by incremental construction (see above). As such, the same incremental construction model should be applied to layered intrusions (*cf*. Leuthold *et al*., 2012). A new conceptual model is presented for the RLS (Fig. 5.7), combining the detailed observations here and in previous chapters, including other suggestions against traditional magma chamber models (Bédard *et al*., 1988; Mungall *et al*., 2016; Cashman *et al*., 2017; Wall *et al*., 2018). In the new model, the RLS represents a sill complex, where peridotites represent the emplacement of sills into pre-existing feldspathic cumulate (i.e., allivalites). The macro-rhythmic units of the ELI therefore represent various levels of peridotite emplacement into a pre-existing feldspathic host cumulate, isotopically distinct from the peridotite (Palacz, 1984; Palacz, 1985; Palacz & Tait, 1985). The WLI was intruded via the same process at a structurally lower level to the ELI, formed by sill emplacement of picritic magma, with the relative age between these two cumulate packages currently unknown. The CI, the youngest part of the RLS still represents the deformed remnants of the WLI and ELI, intruded by significant volumes of peridotite (Volker & Upton, 1990). This new conceptualisation is a significant departure from models of layered intrusion growth, instead suggesting the RLS is a sill

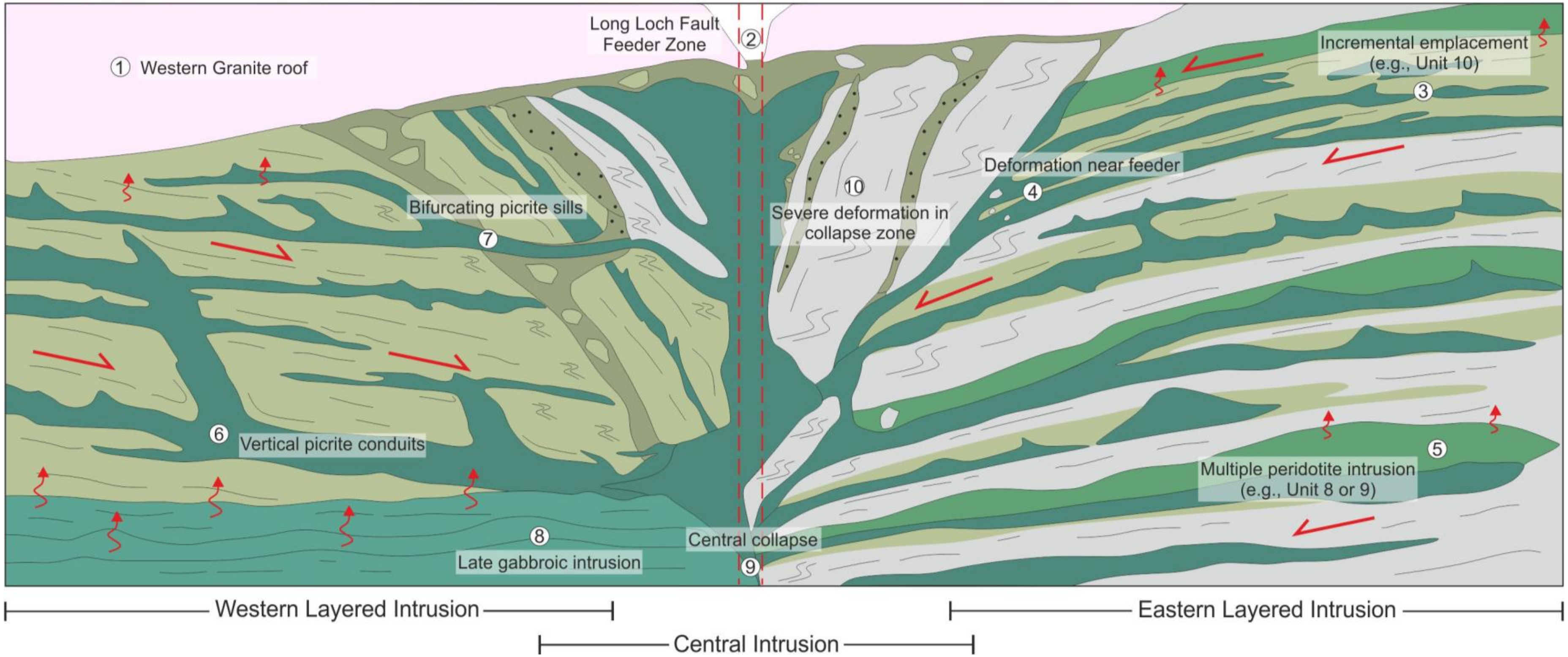
① Western Granite roof
Long Loch Fault Feeder Zone
②
Incremental emplacement (e.g., Unit 10)
③
Deformation near feeder
④
⑩
Severe deformation in collapse zone
Bifurcating picrite sills
⑦
⑥
Vertical picrite conduits
⑤
Multiple peridotite intrusion (e.g., Unit 8 or 9)
⑧
Late gabbroic intrusion
Central collapse
⑨
Western Layered Intrusion
Central Intrusion
Eastern Layered Intrusion

◄FIGURE 5.7: New conceptualisation for the RLS as an incrementally developed crystal mush, with no overlying magma body. Red arrows indicate metasomatism where found in the RLS. Based on the results of this study. (1) The pre-existing Western Granite roofing the western and potentially the eastern extent of the complex. (2) The LLF feeder zone and fault active during the development of the complex, bisecting the entire complex, causing central collapse. (3) Unit 10-like development of peridotite bodies, with repeated small volume replenishment into pre-existing feldspathic cumulate. (4) Proximity to the fault causing localised deformation where autoliths and high mobility crystal mush is found. (5) Unit 9 (and 8)-like development of the crystal mush, with varied input of magma, including small volume and larger volume replenishment into pre-existing feldspathic cumulate. (6) Development of the WLI by small volume replenishment into the crystal mush and the development of conduit systems feeding magma deep into the crystal mush. (7) Sill-like emplacement and bifurcation of intrusive body forming multiple layers per conduit. (8) Late intrusion of gabbroic, HBM, alongside gabbroic plugs and intrusions around Barkeval, for example. (9) Central collapse of the crystal mush into the feeder under gravitational stress during movement of the LLF. (10) Deformation associated with central collapse of the crystal mush, causing shearing, brecciation, and varied influx of magma into the highly mobile zone.

complex intruded into pre-existing feldspathic cumulate, originally suggested by Harker (1908). Under the crystal mush model, processes such as density currents and ‘soft-sediment’ deformation are no longer compatible within a high-crystallinity mush, where rheomorphic processes (i.e., syn-magmatic shearing, gravitational sagging, and cataclasis) must be considered.

5.5 PROBLEMS OF FORCED BIAS, SCALE, AND THE DEFINITION OF LAYERED INTRUSION

There is currently no consensus on the definition of layered intrusion. At the very broadest level, a layered intrusion might be defined simply ‘an intrusion that is layered’. However, this definition is only satisfactory for closed systems such as the Skaergaard Intrusion, where layering is a product of internal fractionation or process within a single magmatic body (a singular intrusion). The definition cannot be applied so easily to open-system layered intrusions, which are built-up of many magma pulses solidifying at different rates (and times), and by the same definition, it is not a layered intrusion but many. The definition is ultimately negated by the evidence presented in this study and by a few authors previously (Harker, 1908; Bédard *et al*., 1988; Mungall *et al*., 2016; Wall *et al*., 2018) where layering, as a defining feature of layered intrusions, is an artefact resulting from the juxtaposition of sills which have not internally fractionated layering. This relationship is more akin to a sill complex or lava pile, constructed of multiple bodies and lobes (*cf*. Houlé *et al*., 2009; Zieg & Marsh, 2012). If a new paradigm of viewing magmatic bodies as incrementally built-up crystal mushes is to be accepted, the definition of layered intrusion must change or be better defined, as many of what are perceived to be layered intrusions are in fact sill complexes. The RLS studied here is a prime example of this contention. Throughout this study it has been proposed that the layered intrusion is not a single intrusion, but a series of sills, intruded into igneous lithologies that are not related, even by parental composition, particularly true for the ELI (Palacz, 1984; 1985; Palacz & Tait, 1985; Greenwood, 1987; Chapter 2; Hepworth *et al*., 2017). This relationship is no different to a composite sill intruded along a bedded sedimentary lithology (e.g., Zieg & Marsh, 2012; Leuthold *et al*., 2012), but the intrusion of ultramafic and mafic lithologies intrusion into other mafic igneous lithologies instils a strong forced bias based upon the basaltic fractionation sequence; olivine–plagioclase–clinopyroxene (e.g., Brown, 1956). As such, the ELI unit divisions are arbitrary, and should not be considered progressive units at all as they represent the random juxtaposition of compositionally, isotopically, and often texturally disparate igneous lithologies (Palacz, 1984; 1985; Tait, 1985; Palacz & Tait, 1985; Renner & Palacz, 1987; Bédard *et al*., 1988; Holness & Winpenny, 2008; Chapter 2; Hepworth *et al*., 2017; see above).

The difference in scale between layered intrusions is marked as a major obstacle when extrapolating processes between them, resulting in a plethora of intrusion-specific processes that are not applicable to one another, despite resulting in the same feature (e.g., chromitite layers). There are strong similarities between the RLS and Bushveld and Stillwater Complexes despite the variation in scale (Jackson, 1961; Latypov *et al*., 2013; Chapter 2; Hepworth *et al*., 2017; Chapter 3; Wilson, 2015; see above). Critically, what a magma chamber floor might be to the Bushveld or Stillwater Complex is merely a sill to the RLS, fundamentally the same process of replenishment, differing only in scale, capable of producing the same feature, scaled in accordance to the volume of replenishment. The only tangible obstacle to study layered intrusions is the ability to study it in three dimensions, where much study of large intrusions is limited to drill-core, masking bifurcation, anastomosing layers, or types of folding and slumping, all key to a well-informed interpretation. The RLS, due to its small size, makes it an ideal locality to study the processes of layered intrusion (or sill complex) formation, where features can easily be documented within the field, and considered (and scaled up) for larger intrusions where field study is logistically impossible.

Finally, many concepts in layered intrusion petrology were developed on discovery of the Skaergaard Intrusion in Greenland, which strongly influenced the way igneous processes and magmatic bodies are viewed (Wager & Deer, 1939; Wager *et al*., 1960). However, there is evidence of open-system behaviour recognised in the Skaergaard Intrusion (Holness *et al*., 2015), making the important point that this type-example may not be formed so disparately from other igneous intrusions, where a uniformitarian model of layered intrusion development as sill complexes (e.g., Mungall *et al*., 2016; Cashman *et al*., 2017), typically dismissed due to differences of scale, lithology, location, and pre-conception, is perhaps more applicable than is currently willing to be accepted (*cf*. Marsh, 2013; Latypov *et al*., 2015; Marsh, 2015).

CHAPTER 6 – CONCLUSIONS

The main conclusions drawn from this study of layered peridotite sequences from the ELI and WLI are summarised below;

- Harrisite layers, consisting of complex (hopper–skeletal) olivine morphologies, best represent sill-like intrusions emplaced directly into a crystal mush, where field observations such as tall upward-oriented apophyses that cross-cut overlying cumulate are not compatible with processes occurring on the magma chamber floor. The importance of magmatic undercooling, controlling the growth of cm-sized branching and skeletal crystals is emphasised in this study, where the degree of undercooling (and therefore supersaturation of olivine) is controlled by the ambient crystal mush temperature on emplacement (i.e., a chilling effect). The ubiquity of harrisite layers throughout peridotites in the RLS highlight the important role of incremental sill emplacement in the construction of the layered intrusion. Mafic–ultramafic pegmatoids present in other layered intrusions, such as the Merensky (Bushveld) and J-M Reefs (Stillwater) might also be explained by this sill (and chill) emplacement model.

- The emplacement of sills is facilitated by shearing and hot tearing of a high crystallinity (60–90%) mush. Gravitational stress from slow collapse of the crystal mush towards the feeder zone produced ideal planar weaknesses allowed magma to infiltrate the mush along structurally controlled horizons parallel to $\boldsymbol{\sigma}^3$ (lateral) stress direction. The high-crystallinity but mobile nature of crystal mushes found on Rum highlight its ability to accommodate near solid-state deformation, producing foliations, folds and some brittle deformation features such as cataclasites; a particularly pertinent area for future study.

- Cr-spinel seams are another ubiquitous feature of peridotites on Rum, closely associated with harrisites. The abundance of these seams further highlights the role of small volume replenishment events during crystal mush construction, where individual seams represent melt infiltration along the same amenable horizons facilitating sill emplacement. The Cr-spinel seams crystallised *in situ* along these horizons as melt channels *within* the crystal mush, evidenced by vertically-oriented, cross-cutting, and braided Cr-spinel seams. The Cr-spinel within seam forms via a reaction between infiltrating picritic melt and intercumulus plagioclase. The texture and chemistry of Cr-spinel within these channels is controlled by the volume of through flow within the channel, with a full spectrum of textures and compositions recorded in this study. High volumes of through flow promoted sulphide saturation and PGE-enrichment, which helps to solve mass balance calculations which cannot account for the R-factors in mm-scale Cr-spinel (or chromitite) layers. Instead, more melt has migrated through the seam than is represented by the volume of the seam. The melt channel model, commonly used within the upper mantle, could easily be applied to other layered intrusions, irrespective of scale, where features of *in situ* crystallisation and intra-mush formation (e.g., braided and cross-cutting seams) might be readily applied to the UG1 chromitites in the Bushveld Complex. The model may be especially relevant where Cr-spinel seams are associated with pegmatoidal lithologies (like harrisite), such as in the Ultramafic Series of the Stillwater Complex or the Merenky Reef in the Bushveld Complex.

- The repeated emplacement of sills into a developing crystal mush caused extensive post-cumulus reabsorption and recrystallization *in situ*, suggesting that the Unit 10 crystal mush existed in protracted periods of cold-storage between replenishments. The identification of significant intracrystalline Sr-isotope heterogeneity strongly supports the presence of multiple, distinct melts during the development of the crystal mush. Since this Sr-isotope heterogeneity in intercumulus phases is linked to Cr-spinel seams, it strongly supports the *in situ* melt channel model. Furthermore, the recognition of highly open systems during crystallisation (i.e., as intracrystalline zonation) may help to solve important petrological mass balance problems in adcumulates, where the modal abundance of a particular mineral is too great for the parent to crystallise *in situ*.

- The conceptualisation of layered intrusions as a body of crystal-free (or poor) magma cannot be reconciled in the RLS from the results of this study, where substantial evidence for sill emplacement and associated *in situ* processes occurring within the crystal mush is presented. The sill complex (or crystal mush) model presented should be carefully considered when presented with features generally attributed to the magma chamber floor, a view which may not be as simple. Instead, rheomorphic processes are likely to be more important in the development of layered intrusions. There is broad scope for this model to be applied to the largest layered intrusions, whereby layered intrusions represent incrementally developed sill complexes. As such, the structural position of cumulates within a sequence bears no information on relative age, i.e., ultramafic cumulate sequences of layered intrusions could represent the youngest periods of replenishment and should not be assigned any relative age without clear field or geochronological evidence.

REFERENCES

Annen, C., Blundy, J. D. & Sparks, R.S.J (2006) The genesis of intermediate and silicic magmas in deep crustal hot zones. *Journal of Petrology* **47**, 505–539

Annen, C., Blundy, J.D., Leuthold, J. & Sparks, R.J.S. (2015) Construction and evolution of igneous bodies: Towards an integrated perspective of crustal magmatism. *Lithos* **230**, 206–221.

Ballhaus, C. (1988). Potholes of the Merensky reef at Branspruit shaft, Rustenburg platinum mines; primary disturbances in the magmatic stratigraphy. *Economic Geology* **83**, 1140–1158

Ballhaus, C. & Sylvester, P. (2000). Noble Metal Enrichment Processes in the Merensky Reef, Bushveld Complex. *Journal of Petrology* **41**, 545–561.

Barnes, S.J., Mole, D.R., Le Vaillant, M., Campbell, M.J., Verrall, M.R., Roberts, M.P. & Evans, N.J. (2016). Poikilitic Textures, Heteradcumulates and Zoned Orthopyroxenes in the Ntaka Ultramafic Complex, Tanzania: Implications for Crystallization Mechanisms of Oikocrysts. *Journal of Petrology* **57**, 1171–1198

Barnes, S.J. & Jones, S. (2013). Deformed Chromitite Layers in the Coobina Intrusion, Pilbara Craton, Western Australia. *Economic Geology* **108**, 337–354

Barnes, S.J. & Naldrett, A.J. (1986). Geochemistry of the J-M Reef of the Stillwater Complex, Minneapolis Adit Area II. Silicate Mineral Chemistry and Petrogenesis. *Journal of Petrology* **27**, 791–825

Barnes, S.J. & Roeder, P.L. (2001). The Range of Spinel Compositions in Terrestrial Mafic and Ultramafic Rocks. *Journal of Petrology* **42**, 2279–2302

Bédard, J. H., Sparks, R. S. J., Renner, R., Cheadle, M. J. & Hallworth, M. A. (1988). Peridotite sills and metasomatic gabbros in the Eastern Layered Series of the Rhum Complex. *Journal of the Geological Society, London* **145**, 207–224

Bell, B.R. & Claydon, R.V. (1992). The cumulus and post-cumulus evolution of chrome-spinels in ultrabasic layered intrusions: evidence from the Cuillin Igneous Complex, Isle of Skye, Scotland. *Contributions to Mineralogy and Petrology* **112**, 242–253

Bézos, A., Lorand, J.P., Humler, E. & Gros, M. (2005). Platinum-group element systematics in Mid-Oceanic Ridge basaltic glasses from the Pacific, Atlantic, and Indian Oceans. *Geochimica et Cosmochimica Acta* **69**, 2613–2627

Binns, P.E., McQuillan, R. & Kenolty, N. (1974). The geology of the Sea of Hebrides. *Institute of Geological Sciences Report*, **73/14**.

Boorman, S., Boudreau, A. & Kruger, F.J. (2004). The Lower Zone–Critical Zone transition of the Bushveld Complex: a quantitative textural study. *Journal of Petrology* **45**, 1209–1235

Boudreau, A.E. (2011). The evolution of texture and layering in layered intrusions. *International Geology Review* **53**, 330-353

Boudreau, A.E. (2016). The Stillwater Complex, Montana – Overview and the significance of volatiles. *Mineralogical Magazine* **80**, 585–637

Boudreau, A.E. (1994). Mineral segregation during crystal aging in two-crystal, two-component systems. *South African Journal of Geology* **97**, 473–485

Boudreau, A.E. (1999) Fluid fluxing of cumulates: The J-M reef and associated rocks of the Stillwater complex, Montana. Journal of Petrology **40**, 755–772

Boudreau, A.E. & McBirney, A. R. (1997) The Skaergaard Layered Series. Part III. Non-dynamic Layering. *Journal of Petrology* **38**, 1003–1020

Boudreau, A.E. & McCallum, I.S. (1992) Concentration of platinum-group elements by magmatic fluids in layered intrusions. *Economic Geology* **87**, 1830–1848

Butcher, A.R., Pirrie, D., Prichard, H.N. & Fisher, P. (1999). Platinum-group mineralisation in the Rum layered suite, Scottish Hebrides, UK. *Journal of the Geological Society, London* **156**, 213–216

Brandiss, M.E., Mason, S. & Winsor, K. (2014) Rhythmic Layering Formed by Deposition of Plagioclase Phenocrysts from Influxes of Porphyritic Magma in the Cuillin Centre, Isle of Skye. *Journal of Petrology* **55**, 1479–1510.

Brown, G.M. (1956). The layered ultrabasic rocks of Rhum, Inner Hebrides. *Philosophical Transactions of the Royal Society of London Series B* **668**, 1–53

Cameron, E.N. (1977) Chromite in the central sector of the Eastern Bushveld Complex, South Africa. *American Mineralogist* **62**, 1082–1096.

Campbell, I.H. (1978). Some problems with the cumulus theory. *Lithos* **11,** 311–323

Campbell, I.H. & Murck, B.W. (1993). Petrology of the G and H Chromitite Zones in the Mountain View Area of the Stillwater Complex, Montana. *Journal of Petrology* **34**, 291–316

Campbell, I.H. & Naldrett, A.J. (1979) The influence of silicate silicate:sulfide ratios on the geochemistry of magmatic sulfides. *Economic Geology* **74**, 1503–1505

Campbell, I.H., Naldrett, A.J. & Barnes, S.J. (1983). A Model for the Origin of the Platinum-Rich Sulfide Horizons in the Bushveld and Stillwater Complexes. *Journal of Petrology* **24**, 133–165.

Cashman, K.V. & Marsh, B.D. (1988). Crystal size distribution (CSD) in rocks and the kinetics and dynamics of crystallisation II. Makaopuhi lava lake. *Contributions to Mineralogy and Petrology* **99**, 292–305

Cashman, K.V., Sparks, R.J.S. & Blundy, J.D. (2017). Vertically extensive and unstable magmatism systems: A unified view of igneous processes. *Science* **355** (6331)

Cawthorn, R.G. (2005). Pressure fluctuations and the formation of the PGE-rich Merensky and chromitite reefs, Bushveld Complex. *Mineralium Deposita* **40**, 231–235

Cawthorn, R.G, Barnes, S.J., Ballhaus, C., Malitch, K.N. (2005) Platinum-group element, chromium and vanadium deposits in mafic and ultramafic rocks. *Economic Geology 100th Anniversary Volume*: 215–249

Cawthorn, R.G. & Boerst, K. (2006). Origin of the Pegmatitic Pyroxenite in the Merensky Unit, Bushveld Complex, South Africa. *Journal of Petrology* **47**, 1509–1530

Chadam. J., Hoff, D., Merino, E., Ortoleva, P. & Sen, A. (1986) Reactive Infiltration Instabilities. *IMA Journal of Applied Mathematics* **36**, 207–221.

Charlier, B.L.A., Ginibre, C., Morgan, D., Nowell, G.M., Pearson, D.G., Davidson, J.P. & Ottley, C.J. (2006). Methods for the microsampling and high-precision analysis of strontium and rubidium isotopes at single crystal scale for petrological and geochronological applications. *Chemical Geology* **232**, 114–133.

Claiborne, L.L., Miller, C.F. Flanagan, D.M., Clynne, M.A. & Wooden, J.L. (2010) Zircon reveals protracted magma storage and recycling beneath Mount St. Helens. *Geology* **38**, 1011–1014

Cooper, K.M. & Kent, A.J.R. (2014) Rapid remobilization of magmatic crystals kept in cold storage. *Nature* **506**, 480–483

Daines, M. J. & Kohlstedt, D. L. (1993). A laboratory study of melt migration. *Philosophical Transactions: Physical Sciences and Engineering* **342**, 43–52

Daines, M. J. & Kohlstedt, D. L. (1994). The transition from porous to channelized flow due to melt/rock reaction during melt migration. *Geophysical Research Letters* **21**, 145–148

Davidson, J.P. & Tepley III, F.J. (1997). Recharge in Volcanic Systems: Evidence from Isotopic Profiles of Phenocrysts. *Science* **275**, 826–829

Davidson, J.P. & Tepley III, F.J. & Knesel, K.M. (1998). Isotopic Fingerprinting May Provide Insights into Evolution of Magmatic Systems. *EOS Transactions, American Geophysical Union* **79**, 185–196

Donaldson, C.H. (1974). Olivine Crystal Types in Harrisitic Rocks of the Rhum Pluton and in Archaean Spinifex Rocks. *Geological Society of America Bulletin* **85**, 1721–1726

Donaldson, C.H. (1975). A petrogenetic study of harrisite in the Isle of Rhum pluton, Scotland. *Unpublished PhD Thesis, University of St. Andrews*

Donaldson, C.H. (1976). An Experimental Investigation of Olivine Morphology. *Contributions to Mineralogy and Petrology* **57**, 187–213

Donaldson, C.H. (1982). Origin of some of the Rhum harrisite by segregation of intercumulus liquid. *Mineralogical Magazine* **45**, 201–209

Donaldson, C.H. (1985). The rates of dissolution of olivine, plagioclase and quartz in a basaltic melt. *Mineralogical Magazine* **49**, 683–693

Donaldson, C.H., Drever, H.I. & Johnston, R. (1973). Crystallisation of Poikilo-macro-spherulitic Feldspar in a Rhum Peridotite. *Nature Physical Science* **243**, 69–70

Droop, G.T.R. (1987). A general equation for estimating Fe^{3+} concentrations in ferromagnesian silicates and oxides from microprobe analyses using stoichiometric criteria. *Mineralogical Magazine* **51**, 431–435

Dunham, A.C. & Wadsworth, W.J. (1978). Cryptic variation in the Rhum layered intrusion. *Mineralogical Magazine* **42**, 347–356

Eales, H.V. & Cawthorn, R.G. (1996) The Bushveld Complex. In: Cawthorn RG (ed) *Layered Intrusions*. The Netherlands, Elsevier, Amsterdam.

Elliot, M.T., Cheadle, M.J. & Jerram, D.A. (1997) On the identification of textural equilibrium in rocks using dihedral angle measurements. *Geology* **25**, 355–358

Emeleus, C.H. (1994). Rum solid geology map 1:20000. Scottish Natural Heritage.

Emeleus, C.H. (1997) Emeleus, C.H, 1997. *Geology of Rum and the adjacent islands. Memoir of the British Geological Survey, Sheet 60,* Scotland.

Emeleus, C.H. & Bell, B.R. (2005). *British Regional Geology: the Palaeogene Volcanic Districts of Scotland*. (4th Ed). Keyworth: British Geological Survey

Emeleus, C.H., Cheadle, M.J., Hunter, R.H., Upton, B.G.J. & Wadsworth, W.J. (1996). The Rum Layered suite. *In*: Cawthorn, R.G (ed). *Layered igneous rocks. Developments in petrology,* vol 15, Elsevier Science BV: Amsterdam, 404–440

Emeleus. C.H. & Troll, V.R. (2014). The Rum Igneous Centre, Scotland. *Mineralogical Magazine* **78**, 805–839

Eskin, D.G., Suyitno. & Katgerman, L. (2004). Mechanical properties in the semi-solid state and hot tearing of aluminium alloys. *Progress in Materials Science* **49**, 629–711.

Faure, F., Trolliard, G., Nicollet, C. & Montel, J-M. (2003). A developmental model of the olivine morphology as a function of the cooling rate and the degree of undercooling. *Contributions to Mineralogy and Petrology* **145**, 251–263

Forien, M., Tremblay, J., Barnes, S-J., Burgisser, A. & Pagé, P. (2016). The Role of Viscous Particle Segregation in Forming Chromite Layered from Slumped Crystal Slurries: Insights from Analogue Experiements. *Journal of Petrology* **56**, 2425–2444

Geshi, N. (2001). Melt segregation by localized sear deformation and fracturing during crystallization of magma in shallow intrusions of the Otoge volcanic complex, central Japan. *Journal of Volcanology and Geothermal Research*, **106**, 285–300#

Giletti, B.J. & Casserly, J.E.D. (1994) Strontium diffusion kinetics in plagioclase feldspars. *Geochimica et Cosmochimica Acta* **58**, 3785–3793

Glazner, A. & Boudreau A.E. (2011) Metamorphism of thought about igneous rock textures. *International Geology Review* **53**, 327-329

González-Jiménez, J.M., Griffin, W.L., Proenza, J.A., Gervilla, F., O'Reilly, S.Y., Akbulut, M., Pearson, N.J. & Arai, S. (2014). Chromitites in ophiolites: How, where, when, why? Part II. The crystallization of chromitites. *Lithos* **189**, 140–158

Godel, B. (2015) Platinum-Group Element Deposits in Layered Intrusions: Recent Advances in the Understanding of the Ore Forming Processes. In: Charlier B, Namur O, Latypov R, Tegner C (eds) *Layered Intrusions*. Springer Science, Netherlands.

Godel, B.M., Barnes, S.J., Gürer, D., Austin, P. & Fiorentini, M.L. (2013). Chromite in komatiites: 3D morphologies with implications for crystallization mechanisms. Contributions to Mineralogy and Petrology **165**, 173–189

Greenwood, R.C. (1987). Geology and petrology of the margin of the Rhum ultrabasic intrusion, Inner Hebrides, Scotland. *Unpublished PhD thesis.* University of St Andrews

Greenwood, R.C., Donaldson, C.H. & Emeleus, C.H. (1990) The contact zone of the Rhum ultrabasic intrusion: evidence of peridotite formation from magnesian magmas. *Journal of the Geological Society, London* **147**, 209–212

Hamilton, M.A., Pearson, D.G., Thompson, R.N., Kelley, S.P. & Emeleus, C.H. (1998). Rapid eruption of Skye lavas inferred from precise U–Pb and Ar–Ar dating of the Rum and Cuillin plutonic complexes. *Nature* **394**, 260–263

Harker, A. (1908). *The Geology of the Small Isles of Inverness-shire. Memoir of the Geological Survey of Scotland*, HMSO, Edinburgh

Henderson, P. (1975). Reaction trends shown by chrome-spinels of the Rhum layered intrusion. *Geochimica et Cosmochimica Acta* **39**, 1035-1044

Henderson, P. & Suddaby, P. (1971). The Nature and Origin of the Chrome-Spinel of the Rhum Layered Intrusion. *Contributions to Mineralogy and Petrology* **33**, 21–31

Hepworth, L.N., O'Driscoll, B., Gertisser, R., Daly, J.S. & Emeleus, C.H. (2017). Incremental Construction of the Unit 10 Peridotite, Rum Eastern Layered Intrusion, NW Scotland. *Journal of Petrology* **58**, 137–166

Higgins, M.D. (1994). Numerical modelling of crystal shapes in thin-sections; estimation of crystal habit and true size. *American Mineralogist* **79**, 113–119

Higgins, M.D. (2002a). Closure in crystal size distributions (CSD), verification of CSD calculations, and the significance of CSD fans. *American Mineralogist* **81**, 171–175

Higgins, M.D. (2002b). A crystal size-distribution study of the Kiglapait layered mafic intrusion, Labrador, Canada: evidence for textural coarsening. *Contributions to Mineralogy and Petrology* **144**, 314–330

Higgins, M.D. (2006). *Quantitative textural measurements in igneous and metamorphic petrology*: Cambridge, Cambridge University Press, UK

Higgins, M.D. (2000). Measurement of Crystal Size Distributions. *American Mineralogist* **85**, 1105–1116

Holness, M.B. (1999). Contact metamorphism and anatexis of Torridonian arkose by minor intrusions of the Rum Igneous Complex, Inner Hebrides, Scotland. *Geological Magazine* **136** (5), 527–542.

Holness, M.B. (2005). Spatial Constraints on Magma Chamber Replenishment Events from Textural Observations of Cumulates: the Rum Layered Intrusion, Scotland. *Journal of Petrology* **46**, 1585–1601

Holness, M.B. (2007). Textural immaturity of cumulates as an indicator of magma chamber processes: infiltration and crystal accumulation in the Rum Eastern Layered Intrusion. *Journal of the Geological Society, London* **164**, 529–539

Holness, M.B., Hallworth, M.A., Woods, A. & Sides, R.E. (2007). Infiltration Metasomatism of Cumulates by Intrusive Magma Replenishment: the Wavy Horizon, Isle of Rum, Scotland. *Journal of Petrology* **48**, 563–587

Holness, M.B., Humphreys, M.C.S., Sides. R., Helz, R.T. & Tegner, C. (2012) Toward an understanding of disequilibrium dihedral angles in mafic rocks. *Journal of Geophysical Research: Solid Earth* **117,** B06207

Holness, M.B., Sides, R.E., Prior, D.J., Cheadle, M.J. & Upton, B.G.J. (2012). The peridotite plugs of Rum: Crystal settling and fabric development in magma conduits. *Lithos* **135**, 23–40

Holness, M.B., Tegner, C., Namur, O. & Pilbeam, L. (2015). The Earliest History of the Skaergaard Magma Chamber: a Textural and Geochemical Study of the Cambridge Drill Core. *Journal of Petrology* **56**, 119–1227

Holness, M.B., Tegner, C., Nielsen, T.F.D. & Charlier, B. (2017b). Thickness of the Mushy Layer on the Floor of the Skaergaard Magma Chamber at Apatite Saturation. *Journal of Petrology* **58**, 909–932

Holness, M.B., Vukmanovic, Z., Mariani, E. (2017a) Assessing the Role of Compaction in the Formation of Adcumulates: a Microstructural Perspective. *Journal of Petrology* **58**, 643–674

Holness, M.B. & Winpenny, B. (2008). The Unit 12 allivalite, Eastern Layered Intrusion, Isle of Rum: a textural and geochemical study of an open-system magma chamber. *Geological Magazine* **146**, 437–450

Houlé, M.G., Préfontaine, S., Fowler, A.D. & Gibson, H.L. (2009). Endogeneous growth in channelized komatiite lava flows: evidence from spinifex-textured sills at Pyke Hill and Serpentine Mountain, Western Abitibi Greenstone Belt, Northeastern Ontario, Canada. *Bulletin of Volcanology* **71**, 881–901

Humphreys, M.C.S. (2009). Chemical Evolution of Intercumulus Liquid, as Recorded in Plagioclase Overgrowth Rims from the Skaergaard Intrusion. *Journal of Petrology* **50**, 127–145

Humphreys, M.C.S. (2011). Silicate Liquid Immiscibility within the Crystal Mush: Evidence from Ti in Plagioclase from the Skaergaard Intrusion. *Journal of Petrology* **52**, 147–174.

Humphreys, M.C.S. & Holness, M.B. (2010). Melt-rich segregations in the Skaergaard Marginal Border Series: Tearing of a vertical silicate mush. *Lithos* **119**, 181–192

Hunt, E.J., Finch, A.A. & Donaldson, C.H. (2017) Layering in peralkaline magmas, Ilímaussaq Complex, S Greenland. *Lithos*. **268**, 1–15

Huppert, E., Sparks, R.S.J., Wilson, J.R. & Hallworth, M.A. (1986). Cooling and crystallisation at an inclined plane. *Earth and Planetary Science Letters* **79**, 319–328.

Irvine, T.N. (1975). Crystallisation sequences in the Muskox intrusion and another layered intrusions – II. Origin of chromitite layers and similar deposits of other magmatic ores. *Geochimica et Cosmochimica Acta* **39**, 991–1020.

Irvine, T.N. (1977). Origin of chromitite layers in the Muskox intrusion and other stratiform intrusions: A new interpretation. *Geology* **5**, 273–277

Jackson, E.D. (1961). Primary Textures and Mineral Associations in the Ultramafic Zone of the Stillwater Complex, Montana. *Geological Survey Professional Paper* **358**

Jerram, D.A., Cheadle, M.J., Hunter, R.H. & Elliot, M.T. (1996). The spatial distribution of grains and crystals in rocks. *Contributions of Mineralogy and Petrology* **125**, 60–74

Jerram, D.A., Cheadle, M.J. & Philpotts, A.R. (2003). Quantifying the Building Blocks of Igneous Rocks: Are Clustered Crystal Frameworks the Foundation? *Journal of Petrology* **44**, 2033–2051

Junge, M., Oberthür, T. & Melcher, F. (2014). Cryptic variation of chromite chemistry, platinum group element and platinum group mineral distribution in the UG-2 chromitite: an example from the Karee mine, western Bushveld Complex, South Africa. *Economic Geology* **109**, 795–810

Kamenetsky, V.S., Crawford, A.J. & Meffre, A. (2001) Factors Controlling Chemistry of Magmatic Spinel: an Empirical Study of Associated Olivine, Cr-spinel, and Melt Inclusions from Primitive Rocks. *Journal of Petrology* **42**, 655–671

Kelemen, P. (1990). Reaction Between Ultramafic Rock and Fractionating Basaltic Magma I. Phase Relations, the Origin of Calc-alkaline Magma Series, and the Formation of Discordant Dunite. *Journal of Petrology* **31** (1), 51–98

Kelemen, P., Shimizu, N. & Salters, V.J.M. (1995). Extraction of mid-ocean-ridge basalt from the upwelling mantle by focused flow of melt in dunite channels. *Nature* **375**, 747–753

Lahaie, D.J. & Bouchard, M. (2001). Physical Modelling of the Deformation Mechanisms of Semisolid Bodies and a Mechanical Criterion for Hot Tearing. *Metallurgical and Materials Transactions B.* **32**, 697–705

Larsen, R.B. & Brooks, C.K. (1994). Origin and Evolution of Gabbroic Pegmatites in the Skaergaard Intrusion, East Greenland. *Journal of Petrology* **35**, 1651–1679

Latypov, R. (2003). The Origin of Marginal Compositional Reversals in Basic–Ultrabasic Sills and Layered Intrusions by Soret Fractionation. *Journal of Petrology* **44**, 1579–1618

Latypov, R. Chistyakova, S., Barnes, S.J. & Hunt, E.J. (2017). Origin of Platinum Deposits in Layered Intrusions by *In Situ* Crystallisation: Evidence from Undercutting Merensky Reef of the Bushveld Complex. *Journal of Petrology* **58**, 715–762

Latypov, R., Chistyakova, S., Page, A. & Hornsey, R. (2015). Field evidence for the *in situ* crystallisation of the Merensky Reef. *Journal of Petrology* **56**, 2341–2372

Latypov, R., Morse, T., Robins, B., Wilson, R., Cawthorn, G., Tegner, C., Holness, M., Lesher, C., Barnes, S., O’Driscoll, B., Veksler, I., Higgins, M., Wilson, A., Namur, O., Chistyokova, S., Naslund, R. & Thy, P. (2015). A fundamental dispute: A discussion of “On some fundamentals of igneous petrology" by Bruce D. Marsh, Contributions to Mineralogy and Petrology (2013) 166: 665–690. **169:20**

Latypov, R., O'Driscoll, B. & Lavrenchuk, A. (2013). Towards a model for the *in situ* origin of PGE reefs in layered intrusions: insights from chromitite seams of the Rum Eastern Layered Intrusion, Scotland. *Contributions to Mineralogy and Petrology* **166**, 309–327

Le Maitre, R.W. ed. (2002) *Igneous Rocks: A Classification and Glossary of Terms* Cambridge University Press, Cambridge, UK

Lenaz, D., O'Driscoll, B. & Princivalle, F. (2011). Petrology of the anorthosite-chromitite seam association: crystal-chemical and petrological insights from the Rum Layered Suite, NW Scotland. *Contributions to Mineralogy and Petrology* **162**, 1201–1213

Leuthold, J., Blundy, J.D. & Brooker, R.A. (2015). Experimental petrology constraints on the recycling of mafic cumulate: a focus on Cr-spinel from the Rum Eastern Layered Intrusion, Scotland. *Contributions to Mineralogy and Petrology* 170: 12

Leuthold, J., Blundy, J.D., Holness, M.B. & Sides, R. (2014). Successive episodes of reactive liquid flow through a layered intrusion (Unit 9, Rum Eastern Layered Intrusion, Scotland). *Contributions to Mineralogy and Petrology* **167**, 1021–1038

Leuthold, J., Müntener, O., Baumgartner, L.P., Putlitz, B., Ovtcharova, M. & Schaltegger, U. (2012). Time resolved construction of a bimodal laccolith (Torres del Paine, Patagonia). *Earth and Planetary Science Letters* **325**, 85–92

Lindhuber, M.J., Marks,.M.A.W., Bons, P.D., Wenzel, T. & Markl, G. (2015). Crystal mat-formation as an igneous layering-forming process: Textural and geochemical evidence from the 'lower layered' nepheline syenite sequence of the Ilímaussaq complex, South Greenland. *Lithos* **224**, 395309

Lipin, B.R. (1993). Pressure Increases, the Formation of Chromite Seams, and the Development of the Ultramafic Series in the Stillwater Complex, Montana. *Journal of Petrology* **34**, 955–976

Lofgren, G.E. & Donaldson, C.H. (1975). Curved branching crystals and differentiation in comb-layered rocks. *Contributions to Mineralogy and Petrology* **49**, 309–319

Lucas, S.B. & St-Onge, M.R. (1995). Syn-tectonic magmatism and the development of composition layering, Ungava Orogen (northern Quebec, Canada). *Journal of Structural Geology* **17**, 475–491

Maier, W.D. & Barnes, S-J. (2008). Platinum-group elements in the UG1 and UG2 chromitites, and the Bastard reef, at Impala platinum mine, western Bushveld Complex, South Africa: Evidence for late magmatic cumulate instability and reef constitution. *South African Journal of Geology* **111**, 159–176

Maier, W.D., Barnes, S.-J., Groves, D.I. (2013) The Bushveld Complex, South Africa: formation of platinum–palladium, chrome- and vanadium-rich layers via hydrodynamic sorting of a mobilized cumulate slurry in a large, relatively slowly cooling, subsiding magma chamber. *Mineralium Deposita* **48**, 1–56

Marks, M.A.W. & Markl, G. (2015) Th Ilímausaq Alkaline Complex, South Greenland. *In:* Charlier B., Namur, O., Latypov, R. & Tegner, E. (eds.) *Layered Intrusions*. Springer Geology, Dordrect, Netherlands.

Marsh, B.D. (1998). On the Interpretation of Crystal Size Distributions in Magmatic Systems. *Journal of Petrology* **39**, 553–599

Marsh, B.D. (2002). On bimodal differentiation by solidification front instability in basaltic magmas, part 1: Basic mechanics. *Geochimica et Cosmochimica Acta* **66** (12), 2211–2229.

Marsh, B.D. (2015) Reply to: Latypov *et al.* A fundamental dispute: A discussion of “On some fundamentals of igneous petrology” by Bruce D. Marsh, Contributions to Mineralogy and Petrology (2013) 166: 665–690, **169:21**

Marsh, B.D. (2013). On some fundamentals of igneous petrology. *Contributions to Mineralogy and Petrology* **166**, 665–690

McBirney, A.R. (2009). Factors governing the textural development of Skaergaard gabbros: A review. *Lithos* **111**, 1–5

McBirney, A.R. & Nicolas, A. (1997). The Skaergaard Layered Series. Part II. Magmatic flow and Dynamic Layering. *Journal of Petrology* **38**, 569–580.

McBirney, A.R. & Noyes, R.M. (1979) Crystallisation and Layering of the Skaergaard Intrusion. *Journal of Petrology* **20**, 487–554

McKenzie, D. (1984). The Generation and Compaction of Partially Molten Rock. *Journal of Petrology* **25**, 719–765

Means, W.D. & Park, Y. (1994). New experimental approach to understanding igneous texture. *Geology* **22**, 323–326

Morse, S.A. (1980). *Basalts and phase diagrams*. Springer Verlag, New York. 493 pp

Mock, A. & Jerram, D.A. (2005). Crystal Size Distributions (CSD) in Three Dimensions: Insights from the 3D Reconstruction of a Highly Porphyritic Rhyolite. *Journal of Petrology* **46**(8), 1525–1541

Morgan, Z. & Liang, Y. (2005). An experimental and numerical study of the kinetics of harzburgite reactive dissolution with applications to dunite dike formation. *Earth and Planetary Science Letters* **214**, 59–74

Mondal, S.K. & Mathez, E.A. (2007). Origin of the UG2 chromitite seam layer, Bushveld Complex. *Journal of Petrology* **48**, 495–510

Mukherjee, R., Latypov, R. & Balakrishna, A. (2017). An intrusive origin of some UG-1 chromitite layers in the Bushveld Igneous Complex, South Africa: Insights from field relationships. *Ore Geology Reviews* (in press)

Mungall, J.E. & Brenan, J.M. (2014) Partitioning of platinum-group elements and Au between sulfide liquid and basalt and the origins of mantle–crust fractionation of the chalcophile elements. *Geochimica et Cosmochimica Acta* **125**, 265–289

Mungall, J.E., Kamo, S.L. & McQuade, S. (2016). U-Pb geochronoglogy documents out-of-sequence emplacement of ultramafic layers in the Bushveld Igneous Complex of South Africa. *Nature Communications* **7**, 13385

Mungall, J.E & Naldrett, A.J, (2008). Ore Deposits of the Platinum-Group Elements. *Elements* **4**, 253–258

Naldrett, A.J. (2004) *Magmatic sulfide deposits; geology, geochemistry and exploration*. Berlin, Springer Verlag, Germany

Naldrett, A.J & Duke, J.M. (1980) Platinum metals in magmatic sulfide ores. *Science* **208**:1417-1424.

Naldrett, A.J., Gasparrini, E.C., Barnes, S.J., Von Gruenewaldt, G. & Sharpe, M.R. (1986) The Upper Critical Zone of the Bushveld Complex and the origin of Merensky-type ores. *Economic Geology* **81**, 1105–1117

Naldrett, T., Kinnaird, J., Wilson, A. & Chunnett, G. (2008). Concentration of PGE in the Earth's Crust with Special Reference to the Bushveld Complex. *Earth Science Frontiers* **15**, 264–297

Namur, O. & Charlier, B. (2012). Efficiency of compaction and compositional convection during mafic crystal mush solidification: the Sept Iles layered intrusion, Canada. *Contributions to Mineralogy and Petrology* **163**, 1049–1068

Namur, O., Humphreys, M.C.S. & Holness, M.B. (2013). Lateral Reactive Infiltration in a Vertical Gabbroic Crystal Mush, Skaergaard Intrusion, East Greenland. *Journal of Petrology* **54**, 985–1016

Namur, O., Abily, B., Boudreau, A.E., Blanchette, F., Bush, J.W.M., Ceuleneer, G., Charlier, B., Donaldson, C.H., Duchesne, J–C., Higgins, .M.D., Morata, D., Nielsen, T.F.D., O'Driscoll, B., Pang, K.N., Peacock, T., Spandler, C.J., Toramaru, A. 7 Veksler, I.V. (2015) Igneous Layering in Basaltic Magma Chambers. *In:* Charlier B., Namur, O., Latypov, R. & Tegner, E. (eds.) *Layered Intrusions*. Springer Geology, Dordrect, Netherlands.

O'Driscoll, B., Butcher, A.R. & Latypov, R. (2014). New insights into precious metal enrichment on the Isle of Rum, Scotland. *Geology Today* **30**, 134–141

O'Driscoll, B., Emeleus, C.H., Donaldson, C.H. & Daly, J.S. (2010). Cr-spinel Seam Petrogenesis in the Rum Layered Suite, NW Scotland: Cumulate Assimilation and in situ Crystallisation in a Deforming Crystal Mush. *Journal of Petrology* **51**, 1171–1201

O'Driscoll, B., Donaldson, C.H., Troll, V.R., Jerram, D.A. & Emeleus, C.H. (2007a). An Origin for Harrisitic and Granular Olivine in the Rum Layered Suite, NW Scotland: a Crystal Size Distribution Study. *Journal of Petrology* **48**, 253–270

O'Driscoll, B., Ferré, E.C., Stevenson, C.T.E., & Magee, C. (2015). The significance of Magnetic Fabric in Layered Mafic-Ultramafic Intrusions. *In*: Charlier B., Namur, O., Latypov, R. & Tegner, E. (eds.) *Layered Intrusions*. Springer Geology, Dordrect, Netherlands

O'Driscoll, B., Hargraves, R.B., Emeleus, C.H., Troll, V.R., Donaldson, C.H. & Reavy, R.J. (2007b). Magmatic lineations inferred from anisotropy of magnetic susceptibility fabrics in Units 8, 9, and 10 of the Rum Eastern Layered Series, NW Scotland. *Lithos* **98**, 27–44

O'Driscoll, B., Donaldson, C.H., Daly, J.S. & Emeleus, C.H. (2009a). The roles of melt infiltration and cumulate assimilation in the formation of anorthosite and a Cr-spinel seam in the Rum Eastern Layered Intrusion, NW Scotland. *Lithos* **111**, 6–20

O'Driscoll, B., Day, J.M.D., Daly, J.S., Walker, R.J. & McDonough, W.F. (2009b). Rhenium–osmium isotopes and platinum-group elements in the Rum Layered Suite, Scotland: Implications for Cr-spinel seam formation and the composition of the Iceland mantle anomaly. *Earth and Planetary Science Letters* **286**, 41–51

Ortoleva, P., Merino, E., Moore, C. & Chadam, J. (1987). Geochemical self-organisation I: reaction-transport feedbacks and modelling approach. *American Journal of Science* **287**, 979–1007

Palacz, Z.A. (1984). Isotopic and geochemical evidence for the evolution of a cyclic unit in the Rhum intrusion, north-west Scotland. *Nature* **307**, 618–620

Palacz, Z.A. (1985). Sr-Nd-Pb isotopic evidence or crustal contamination in the Rhum intrusion. *Earth and Planetary Science Letters* **74**, 35–44

Palacz, Z.A. & Tait, S.R. (1985). Isotopic and geochemical investigation of unit 10 from the Eastern Layered Series of the Rhum Intrusion, Northwest Scotland. *Geological Magazine* **122**, 485–490

Pec, M., Holtzman, B. K., Zimmerman, M. & Kohlstedt, D. L. (2015). Reaction infiltration instabilities in experiments on partially molten mantle rocks. *Geology*, **G36611-1**

Petronis, M. S., O’Driscoll, B., Troll, V. R., Emeleus, C. H. & Geissman, J. W. (2009). Palaeomagnetic and anisotropy of magnetic susceptibility data bearing on the emplacement of the Western Granite, Isle of Rum, NW Scotland, *Geological Magazine* **146**, 419–436

Philpotts, A.R., Carroll, M. & Hill, J.M. (1996). Crystal-Mush Compaction and the Origin of Pegmatitic Segregation Sheets in a Thick Flood-Basalt Flow in the Mesozoic Hartford Basin, Connecticut. *Journal of Petrology* **37**, 811–836

Pirrie, D., Power, M.R., Andersen, J.C.Ø. & Butcher, A.R. (2000). Platinum-group mineralization in the Tertiary Igneous Province: new data from Mull and Skye, Scottish Inner Hebrides, UK. *Geological Magazine* **137**, 651–658

Power, M.R., Pirrie, D. & Andersen, J.C.Ø. (2003). Diversity of platinum-group element mineralization in the North Atlantic Igneous Province: new evidence from Rum, UK. *Geological Magazine* **140**, 499–512

Power, M.R. Pirrie, D Andersen, J.C.Ø. & Butcher, A.R. (2000). Stratigraphical distribution of platinum-group minerals in the Eastern Layered Series, Rum, Scotland. *Mineralium Deposita* **35**, 762–775

Quick, J.E. (1981). The Origin and Significance of Large, Tabular Dunite Bodies in the Trinity Peridotite, Northern California. *Contributions to Mineralogy and Petrology* **78**, 413–422

Quintiliani, M., Andreozzi, G.B. & Graziani, G. (2006). Fe^{2+} and Fe^{3+} quantification by different approaches and fO_2 estimation for Albanian Cr-spinels. *American Mineralogist* **91**, 907-916

Renner, R. & Palacz, Z.A. (1987). Basaltic replenishment of the Rhum magma chamber: evidence from unit 14. *Journal of the Geological Society, London* **144**, 961–970

Reddy, S.M., Kelley, S.P. & Wheeler, J. (1996) A $^{40}Ar/^{39}Ar$ laser probe study of micas from the Seisa zone, Italian Alps: Implications for metamorphic and deformation histories. *Journal of Metamorphic Geology* **14**, 493–508

Roeder, P.L.& Campbell, I.H. (1985). The Effect of Postcumulus Reactions on Composition of Chrome-spinels from the Jimberlana Intrusion. *Journal of Petrology* **26**, 763–786

Roelofse, F., Ashwal, L.D. & Romer, R. L. (2015). Multiple, isotopically heterogeneous plagioclase populations in the Bushveld Complex suggest mush intrusion. *Chemie der Erde* **75**, 357–364

Scowen, P.A.H., Roeder, P.L. & Helz, R.T. (1991). Requilibration of chromite within Kiliauea Iki lava lake, Hawaii. *Contributions to Mineralogy and Petrology* **107**, 8–20

Shore, M. & Fowler, A.D. (1999). The origin of spinifex texture in komatiites. *Nature* **397**, 691–694

Sneeringer, M., Hart, S.R., & Shimizu, N. (1984). Strontium and samarium diffusion in diopside. *Geochimica et Cosmochimica Acta* **48**, 1589–1608.

Spandler, C., Mavrogenes, J. & Arculus, R. (2005). Origin of chromitites in layered intrusions: Evidence from chromite-hosted melt inclusions from the Stillwater Complex. *Geology* **33**, 893–896

Sparks, R.J.S. & Huppert, H.E. (1984). Density changes during the fractional crystallization of basaltic magmas: fluid dynamic implications. *Contributions to Mineralogy and Petrology* **85**, 300–309

Sparks, R.S.J., Huppert, H.E., Kerr, R.C., McKenzie, D.P. & Tait, S.R. (1985). Postcumulus processes in layered intrusions. *Geological Magazine* **122**, 555–568

Spiegelman, M., Kelemen, P. B. & Aharonov, E. (2001). Causes and consequences of flow organization during melt transport: The reaction infiltration instability in compactible media. *Journal of Geophysical Research: Solid Earth* **106**, 2061–2077.

Špillar, V. & Dolejš, D. (2014) Kinetic model of nucleation and growth in silicate melts: implications for igneous textures and their quantitative description. *Geochimica et Cosmochimica Acta* **131**, 164–183

Špillar, V. & Dolejš, D. (2015a). Heterogeneous nucleation as the predominant mode of crystallization in natural magmas: numerical model and implications for crystal-melt interaction. *Contributions to Mineralogy and Petrology* **169**, 4

Tait, S.R. (1985). Fluid dynamic and geochemical evolution of the Cyclic Unit 10: Rhum intrusion. *Geological Magazine* **122**, 469–484

Tait, S.R., Huppert, H.E. & Sparks, R.J.S. (1984) The role of compositional convection in the formation of adcumulate rocks. *Lithos* **17**, 139–146

Tanner, D., Mavrogenes, J.A., Arculus, R.J. & Frances, E.J. (2014). Trace Element Stratigraphy of the Bellevue Core, Northern Bushveld: Multiple Magma Injections Obscured by Diffusive Processes. *Journal of Petrology* **55**, 859–882

Tegner, C. & Robins, B. (1996). Picrite sills and crystal-melt reactions in the Honningsvåg Intrusive Suite, northern Norway. *Mineralogical Magazine* **60**, 53–66

Tegner, C., Thy, P., Holness, M.B., Jakobsen, J.K. Lesher, C.E. (2009). Differentiation and Compaction in the Skaergaard Intrusion. *Journal of Petrology* **50**, 813–840

Tepley, F.J. III. & Davidson, J.P. (2003). Mineral-scale Sr-isotope constraints on magma evolution and chamber dynamics in the Rum Layered Intrusion, Scotland. *Contributions to Mineralogy and Petrology* **145**, 628–641

Troll, V.R., Donaldson, C.H. & Emeleus, C.H. (2004). Pre-eruptive magma mixing in ash-flow deposits of the Tertiary Igneous Centre, Scotland. *Contributions to Mineralogy and Petrology* **147**, 722–739

Troll, V.R., Emeleus, C.H. & Donaldson, C.H. (2000). Caldera formation in the Rum Central Igneous Complex, Scotland. *Bulletin of Volcanology* **62**, 301–317

Troll, V.R., Nicoll, G.R., Donaldson, C.H. & Emeleus, C.H. (2008). Dating the onset of volcanism at the Rum Igneous Centre, NW Scotland. *Journal of the Geological Society, London* **165**, 651–659

Upton, B.G.J., Scovgaard, A.C., McClurg, J., Kirstein, L., Cheadle, M., Emeleus, C.H., Wadsworth, W.J. & Fallick, A.E. (2002). Picritic magmas and the Rum ultramafic complex, Scotland. *Geological Magazine* **139**, 437–452

Veksler, I.V., Reid, D.L., Dulski, P., Jakob, K.K., Schannor, M., Hecht, L. & Trumbull, R.B. Electrochemical Processes in a Crystal Mush: Cyclic Units in the Upper Critical Zone of the Bushveld Complex, South Africa. *Journal of Petrology* **56**, 1229–1250

Vigneresse, J.L., Barbey, P. & Cuney, M. (1996). Rheological Transitions During Partial Melting and Crystallization with Application to Felsic Magma Segregation and Transfer. *Journal of Petrology* **37**, 1579–1600

Von Bargen, N. & Waff, H.S. (1986) Permeabilities, interfacial areas and curvatures of partially molten systems: results of numerical computations of equilibrium microstructures. *Journal of Geophysical Research* **91**, 9261–9276

Volker, J.A, & Upton, B.G.J. (1990). The structure and petrogenesis of the Trallval and Ruinsival areas of the Rhum ultrabasic complex. *Transactions of the Royal Society of Edinburgh: Earth Sciences* **81**, 69–88

Voordouw, R., Gutzmer, J., Beukes, N.J. (2009). Intrusive origin for Upper Group (UG1, UG2) stratiform chromitite seams in the Dwars River area, Bushveld Complex, South Africa. *Contributions to Mineralogy and Petrology* **97**, 75–94

Vukmanovic, Z., Barnes, S.J., Reddy, S.M., Godel, B. & Fiorentini, M.L. (2013). Morphology and microstructure of chromite crystals in chromitites from the Merensky Reef (Bushveld Complex, South Africa). *Contributions to Mineralogy and Petrology* **165**, 1031–1050

Wadsworth, W.J. (1961). The layered ultrabasic rocks of south-west Rhum, Inner Hebrides. *Philosophical Transactions of the Royal Society of London. Series* B **244**, 21–64

Wager, L.R., Brown, G.M. & Wadsworth, W.J. (1960). Types of Igneous Cumulates. Journal of Petrology **1**, 73–85

Wager, L.R. & Brown, G.M. (1968). *Layered Igneous Rocks*. Edinburgh: Oliver and Boyd

Wager, L.R. & Deer, W.A. (1939) Geological investigations in East Greenland. Part III. The petrology of the Skaergaard intrusion, Kangerdlugssuak, east Greenland. *Meddelelser om Grønland*, **105**, 1-352

Wall. C.J. (2016). Establishing the age and duration of magmatism in large open-system layered intrusions from the high precision geochronology of the Neoarchean Stillwater Complex and Paleoproterozoic Bushveld Complex. *Unpublished Ph.D Thesis*, University of British Columbia, Canada

Welsch, B., Hammer, J. & Hellebrand, E. (2014). Phosphorus zoning reveals dendritic architecture of olivine. *Geology* **42**, 867–870

Wijbrans, C.H., Klemme, S., Berndt, J. & Vollmer, C. (2015). Experimental determination of trace element partition coefficients between spinel and silicate melt: the influence of chemical composition and oxygen fugacity. *Contributions to Mineralogy and Petrology* **169**, 1128-1161

Wilson, A.H. (2015) The Earliest Stages of Emplacement of the Eastern Bushveld Complex: Development of the Lower Zone, Marginal Zone and Basal Ultramafic Sequences. *Journal of Petrology* **56**, 347–388

Worrell, L.M. (2002). The Origin of Igneous Cumulates: Integrated Studies of Peridotites from the Western Layered Series of the Rum Layered Intrusion. *Unpublished PhD Thesis, University of Liverpool*

Zieg, M.J. & Marsh, B.D. (2012) Multiple Reinjections and Crystal-mush Compaction in the Beacon Sill, McMurdo Dry Valleys, Antarctica. *Journal of Petrology* **53**, 2567–2591

APPENDIX 1 (UNIT 10: CHAPTER 2)

1.1 UNIT 10 PERIDOTITE GRAPHIC LOGS

1.2 QUANTITATIVE TEXTURAL ANALYSIS DATA

1.3 WHOLE ROCK GEOCHEMISTRY

1.4 OLIVINE MINERAL CHEMISTRY

1.5 CR-SPINEL MINERAL CHEMISTRY

APPENDIX 2 (REACTIVE MELT FLOW: UNIT 10: CHAPTER 3)

2.1 MINERAL CHEMISTRY AND SR-ISOTOPES

APPENDIX 3 (WESTERN LAYERED INTRUSION: CHAPTER 4)

3.1 WESTERN LAYERED INTRUSION CROSS-SECTIONS

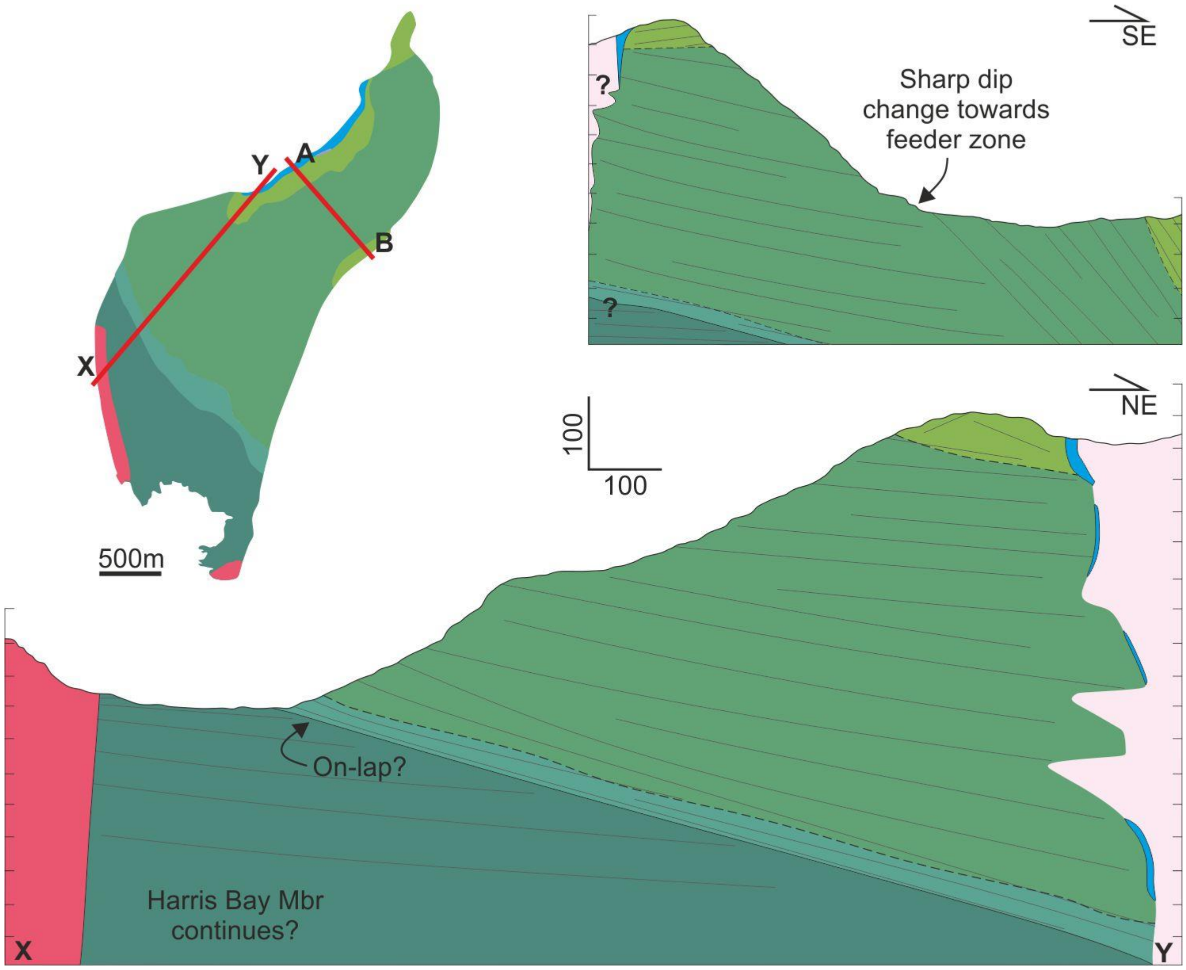

3.2 WESTERN LAYERED INTRUSION GRAPHIC LOGS

3.3 QUANTITATIVE TEXTURAL ANALYSIS

3.4 MINERAL CHEMICAL DATA (CR-SPINEL, CLINOPYROXENE, PLAGIOCLASE, SULPHIDES)